



Swansea University
Prifysgol Abertawe



Swansea University E-Theses

Rutford and Evans Ice Streams investigated using satellite radar interferometry and modelling.

Sykes, Helena Juliet

How to cite:

Sykes, Helena Juliet (2009) *Rutford and Evans Ice Streams investigated using satellite radar interferometry and modelling..* thesis, Swansea University.

<http://cronfa.swan.ac.uk/Record/cronfa42575>

Use policy:

This item is brought to you by Swansea University. Any person downloading material is agreeing to abide by the terms of the repository licence: copies of full text items may be used or reproduced in any format or medium, without prior permission for personal research or study, educational or non-commercial purposes only. The copyright for any work remains with the original author unless otherwise specified. The full-text must not be sold in any format or medium without the formal permission of the copyright holder. Permission for multiple reproductions should be obtained from the original author.

Authors are personally responsible for adhering to copyright and publisher restrictions when uploading content to the repository.

Please link to the metadata record in the Swansea University repository, Cronfa (link given in the citation reference above.)

<http://www.swansea.ac.uk/library/researchsupport/ris-support/>

Rutford and Evans Ice Streams investigated using Satellite Radar Interferometry and modelling

Helena Juliet Sykes

School of the Environment & Society
Swansea University

Submitted to the University of Wales in fulfilment of the
requirements for the Degree of Doctor of Philosophy

2009

ProQuest Number: 10805324

All rights reserved

INFORMATION TO ALL USERS

The quality of this reproduction is dependent upon the quality of the copy submitted.

In the unlikely event that the author did not send a complete manuscript and there are missing pages, these will be noted. Also, if material had to be removed, a note will indicate the deletion.



ProQuest 10805324

Published by ProQuest LLC (2018). Copyright of the Dissertation is held by the Author.

All rights reserved.

This work is protected against unauthorized copying under Title 17, United States Code
Microform Edition © ProQuest LLC.

ProQuest LLC.
789 East Eisenhower Parkway
P.O. Box 1346
Ann Arbor, MI 48106 – 1346



Abstract

The Rutford and Evans Ice Streams together drain over 150,000 km² of the West Antarctic Ice Sheet, a marine ice sheet with much of its bed below sea level. Ice streams make up only 13% of the Antarctic coastline, but are responsible for 90% of the discharge across the grounding line, where the ice starts to float. The Rutford and Evans Ice Streams were investigated using the remote sensing method of interferometry, which uses the phase difference between successive Synthetic Aperture Radar (SAR) satellite images to derive displacement in the line-of-sight (LOS) direction of the satellite and topography, which can be separated with further processing.

The grounding zones of both ice streams were mapped from clearly defined changes in vertical tidal motion visible in the interferograms. The Rutford grounding zone is dominated by a central pinning point, and the Evans grounding zone has a complex shape so that for much of the main trunk of the ice stream the east side is grounded and the west side is floating. The tidal signal for each ice stream was reconstructed, and the tidal ranges of the Rutford and Evans grounding zones are more than 6 m and 5 m respectively, both well above average for Antarctica. Vertical displacement observed in both single and double difference interferograms correlated well to changing tidal height. The width of the grounding zone modelled using an elastic beam was close to the observed grounding zone width for both ice streams.

Successful differential interferometry relies on the validity of the Constant Velocity Assumption (CVA), which states that interferograms differenced to derive topographic phase must contain the same displacement phase. However, due to the large tidal ranges at the grounding lines both ice streams, this assumption, which would be better termed the Constant Displacement Assumption (CDA), was violated to an extent which may be unprecedented in the literature.

The Rutford Ice Stream reached velocities of approximately 400 m a⁻¹ at its grounding line between 1992 and 1996, and the Evans Ice Stream appears to have decreased in speed from 750 m a⁻¹ in 1992 to 540 m a⁻¹ in 1996. This would have a significant effect on mass balance. The behaviour of this ice stream up to the present day clearly requires further investigation.

Declaration

This work has not previously been accepted in substance for any degree and is not being concurrently submitted in candidature for any degree.

Signed

Date

Statement 1

This thesis is the result of my own investigations, except where otherwise stated. Where correction services have been used, the extent and nature of the correction is clearly marked in a footnote(s).

Other sources are acknowledged by footnotes giving explicit references. A bibliography is appended.

Signed

Date

Statement 2

I hereby give consent for my thesis, if accepted, to be available for photocopying and for inter-library loan, and for the title and summary to be made available to outside organisations.

Signed

Date

Acknowledgments

This thesis would not have been possible without valuable contributions from many people.

My supervisors, Tavi Murray and Adrian Luckman, have been fantastic to work with. I can't thank either of them enough for having conceived of such an interesting project, for all their help and support throughout, and for everything that I have gained through being here.

Fellow glaciologists, remote sensing types and others in the Geography departments in both Swansea and Leeds have given me good advice and brightened my days. Suzanne Bevan deserves special mention for her expert advice on interferometry, as does Steve Shaw for his great IT support.

The data used in this project have come from a variety of sources. The VECTRA project has provided me with SAR satellite data by way of Andy Shepherd and Adrian Luckman. The tidal model came to me by way of Guðfinna Aðalgeirsdóttir (now at the Danish Meteorological Institute) from Keith Makinson and Hilmar Gudmundsson (both at the British Antarctic Survey) and Matt King (University of Newcastle). Thanks are also due to Helen Fricker (Scripps Institute of Oceanography, University of California San Diego) for ERS and ICESat altimeter data, and Hamish Pritchard (British Antarctic Survey) and Liz Morris (Scott Polar Research Institute, University of Cambridge) for GPS data. Much freely available data have been downloaded from the National Snow and Ice Data Center (Boulder, Colorado) and thanks are especially due to Jennifer Bohlander and Ted Scambos for making available the grounding line files to go with the MODIS Mosaic of Antarctica (MOA). Balance velocity data came from Jon Bamber (University of Bristol) and Xiaolan Wu (Central Michigan University) for which I am very grateful.

For financial assistance I am especially grateful to the School of the Environment and Society, Swansea University, especially for the fees waiver, and also to the School of Geography, University of Leeds and the Universities Superan-

uation Scheme (USS). I have benefitted greatly from conference funding from the Remote Sensing and Photogrammetry Society (RSPSoc), the British Branch of the International Glaciological Society (IGS), and the British Antarctic Survey (BAS). In 2005 I was privileged to attend a summer school on *Ice Sheets and Glaciers in the Climate System* in Karthaus, Italy, which was an amazing experience funded by the University of Utrecht and the European Union.

Thanks are also due to my examiners, Prof. Rory Walsh (Swansea University) and Prof. Dave Collins (University of Salford), for their extremely valuable comments and feedback, and to the chair of my examining board, Prof. Dave Clarke (Swansea University).

Finally I would like to thank my family and friends - I don't think they know exactly what I do, but they have put up with me being at university for eight years! I am eternally grateful to you all.

Contents

Abstract	i
Declaration and Statements	ii
Acknowledgments	iii
List of Figures	xiv
List of Tables	xvi
List of Symbols	xvii
List of Symbols	xvii
List of Abbreviations	xx
1 Introduction	1
1.1 Context	1
1.2 Ice streams	3
1.3 Aims	4
1.3.1 Objectives	7
1.4 Thesis Structure	8
2 The West Antarctic Ice Sheet	10
2.1 Introduction	10
2.2 Geography of the WAIS	10
2.3 History of the WAIS	14

2.3.1	The Marine Geologic Record	15
2.3.2	The Terrestrial Geologic Record	16
2.3.3	Modelling	16
2.3.4	Limitations of Models	17
2.4	Ice Streams	18
2.4.1	Driving Stress	19
2.4.2	Basal Conditions	21
2.4.3	Lateral Drag	25
2.4.4	Longitudinal Stress	26
2.4.5	Ice Stream Onsets	27
2.4.6	Ice Stream Tributaries	29
2.5	Oscillation Between Catchments	30
2.5.1	Surging	34
2.5.2	Timescales of Variability	35
2.6	The Grounding Zone	36
2.6.1	Grounding Zone Mapping	36
2.6.2	WAIS Grounding Lines	38
2.6.3	The Tide	39
2.7	The Future of the WAIS	42
2.7.1	Climate Change	42
2.7.2	Regional Climate	47
2.7.3	Implications	48
2.8	Study Area	50
2.8.1	The Rutford Ice Stream	50
2.8.2	The Evans Ice Stream	59
2.9	Summary	61
3	Synthetic Aperture Radar Interferometry	62
3.1	Introduction	62
3.2	Basic Principles of Radar	63
3.3	The European Remote-Sensing Satellites	65
3.3.1	ERS SAR System	66
3.4	Imaging	68

3.4.1	Backscatter	68
3.4.2	Range	69
3.4.3	Phase	70
3.4.4	Limitations of SAR	72
3.4.5	SAR Images	73
3.4.6	Resolution	73
3.5	The Interferometric Method	75
3.5.1	The Gamma Software	76
3.5.2	Data Format	76
3.5.3	Parameter File Generation	76
3.5.4	Orbital State Vectors	78
3.5.5	Processing Raw SAR Data	78
3.5.6	Offsets	82
3.5.7	Interferograms	85
3.5.8	The Baseline	88
3.5.9	Coherence	93
3.6	Phase Unwrapping	95
3.6.1	Branch-cut Region Growing	96
3.7	Geocoding	98
3.8	Differential Interferometry	99
3.8.1	2-Pass Differential Interferometry	101
3.8.2	3-Pass Differential Interferometry	101
3.8.3	Combination of Complex Interferograms	102
3.8.4	Height Map	105
3.8.5	Simulation of Topographic Phase	106
3.8.6	Separation of Topographic and Displacement Phase	107
3.8.7	Line-Of-Sight Velocities	108
3.8.8	Displacement Maps	108
3.8.9	Downslope Velocities	109
3.8.10	Dual Azimuth Interferometry	110
3.9	Constant Velocity Assumption	111
3.10	Grounding Zone Mapping	113
3.11	Application to Glaciology	114

3.12 Summary	118
4 Data and Models	119
4.1 Introduction	119
4.2 Satellite Data	119
4.2.1 Scenes of Rutford Ice Stream	122
4.2.2 Scenes of Evans Ice Stream	124
4.3 Ground Control	128
4.3.1 Global Positioning System (GPS) Data	128
4.3.2 Altimetry	131
4.3.3 Point Data Preprocessing	133
4.3.4 Digital Elevation Models	137
4.3.5 DEM Preprocessing	140
4.4 Balance Velocity Data	141
4.5 Tidal Model	143
4.5.1 Tidal Modelling	143
4.6 Elastic Beam Model	147
4.7 Summary	150
5 Ice Stream Displacements	151
5.1 Introduction	151
5.2 Interferogram Mosaics	151
5.3 DEM Creation	159
5.3.1 Ground Control	161
5.3.2 Simulation of Topographic Phase from DEMs	162
5.4 Displacements	165
5.4.1 Rutford Ice Stream	165
5.4.2 Evans Ice Stream	170
5.5 Estimated Ice Stream Discharge	173
5.6 Comparison to Balance Velocities	174
5.7 Summary	175
6 The Grounding Zone	176
6.1 Introduction	176

6.2	Mapping the Grounding Zone	177
6.3	Tidal Model Results	181
6.3.1	Rutford Ice Stream	181
6.3.2	Evans Ice Stream	185
6.3.3	Vertical Tidal Displacement	189
6.4	Elastic Beam Model Results	192
6.5	Summary	202
7	Discussion	203
7.1	Introduction	203
7.2	Ice Stream Velocities	204
7.2.1	Ice Stream Discharge	205
7.2.2	Comparison to Balance Velocities	206
7.2.3	Implications	209
7.3	The Interferometric Method	210
7.3.1	Uncertainties in Velocity	210
7.3.2	Interferometric Pairs	211
7.3.3	Differential Interferometry	213
7.3.4	Failure of the Constant Velocity Assumption	214
7.3.5	Comparison Between DEMs	219
7.3.6	Ground Control	221
7.3.7	Implications	223
7.3.8	Displacement Maps	223
7.4	The Grounding Zone	226
7.4.1	The Rutford Ice Stream Grounding Zone	226
7.4.2	The Evans Ice Stream Grounding Zone	228
7.4.3	Are These Grounding Zones Typical?	232
7.5	The Tide	234
7.5.1	Vertical Ice Stream Motion	236
7.6	Elastic Beam Modelling	239
7.7	Summary	240

8	Conclusions and Further Work	241
8.1	Introduction	241
8.2	Summary of Results	242
8.2.1	Ice Stream Velocities	242
8.2.2	Interferometry	243
8.2.3	Grounding Zones	245
8.2.4	The Tide	246
8.3	Further Work	246
8.4	Final Remarks	248
	References	249

List of Figures

1.1	The location of the Rutford and Evans Ice Streams.	4
2.1	The location of the West Antarctic Ice Sheet (WAIS).	11
2.2	The main ice streams draining the WAIS.	13
2.3	An ice shelf grounding zone	37
3.1	Amplitude, wavelength and phase.	67
3.2	Imaging radar geometry.	68
3.3	Correspondence between phase cycles	71
3.4	A flow chart to show the preprocessing steps required for data which arrived raw, and data which arrived in SLCI format.	77
3.5	An example of a coherence image, a raw interferogram and a flat- tened interferogram.	91
3.6	Example of grounding zone mapping for the Rutford Ice Stream. .	115
4.1	Frames of the Rutford Ice Stream.	122
4.2	Frames of the Evans Ice Stream.	125
4.3	GPS stations on and around the Rutford Ice Stream.	129
4.4	GPS stations in the Evans Ice Stream area.	130
4.5	Altimetry data of the study area.	132
4.6	A flow chart to show the steps taken in preprocessing Ground Control Point data for use in interferometry.	134
4.7	A flow chart to show the steps taken in preprocessing DEM data for use in interferometry.	140
4.8	The location where the tidal model was run for the Evans Ice Stream.	145

4.9	The location where the tidal model was run for the Rutford Ice Stream.	146
4.10	Schematic representation of the elastic beam model	149
5.1	Interferogram mosaic of the Rutford Ice Stream, 1994, showing the main features of the study area.	152
5.2	Interferogram mosaic of the Rutford Ice Stream, 1992	154
5.3	Interferogram mosaic of the Rutford Ice Stream, 1994, using the first pair from frame 008_5337.	154
5.4	Interferogram mosaic of the Rutford Ice Stream, 1994, using the second pair from frame 008_5337.	155
5.5	Interferogram mosaic of the Rutford Ice Stream, 1996, using the first tandem pairs.	155
5.6	Interferogram mosaic of the Rutford Ice Stream, 1996, using the second tandem pairs.	156
5.7	Interferogram mosaic of the Evans Ice Stream, 1994, showing the main features of the study area.	157
5.8	Interferograms of the Evans Ice Stream in 1992.	158
5.9	Interferogram mosaic of the Evans Ice Stream, 1996.	158
5.10	A “topography-only” interferogram for the 1994 triplet of frame 008_5337 of the Rutford Ice Stream.	159
5.11	“Topography-only” interferograms for frames 023_5229 and 392_5553 of the Evans Ice Stream.	160
5.12	Topography-only interferogram and height map, frame 080_5265.	161
5.13	Simulated topographic phase using the ERS DEM for frame 008_5319.	163
5.14	Simulated topographic phase using the ICESat DEM for frame 108_5337.	164
5.15	Horizontal displacement maps for the onset region of the Rutford Ice Stream for frame 023_5265 in 1992 and 1994 and frame 080_5265 in 1996.	165
5.16	Horizontal displacement for frame 008_5319 of the Rutford Ice Stream, 1996.	167

5.17	Horizontal and vertical displacement for frame 008_5337 of the Rutford Ice Stream grounding zone, 1994.	168
5.18	Vertical displacement for frame 108_5337 of the Rutford Ice Stream grounding zone, 1996.	169
5.19	Horizontal displacements for frame 023_5229 of the Evans Ice Stream in 1992 and 1994.	170
5.20	Horizontal displacement for frame 020_5553 of the Evans Ice Stream, 1994.	171
5.21	Horizontal displacements for frames 392_5553 and 206_5535 of the Evans Ice Stream, 1996.	172
5.22	Vertical displacement for frame 037_5265 of the Evans Ice Stream grounding zone, 1994.	173
6.1	The grounding zone of the Rutford Ice Stream, as mapped from interferometry.	178
6.2	Interferograms of the Rutford Ice Stream showing different grounding zone features.	179
6.3	The grounding zone of the Evans Ice Stream, as mapped from interferometry.	180
6.4	Tidal signal for the Rutford Ice Stream, 1992.	182
6.5	Tidal signal for the Rutford Ice Stream, 1994.	182
6.6	Tidal signal for the early part of the 1996 study period for the Rutford Ice Stream.	183
6.7	Tidal signal for the later part of the 1996 study period for the Rutford Ice Stream.	183
6.8	A comparison between the tidal signal reconstructed for the Rutford Ice Stream from GPS data and the CATS 02.01 model.	185
6.9	Tidal signal for the Evans Ice Stream, 1992.	186
6.10	Tidal signal for the Evans Ice Stream, 1994.	186
6.11	Tidal signal for the early part of the 1996 study period for the Evans Ice Stream.	187
6.12	Tidal signal for the later part of the 1996 study period for the Evans Ice Stream.	187

6.13	Vertical displacements from interferometry compared to modelled tidal height changes for the Rutford and Evans Ice Streams. . . .	191
6.14	Grounding zone width modelled by an elastic beam for the Rutford Ice Stream - ice thickness 1648 m	193
6.15	Grounding zone width modelled by an elastic beam for the Rutford Ice Stream - ice thickness 1929 m	194
6.16	Grounding zone width modelled by an elastic beam for the Rutford Ice Stream - ice thickness 1955 m	195
6.17	Grounding zone width modelled by an elastic beam for the Evans Ice Stream - ice thickness 1017 m	196
6.18	Grounding zone width modelled by an elastic beam for the Evans Ice Stream - ice thickness 1913 m	197
6.19	Spring and neap tidal ranges used to model the width of the grounding zone of the Rutford Ice Stream.	200
7.1	Balance velocities for the Rutford and Evans Ice Stream area, taken from Bamber <i>et al.</i> (2000c)	206
7.2	Balance velocities for the Rutford and Evans Ice Stream area, taken from Wu and Jezek (2004)	207
7.3	A classified map to show the difference between the ICESat and RAMP DEMs for the study area.	220
7.4	Versions of the grounding line of the Rutford Ice Stream	227
7.5	Versions of the grounding line of the Evans Ice Stream	230

List of Tables

2.1	The old and new names for the Siple Coast Ice Streams.	19
2.2	Principal tidal coefficients	40
2.3	The main characteristics of the Rutford and Evans Ice Streams.	60
3.1	Summary of Gamma routines and options used in single difference interferometry, and geocoding, in this study.	100
3.2	Summary of Gamma routines and options used in differential interferometry in this study.	112
4.1	SAR scenes for the Rutford Ice Stream.	123
4.2	SAR scenes for the Evans Ice Stream.	126
4.3	Image pairs, triplets and quads for differential interferometry.	127
5.1	RMS errors of control points used to refine the baseline of the topography-only interferogram of frame 080_5265.	162
5.2	Downslope velocities for the onset region of the Rutford Ice Stream from 1992 to 1996.	166
6.1	Tidal heights at the time of acquisition of each SAR image of the Rutford Ice Stream.	184
6.2	Tidal height differences between scenes making up interferometric pairs, triplets and quads of the Rutford Ice Stream.	184
6.3	Tidal heights at the time of acquisition of each SAR image of the Evans Ice Stream.	188
6.4	Tidal height differences between scenes making up interferometric pairs, triplets and quads of the Evans Ice Stream.	188

6.5	Altitudes of ambiguity for each pair and vertical change, assuming all change is vertical, for the Rutford Ice Stream.	190
6.6	Altitudes of ambiguity for each pair and vertical change, assuming all change is vertical, for the Evans Ice Stream.	190
6.7	The width of the grounding zone of the Rutford Ice Stream as modelled using an elastic beam.	198
6.8	The width of the grounding zone of the Evans Ice Stream as modelled using an elastic beam.	198
7.1	Published velocities for the Rutford and Evans Ice Streams.	204
7.2	Average balance velocities across both ice streams.	208
7.3	Comparison of elevations from different datasets.	221
7.4	Desirable characteristics of SAR data, and actual characteristics of the SAR data used in this study.	224

List of Symbols

Symbol	
α	Absorbed radiation
γ	Cross correlation coefficient
ΔT	Temporal baseline, in days
δ_ϕ	Phase noise
δ_{az}	Azimuth resolution
δ_{cr}	Cross range resolution
δ_r	Range resolution
δ_z	Altitude of ambiguity
ϵ	Coherence
θ	Incidence angle
κ	Surface slope
λ	Wavelength
μ	Aperture angle
ρ	Density
σ	Radar cross section
σ^0	Radar scattering per unit area
τ_b	Basal shear stress
τ_d	Driving stress
ϕ	Interferometric phase
ω	Look angle
A	Area of resolution cell

A_0T	Instantaneous sea level
A_s	Target receiving area
B	Pulse bandwidth
B_{para}	Parallel baseline
B_{perp}	Perpendicular baseline
c	Speed of light, $3.00 * 10^8$ m s ⁻¹ in a vacuum
$Disp_{LOS}$	Displacement in the line-of-sight direction
$Disp_{slope}$	Displacement in the downslope direction
E	Young's modulus
e	Elevation of surface
f	Frequency
G	Antenna gain
g	Gravitational acceleration
g_s	Antenna gain in the direction of the sensor
H_e	Height error
H_s	Altitude of sensor
h	Ice thickness
I	Real, in-phase, component of complex number
k	Radar wavenumber
L	Azimuthal length of antenna
Q	Imaginary, quadrature, component of complex number
P_R	Returned power
P_T	Transmitted power
q	Angle between look direction and flow direction
R	Slant range
R_T	Range to target
t	Time taken for return of transmitted SAR signal
U_b	Basal sliding
V	Amplitude

- v Poisson's ratio
- v_n Non-constant displacement
- v_{rel} Relative velocity between sensor and target
- w Vertical displacement of ice shelf from mean position
- z_1 Complex pixel value in image 1
- z_2 Complex pixel value of conjugate pixel in image 2

List of Abbreviations

Abbreviation / Acronym

AAD	Australian Antarctic Division
ACC	Antarctic Circumpolar Current
ADD	Antarctic Digital Database
AIS	Antarctic Ice Sheet
AMM	Antarctic Mapping Mission(s)
ASTER	Advanced Spaceborne Thermal Emission and Reflection Radiometer
BAS	British Antarctic Survey
BP	Before Present
CADA	Circum-Antarctic Data Assimilation
CATS	Circum-Antarctic Tidal Simulation
CCI	Cross Correlation of Intensities
CDA	Constant Displacement Assumption
CVA	Constant Velocity Assumption
CDW	Circumpolar Deep Water
DEM	Digital Elevation Model
DIFF/GEO	Differential Interferometry and Geocoding (Gamma)
DISP	Display (Gamma)
EAIS	East Antarctic Ice Sheet
EM	Electro-Magnetic
ENSO	El Niño Southern Oscillation

ENVI	The ENvironment for Visualizing Images
ERS	European Remote-Sensing Satellite(s)
ESA	European Space Agency
ESRIN	European Space Research INstitute
FRIS	Filchner-Ronne Ice Shelf
FFT	Fast Fourier Transform
FV	Fringe Visibility
GCM	General Circulation Model
GCP	Ground Control Point
GIS	Geographic Information System
GLAS	Geoscience Laser Altimeter System
GPS	Global Positioning System
GRACE	Gravity Recovery And Climate Experiment
ICESat	Ice, Cloud and land Elevation SATellite
IDL	Interactive Data Language
IDW	Inverse Distance Weighted
InSAR	INterferometric Synthetic Aperture Radar
IPCC	Intergovernmental Panel on Climate Change
ISP	Interferometric SAR Processor (Gamma)
LAT	Land Application Tools (Gamma)
Lidar	LIght Detection And Ranging
LGM	Last Glacial Maximum
LOS	Line Of Sight
MLBF	Multi Look Beat Frequency
MLCC	Multi Look Cross Correlation
MLI	Multi Look Image
MOA	Mosaic Of Antarctica
MODIS	MODerate resolution Imaging Spectroradiometer
MSP	Modular SAR Processor (Gamma)

NSIDC	National Snow and Ice Data Center
OSU91A	Ohio State University geoid (1991)
PAF	Processing Archive Facility
PRF	Pulse Repetition Frequency
PCA	Principal Components Analysis
RA	Radar Altimetry/Altimeter
RABID	Rutford Area Base of Ice Drilling
Radar	RAdio Detection and Ranging
RAMP	Radarsat Antarctic Mapping Project
RAR	Real Aperture Radar
RES	Radio Echo Sounding
RMSE	Root Mean Square Error
SAR	Synthetic Aperture Radar
SIR	Shuttle Imaging Radar
SLR	Satellite Laser Ranging
SLAR	Side Looking Airborne Radar
SMA	Spatially Moving Average
SRI	Satellite Radar Interferometry/ Synthetic Aperture Radar Interferometry
SLCI	Single Look Complex Image
SNR	Signal to Noise Ratio
TCN	Tangential Cross Normal
USGS	United States Geological Survey
WAIS	West Antarctic Ice Sheet
WGS84	World Geodetic System (1984)

Chapter 1

Introduction

1.1 Context

The Antarctic continent is 98% covered by an ice sheet which contains 91% of the world's ice and stores over 80% of the world's fresh water (LARA Steering Committee, 2005; Swithinbank, 1988). Including its ice shelves, the Antarctic Ice Sheet (AIS) covers an area of 13 million km² and contains 90% of the planet's freshwater ice (Vaughan and Spouge, 2002). The world's last two major ice sheets, the Antarctic and Greenland, together dominate uncertainties in future sea level predictions (Alley *et al.*, 2005). The Antarctic ice sheet contains 25.4 million km³ of ice, equivalent to 57 metres of sea level rise (Lythe *et al.*, 2001). While the contribution of the West Antarctic Ice Sheet (WAIS) would be slightly less than 10% of this total, it is much more likely to undergo collapse than the much larger East Antarctic Ice Sheet (EAIS), which contains 90% of the ice in Antarctica (Bamber *et al.*, 2000c), because the WAIS is a marine ice sheet, terminating in ice shelves and ice cliffs, and because much of its bed lies below sea level. Although the conclusion in the literature over the past three decades has increasingly been that collapse of the WAIS, i.e. the complete loss of the ice sheet, is unlikely, it is only relatively recently that the contribution of individual ice streams to the stability of the WAIS has been examined.

The future of the world's ice masses is of increasing importance under conditions of anthropogenic climate change. Mean global sea level rose $1.8 \pm 0.5 \text{ mm a}^{-1}$ over the period 1961 to 2003 and $3.1 \pm 0.7 \text{ mm a}^{-1}$ over the period 1991 to 2003, with the highest rates in the most recent years. Even if atmospheric greenhouse gases were to stabilise at their current levels, warming and sea level rise would continue for several centuries. For the period 1993 to 2003, 38% of the current sea level rise came from the melting of terrestrial ice (1.19 mm a^{-1}), with the rest coming from thermal expansion of ocean water (1.6 mm a^{-1}), although there is a 0.3 mm a^{-1} discrepancy between the observed sea level rise and the total of the estimated climate contributors. Of the cryospheric contribution, 65% ($0.77 \pm 0.22 \text{ mm a}^{-1}$) was from mountain glaciers and ice caps, rather than the two main ice sheets ($0.21 \pm 0.07 \text{ mm a}^{-1}$ for Greenland and $0.21 \pm 0.35 \text{ mm a}^{-1}$ for Antarctica), although the contribution of the Antarctic and Greenland ice sheets has increased over the past decade because of dynamic mass loss not generally accounted for by models, and the WAIS contributes 0.2 mm a^{-1} (Intergovernmental Panel on Climate Change: Fourth Assessment Report, 2007; LARA Steering Committee, 2005; Meier *et al.*, 2007). A reconstruction of sea level rise based on tide gauge data from 1870 to 2004 showed a 195 mm increase in mean sea level, with a 20th century acceleration of $0.013 \pm 0.006 \text{ mm a}^{-2}$, which, if it were to continue, would lead to sea level rise from 1990 to 2100 of between 280 and 340 mm (Church and White, 2006). Although the Intergovernmental Panel on Climate Change (IPCC) predicts that Antarctica will gain mass in future, they highlight the limited understanding of the nature and magnitude of dynamical changes in the ice sheet and state that if complete deglaciation of the WAIS were to occur, sea level would rise by 5 metres (Alley and Bindshadler, 2001; IPCC Working Group I, 2007; Joughin *et al.*, 1999; Lythe *et al.*, 2001).

1.2 Ice streams

Ice streams are channels of fast moving ice draining ice sheets and ice caps by transporting ice outwards from the interior (Benn and Evans, 1998). Ice streams differ from outlet glaciers in that outlet glaciers are bounded by rock whereas ice streams are bounded by slow moving ice which is frozen to its bed. As ice streams move up to two orders of magnitude faster than the surrounding ice, heavily crevassed zones up to 5 km wide are formed at their shear margins (Hooke, 2005; Smith, 1997c). Ice streams may, however, form the heads of outlet glaciers, as is the case for Jakobshavn Isbræ in Greenland, and it is noted that the Rutford Ice Stream, part of the study area for this project, is bounded on one side by ice and on the other by rock (Paterson, 1994). The driving stresses (discussed in section 2.4.1) of outlet glaciers are also much higher, usually by more than an order of magnitude (Joughin *et al.*, 2002). In this thesis, the term ice streams will be used to cover both ice streams and outlet glaciers, in keeping with much of the rest of the literature.

Ice streams and outlet glaciers make up only 13% of the coastline of the Antarctic Ice Sheet, while being responsible for approximately 90% of the discharge across the grounding line (Drewry *et al.*, 1982; McIntyre, 1985). They discharge about 90% of the inland accumulation of the WAIS (Doake *et al.*, 2001) and as such have a major influence on mass balance, with variations in their velocities determining the volume of the ice sheet by regulating its extent and thickness. Much still remains to be understood about Antarctic ice streams and their role (Doake *et al.*, 2001). It is therefore clear that more work is needed to examine the role of individual ice streams in the dynamics and overall stability of the WAIS. The remoteness and inaccessibility of the Antarctic continent make remote sensing an attractive approach because of the extensive spatial and temporal coverage of satellite data.

1.3 Aims

This project aims to contribute to the glaciological community's understanding of the dynamics and stability (or otherwise) of the WAIS by examining two of its ice streams, the Rutford and Evans Ice Streams (figure 1.1), using remote sensing and modelling methods.

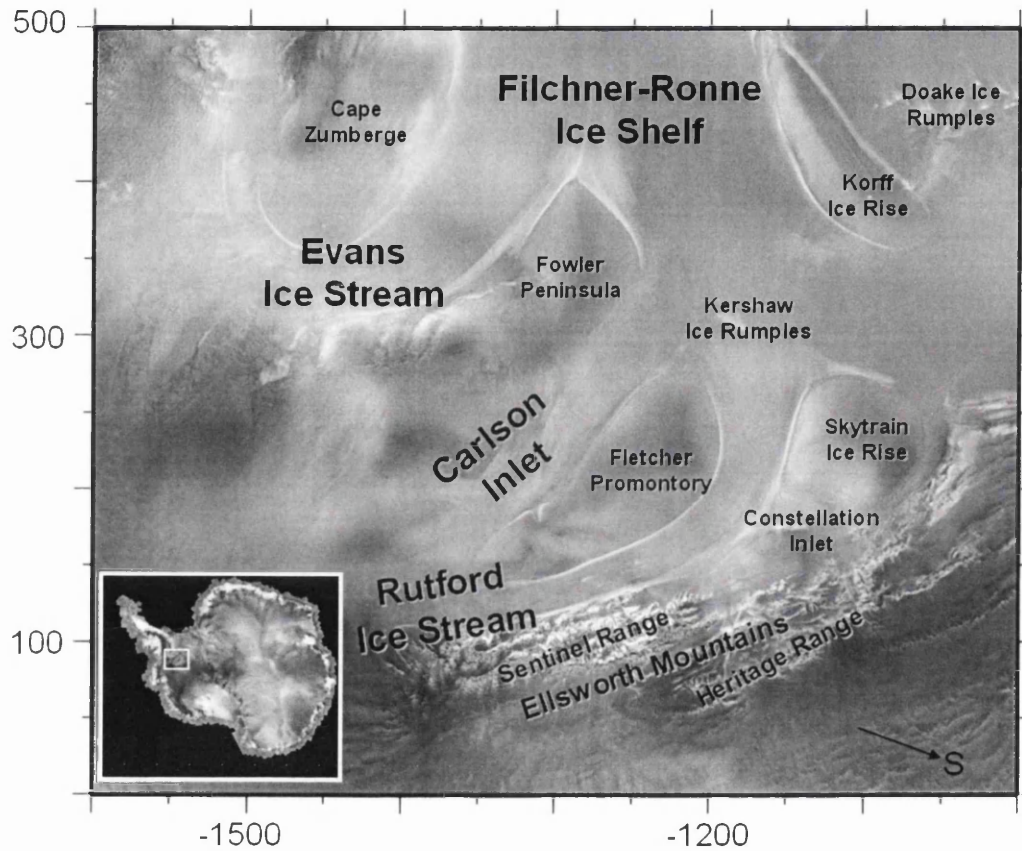


Figure 1.1: The location of the Rutford and Evans Ice Streams. Coordinates are Polar Stereographic, in kilometres, with the origin at the South Pole. The background image is taken from the RADARSAT Antarctic Mapping Project (RAMP) mosaic of Jezek and the RAMP Product Team (2002).

The Rutford Ice Stream was chosen for investigation in this study due to its long history of previous work using both field and remote sensing methods (section 2.8.1). It is in the British sector of Antarctica, and has been a field site for over thirty years (Smith, 2006b). Although it was initially chosen for fieldwork due to logistical considerations (Stephenson and Doake, 1982) rather than for glaciological or methodological reasons, study of the Rutford Ice Stream has produced important work such as Goldstein *et al.* (1993)'s pioneering use of Satellite Radar Interferometry (SRI), one of the major methods used in this study, to derive ice velocities, and to the discovery of the highest tidal range in Antarctica (Doake, 1992; Padman *et al.*, 2002), which is also further investigated in this study.

The Evans Ice Stream is part of the same glaciological system as Rutford, lying on the same coast and draining into the same ice shelf (figure 1.1): in between lies a former ice stream, Carlson Inlet, which is currently slow-moving and frozen to its bed (discussed further in section 2.5). The Evans Ice Stream was chosen for investigation as part of a comparative study for the opposite reason to Rutford, namely that it has been the subject of little previously published work. The Evans Ice Stream also lies in the British sector of Antarctica, but has received little previous research attention, partly because British resources had been directed at Rutford and partly because when work did take place on the Evans Ice Stream, field conditions were found to be highly unfavourable (section 2.8.2). It was felt that more should be learnt about this major ice stream. Previous work examining neighbouring ice streams which form part of the same drainage system has proved interesting, and found important similarities, differences and linkages between them (section 2.5). A comparative study of the flow of these two near-neighbour ice streams was therefore carried out.

Because of the size of these glaciological features, which have catchments tens of thousands of square kilometres in size, and the inaccessible nature of the area, the Rutford and Evans ice streams are highly suited to investigation using remote sensing and modelling methods. Active microwave sensors such as the European Remote-Sensing Satellites ERS-1 and ERS-2 used in this study, operated by the European Space Agency (ESA), transmit their own source of energy for imaging and are therefore especially suited to investigating the polar regions as these

sensors are not affected by cloud and can image through the polar night. Satellite Radar Interferometry (SRI), which uses the phase difference between successive Synthetic Aperture Radar (SAR) images from satellites such as ERS-1 and ERS-2 to derive ice displacement and topography, will be used in this study to derive ice stream velocities and to map the grounding zones of both ice streams. The grounding zone, where the ice starts to float, is the transition from an ice stream to an ice shelf, and is an important control on ice sheet stability, discussed further in section 2.6. Its location, width and tidal range should therefore be known as accurately as possible.

Previously published versions of the grounding zones of both ice streams were inconsistent (as discussed further in sections 7.4.1 and 7.4.2), and this study therefore aims to accurately locate the grounding zones of both ice streams and to investigate the effects of the vertical tidal forcing taking place there. Tidal modelling will be used to show the tidal range of each ice stream, and the tidal height difference for each interferogram produced using SRI. Elastic beam modelling will be used to model the width of the grounding zone under different conditions and compare this to the observed width of the grounding zone.

This study also aims to examine the conditions under which Synthetic Aperture Radar (SAR) interferometry, or Satellite Radar Interferometry (SRI), of ice streams, floating ice shelves, and the transition between these areas, the grounding zone, is successful, and to use this to advise other remote sensing scientists working in similar fields. The effects that tidal motion of ice stream grounding zones have on SRI will also be investigated. One of the key principles of differential interferometry, a technique which is used to isolate the signal from displacement in the line-of-sight direction of the satellite from that due to scene topography, in order to separate the two and derive velocity fields for ice streams, is the Constant Velocity Assumption (CVA, discussed further in sections 3.9 and 7.3.4). This study will present investigations into the effects of the failure of the CVA due to tidal motion of ice stream grounding zones on interferometry, the errors it introduces, and the implications of this for future work.

This thesis also aims to highlight discrepancies between other datasets of the

study area, some of which are widely used in the glaciological community. Inaccuracies in these datasets will clearly lead to inaccuracies in any work using them as an input or a means of validation. These investigations include comparing Digital Elevation Models (DEMs) of the area, which were a potential source of ground control in this study, and other elevation data for the area, as well as comparing previously published grounding line locations for these two ice streams to the grounding line locations defined in several major datasets and models.

These aims will be met through the following specific research objectives:

1.3.1 Objectives

- To establish the velocity of the Rutford and Evans Ice Streams over the time period for which the European Remote-Sensing Satellites, ERS-1 and ERS-2, had suitably short orbital repeat periods to carry out interferometry, a technique which utilises the phase difference between successive radar satellite images, 1992 to 1996.
- To use these velocities, in combination with other data, to estimate the discharge of both ice streams.
- To compare these velocities to published balance velocities in order to assess the state of health of this sector of the ice sheet.
- To use interferometry to map the grounding zones of both ice streams, and to compare this to published locations.
- To examine the effects of vertical tidal motion on the grounding zones of both ice streams, through the use of tidal modelling to reconstruct the tidal signal through the study period and calculate the tidal height difference for each interferogram.
- To model the width of the grounding zones using an elastic beam; and compare this to the observed width mapped from interferometry.

- To assess likely sources of error in the measurements made, focussing particularly on the effect vertical tidal motion has on one of the key assumptions upon which differential interferometry relies, the Constant Velocity Assumption (CVA).
- To fit the findings of this project into the context of current work on other WAIS ice streams.

1.4 Thesis Structure

Following on from this chapter, Chapter Two presents a review of the relevant literature, giving more detail on the characteristics and recent glacial history of WAIS, and discussing the main characteristics of WAIS ice streams and the implications of previous research on them. The grounding zone, where the ice starts to float, will be defined and its importance highlighted. The future of the ice sheet, and its ice streams and shelves, under conditions of climate change will be discussed, and finally Chapter Two introduces the two study areas, the Rutford and Evans Ice Streams.

Chapter Three describes the principles of Synthetic Aperture Radar (SAR) and the processing chain of the main method used in the project, interferometry, as well as reviewing the literature, giving examples of studies where this method has previously been successfully applied to the cryosphere. Chapter Four opens by highlighting the constraints on the selection of appropriate source data, and cataloguing the satellite scenes used in this study. The sources of ground control used to refine the baseline for interferometry - Global Positioning System (GPS), spaceborne radar and lidar altimetry - and the Digital Elevation Models (DEMs) used to simulate topographic phase - are discussed, along with their limitations. Two balance velocity datasets, which were compared to the velocities derived from interferometry, are described. Finally, two tidal models and an elastic beam model used in this study are outlined.

Chapters Five and Six present the results of this study. Chapter Five presents in-

terferogram mosaics of both ice streams for the three study periods and highlights the main features, before presenting the results from differential interferometry. This was used to create DEMs and derive ice stream velocities, which were then compared to published balance velocities. Chapter Six investigates the grounding zones of both ice streams, which were mapped from interferometry, and presents the results of the tidal and elastic beam models.

Chapter Seven discusses the results of the study, examining the Rutford and Evans Ice Streams in the context of other WAIS streams. The focus is especially on the grounding zones of both ice streams and their large tidal ranges, which complicated the interpretation of velocities. The limitations of the method are also discussed, focussing especially on the difficulties of carrying out differential interferometry in areas with a high tidal range, leading to the failure of the CVA, and the implications of this for other research. Finally, Chapter Eight presents the conclusions of the study and makes suggestions for further work.

Chapter 2

The West Antarctic Ice Sheet

2.1 Introduction

This chapter will review the relevant literature on the recent glacial history, present conditions and potential future behaviour of the West Antarctic Ice Sheet (WAIS). The characteristics of ice streams and their most important controls will be described, with examples of variability at different timescales and of oscillation between catchments. The nature of the grounding zone of the ice sheet, where it starts to float, and the importance of mapping it, will be discussed, as it is an important control on ice sheet stability. The characteristics of the tidal signal will be explained, as many ice streams have shown tidally induced motion. The future of the WAIS and its ice streams and ice shelves will be discussed in the context of climate change. Finally, the focus will shift onto reviewing previous work on the two study areas of the project, the Rutford and Evans Ice Streams.

2.2 Geography of the WAIS

The WAIS has been the focus of much recent research concerning its past and present stability, in order to assess that of its future. The WAIS lies south of

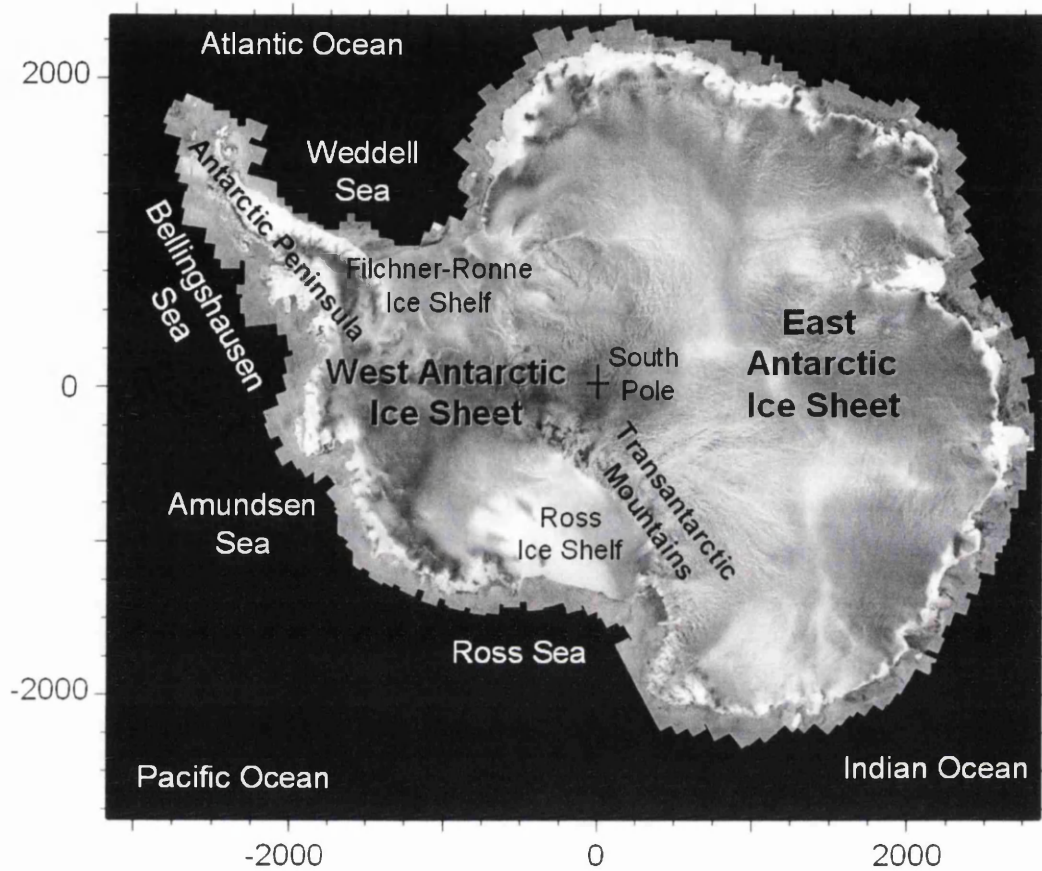


Figure 2.1: The location of the West Antarctic Ice Sheet (WAIS). Coordinates are Polar Stereographic, in kilometres, with the origin at the South Pole. The background image is taken from the RADARSAT Antarctic Mapping Project (RAMP) mosaic of Jezek and the RAMP Product Team (2002).

approximately 72°S, between the longitudes of 45°W and 165°E (Colbeck, 1980), and covers an area of 1,809,760 km² (Drewry *et al.*, 1982). The bed of the WAIS is irregular and slopes down toward the centre of the ice sheet, but more significantly, lies mostly below sea level, and as the WAIS is a marine ice sheet, terminating in ice shelves and ice cliffs rather than on land, these factors make it potentially unstable (Paterson, 1994). The stability of the WAIS, and therefore the discharge of its ice streams, is of global concern due to the potential effect on eustatic sea level should the WAIS suffer retreat or collapse (Parizek *et al.*, 2003).

Geologically the WAIS is located on top of the West Antarctic rift system (Anandakrishnan and Winberry, 2004) and there is active volcanism beneath the WAIS, although the locations of subglacial volcanoes have still to be identified (LARA Steering Committee, 2005). Geothermal heat flow is three times higher and much more variable for the WAIS than the East Antarctic Ice Sheet (EAIS), as the crust beneath the WAIS is much thinner. Geothermal heat accumulates at the base of ice sheets as the ice acts as an insulator if it is sufficiently thick, causing melting, and therefore may have an important effect on the overall stability of the ice sheet (Bindschadler, 2006; Shapiro and Ritzwoller, 2004; Van der Veen, 1999).

The bed of the WAIS is a former ocean basin and the WAIS is underlain by a thick layer of marine sediment. The topography of the bed reaches depths of more than 2000 m below sea level, and would mostly remain below sea level after isostatic rebound following the complete removal of the ice (Paterson, 1994; Van der Veen, 1999). This is in contrast to the EAIS. The flow of the WAIS is also much more complex than that of the EAIS, which moves mostly by internal deformation (Van der Veen, 1999). Although the conclusion in the literature has increasingly been that collapse of the WAIS is unlikely, many of its ice streams, when viewed individually, exhibit greater potential for instability than the ice sheet when viewed as a whole.

The WAIS is drained by three main groups of ice streams and outlet glaciers (figure 2.2): the Siple Coast ice streams, draining into the Ross Ice Shelf; the Pine Island and Thwaites Glacier area, draining into the Amundsen and Bellingshausen

Seas; and the Weddell Sea sector, draining into the Ronne Ice Shelf, part of which is the study area for this research (Bentley, 1998; Bindschadler, 2006).

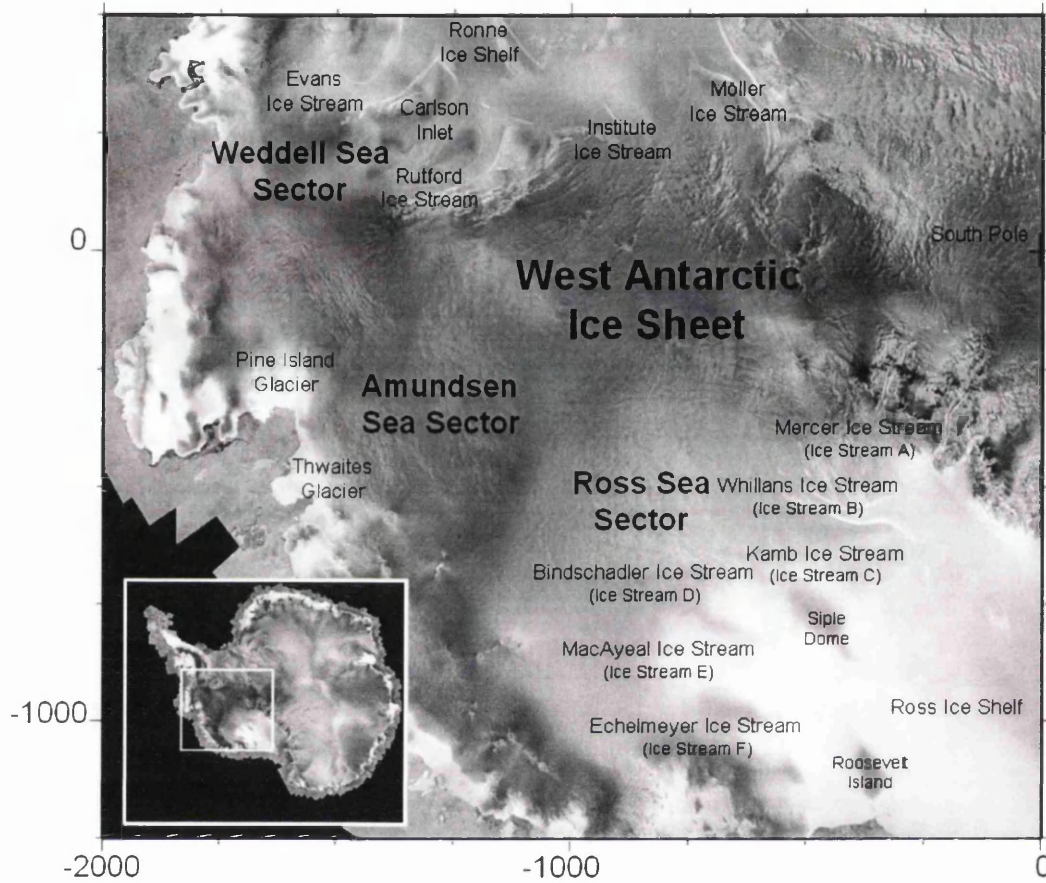


Figure 2.2: The main ice streams draining the WAIS. Coordinates are Polar Stereographic, in kilometres, with the origin at the South Pole. The background image is taken from the RADARSAT Antarctic Mapping Project (RAMP) mosaic of Jezek and the RAMP Product Team (2002).

2.3 History of the WAIS

The Antarctic Ice Sheet formed after the continent was isolated tectonically and surrounded by ocean, allowing the initiation of the Antarctic Circumpolar Current (ACC). The East Antarctic became glaciated in the Eocene, 40 million years BP (Ma) (Anderson, 1999). Isolated ice caps existed in West Antarctica through the Oligocene (35.4 to 23.3 Ma) and early Miocene (beginning 23.3 Ma), and these came together in the late Miocene prior to the beginning of the Pliocene approximately 5.2 Ma (Anderson and Shipp, 2001; Harland *et al.*, 1990). By 15 Ma the Antarctic ice sheet was half its present volume, and may have exceeded its present volume by 12 Ma, when large ice caps were also present on the Antarctic Peninsula. Polar conditions were established on the continent by 10 Ma (Anderson, 1999).

The previous behaviour of the ice sheet may be used to infer that of its future. During the Pleistocene the EAIS and WAIS were both much thicker than at present and advanced to the continental shelf edge several times; the Vostok ice core, and ocean sediment cores from the Weddell sea, show the pattern of advance and retreat to be synchronous with that of Northern Hemisphere glaciation (Anderson, 1999). However, it is not known whether the WAIS survived interglacials warmer than the present one (Oppenheimer, 1998), and marine diatom evidence from beneath the WAIS shows that the ice sheet has been absent at least once in a relatively recent Pleistocene interglacial; the fact that sea level was 6 m higher during the Eemian interglacial, 120,000 years before present (BP), may suggest the absence of the WAIS was at this time (Vaughan and Spouge, 2002), although the Greenland Ice Sheet may also have been partially or wholly responsible (Letréguilly *et al.*, 1991; Van der Veen, 1999).

At the Last Glacial Maximum (LGM), 18,000 BP, the WAIS had a much greater horizontal and vertical extent than at present, although the present Antarctic ice sheet as a whole is not much smaller than it was during the last glacial period, retaining about 80% of its volume (Anderson, 1999). The WAIS is presently in a state of retreat following the LGM, and will consequently continue to contribute

to eustatic sea level rise for some time (Alley and Bindshadler, 2001). It is the nature of the present retreat of the WAIS which is of the most significance in predicting the nature of any future retreat. Evidence on the past behaviour of the ice sheet may come from several sources, including the marine and terrestrial geologic records, and modelling.

2.3.1 The Marine Geologic Record

During the retreat of the WAIS since the LGM, features were left behind on the exposed continental shelf, the present day sea bed. Subglacial features left behind on the sea bed showed that at the LGM, the WAIS had advanced to the continental shelf break in the eastern and central Ross Sea, and to less than 100 km from the continental shelf break in the western Ross Sea, the Amundsen Sea, and the Bellingshausen Sea (Anderson and Shipp, 2001).

Features on the exposed continental shelf indicate that the ice sheet took from 10,000 to 6000 BP to retreat from the continental shelf and that collapse was not catastrophic (Anderson, 1999). The retreat of the grounding line in the Ross Sea occurred mostly in the mid to late Holocene, without further forcing from climate or sea level once events had been set in motion by the sea level rise following Northern Hemisphere deglaciation. The chronology of the retreat was established through evidence such as ^{14}C dating of molluscs and shells (Conway *et al.*, 1999). Two significant conclusions in relation to the contribution of individual ice streams to the dynamics of the WAIS as a whole during its retreat can be drawn from the marine geologic record: firstly, subglacial meltwater played a significant role in the collapse of the ice sheet, as revealed by evidence such as the subglacial channels observed in Pine Island Bay, part of the Amundsen Sea, and the lack of recessional moraines; and secondly, ice streams acted independently during the retreat, as shown by the differences from one trough to the next in grounding line wedges, formed by the redistribution of deforming till as it is deposited where the fast flowing ice stream meets the floating ice shelf (Anderson and Shipp, 2001). These two significant factors in the past behaviour of the WAIS may also be

significant in its future.

2.3.2 The Terrestrial Geologic Record

The terrestrial record in Antarctica is sparse and suffers from lack of chronology (Borns, 2001). However, some limited evidence of the previous behaviour of the WAIS has been gained. For example, moraines in the Transantarctic Mountains show that the ice sheet was thicker during the LGM than at present, although it is difficult to establish how much so (Anderson, 1999). The terrestrial geologic record is therefore of the most use as supporting evidence for findings from other records and modelling.

2.3.3 Modelling

Models do not agree on the timing of collapse of the WAIS. Flow models of the Antarctic Ice Sheet showed that ice volume continued to increase after the LGM until 8000 BP, when the ice sheet also reached its maximum elevation (Huybrechts, 1990a,b, 1992). This is supported by direct dating of the Byrd ice core using the cosmogenic isotope helium-3 (^3He), which shows an overall decrease in elevation of two hundred metres over the last 8000 years (Steig *et al.*, 2001). However, a numerical model of the basal energy balance was used to show that the rapid decay of the WAIS since the LGM may have been triggered by an increase in basal water from basal melting, the availability of which peaked 15,000 BP, and throughout the Holocene the energy balance may have shifted to favour basal freezing, reducing the availability of basal water and thus slowing retreat (Vogel *et al.*, 2003), as decreased basal water provides decreased lubrication for fast ice stream flow, which therefore allows less ice discharge.

It is often difficult to verify model findings with field data. Since 8000 BP, estimated sea level in Huybrechts' model has been stable, and while the grounding line in the model is still retreating at present, it has not been possible to verify this in the field due to lack of information on the present behaviour of the grounding

line (Paterson, 1994). However, while Huybrechts' model would appear to agree with what data are available on the present behaviour of the WAIS, the model does not take individual ice streams into account and nor do numerous more recent models.

2.3.4 Limitations of Models

Modelling studies of ice sheets capture ice streams and shelves inadequately because of their resolution, and because of their use of the shallow ice approximation. Grid resolution needs to be 20 km at the coarsest (as in the GLIMMER model) for ice streams to be adequately captured (Takeda *et al.*, 2002), although there are finer resolution models focussing on subsections of the ice sheet. Bamber *et al.* (2000c), when calculating balance velocities, also state that numerical models have yet to capture the complexities of the actual ice sheet flow. The shallow ice approximation balances gravitational driving stress with basal drag only, ignoring lateral drag and longitudinal stress (which are discussed in turn in section 2.4). It is therefore inappropriate for ice streams (Payne, 1999), and also leads to ice sheets being modelled separately to ice shelves, which do not use the shallow ice approximation due to having no basal drag, necessitating boundary conditions to be imposed at the grounding line, when in reality the transition from sheet to shelf is one of the most important controls on ice sheet flow (Wilchinsky, 2007) and should be modelled as realistically as possible.

Accurate modelling also requires good knowledge of basal conditions (Anandakrishnan and Winberry, 2004), and while geophysical methods provide valuable information, this is usually spatially concentrated on some ice streams, and direct observations of the bed, for example using boreholes, are rarer still. The spatial and temporal availability of basal water must also be included in models, and again observations are sparse, which is problematic as the subglacial drainage of the WAIS is known to be complex (Vogel *et al.*, 2003). Good representation of subglacial topography, such as the troughs in which many ice streams flow, is also important but often lacking (Joughin *et al.*, 2006). Accurate climatic data are

also required for modelling (Hulbe and Payne, 2001). Models with better resolution than current General Circulation Models (GCMs) are required for accurate mass balance modelling, especially to examine the steep margins of ice sheets, where most accumulation and ablation occurs (Gregory and Huybrechts, 2006).

The latest report by the Intergovernmental Panel on Climate Change (IPCC) includes models with ice dynamics, but not changes in ice dynamics (IPCC Working Group I, 2007). Although establishing the likelihood of collapse of the WAIS is of the highest importance as, should the WAIS melt entirely in the future, global sea level would rise by five to six metres (Alley and Bindshadler, 2001; Joughin *et al.*, 1999), present models are not capable of assessing the likelihood of the collapse of the WAIS (Arthern and Hindmarsh, 2006). Models are computationally expensive due to the non-linearity of the equations involved, although as computer power doubles every 24 months (Moore's law) this becomes less of an issue over time. The way in which ice streams are included in future models is therefore an area which must be investigated (Hulbe and Payne, 2001).

2.4 Ice Streams

The ice streams draining the WAIS are generally tens of kilometres wide, hundreds of kilometres long, thousands of metres thick and reach velocities of up to hundreds of metres per year. Ice flow is driven by gravity (driving stress) and resisted by basal and lateral drag and longitudinal stress gradients, including back pressure from ice shelves and tension from upglacier (Alley *et al.*, 2004; Joughin *et al.*, 2002). In this section, these terms will be examined in turn, and followed by discussion of an ice stream from its onset, through its tributaries and main trunk, to its grounding zone, citing case studies and examples from several West Antarctic ice streams.

The six Siple Coast ice streams entering the Ross Ice Shelf (fig 2.2) exhibit some similarities, but some significant differences. These ice streams were assigned the letters A to E, from south the north, by British glaciologists in 1970, with ice

stream F added in 1972. However, in 2003 the ice streams and associated inter-stream ridges were renamed after American glaciologists (see table 2.1 and figure 2.2). Understanding the reasons for the relationship and differences between these ice streams will help better understand the ice stream mechanism.

Table 2.1: The old and new names for the Siple Coast Ice Streams.

Old Name	New Name
Ice Stream A	Mercer Ice Stream
Ice Stream B (Tributary B1)	Van Der Veen Ice Stream
Ice Stream B (Tributary B2)	Whillans Ice Stream
Ice Stream C	Kamb Ice Stream
Ice Stream D	Bindschadler Ice Stream
Ice Stream E	MacAyeal Ice Stream
Ice Stream F	Echelmeyer Ice Stream

Pine Island and Thwaites Glaciers, both of which transport ice to the Amundsen Sea, are the second and fifth most active basins in Antarctica respectively. Pine Island Glacier is responsible for 4% of the flow from the entire Antarctic ice sheet, draining 10% of the WAIS. This area is thinning rapidly (Bindschadler *et al.*, 2003) and ice streams there are accelerating (Rignot *et al.*, 2004b; Scambos *et al.*, 2004).

Discussion of the Rutford and Evans Ice Streams is mainly saved for the Study Area section towards the end of this chapter (section 2.8).

2.4.1 Driving Stress

Driving stress (τ_d), or basal shear stress (τ_b), is calculated as follows (Benn and Evans, 1998; Bindschadler *et al.*, 2001):

$$\tau_d = \rho gh \sin \kappa \quad (2.1)$$

where ρ is the average column density of the ice, g the gravitational acceleration, h the ice thickness and κ the surface slope. The most significant feature of the WAIS ice streams is that, in contrast to the ice streams contributing to the drainage of the EAIS and Greenland, they operate under low driving stresses. As such, movement is considered to be dominated by basal sliding, as opposed to internal deformation, which makes a significant contribution to the movement of the ice streams of the EAIS and Greenland.

Driving stress changes down the profile of an ice stream. For Pine Island Glacier, the driving stress may be divided into four distinct zones: the interior of the basin, where driving stress is 50-75 kPa; the main tributary, where values are around 30 kPa; the main trunk, where values are greater than 100 kPa, and; the floating ice, where driving stresses are below 10 kPa (Vaughan *et al.*, 2001). The high driving stress of the main trunk is one of the defining features of an outlet glacier as opposed to an ice stream, although Pine Island Glacier also has some characteristics of an ice stream, such as the presence of crevassed shear margins between the rapidly moving channel and the slow moving ice either side. The driving stresses of the Siple Coast ice streams, for example, are typically between 0 and 20 kPa (Hooke, 2005). As a comparison, the velocity of Byrd Glacier in East Antarctica is approximately 800 m a^{-1} under a driving stress of 220 kPa, whereas Whillans Ice Stream achieves similar velocities under 7% of the driving stress, 15 kPa (Whillans *et al.*, 2001). Driving stress is an important factor in the differences between the Siple Coast ice streams. The deceleration of Mercer Ice Stream, shown by a velocity map which compares present velocities to those of the 1970s and 1980s, is thought to be due to decreased driving stress over time (Joughin *et al.*, 2002).

Despite the low driving stresses on the WAIS ice streams, rapid flow occurs because of high shear stress due to a large ice thickness and/or weak basal resistance (Alley *et al.*, 2004; Fahnestock and Bamber, 2001). However, the reasons for this weakness are not yet established (Whillans *et al.*, 2001).

2.4.2 Basal Conditions

Basal motion occurs through three main processes: the sliding of ice over till; deformation within till; or deformation within a layer of basal ice. However, the contribution of each is “still debated and is probably spatially variable” (Bindschadler *et al.*, 2001, p.124), and the proportion of ice stream movement by different mechanisms varies by ice stream.

Basal Sliding

Basal sliding (U_b) is given by the following equation (Bindschadler *et al.*, 2001):

$$U_b = K\tau_b^m \quad (2.2)$$

where τ_b is the basal shear stress, K is a coefficient depending on factors such as water pressure, and m is an exponent, usually taken as 1, although in earlier studies this was commonly taken as 2 (Paterson, 1994).

There two most important basal conditions favouring streaming flow are the presence of subglacial water, and weak subglacial till (Bindschadler *et al.*, 2001), although these conditions alone are not enough to cause streaming flow (Anandakrishnan *et al.*, 1998). Basal melting is the only source of subglacial water beneath the WAIS (Vogel *et al.*, 2003). In order to allow streaming flow, subglacial water must be at a high enough pressure to balance the weight of ice above it, and the underlying till must not be frozen. Subglacial water is produced when the movement of an ice stream over its bed generates frictional heat which allows the bed to thaw (Jacobson and Raymond, 1998). The faster the ice moves, the more basal heating takes place, which increases basal melting, a finding which has also been supported by models. Basal melting may also be associated with volcanism, although other factors also need to be favourable for streaming flow

to occur, as even an active subglacial volcano is not, alone, enough to initiate the onset of an ice stream; ice stream onsets are discussed in section 2.4.5.

Borehole studies on some of the Siple Coast ice streams have shown basal temperatures above the pressure melting point beneath the ice streams, and below the pressure melting point for the slow moving ice which separates them, where the bed has been found to be frozen (Kamb, 2001). The Siple Coast ice streams, which have a high velocity and a low basal shear stress (Alley *et al.*, 2004), have probably had the most extensive investigations into their basal conditions. Boreholes to the bed of Whillans Ice Stream, for example, have shown water pressures close to the overburden pressure, and till with a high clay content, fulfilling the basal conditions necessary for streaming flow (Engelhardt and Kamb, 1997; Hooke, 2005). Engelhardt and Kamb (1998) report the use of a tethered stake to measure basal sliding 300 km upstream of the grounding line of Whillans Ice Stream, and concluded that basal sliding makes up approximately 83% of the total motion.

Above a threshold speed, the melting which occurs at the bed allows ice stream widening. For conditions of no inflow, this threshold is approximately 100 m a^{-1} , but for an input of a few metres per year this rises to approximately 500 m a^{-1} , a velocity reached and exceeded by several WAIS ice streams. When velocity is below this threshold, conditions at the bed, which normally enable streaming flow, may impede the expansion of the ice stream. Modelling of basal temperature gradients beneath Mercer Ice Stream and one tributary of Whillans Ice Stream, both of which are currently decelerating, shows that temperatures may not be high enough to maintain basal melt required for streaming flow (Joughin *et al.*, 2003).

Seismic and aerogeophysical observations of Whillans and Kamb Ice Streams have also been conducted to identify geological controls on high velocity ice flow, finding that Whillans Ice Stream was underlain by saturated sediments and thin water layers. Flow of Kamb Ice Stream is mainly resisted by basal drag (Whillans *et al.*, 2001), although this ice stream is a special case and is discussed further in section 2.5.

Geothermal heat flux has an important role to play in the basal conditions of the Siple Coast ice streams due to their tectonic evolution, as rifting in the Cretaceous Period (145.6 to 65.0 Ma) led to the crust beneath these ice streams being especially thin (Blankenship *et al.*, 2001). However, Raymond (2000) suggests that geothermal heat flux beneath the lower part of Whillans Ice Stream may not be sufficient to maintain melting, and as such the base of the ice stream may be freezing, explaining its current deceleration. Basal freezing will continue until such time as the geothermal heat flux becomes sufficient to allow enough basal heat to facilitate sufficient melting to allow basal lubrication. Deceleration may occur when ice streams thin due to negative mass balance, changing the basal regime from melting to freezing (Joughin and Tulaczyk, 2002). This research also highlights the need for work focussed on naturally occurring processes on WAIS ice streams, as well as that focussing on the effects of climate change.

Till Deformation

As well as basal sliding, ice streams move by till deformation. Till is the sediment deposited by a glacier without the need for running water, the pore space of which is fully water saturated. Its strength is affected by water content, void ratio, effective pressure and shear stress (Bindschadler, 2006). Theoretical till strength is greater than that measured, and the ability of the till beneath ice streams to deform is crucial in allowing streaming flow.

Tulaczyk *et al.* (2001) highlight the need for a conceptual model of subglacial till beneath ice streams, and present their “till ploughing model” of till formation and redistribution. This ploughing occurs during ice movement, when protrusions on the underside of the ice, known as ice keels, dig into the underlying till. When the ice stream moves, the till is dragged with it, deforming the till to a depth equal to the size of the largest ice keels, and necessitating the replenishment of the removed sediment from upstream in order for streaming flow to be maintained (Doake *et al.*, 2001). Although there is no direct observational evidence of ice keels beneath the WAIS, bedforms left behind by other Pleistocene ice sheets show that their bases were irregular (Tulaczyk *et al.*, 2001).

Till deformation follows a Coulomb-plastic rule, with no deformation below a certain threshold, but deformation can occur anywhere once the threshold is exceeded without a further increase. More till deformation occurs in dilatant till (the volume of which changes under deformation) than non-dilatant (the volume of which does not change under deformation), as clasts are able to move past each other more easily (Alley *et al.*, 2004). A soft bed not only deforms more easily and generates till, but additionally may bury rough bedrock features that may otherwise impede flow (Anandakrishnan *et al.*, 1998). For Bindschadler Ice Stream, approximately 80% of the motion is by till deformation.

The effects of till ploughing were modelled over 8500 years for Kamb Ice Stream. The model predicts 0.6 mm a^{-1} erosion beneath ice stream tributaries, as they are underlain by deep troughs, and 0.2 mm a^{-1} beneath the main trunk. This suggests erosion should be modelled using the till ploughing model, rather than taking the traditional method of scaling erosion with ice velocity (Bougamont and Tulaczyk, 2003).

The underlying geology of the WAIS is also significant in till deformation. The availability of mid-Cenozoic marine sediments is the most likely geological control on streaming flow (Blankenship *et al.*, 2001). Under the till ploughing model (Tulaczyk *et al.*, 2001), these sediments allow ice streams to flow unimpeded, whereas a harder bed would impede the movement of an ice stream by this mechanism. Modelling ice streams using this type of bed, which assumes till behaves as a granular solid, as opposed to assuming the bed is viscous, as favoured by authors such as Kamb (2001), shows greater potential for ice stream instability (Tulaczyk *et al.*, 2001).

Subglacial Lakes

The movement of subglacial lake water beneath ice streams may also affect their flow. Recovery Glacier in East Antarctica, for example, speeded up due to subglacial lake drainage (Bell *et al.*, 2007). 145 subglacial lakes have now been discovered in Antarctica, and surface elevation changes of Whillans and Mercer Ice

Streams due to rapid water movement have been identified by ICESat altimetry (Fricker *et al.*, 2007).

2.4.3 Lateral Drag

In addition to basal conditions, lateral shear is also an important resistance to flow, as shear margins can support stresses of up to 100 kPa. As the stress at the ice margins can be far greater than the basal shear stress, much of the downslope weight, usually in the region of 50%, can be supported here, although this value may be up to 100% in some cases (Raymond *et al.*, 2001). Lateral forces, while important in the onset and grounding zones, have a comparatively minor role to play elsewhere (Raymond *et al.*, 2001), although lateral drag is most important when basal lubrication is especially good (Alley *et al.*, 2004). As the bed of Whillans Ice Stream is almost perfectly lubricated, the main resistance to flow is therefore lateral drag (Van der Veen *et al.*, 2007; Whillans *et al.*, 2001), whereas for Kamb Ice Stream, lateral drag balances only about 25% of the driving stress.

Increased melting at the shear margins of an ice stream may force the margins to migrate outwards (Raymond *et al.*, 2001). Widening of an ice stream causes a major increase in centreline velocity which increases with the fourth power of shear stress if most of the driving stress is supported by lateral drag (Alley *et al.*, 2004; Van der Veen, 1999). However, some ice streams, such as Bindschadler and MacAyeal Ice Streams, are bounded by especially steep slopes, which decreases their potential for widening (Whillans *et al.*, 2001). Bindschadler Ice Stream is 55 km wide and it is estimated that lateral drag supports just over half the driving stress.

Raymond (1996) identified three flow regimes which were dictated by the interaction between resistance from the bed and the margins of an ice stream: low relative sliding speeds, with the margins affecting only part of the ice stream width, and the flow in the centre controlled by basal conditions; intermediate sliding speeds, with the flow controlled by a combination of both marginal and basal resistance; and very high sliding speeds, where the resistance from the mar-

gins dictates the speed of the ice stream across the entirety of its width. Ice stream velocity is therefore sensitive to ice stream width, which may be affected by a number of factors, and indeed, for a number of WAIS ice streams, the effects of changes in ice stream width on velocity have already been observed.

Whillans Ice Stream has velocities of up to 865 m a^{-1} and negative mass balance. It has widened 4 km since 1963 (Bindschadler and Vornberger, 1998), while decelerating by 50%, and is thinning by 0.6 to 0.8 m a^{-1} , and would become stagnant in matter of fifty to one hundred years should its current rate of deceleration be maintained. Its widening, and the 14 km erosion of the ridge between Whillans and Kamb Ice Streams (Bindschadler and Vornberger, 1998), were not predicted by models, and suggest a shift in the velocity field of the region during the twentieth century.

Pine Island and Thwaites Glaciers also showed widening, thinning, and acceleration as a response to negative mass balance (Rignot, 2001). Thwaites Glacier is predicted to widen to become twice its current width when its eastern ice shelf disintegrates (Rignot, 2006).

2.4.4 Longitudinal Stress

Longitudinal stress is caused by the upstream and downstream ice pushing and pulling. As it acts parallel to slope and ice flow, it modifies the shear stress, and ice thickness and slope may be averaged over 8 - 16 ice thicknesses to incorporate longitudinal stress into the equation for shear stress (Benn and Evans, 1998). Longitudinal stress may be either compressive, if the ice is decelerating, or tensile, if the ice is accelerating (Benn and Evans, 1998). It is an important control on ice sheet stability, as it is longitudinal stress which stops large increases in velocity downstream of the grounding line when basal drag is removed and the role of lateral drag decreases (Bindschadler, 2006).

Longitudinal stress is at its most significant in the transition zone between grounded and floating ice, within which the pattern of ice deformation changes from the

shearing of the grounded ice to the longitudinal stretching of the ice shelf. It may also be important in areas of ice stream tributaries, as above Whillans Ice Stream, where there is high driving stress but poorly developed margins and low lateral shear stress (Stearns *et al.*, 2005). Longitudinal resistive stress is assessed by calculating the along-flow stretching down the centreline of an ice stream from the velocity gradient in the downstream direction (Van der Veen, 1999). The longitudinal strain rate of an ice stream may be approximated by dividing the maximum velocity of an ice stream by its length.

Hindmarsh (2006) investigates the decay in these stresses, which he calls membrane stresses when they are in 2D, with distance upstream from the grounding line, using a finite difference model. The transition zone between ice shelf and ice sheet flow takes place over several tens of kilometres, and high velocity and high stress within this zone give model solutions allowing the stresses to adjust fast enough for a steady state to be maintained. Paterson (1994, p.312) states that processes within this zone “may control the stability of a grounded ice sheet with its base below sea level,” an idea which is discussed further in section 2.7.1.

2.4.5 Ice Stream Onsets

Ice stream onsets can be defined as the point where ice becomes unfrozen from its bed because its velocity is significantly greater than that of the interior ice sheet. Onset usually occurs in a distance less than the ice stream width (Hodge and Doppelhammer, 1996). Onsets may be identified by a number of factors, although Blankenship *et al.* (2001) note the difficulties in defining the transition from the slow flow of an inland ice sheet to the rapid flow of an ice stream.

Ice stream onsets are most reliably identified by changes in the driving stress compared to the inland ice sheet, which increases to a maximum at the onset in order to transport the greater flux of ice. The maximum driving stress above Mercer, Whillans, Kamb, Bindschadler and MacAyeal Ice Streams is 80 to 150 kPa, and this declines gradually down the length of ice stream profile to about 20 kPa by the ice shelf entrance.

Onset regions may also be identified by the presence of crevasses associated with large velocity gradients and lateral shear, flowstripes, and changes in surface and bed elevation. Lateral convergence of the surface slope of the inland ice sheet also points to the onset of an ice stream (Bindschadler *et al.*, 2001), with the boundary between the inland ice and the ice stream itself marked by the area of maximum surface slope. McIntyre (1985)'s model indicates a change in the surface slope where the movement changes from the internal deformation of the inland ice sheet to the basal sliding of an ice stream, although some basal sliding does occur for the interior WAIS and Blankenship *et al.* (2001) identify a band of transitional flow between these two conditions. While both slope and driving stress then decrease downstream from their maxima, velocity continues to increase to the grounding line, with a corresponding decrease in ice thickness due to the flattening of the ice stream bed.

There are a number of criteria recognised as necessary for the onset of an ice stream, all of which relate to basal conditions, rather than internal deformation or strain. Ice stream onsets tend to be located in a channel, on a sedimentary bed, with temperate, rather than frozen, basal conditions (Bindschadler *et al.*, 2001), although Whillans *et al.* (2001), in the same volume, disagreed on the first point, stating the onsets are not necessarily related to subglacial topography. The WAIS does not follow the usual convention that fast flow is initiated at a bedrock step. There are no large gradients in the bedrock at the areas of onset of Mercer, Whillans and Kamb Ice Streams in the Ross Sea Sector of the WAIS (Retzlaff *et al.*, 1993), and Paterson (1994) extends this observation to Bindschadler and MacAyeal Ice Streams as well. The location of ice stream onsets has been shown to correspond to transitional crust between the thick crust of the Ellsworth/Whitmore block and the thin crust of the Ross Embayment (Blankenship *et al.*, 2001).

The WAIS is, however, similar to other ice sheets in that basal lubrication at the onset causes low basal shear stress, therefore initiating the ice stream. The onset region above Whillans and Kamb Ice Streams is a steep sided sedimentary basin (Bell *et al.*, 1998), and the sediment there has frictional resistance an order of magnitude lower than that outside the basin beneath the slow moving ice

(Anandakrishnan *et al.*, 1998). Subglacial lakes, or pockets sediments saturated with liquid water, were also identified at the heads of some EAIS ice streams such as Byrd and David Glaciers, and Whillans Ice Stream, by Siegert and Bamber (2000), who attribute the lack of lakes under some ice stream tributaries to either lack of data or lack of subglacial hollows in which water could gather.

2.4.6 Ice Stream Tributaries

As ice stream tributaries move mostly by basal sliding characteristic of an ice stream, rather than by internal deformation characteristic of an ice sheet, they are defined as being downstream of the onset, and may separate ice streams from their onset regions by distances of up to several hundred kilometres. Driving stresses of tributaries are similar to those of the inland ice sheet, approximately 30 to 90 kPa, rather than the low driving stresses associated with ice streams. The primary control on the location of ice stream tributaries is topography, with tributaries following subglacial valleys (Hulbe *et al.*, 2000; Joughin *et al.*, 2002), while the secondary control is the location of consolidated sediment. However, not all subglacial valleys contain tributaries, and Hulbe *et al.* (2000)'s investigation of valley conditions favouring tributary flow found no consistent conclusions.

Examining the three tributaries of Slessor Glacier, East Antarctica, using Radio Echo Sounding (RES), Rippin *et al.* (2006) found that tributary flow was intermediate between internal deformation and basal motion, and for the two tributaries with rougher beds, basal motion played less of a role despite the presence of subglacial water. Hulbe *et al.* (2003), looking at the Siple Coast region, also found that the onset of streaming flow occurs where bedrock topography changes from rough to smooth. Bindschadler and Choi (2007) found a positive feedback mechanism whereby the acceleration of an ice stream tributary produces more subglacial water, causing further acceleration, by applying their "lubrication index" to field data from Bindschadler Ice Stream.

The same source area may be drained by more than one ice stream (Hooke, 2005). Joughin *et al.* (1999), for example, found that a number of tributaries in the Siple

Coast region feed more than one ice stream, using interferometry of RADARSAT images from the Antarctic Mapping Mission (AMM). Similar phenomena have been shown using balance velocity maps, which are discussed further in section 4.4 and present the velocities that would be required to maintain a state of neutral mass balance for the ice sheet. Bamber *et al.* (2001)'s balance velocity map, shows complex systems of ice stream tributaries up to 1000 km inland from the grounding line, and similarly Wu and Jezek (2004)'s balance velocities show that contributing flow to Support Force Glacier and Foundation Ice Stream extends almost up to the ice divide in East Antarctica. However, Bingham *et al.* (2007), used RES to identify ice stream tributaries by their disrupted internal layers and smoother surfaces. They discovered a widespread network of tributaries transporting ice from the South Pole region, via various fast flow features, to the Filchner-Ronne Ice Shelf (FRIS), which did not correspond to balance models. More work identifying the correct location of ice stream tributaries is therefore required.

2.5 Oscillation Between Catchments

Oscillation between ice streams with adjacent catchments may occur (Doake *et al.*, 2001). There are two classic examples of this in West Antarctica: the Siple Coast, especially Whillans and Kamb Ice Streams; and Rutford Ice Stream and Carlson Inlet.

The characteristics which are currently exhibited by Mercer, Whillans, Bindshadler and MacAyeal Ice Streams, such as high velocities and low surface slopes (Fahnestock and Bamber, 2001), were also exhibited by Kamb Ice Stream, prior to the cessation of fast flow of its lower section about 150 years ago, which is one of the most widely researched and documented events in the recent history of the WAIS. The lower and middle sections of Kamb Ice Stream have stopped moving, which is thought to have led to positive mass balance (Conway *et al.*, 2002), while the upper part remains active. The active parts of Kamb Ice Stream move at 60 to 70 m a⁻¹, and the stagnant part still has two tributaries flowing

into it, and as such the ice is thickening at a rate of 0.49 m a^{-1} (Joughin *et al.*, 1999), having thickened 50 m since stagnation. The thickness of the active part of the ice stream is 1400 to 2000 m, compared to 600 to 1200 m for the stagnant part. The lower section of Kamb Ice Stream previously flowed at 350 m a^{-1} . Had Kamb Ice Stream not stagnated, the loss of ice there would cancel out the current positive mass balance of the Siple Coast region (Ng and Conway, 2004).

It is important to identify the conditions at the boundary between the active and stagnant sections of the ice stream which are responsible for the state of the lower section (Whillans *et al.*, 2001). The presence of subsurface crevasses in the lower section of Kamb Ice Stream is evidence of former activity, as these crevasses would have reached the surface when this section of the ice stream was active, and no longer do so because of accumulation since this time (Whillans *et al.*, 2001). Stagnation probably first occurred near the Siple Dome (Anandkrishnan *et al.*, 2001). The shutdown of Kamb Ice Stream began with unstable ice plain behaviour, such as deceleration as (Joughin *et al.*, 2002) also observed on Whillans Ice Stream which may be explained by a plastic bed model, and indeed Joughin *et al.* (2002, p.3-1) described ice plains as “inherently unstable.” This has particularly significant implications for Whillans Ice Stream, which flattens out onto an ice plain of similar morphology to that of Kamb Ice Stream, close to the Ross Ice Shelf. Should the ice plain of Whillans Ice Stream shut down in the manner of that of Kamb Ice Stream, the ice behind it would be dammed, and therefore thickening, widening and deceleration of the ice behind the stagnant ice would occur. A relict ice plain was identified on Kamb Ice Stream after ice penetrating radar discovered basal crevasses which are associated with floating ice. It may only have become fully grounded 200 years prior to the ice stream’s stagnation (Catania *et al.*, 2006).

The reasons for this shutdown are the subject of some debate, but it is important to establish the cause to ascertain whether other WAIS ice streams could undergo similar shutdowns. The most popular hypotheses are that either the ice itself, the basal water needed to lubricate it, or both, have been diverted into Whillans Ice Stream instead, a theory known as piracy.

While the ice feeding into Kamb Ice Stream appears to be behaving normally, Conway *et al.* (2002), using surface measurements and remote sensing, suggest that tributary ISC0 of Kamb Ice Stream has been captured by Whillans Ice Stream's tributary WIS2, as WIS2 thinned more than ISC0 over the last thousand years. This may have led to alterations in the surface topography, which in turn may have caused the driving stress and flow of subglacial water to change, leading to this diversion of ice flow. However, this has not yet been proven and the direction of driving stress here is not clear (Anandakrishnan *et al.*, 2001).

The water piracy theory favoured by many authors states that basal water near the onset is diverted away from the slow moving ice and into Whillans Ice Stream. The water diverted lubricates the ice motion of Whillans Ice Stream, but the deficit of water in Kamb Ice Stream means that the lubricating layer is not thick enough, an idea which supersedes a previous hypothesis that the ice had frozen to its bed. Diversion may be due to a flattening of the surface slope in response to the growth of the upper section of Kamb Ice Stream (Anandakrishnan *et al.*, 2001), or because the head of Kamb Ice Stream reached steeper subglacial topography (Van der Veen, 1999). A hydrological potential map of Whillans and Kamb Ice Streams shows that the possible site of diversion is where the tributaries join the main trunk, and even partial diversion would be enough to cause the observed stagnation of the trunk of Kamb Ice Stream (Anandakrishnan *et al.*, 2001). However, it has been suggested that the diversion of basal water from Kamb to Whillans was a consequence, rather than a cause of stagnation (Bindschadler, 2006).

A further hypothesis is the thermal model, and this may be complementary to water piracy. Sticky spots at the bed, which are areas with larger basal drag than the surroundings which can occur because of bumps in the basal topography, may be restraining the flow of the ice stream. Under normal conditions of streaming flow there would be enough basal water to lubricate these, but the trunk of Kamb Ice Stream is highly seismically active, indicating a poorly lubricated bed (Anandakrishnan *et al.*, 2001).

One final theory is the loss of lubricating till from Kamb Ice Stream, as indicated

by borehole studies, as flow would decelerate if the amount of till transported downstream was not replenished by new till being eroded (Alley *et al.*, 2004) although there is evidence of a deep sedimentary reservoir upstream (Anandakrishnan *et al.*, 2001). It may be that some or all of these hypotheses are correct, and acting in combination to produce the observed effect (Whillans *et al.*, 2001).

The idea of oscillation between catchments also applies to Carlson Inlet and Rutford Ice Stream. Carlson Inlet is a former ice stream which is now in a stagnant phase, much like the lower section of Kamb ice Stream (Vaughan *et al.*, 2003). Frolich *et al.* (1989) produced a comparison of flow between the Rutford Ice Stream and Carlson Inlet, using 239 survey stations. The two have similar dimensions and driving stresses and share a 50 km shear margin (Vaughan *et al.*, 2008). They found that Carlson Inlet moves at speeds of only 7 m a⁻¹ due to being frozen to its bed, whereas the Rutford Ice Stream, which moves mostly by basal sliding, was moving 300 m a⁻¹ in the area immediately across the shear margin, 130 km upstream of its grounding line. These numbers have been updated in more recent work by Vaughan *et al.* (2008) who used ice thickness data and bed DEMs, and revised the estimate of Carlson Inlet's velocity to 5 to 35 m a⁻¹. Examining different aspects of Carlson Inlet, they found much supporting evidence of it being a former ice stream, such as its flat surface morphology, situation in a 1200 m deep trough, 66 kPa driving stress (compared to 54 kPa for Rutford), and erosional and depositional features and wet sediment at the bed. Buried crevasses show that the shutdown of streaming flow must have occurred before 240 BP, i.e. around 1710 AD.

A number of authors liken the relationship between Rutford Ice Stream and Carlson Inlet to that between Whillans and Kamb Ice Streams, and, as with Whillans and Kamb Ice Streams, the reason for the shutdown of Carlson Inlet appears to be water piracy, in this case by Rutford Ice Stream, shown by hydrological potential calculations (Vaughan *et al.*, 2008). Rignot (1998a) found that the mass balance of Carlson Inlet might be slightly positive, like that of Kamb Ice Stream, and Vaughan *et al.* (2003) found that the bed of Carlson Inlet was composed of non-deforming sediments, over which ice must move by basal sliding rather than bed deformation. It is therefore theoretically possible that Carlson Inlet might

be revived by an increase in basal water allowing basal sliding at ice stream velocities over the non-deforming sedimentary bed. An 80 m thickening of Rutford would allow Carlson Inlet to retain most subglacial water generated within its own basin; a 120 m thickening of Rutford would route much of the subglacial water generated in both basins under Carlson Inlet, potentially causing Rutford to shut down streaming flow (Vaughan *et al.*, 2008).

The implications of this are significant both in terms of the possibility of a feedback mechanism where increased melting, for example, of the Rutford Ice Stream, could lead to a significant increase in the discharge of Carlson Inlet, and also in terms of any possible cycle of deceleration, stagnation, and reactivation which may affect the other West Antarctic ice streams.

2.5.1 Surging

It is also possible that surging of ice streams may be occurring, in a similar manner to mountain glaciers, which spend most of their time in a slow flow mode. Clarke (1987) also states that ice streams can switch between slow and fast flow modes, but whether the controls on this are internal or external is not established. Surging was described by Anandakrishnan *et al.* (2001, p.286) as “periodic dynamic oscillation,” but, more ominously in terms of the overall stability of the ice sheet, by Colbeck (1980, p.71) as “the most impressive type of instability.”

It has been suggested that the WAIS ice streams could be at varying stages of surge cycles (Whillans *et al.*, 2001) and it could be that oscillation between catchments is responsible for this. Kamb and Whillans Ice Streams may be part of a larger system - Bindshadler *et al.* (2003) state that Whillans, Kamb and Bindshadler Ice Streams, which are physically quite similar and are respectively decelerating, stopped, and maintaining speed, are affected by the same ice-till-water system, and all three are underlain by weak unfrozen till with similar lithology and porosity. Flow stripes on the ice shelf may be used to indicate the nature of former ice stream flow; for example, ice near the shelf front of the

Ross Ice Shelf at present crossed the grounding line 1000 years ago (Bindschadler, 2006). Siple Ice stream, which is situated between Siple Dome and Bindschadler Ice Stream, stagnated 450 years ago, and evidence of former ice streams has been identified on both Siple Dome and Roosevelt Island by Scambos *et al.* (1998) using GPS and photogrammetry. The ridge between Whillans and Mercer Ice Streams also used to be fast-moving (Bindschadler, 2006). This evidence suggests the present and former ice streams of the Siple Coast have a complex interrelationship. Variations in velocity on these timescales should therefore be investigated for other WAIS ice streams. The EAIS, in contrast, seems to have had steady flow over millennial timescales (Bindschadler, 2006).

2.5.2 Timescales of Variability

The ice streams draining the WAIS currently exhibit variability in velocity over timescales ranging from the retreat of the entire ice sheet since the LGM to sub-diurnal scale variability with acceleration and deceleration occurring over periods of minutes due to tidal forcing (e.g. Bindschadler *et al.* (2003)). Variability on all intermediate timescales has also been observed.

As discussed above, several ice streams draining the WAIS show variability over timescales of hundreds of years, which is not the case for ice streams draining other ice sheets. Fahnestock and Bamber (2001) highlight the importance of the bed of the WAIS being below sea level in influencing this, which again is not in common with other ice sheets, and implicate the marine nature of the WAIS in this variability.

Short-term variability on the decadal scale has also been recorded, and has been attributed to climatic factors such as the accumulation changes caused by El Niño Southern Oscillation (ENSO) events, which Bromwich and Rodgers (2001) suggest be further investigated with ice core studies. More recent work has found that dynamics can vary on a subdiurnal scale, thought to be due to tidal influences, as discussed in section 2.6.3 below.

2.6 The Grounding Zone

The grounding zone is the transition between an ice sheet and an ice shelf, where the ice starts to float when it reaches hydrostatic equilibrium, with water depths equivalent to 0.87 times the ice thickness required for flotation in sea water (Benn and Evans, 1998). Traditionally it has been referred to in the literature as the grounding line, and its behaviour is a major control on the stability of the ice sheet (Vielé and Payne, 2005). The grounding line advances if the ice shelf thickens sufficiently to come into contact with the seabed, and conversely retreats if the ice thins enough to allow sea water to penetrate beneath it and cause contact with the bed to be lost (Wilchinsky, 2007). If the grounding line begins to retreat, it may either stabilise on reaching a downward sloping section of bed, which causes a positive feedback where ice will be thicker and therefore discharge at the grounding line greater, or continue retreating until the ice sheet has completely gone. Grounding line retreat may be irreversible if there is overdeepening of the bed close to the grounding line, and indeed as the bed of the WAIS slopes up towards the grounding line in many places, a stable grounding line location is unlikely to exist (Schoof, 2007). Feedbacks between the grounding line position and ice flux determine the stability of the ice sheet (Pattyn *et al.*, 2006). If the grounding line of the ice sheet can move too quickly for ice to be replaced by flow from inland, then a steady state cannot exist for the ice sheet (Hindmarsh, 2006). Identifying the location of the grounding line in relation to bed topography, and mapping its migration over time, is therefore a highly important exercise.

2.6.1 Grounding Zone Mapping

The grounding line may be defined in different ways (figure 2.3): F is the limit of tidal flexing, also known as the hinge line; G the limit of flotation; I the inflexion point, where longitudinal stresses from tidal bending cause the ice to be depressed below the hydrostatic level; and H the seaward limit of ice flexure, which is also the landward limit of the hydrostatic zone of the ice shelf. The distances between F, G, I and H vary due to ice thickness and basal topography.

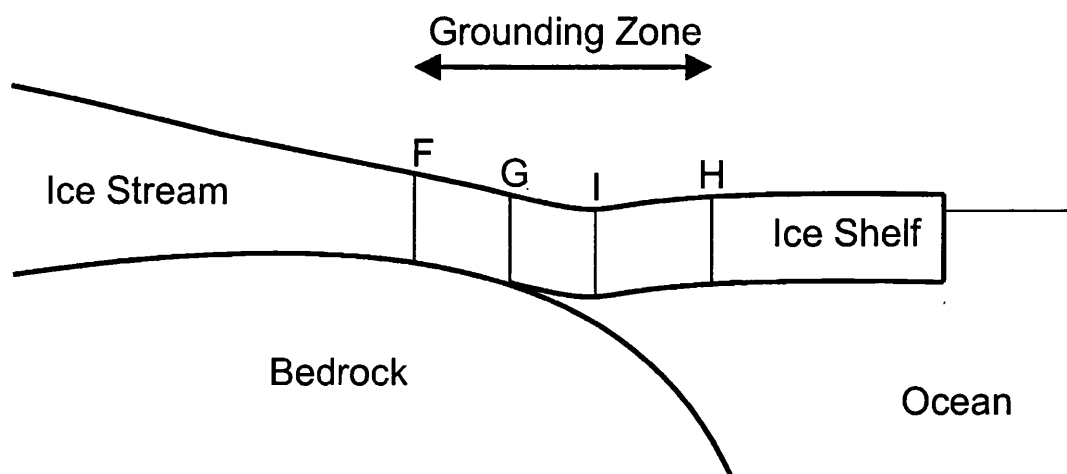


Figure 2.3: An ice shelf grounding zone - F and H mark the landward and seaward limits of tidal flexure, G the limit of flotation, and I the inflection point. Adapted from Fricker and Padman (2006), Vaughan (1994) and Smith (1991).

It has more recently been recognised that on many ice streams, an area several kilometres wide is intermittently grounded at different points in the tidal cycle, and thus the term grounding zone is more appropriate. The grounding zone may be defined as the area between F and H (Fricker and Padman, 2006). The tidal cycle is discussed further in section 2.6.3.

Several methods have previously been used to map ice shelf grounding lines, usually by locating the decrease in surface slope occurring because of the transition to zero basal shear stress where the ice starts to float (Benn and Evans, 1998). Different methods may delimit one or more of F, G, I and H. Altimetry from satellites such as ERS-1 and ICESat may be used to detect the landward and seaward limits of tidal flexing, F and H, by comparing repeated tracks and orbital crossovers from different stages in the tidal cycle. These elevation change data can subsequently be used to extract the phase and amplitude of the different components of the tidal signal for tidal modelling, as well as to delimit the grounding zone (Fricker and Padman, 2002, 2006). The grounding zone, between F and H, can also be identified using interferometry. This method was utilised as part of this study and is discussed in section 3.10.

Additionally, F can also be identified from both tiltmeter and kinematic GPS data. Smith (1991), for example, used tiltmeters 5 m apart buried at a depth of 1.5 m on Doake Ice Rumples (figure 1.1), where the Ronne Ice Shelf grounds on a bedrock obstruction, to derive a record of tidal motion at 12 sites. H may also be modelled using buoyancy calculations based on the elevation of the ice shelf surface and Archimedes' Principle (Benn and Evans, 1998; Bentley, 2004; Fricker and Padman, 2006).

The grounding zone is not static and moves backwards and forwards with the tide (Reeh *et al.*, 2003; Rignot, 1998b), the grounding line of Ekstroem Ice Shelf, East Antarctica, for example, moving 1 km per cycle at spring tides (Heinert and Riedel, 2007). The nature of the tide is discussed in section 2.6.3 below.

2.6.2 WAIS Grounding Lines

The grounding line of the WAIS is known to have retreated 1300 km since the LGM (Conway *et al.*, 1999). However, its behaviour on shorter timescales has been more difficult to establish. The grounding lines of the Siple Coast ice streams have not migrated over the past two decades, which shows that changes in flow may occur without the need for grounding line migration (Horgan and Anandakrishnan, 2006).

Because all the glaciers draining the Amundsen Sea sector of the ice sheet lie in deep troughs which persist far inland, there is great potential for rapid retreat (Rignot *et al.*, 2004b). This area contains 1.25 m of potential sea level rise, and at its present rate of mass loss, would fully discharge in about 20,000 years (Bentley, 2004). Synthetic Aperture Radar (SAR) interferometry (SRI, also known as InSAR) of Thwaites Glacier showed a retreat in the grounding line of 1.4 ± 0.2 km a^{-1} between 1992 and 1996, with thinning at a mean rate of 11.7 ± 1.0 cm a^{-1} over the same period. SAR interferometry of Pine Island Glacier showed that the hinge line, the limit of tidal flexing, retreated 1.2 ± 0.3 km a^{-1} between 1992 and 1996, and, over this same period, the glacier thinned 3.5 ± 0.9 m a^{-1} , and the grounding line retreated a total of 5 km (Rig-

not, 1998a; Shepherd *et al.*, 2001). The effects of the grounding line retreat, such as the thinning, reached 150 km upstream (Shepherd *et al.*, 2001). This was established as being due to a change in dynamics due to increased basal melting caused by warm ocean water, which has been identified as a “possible trigger for the disintegration of the West Antarctic Ice Sheet” (Rignot, 1998a, p.549), and was not the result of accumulation changes, although Rabus and Lang (2003) thought that the thinning of Pine Island Glacier might be due to internal instability. Rabus and Lang (2003) did not find any correlation between the increase in velocity of Pine Island Glacier and migration of the grounding line, although they did not exclude the possibility that an external forcing event may have taken place before the beginning of observations on the glacier. Thomas *et al.* (2004), using force perturbation analysis, predict that the grounding line of Pine Island Glacier will settle on a flat part of the bed 1200 m below sea level, and as such high velocities will continue due to low basal drag. Whether the retreat of Pine Island Glacier is part of a wider scale and longer term trend in the collapse of the WAIS remains to be seen (Rignot, 1998a).

Although some parts of the EAIS are also grounded below sea level, such as Mertz, Frost and Totten Glaciers, and are vulnerable to the type of change affecting the WAIS (Rignot, 2006) caused by grounding line migration and the effects of decreased ice shelf buttressing, the mass imbalance of the EAIS is small and its sign has not yet been determined (Rignot and Thomas, 2002).

Further details and examples specific to the grounding zone of the study area are discussed in section 2.8.1.

2.6.3 The Tide

At any given location, the tidal signal can be described as the sum of a number of sine functions representing different diurnal, semidiurnal and longer term components, each of which is caused by the gravitational forces between the Sun, the Moon and the Earth. The components of the tidal signal are described according to Doodson numbers, which are integers representing six astronomical phenom-

ena: the Earth's rotation; the Earth's orbit; the Moon's orbit; the periodicity of lunar perigee; lunar orbital tilt; and the location of perihelion in the Earth's orbit (Pawlowicz *et al.*, 2002). These numbers predict the phase and amplitude of the tidal signal were the Earth's response fast enough for the ocean to be in equilibrium with its forcing. Table 2.2 shows the frequencies of ten principal tidal components, in hours: the nine most important components defined by Open University Course Team (1999), and Q_1 , which is the tenth component used in the CATS02.01 tidal model, discussed in section 4.5.1.

Table 2.2: Principal tidal coefficients. All except Q_1 taken from Open University Course Team (1999).

Component		Hours	Coefficient ratio ($M_2 = 100$)
Semi-diurnal:			
Principal Lunar	M_2	12.42	100
Principal Solar	S_2	12.00	46.6
Larger Lunar Elliptic	N_2	12.66	19.2
Luni-Solar	K_2	11.97	12.7
Diurnal:			
Luni-Solar	K_1	23.93	58.4
Principal Lunar	O_1	25.82	41.5
Principal Solar	P_1	24.07	19.4
Elliptical Lunar	Q_1	26.87	7.9
Longer period:			
Lunar Fortnightly	M_f	327.86	17.2
Lunar Monthly	M_m	661.30	9.1

The length of the lunar day, or the period of the Earth's rotation with respect to the Moon, is 24 hours and 50 minutes, and thus tides occur at intervals of 12 hours 25 minutes, which means there are 6 hours 12.5 minutes between high and low tide. The range of a spring tide, which occurs when the gravitational pulls of the Sun and Moon are aligned, is typically more than twice that of a neap tide, and the spring-neap cycle is 29.5 days (Open University Course Team, 1999).

Tidal Forcing

The shortest timescale changes exhibited by ice streams are related to tidal processes. The effects of a tidal range of approximately one metre on Whillans, Kamb and Bindschadler Ice Streams can be detected up to 100 km upstream, although propagation upglacier is greater for Whillans Ice Stream than for Kamb or Bindschadler (Alley *et al.*, 2004). A two week Global Positioning System (GPS) survey showed that Whillans Ice Stream moves by isolated rapid events lasting ten to thirty minutes each, interspersed with periods of no movement at all, lasting six to eighteen hours. Velocities reached one metre per hour, which, as Bindschadler *et al.* (2003) stated, is thirty times more than the usual ice stream velocity. Stress needs to be at least 4 kPa for a slip event to occur, and the speeds achieved were very close to those calculated if assuming a frictionless bed (Bindschadler *et al.*, 2003). These events were quite dramatic, with acceleration occurring in as little as half a minute, and deceleration over two to five minutes, and with a mean speed propagation of $88 \pm 79 \text{ m s}^{-1}$, close to the 150 m s^{-1} shear wave measured in the till upstream. Events were regular during spring tides, with an event shortly after high tide and one in the mid to late stages of the falling tide.

Kamb and Bindschadler Ice Streams also show a response to tidal variation, although in contrast to Whillans Ice Stream, this response is in antiphase (Bindschadler *et al.*, 2003). However, the tidal signal is dampened upstream, with propagation velocities of 1.5 and 5.6 m s^{-1} for Kamb and Bindschadler Ice Streams respectively. The seismicity rate, or the rate of basal microearthquake generation, beneath Kamb Ice Stream is affected by tidal influences from the Ross Ice Shelf up to 85 km upstream of the grounding line (Anandakrishnan and Alley, 1997), but the velocity response of Kamb has not yet been observed (Alley *et al.*, 2004). The velocity of Bindschadler Ice Stream varies by a factor of two over tidal cycles (Alley *et al.*, 2004). Diurnal variations in basal water pressure observed by Engelhardt and Kamb (1997) may also be tidally induced.

Interestingly, tidal modulation of the forward velocity of Brunt Ice Shelf showed a peak about 4 hours before the maximum tidal height, and so may be caused by currents rather than the actual tide (Doake *et al.*, 2002). Examples of tidally

induced variations in flow specific to the study area are discussed in section 2.8.1.

2.7 The Future of the WAIS

The future of the WAIS is highly uncertain. There is no definitive evidence for, or against, collapse in the relatively near future and the ability of models to quantify the likelihood of collapse is limited not only by uncertainties in parameterisation of the models but by incomplete understanding of the non-linear processes affecting the ice sheet (Alley and Bindshadler, 2001; Arthern and Hindmarsh, 2006).

2.7.1 Climate Change

Under warmer climatic conditions, ice streams may speed up by two main mechanisms: reduced buttressing from the ice shelves into which they drain, which may be melted by the warming ocean beneath and increasing air temperatures, and increased meltwater reaching the bed (Alley *et al.*, 2004), although this last is not a major consideration in the Antarctic.

Ice Shelves

Weertman (1974) originally proposed the theory that ice sheets may be buttressed by back pressure from their surrounding ice shelves, and as such their velocity would increase if this surrounding ice were to be removed. “Ice-shelf buttressing may offer the greatest opportunity for ice stream perturbations” (Alley *et al.*, 2004, p.725).

Ice shelves off the WAIS are highly significant, and cover half the area of the ice sheet itself, with the Ross and Filchner-Ronne being the two largest ice shelves on the planet, 850,000 km² and 360,000 km² respectively, and flowing between 800 and 2600 m a⁻¹ (Benn and Evans, 1998; Bindshadler, 2006). The FRIS is part of the study area, and buttresses the Rutford and Evans Ice Streams,

among others. Of the WAIS ice streams and outlet glaciers, only Pine Island and Thwaites Glaciers are largely unbuttressed and this drainage system flowing into Pine Island Bay in the Amundsen Sea may be the most unstable part of the WAIS because of this (Bentley, 1998). Sediment cores from the Pine Island Bay show that the buttressing ice shelf was more significant as little as one hundred years ago. When ice shelves are spatially constrained in embayments, as is the case for many Antarctic ice shelves, resistance to flow comes mainly from lateral drag (although basal drag acts when ice shelves become grounded on ice rises, as is common for WAIS ice shelves). Lateral drag is decreased if the distance between the grounding line and the shelf front becomes shorter due to either grounding line advance, calving, or ice shelf collapse, thus decreasing back pressure (Van der Veen, 1999). Sea level rise may also reduce the back pressure from ice shelves if it is enough to cause ungrounding of the ice shelf from ice rises, reducing basal drag. Ice streams with greater width or driving stress are most vulnerable to the effects of the loss of a buttressing ice shelf (Dupont and Alley, 2005).

Bentley (1998, p.157) stated that it is “difficult to see how climate warming... could trigger a collapse of the WAIS in the next century or two.” However, the collapse of the Larsen B ice shelf since the time Bentley was writing, and the effect on the glaciers previously buttressed it, have opened up new possibilities.

Ice Shelf Collapse

Following the collapse of the 1600 km² Larsen A ice shelf, off the east coast of the Antarctic Peninsula, in January 1995, the Larsen B ice shelf collapsed in February and March 2002, with 500 billion tonnes of the 200 m thick ice shelf disintegrating over a 3250 km² area in less than a month. The British Antarctic Survey (BAS) had predicted this in 1998 due to a 2.5°C warming in the region over the preceding 50 years, and Skvarca *et al.* (1999) had also predicted it after observing southward-moving melting and the development of rifts, using both remote sensing methods and field surveys, since a major calving event in 1995. The initial collapse was spotted by the MODIS (Moderate Resolution Imaging Spectroradiometer) satellite, following which BAS sent their ship the James Clark

Ross to observe.

The Antarctic Peninsula ice shelves had two phases of collapse, firstly retreating due to climatic factors such as warming air and sea temperatures, before catastrophically collapsing. The final collapse of Larsen B was believed to be triggered by rupturing at suture zones between the four main flow units of the ice shelf, which are thinner than the surrounding ice and weakened by a decrease in lateral resistive stress following retreat of the shelf front between 1998 and 2000 (Glasser and Scambos, 2008). Landsat, Advanced Spaceborne Thermal Emission and Reflection Radiometer (ASTER) and RADARSAT data showed that the large rift systems offshore of Foyen Point and Cape Disappointment had developed in the last 20 years and became more pronounced immediately before the ice shelf collapsed and marked the landward limit of collapse. The four units were fed by four groups of tributary glaciers to Larsen B (Crane, Jorum, Punchbowl and Hektoría/Green/Evans), which are believed to have triggered collapse by changing their differential inputs to the ice shelf (Glasser and Scambos, 2008).

Effect on Previously Buttressed Glaciers

The collapse of the Larsen ice shelves led to velocity increases and thinning of glaciers discharging into the Weddell Sea, which had previously been buttressed. Following the collapse of Larsen A, satellite images and aerial surveys showed surging of Boydell, Sjögren, Edgeworth, Bombadier and Drygalski glaciers, with Drygalski glacier's velocity increasing three-fold between 1995 and 1999, accompanied by an areal loss of 24 km² from its ice front (de Angelis and Skvarca, 2003). This was a very significant finding, as buttressing was not usually included in ice sheet models at that time and de Angelis and Skvarca (2003) called for a re-examination of that theory, which indeed subsequently happened.

Similarly, following the collapse of Larsen B, Landsat images showed two to six-fold increases in the centre-line velocities of four previously buttressed glaciers, Hektoría, Green, Jorum and Crane glaciers, while ICESat laser altimeter data also showed thinning of Hektoría, Jorum and Crane glaciers (Scambos *et al.*,

2004). InSAR also showed an eightfold increase in the velocities of Hektor, Green and Evans glaciers between 2000 and 2003, followed by a deceleration, and a threefold increase in the velocities of Jorum and Crane glaciers by the end of 2003 (Rignot *et al.*, 2004a), in total leading to mass loss of $27 \text{ km}^3 \text{ a}^{-1}$ and thinning of tens of metres. In contrast, the velocity of nearby glaciers further south which remained buttressed, such as Flask and Leppard glaciers, did not increase (Rignot *et al.*, 2004a; Scambos *et al.*, 2004). There is no doubt that grounded ice on the northeastern parts of the Antarctic Peninsula is retreating, and contributing to sea level rise (de Angelis and Skvarca, 2003).

Other glaciers along the Antarctic Peninsula are also retreating. Two hundred and forty-four tidewater and marine glacier fronts on the Antarctic Peninsula and its islands were examined using aerial photographs and satellite images from 1940 to 2001 in a Geographic Information System (GIS) by Cook *et al.* (2005), who found that 87% of them were retreating, probably as a dynamic response to thinning of the glacier fronts (Pritchard and Vaughan, 2007), and a clear divide between mean advance and mean retreat moved southward over the study period. The combined contribution to sea level from the Antarctic Peninsula region, including increased runoff due to more snowmelt, and the acceleration of glaciers previously buttressed by ice shelves, was estimated at $0.16 \pm 0.06 \text{ mm a}^{-1}$, which may be enough to cancel out mass gained by the EAIS (Pritchard and Vaughan, 2007).

Pine Island, Thwaites and Smith Glaciers may also have been affected by the collapse of their buttressing ice shelves. The ice shelf in Pine Island Bay thinned 5.5 m a^{-1} in the decade leading up to 2004 because of ocean currents 0.5° above freezing (Shepherd *et al.*, 2004), and the observed increase in the velocity of Pine Island Glacier over the period 1996 - 2000 may have been caused by 25 km of the ice plain becoming ungrounded (Thomas *et al.*, 2004). Pine Island Glacier has accelerated 38% since 1975 (Rignot, 2006) and the ice stream can discharge 80 km^3 ice per year (Thomas *et al.*, 2004). Velocity increased 12% up to 80 km inland over the period 1992 - 2000 as shown by SAR feature tracking (Rabus and Lang, 2003). The ice front has fluctuated over the last few decades and is retreating over the longer term (Vaughan *et al.*, 2001). Schmeltz *et al.* (2002)'s finite element model of Pine Island Glacier also suggested that a decrease of 5.5%

to 13% in the area of the ice shelf would lead to a velocity increase of 3.5 to 10% at the grounding line, and the removal of the entire ice shelf would lead to a 70% increase. As with the shelves surrounding the Antarctic Peninsula, the ice shelf here was affected by the warm Circumpolar Deep Water (CDW) (Rignot *et al.*, 2008) causing basal melting, and may continue to be so, and 15 to 35% of the mass lost by the Antarctic Ice Sheet may already be from melting at the base of ice shelves (Jenkins *et al.*, 2006).

Ice Shelf Viability

It is entirely possible that the potential collapse of parts of the Ross and Filchner-Ronne ice shelves could have the same effect on WAIS ice streams that the collapse of the Larsen B ice shelf had on the glaciers of the Antarctic Peninsula. Some models suggest that the type of collapse which affected Larsen B could also affect the larger ice shelves (LARA Steering Committee, 2005). The FRIS is fed by ten ice streams, nine of which are currently active (Joughin and Vaughan, 2004). Ice streams and outlet glaciers have long been known to persist considerable distances out onto the ice shelf (Paterson, 1994) and velocity differentials between them, like those which may have caused the collapse of Larsen B, may also persist. However, the Larsen ice shelves differ from the much larger Ross and Filchner-Ronne Ice Shelves in that they were formed from the outflow of terrestrial mountain glaciers and basal freeze-on, whereas the Ross and Filchner-Ronne are extensions of the marine ice sheet (Anderson, 1999), and as such may be affected by different mechanisms.

The limit of ice shelf viability is estimated to be the -5°C mean annual isotherm, or the -1.5°C January isotherm. The FRIS currently lies between the -17°C and -25°C mean annual isotherms (Glasser and Scambos, 2008; Morris and Vaughan, 2003). Mercer (1978) expected southward recession of ice shelves close to the 0°C January isotherm at that time, predicting the loss of the ice shelf in Prince Gustav Channel, at the north end of the Antarctic Peninsula, among others, although he was not pessimistic enough to predict the loss of the Larsen Ice Shelves. He noted that average midsummer temperatures at the shelf fronts of

both the Ross Ice Shelf and the FRIS were between -4°C and -5°C , and stated a 5°C warming at 80°S could be enough to initiate southward recession of these major ice shelves, although Huybrechts (2004) states that a 10°C warming would be required, and highlights that in any case, the response time of these large ice shelves would be hundreds of years. Although the locations of the Ross and Filchner-Ronne ice shelves, much further south than the Larsen ice shelves, make them less vulnerable to imminent collapse, weakening of these ice shelves may also be caused by thinning due to basal melting, as ice shelves are vulnerable not only to increasing air temperatures above but also to warming of the ocean water beneath (Vaughan and Spouge, 2002), and a 1°C rise in ocean temperatures could lead to a 10 m a^{-1} increase in basal melting (Solomon *et al.*, 2007). Near the ice front, shelves may also be melted by seasonally warmed currents being pumped beneath them by tidal action (Bentley, 2004).

2.7.2 Regional Climate

As well as ice streams being affected by climate, regional climate may be affected by the characteristics of the WAIS ice streams. The surface slope of ice streams is approximately 10^{-3} , as opposed to the crests of slow moving ice which separate ice streams, where it is 10^{-2} (Raymond *et al.*, 2001). The slope of the ice stream decreases downstream as it flows to the ice shelf, with decreases in slope corresponding to increases in velocity, while upstream the surface slope is still influenced by the inland flow regime. The low surface slope leads to inland ice lying at a lower elevation than would otherwise be the case, allowing precipitation bearing weather systems to move further inland, thus increasing accumulation (Bindschadler *et al.*, 2001). The interior of the EAIS gained mass due to increased precipitation during the period 1992-2003 (Davis *et al.*, 2005) which may be due to this effect. However, Rignot *et al.* (2008) found no changes in modelled accumulation from 1980 to 2004.

2.7.3 Implications

It may be that ice streams are the first areas of an ice sheet to be affected by changes in the mass balance of the ice sheet, whether these changes are from internal changes in ice dynamics or external climate effects, or that their high velocities mean they are the first areas where these changes are identified. The fast flow of ice streams means that the response time of the WAIS is rapid, as “perturbations of flow are transmitted rapidly upstream into the inland ice and downstream onto the ice shelf” (Bindschadler *et al.*, 2001, p.123-124).

The magnitude and sign of the mass balance of the Antarctic Ice Sheet and its contribution to sea level rise cannot currently be determined (Bentley, 2004). Overall, the three main groups of ice streams draining the WAIS are behaving differently. The Ross Sea Sector was shown using SAR-derived velocities to have a positive mass balance of 26.8 Gt a^{-1} by Joughin and Tulaczyk (2002), a revision of previous estimates which were negative. The Amundsen Sea Sector shows increasingly negative revisions of estimates of mass balance the more it is studied, with an imbalance of Pine Island, Thwaites, Smith, Pope and Kohler Glaciers of $-81 \pm 17 \text{ km}^3 \text{ a}^{-1}$ (Rignot *et al.*, 2004b). The Weddell Sea Sector, which includes the study area (figure 2.2), is probably in equilibrium (Bindschadler, 2006; Rignot and Thomas, 2002). For the Antarctic as a whole, Rignot *et al.* (2008) compared accumulation from a regional climate model to satellite-derived mass flux to the ocean around 85% of the Antarctic coastline, and found that loss had increased 75% in 10 years, mostly from the Antarctic Peninsula and the Amundsen Sea Sector. In any case, most sea level rise from a collapse of the WAIS, whatever the cause, would occur later than the 21st century because of the response time of the ice sheet and the potential for future ice shelf loss under a warmer climate, reducing buttressing effects and allowing more ice to cross the grounding line (Oppenheimer, 1998).

Whether the collapse of the present WAIS is likely, or indeed possible, is “glaciology’s grand unsolved problem” (Vaughan and Spouge, 2002, p.65). Hughes (1973) suggested the West Antarctic Ice Sheet “might be disintegrating now as a continuation of recession since the last ice age” (Paterson, 1994, p.312), although Steig

et al. (2001) state the WAIS seems to have adjusted to sea level rise and the increase in accumulation since the LGM. Suggestions that the WAIS could collapse as a result of greenhouse warming date back to Mercer (1978, p.321), who felt that “a major disaster... may be imminent or in progress,” but estimates of the probability of WAIS collapse seem to have decreased over time in the literature. Alley and Bindshadler (2001) state that there is no evidence to suggest impending collapse of the WAIS, but no evidence to suggest the WAIS will not collapse either. Even if the WAIS does collapse, its cause may not be anthropogenic, and it may instead be due to internal instabilities and/or adjustment since the LGM (Oppenheimer, 1998; Vaughan and Spouge, 2002).

Research into the velocity of West Antarctic ice streams is ongoing through the complementary approaches of remote sensing, modelling, and direct field measurements. The most significant conclusions of recent research have come from studies focussed on the velocity and characteristics of individual ice streams, and as such the study of ice streams has a vital role in assessing whether or not the WAIS has the potential for rapid collapse, and, should this be the case, under what conditions.

While the response of the ice sheet as a whole is unclear, with many contradictory views on this held, previous work focussing on the response of individual ice streams has produced some significant conclusions. Two of the ice streams draining the WAIS, the Rutford and Evans Ice Streams, will be examined in more detail using the remote sensing method of interferometry, complemented by tidal and elastic beam modelling.

2.8 Study Area

2.8.1 The Rutford Ice Stream

The Rutford Ice Stream is situated in West Antarctica (figure 1.1), draining a 49,000 km² area of the WAIS (Doake *et al.*, 2001). The ice stream is between 20 and 30 km wide, and is 150 km long from onset to grounding line, flowing in a southeasterly direction to the Ronne Ice Shelf. Grounding occurs below sea level, as the bed of the ice stream slopes down toward the centre of the ice sheet. The ice stream is constrained in a subglacial trough, with the slow moving ice of the Fletcher Promontory, which is frozen to its bed, to the east, and the Ellsworth Mountains, which dam the natural direction of drainage of ice from the interior of the continent, to the west. The well-defined southern margin of the onset region overlies a bedrock step (King *et al.*, 2007). This project will focus especially on the area around Rutford Ice Stream due to other work in this region.

The Rutford Ice Stream basin is unusual, having the most extreme vertical relief of any basin globally. The Vinson Massif situated in the Ellsworth Mountains is the highest mountain in Antarctica, at 4897 m, while the bed of the ice stream descends to elevations more than 2000 m below sea level, making a 7 km elevation range over just 40 km horizontal distance (Doake *et al.*, 2001; Smith and Doake, 1994; Swithinbank, 1988). Rutford lies over an asymmetrical W-shaped trough (with a ridge in bed topography in the middle), which continues both downstream of and at least 170 km upstream of the grounding line (Smith and Doake, 1994). The deeper, outer sections of the W-shaped trough contain deforming sediment, whereas the central section undergoes a transition from deforming to sliding conditions downstream (Smith and Murray, 2008). The west side of the trough is much steeper than the east, with slopes of 1:2 compared to 1:10 (Doake *et al.*, 1987).

Rutford has been a field site since 1978 (Smith, 2006b), and is suitable for field-work due to the limited amount of crevassing, and the presence of the Ellsworth mountains adjacent to the ice stream, which can be used as reference points for

movement surveys (Stephenson and Doake, 1982), a factor which is also significant in remote sensing work.

Flow

Ice velocity at the onset of the Rutford Ice Stream is 200 m a^{-1} , increasing to 300 m a^{-1} as far downstream as the shear margin with Carlson Inlet (figure 1.1), 130 km upstream of the grounding line. The maximum velocity is 400 m a^{-1} , 40 km upstream of the grounding line, before velocity decreases downstream of the grounding line for 190 km (Frolich *et al.*, 1989; Swithinbank, 1988). GPS data taken 40 km upstream of the grounding line during the 2004 - 2005 field season showed velocity was 377 m a^{-1} (Murray *et al.*, 2007). GPS data from that season also support the findings of Frolich and Doake (1988) that the fastest flow coincides with that of the thickest ice and the deepest bed, displaced towards the Ellsworth Mountains to the west of the ice stream, as the fastest velocity of 380 m a^{-1} occurred at the westernmost station, 13 m a^{-1} faster than at the easternmost station (Aðalgeirsdóttir *et al.*, 2008). The strain rate is $3 \times 10^{-3} \text{ a}^{-1}$, similar to that of Whillans Ice Stream on the Siple Coast and highest strain rates on the Ross Ice Shelf, into which Whillans Ice Stream drains (Paterson, 1994; Stephenson and Doake, 1986).

The mean driving stress of the Rutford Ice Stream is 40 kPa, which is resisted by marginal stress up to 10 km in from the sides of the ice stream, and basal shear stress in the centre. Because of this, the marginal and central ice have differing flow regimes. Using three transverse profiles of the ice stream, Frolich and Doake (1988) found that a basal shear stress of 40 kPa was necessary for restraining the middle third of the ice stream, as lateral shear stresses of up to 100 kPa restrained the ice stream up to 10 km from each of its margins. Stress at the margins is up to a maximum of 160 kPa, and the resultant crevassing is shown clearly on SAR images (Doake *et al.*, 2001).

Stephenson and Doake (1982) reported the findings of ground surveys of the ice stream from the 1978-1979 and 1979-1980 field seasons, using stakes to derive

velocity and strain rates for longitudinal and transverse profiles, and of an air survey from the following season, using RES. They found that the ice stream moved by “fingers” of thicker ice, with thinner ice in between. The same authors, in a 1986 paper examining strain rates, which found compressive flow in the longitudinal direction and extensive flow in the lateral direction, found peaks in the lateral strain rate which showed that the thicker ice was spreading more rapidly at the expense of the thinner ice (Stephenson and Doake, 1986).

Mass Balance

While Doake *et al.* (2001) state that the input and output of the Rutford Ice Stream seem to be in balance at present, with ice discharge across the grounding line being 18.5 ± 2 Gt per year, Rignot (1998b) suggests that the mass budget may be slightly positive, with discharge across the grounding line being 17 ± 2 km³a⁻¹ compared to a mass input of 20 ± 3 km³a⁻¹. However, more recently, Joughin and Bamber (2005) calculated slightly negative mass balance using flux gate methods (which compare an ice stream’s estimated annual discharge to the ocean with estimated annual accumulation), with discharge of 17.8 ± 1.8 Gt a⁻¹ compared to accumulation of 15.1 ± 3.9 Gt a⁻¹, leaving a mass balance of -2.7 ± 4.3 Gt a⁻¹, or a 6.3 ± 10.0 cm a⁻¹ thinning of the ice stream. It is not known whether the sediment supply of the ice stream is also in balance (Doake *et al.*, 2001).

The Bed

Some of the more recent work on Rutford has focused on the bed of the ice stream. Numerous seismic surveys have been carried out. The Rutford Ice Stream has varying basal conditions. The type of sediment beneath each part of the ice stream affects the mechanism by which the ice stream moves. In areas of high bed porosity, the upper ten metres of the bed are deformed by the ice, allowing its movement, while in areas of low porosity, the ice moves by basal sliding. The divide between these areas may be sharp and the sediment type varied both along and across the ice stream (Smith, 1997c).

The average acoustic impedance of the bed, which is a measure of its mechanical properties using seismic techniques, at a transverse seismic line (New Line) approximately 95 km upstream of the grounding line (Vaughan *et al.*, 2003) and therefore approximately halfway down the length of the ice stream, showed values typical for deforming sediments, decreasing from $3.88 * 10^6 \text{ kg m}^{-2}\text{s}^{-1}$ to $3.19 * 10^6 \text{ kg m}^{-2}\text{s}^{-1}$ at another line (Tyree Line) a further 52 km downstream, meaning that the amount of saturated deforming sediments increased downstream, and as such the amount of non-deforming sediment, over which ice must move by basal sliding, decreased (Smith, 1997c). Smith (1997a) also reports results from Tyree Line, finding that most or all of the bed material there was saturated, although not all was deforming and for a quarter of the seismic line the ice was thought to be moving by basal sliding, causing increased basal friction and therefore increased basal melting compared to the areas of deforming sediment. Localised areas were found to be supporting a disproportionate amount of the basal shear stress, and these areas did not correlate to measured surface velocities or those derived from remote sensing methods Smith (1997a). However, no stick-slip motion of the Rutford Ice Stream was found during investigations in the 2004-2005 field season (Smith, 2006b).

Vaughan *et al.* (2003) used seismic techniques to measure the acoustic impedance of material beneath four WAIS ice streams, and found that deforming, or dilated, sediments and non-deforming, or lodged, sediments, coexisted beneath the Rutford Ice Stream in bands with a width of several kilometres each. This observation was confirmed with passive seismics, showing that areas of the bed undergoing basal sliding generated six times more microearthquake events than areas with a deforming bed (Smith, 2006a). The locations of these two sediment types did not correlate to subglacial topography or ice thickness.

One cross stream seismic line on Rutford, Tyree Line, was surveyed three times. Between 1991 and 1997 a 500 m wide section of the bed showed 6 metres of erosion in as many years, and between 1997 and 2004, a drumlin 10 m high, 100 m wide and at least 1 km in the upstream direction had formed of deforming water-saturated sediment (Smith, 2006b; Smith *et al.*, 2007). Debris fluxes of up to 100 m^3 per metre width may be transported by WAIS ice streams (Bougamont

and Tulaczyk, 2003), and this is an unprecedented observation of the rapid reorganisation of the bed of an ice stream. Subglacial bedforms in the onset region of the ice stream, where ice flow increases from 72 m a^{-1} to 200 m a^{-1} , have also been investigated using geophysical methods, with seismic and radar data showing moraines being formed from the deforming, unconsolidated sediments at the bed when the flow speed is less than 95 m a^{-1} , and drumlins being formed when flow exceeds this (King *et al.*, 2007). Both these features are part of the bedform assemblage associated with the onset region of palaeo-ice streams, and show active erosion and deposition beneath the onset region of Rutford (King *et al.*, 2007). Investigations by Smith and Murray (2008) over a 150 km^2 area on the main trunk of the ice stream found subglacial bedforms with a mean height of 22 m and width of 267 m, up to 2 km long, made up of deforming sediment and overlying both areas of deforming bed and areas of basal sliding. Subglacial drainage has also been investigated using seismics, with King *et al.* (2004) discovering an area at least 1 km by 0.2 km beneath the ice stream with water less than 1 m deep, providing evidence of theoretically predicted shallow subglacial channels in the sediment.

Remote Sensing

The Rutford Ice Stream has previously been studied by remote sensing methods as well as by direct observations through fieldwork. Vaughan and Doake (1989) undertook an early remote sensing study of the Rutford Ice Stream, comparing a Landsat image from 1974 and a SPOT image from 1987. They found that topography on the surface of the ice stream had been displaced downstream over the thirteen year period between the images by distances of several kilometres, which suggested ice velocities agreeing with those established by ground surveys. This also suggested that the bed of the ice stream was being transported with the moving ice. At the time they declared this explanation unlikely, but it is in keeping with the later till ploughing model of Tulaczyk *et al.* (2001) and Frolich and MacAyeal (1990)'s model also required vertical shear to be confined to a then unobserved deformable substrate, or a basal layer, although it was known that

an equivalent mechanism must exist from previous studies.

The Rutford Ice Stream has previously been studied using SAR, and indeed was the subject of one of the most significant studies using ERS SAR data. Goldstein *et al.* (1993) undertook a groundbreaking study using interferometry to calculate flow velocities for the Rutford Ice Stream, using 6-day repeat ERS-1 scenes, and mapped the grounding line to a precision of half a kilometre. Their velocities and grounding line position agreed well with previously acquired ground based data. They also discovered that the detection limit from SAR interferometry was 1.5 mm for vertical motion and 4 mm for horizontal motion. Frolich and Doake (1998) used interferometry on the Rutford Ice Stream and Carlson Inlet, finding that the upper 50 km of Carlson Inlet have a velocity less than one tenth that of the Rutford Ice Stream. However, they also found that the lower section of Carlson Inlet had faster moving ice flowing into it. SAR images have also shown decadal variations in the velocity of the upstream shear margin (Doake *et al.*, 2001), and that there was no change in the position of the hinge line, the limit of tidal flexing, from 1992-1996 (Doake *et al.*, 2001; Rignot, 1998b).

Frolich and Doake (1998) used interferograms of the Rutford Ice Stream to compare ice velocity in 1992 with that in 1978, finding no significant difference over that time period, with the exception of fluctuations of the order of ten metres per year at the shear margin between Rutford Ice Stream and Carlson Inlet. This project will carry on where Frolich and Doake (1998)'s paper left off, deriving velocity fields for the Rutford Ice Stream from 1992 onwards throughout the period when satellite scenes with suitable orbital repeat periods for interferometry were available (section 4.2).

The Grounding Zone

Early fieldwork on the Rutford Ice Stream focussed on the grounding line area. Hydrostatic tiltmeters were used by Stephenson and Doake (1982), who found that the grounding line follows a sinusoidal path around what they rightly thought to be local pinning points, rather than following a straight and simple hinge line,

as was assumed for other ice streams that had not had extensive field surveys conducted on them at that time. They found that even grounded ice was still affected by tidal flexing for a distance approximately equal to the ice thickness, and ice which had reached hydrostatic equilibrium may not start to float if the topography of the bedrock underlying the ice stream was unfavourable (Stephenson, 1984; Stephenson and Doake, 1982). Early modelling suggested that the position of the grounding line is extremely sensitive to changes in ice thickness, with a 0.5 m perturbation in ice thickness leading to a 250 m migration of the grounding line (Stephenson and Doake, 1982). An extensive study using GPS and phase sensitive radar, among other methods, to examine 14 sites downstream of the grounding line on the Ronne Ice Shelf, was undertaken by Jenkins *et al.* (2006), who found mean basal melt rates of 0.85 m a^{-1} . Doake *et al.* (1987) report that ice 100 km downstream of the assumed grounding line is intermittently grounded, and ice further upstream than the assumed grounding line may have started floating. Grounded areas on the ice shelf corresponded to depressions in surface elevations, and had values of $1 - (e/h)$ lower than floating ice, where e is the surface elevation and h the ice thickness, although surface elevations could not be defined accurately enough to compare to the hydrostatic profile.

Stephenson (1984) reports on two methods used to map the grounding line of the ice stream. Topographic data from optical levelling and RES ice thickness data were combined to determine where the ice reached hydrostatic equilibrium (although in a much later study, Jenkins *et al.* (2006) found that ice was not at hydrostatic equilibrium close to the grounding line), and tiltmeters were used to determine the limit of tidal flexing. Flexing occurs 1-3 km above where hydrostatic equilibrium is reached, and an elastic-beam model showed that a tidal amplitude of 3 m would produce a 300 m zone of migration of the grounding line throughout the tidal cycle, assuming a bedrock gradient of 10^{-2} to match the surface gradient.

Smith (1991) used tiltmeter data to investigate the decay in tidal flexure with distance from the grounding line for the semi-diurnal tidal component M_2 at Doake Ice Rumples, and applied findings from there to Stephenson (1984)'s data from the grounding zone of the Rutford Ice Stream, recalculating the location of

the grounding line and removing the need to assume an ice thickness much less than that measured in order for the data to fit the original model. The Ronne Ice Shelf plays a more important role in determining ice flow than lateral shear stress (Stephenson and Doake, 1982), and according to a 2D finite element model, a 10% reduction in back stress would lead to a 15% increase in flux across the grounding line (Frolich and MacAyeal, 1990).

Interferometry has previously been used to map the grounding zone of the Rutford Ice Stream. Rignot (1998b) used double difference interferograms from 1992, 1995 and 1996, and found no migration of the hinge zone of either Rutford Ice Stream, or neighbouring Carlson Inlet during that period. Similar methods, which are discussed further in section 3.10, will be applied to both the Rutford and Evans Ice Streams in this study.

Tidal Motion

Some recent work on Rutford has focussed on tidally induced motion of the ice stream. The usual peak-to-peak tidal range for the ice shelves surrounding the Antarctic is 1-2 m, with the largest tides occurring in the Weddell Sea, but the range is greater than 3 m for the FRIS, and twice that at spring tides, and 6 m for the Rutford Ice Stream grounding line (Doake, 1992; Padman *et al.*, 2002). The Circum-Antarctic Data Assimilation (CADA10) model found tidal ranges of over 7 m in the channels south of Henry and Korff Ice Rises, consistent with this, and also at Doake Ice Rumples (figure 1.1). It is therefore clear that the study area has an exceptionally large tidal range.

Variations in ice stream velocity have been found on fortnightly timescales corresponding to spring-neap tidal cycles. GPS from the 2003-2004 field season were sampled every five seconds for seven weeks at five sites ranging from 20 km downstream to 40 km upstream of the grounding line. Over one week, velocities at the grounding line changed from 0.9 to 1.2 m day⁻¹, 27% of the total velocity, whereas 40 km upstream, velocities changed from 0.95 to 1.07 m day⁻¹, 12% of the total velocity (Gudmundsson, 2006). Velocities increased leading up to the

spring tide, and decreased until the neap tide, with diurnal variations superimposed on the signal. This suggests that changes in the peak-to-peak amplitudes of the semi-diurnal tides may be the cause (Gudmundsson, 2007). Using the t_tide model, discussed in section 4.5.1, the fortnightly tidal constituent MSf was found to be dominant at all sites. Gudmundsson (2006) suggests that basal shear stress distribution is affected by tidally modulated elastic stresses, but that the relationship is non-linear, with a positive perturbation leading to a greater increase in basal motion than the magnitude of decrease caused by a negative perturbation of equal size. Tidally induced modulation of the basal sliding velocity may occur if the tidally induced changes in basal shear stress are large enough compared to mean basal shear stress. The observed variations in velocity were modelled assuming a linear relationship between tidal stresses and tidal amplitude, and thus tidal amplitude and basal shear stress, and that viscous till deformation allows a non-linear relationship between shear stress and the rate of basal motion. The model fitted the data well (Gudmundsson, 2007). The surface velocity and passive seismic records have also been compared to tidal cycles, and peaks in velocity found to correspond to both high and low tides, and, in some cases, falling tides (Aðalgeirsdóttir *et al.*, 2008).

Tidally modulated variations in ice stream flow velocity have also been found over longer periods using two years of GPS data from 40 km upstream of the Rutford grounding line, the first such observation over such a long time period (Murray *et al.*, 2007). The mean displacement rate of the ice stream was removed from the data to examine tidal perturbations. During equinoxes, flow is fastest, as the two semi-diurnal tides are of equal magnitude because the two main semi-diurnal components, M_2 and S_2 are in phase; conversely, flow is slowest at solstices when the two semi-diurnal tides are at their most unequal, despite this leading to the largest tidal range at the spring tide (Murray *et al.*, 2007).

Gudmundsson (2007) states that similar variations should be expected in other ice streams with similar tidal forcing, such as those draining into the Filchner-Ronne Ice Shelf, and the reason such variations have yet to be observed is lack of data. It is therefore likely that similar effects are present on the Evans Ice Stream. Tidal effects on both ice streams are discussed further in chapter 6.

2.8.2 The Evans Ice Stream

The Evans Ice Stream (figure 1.1) is approximately 250 km long, 60-75 km wide and drains into the Ronne Ice Shelf north of Rutford; in between the two lies Carlson Inlet, which is currently frozen to its bed and therefore not fast moving. The Evans Ice Stream is a large ice stream with a 104,000 km² catchment and five tributaries, about which there is surprisingly little published work, especially considering its discharge is the greatest of any ice stream draining into the FRIS, estimated at $35.7 \pm 3.6 \text{ Gt a}^{-1}$ (Bamber *et al.*, 2000c; Joughin and Bamber, 2005; Joughin *et al.*, 2006). The velocity of Evans is greater than that of Rutford, with which it has an ice divide, as shown by speckle-tracking (utilising successive radar satellite scenes to show ice movement) with tidal corrections (Joughin and Padman, 2003; Larour *et al.*, 2005). Accumulation is estimated at $40.0 \pm 7.8 \text{ Gt a}^{-1}$, leading to an estimated mass balance of $4.3 \pm 8.6 \text{ Gt a}^{-1}$, or a $4.6 \pm 9.1 \text{ cm a}^{-1}$ thickening of the ice stream (Joughin and Bamber, 2005). However, as with the figures from the same paper for Rutford, uncertainties are high because of uncertainties in the accumulation data. Table 2.3 compares the dimensions and main characteristics of the Rutford and Evans Ice Streams.

The bed of the seismically surveyed part of the Evans Ice Stream is composed entirely of dilated sediments allowing fast flow, unlike that of the Rutford Ice Stream which also has bands of non-dilated sediment (Vaughan *et al.*, 2003). An inversion of a finite-element ice stream model was used to estimate the basal shear stress, which was found to be low under the eastern part of the main trunk and the easternmost tributary, in keeping with the porosity observations of Vaughan *et al.* (2003), and higher under the western part of the main trunk and the other tributaries (Joughin *et al.*, 2006).

The Evans Ice Stream has an interesting grounding zone. Prior to this present work, three published versions of the grounding line, from Vaughan *et al.* (2003), Joughin *et al.* (2006) and the MODIS mosaic (Haran *et al.*, 2006) did not agree on the location or shape of the grounding line, as discussed further in chapter 7. Gudmundsson (2007) also expects the Evans Ice Stream to show similar fortnightly tidal variations to Rutford.

Table 2.3: The main characteristics of the Rutford and Evans Ice Streams.

	Rutford	Evans
Length (main trunk)	150 km	250 km
Width (main trunk)	20-30 km	60-75 km
Typical ice thickness (Lythe <i>et al.</i> , 2001)	2200 m	1400 m
Flow direction (main trunk)	Southeast	East
Catchment area	49,000 km ²	104,000 km ²
Discharge (Joughin and Bamber, 2005)	17.8 ± 1.8 Gt a ⁻¹	35.7 ± 3.6 Gt a ⁻¹
Bounded	Slow-moving ice to east; mountains to west	Slow-moving ice to both sides
Tributaries	1	5
Trough	Bedrock step at head; W-shaped trough	Shallower, less well-defined
Bed	Dilated and undilated sediment	Dilated sediment
Terminates	Ronne Ice Shelf	Ronne Ice Shelf

Despite the historical lack of interest in the glaciology of the Evans Ice Stream, it has been a base for geological fieldwork due to its tectonic location at the boundary between the Antarctic Peninsula and Haag Nunataks crustal blocks (e.g. McGibbon and Smith (1991)). However, field expeditions to the Evans Ice Stream are hampered by crevasse fields and bad weather conditions, with weather systems from the Weddell and Bellingshausen Seas moving in from both sides to cause poor visibility, severely limiting work on the ground and preventing the landing of aircraft (E. King pers. comm., 2006, E. Morris pers. comm., 2007, A. Smith pers. comm. 2008). It is clear a gap in the glaciological literature needs to be filled. Remote Sensing methods, particularly using active microwave sensors such as Synthetic Aperture Radar (SAR), which can penetrate clouds, are therefore highly suitable methods for looking at the Evans Ice Stream.

2.9 Summary

This chapter has reviewed the literature on relevant aspects of the West Antarctic Ice Sheet and its ice streams. The WAIS may not have survived interglacials warmer than the present one, and it is not known whether collapse of the WAIS, either because of internal dynamics or anthropogenic climate change, is imminent, likely, or even possible. The grounding zone of the ice sheet is a major control on stability, and the effects of the loss of buttressing ice shelves have already been observed. The ice streams draining the WAIS are a complex system, and have shown differing behaviour as a response to different factors. There are currently examples of ice streams that are accelerating, decelerating, and stopped, and areas of the ice sheet with positive, negative and neutral mass balance. Direct study of the continent is hampered by its inaccessibility, and modelling is hindered by lack of data. Using remote sensing methods to examine ice streams and their grounding zones overcomes these limitations. The two ice streams studied in this project, which are on the same coast and part of the same system, were chosen for different reasons: Rutford Ice Stream because it has a long history of previous work, and Evans Ice Stream because it has so little and may be affected by similar factors to Rutford. These ice streams were examined using Synthetic Aperture Radar interferometry, discussed in the next chapter, and tidal and elastic beam modelling, discussed in chapter 4, in order to derive velocity fields, map their grounding zones, and assess any changes in these related to tidal effects.

Chapter 3

Synthetic Aperture Radar Interferometry

3.1 Introduction

The remote sensing method of interferometry will be applied to the Rutford and Evans Ice Streams. This chapter will discuss the principles and limitations of the type of satellite data used, Synthetic Aperture Radar (SAR), with particular reference to the characteristics specific to the European Remote-Sensing Satellites ERS-1 and ERS-2. The interferometric processing chain will be explained, with further sections outlining how the interferograms produced may be used to derive Digital Elevation Models (DEMs) and ice stream velocities through the use of Ground Control Points (GCPs) and phase unwrapping. This chapter will also serve to outline the remote sensing part of the methodology of this study, and at each stage, the Gamma software routines used will be outlined, along with justification of the decisions taken on alternative methods, routines and options within them. It will be shown how interferograms may also be used to map ice stream grounding zones. Examples of previous studies which have successfully applied interferometry to the cryosphere will also be described.

3.2 Basic Principles of Radar

Radar (RA^Dio De^Tection and RA^Nging) uses the time delay between the transmission of an electro-magnetic (EM) signal and the reception of its echo to show the distance to the target, knowing that EM waves travel at the speed of light, c . Synthetic Aperture Radar (SAR) uses a short antenna which is moving, to simulate a longer antenna in order to improve the resolution of the image in the along-track, or azimuth, direction. This is necessary for airborne and spaceborne platforms because of the large distances from sensor to target. This is in contrast to Real Aperture Radar (RAR) where resolution is dependent on the physical length of the antenna.

SAR satellites such as ERS-1 and ERS-2 are active microwave sensors, transmitting their own source of energy for imaging. When energy transmission is isotropic, that is, equal in all directions, the radar equation for power density at range R is as follows (Henderson and Lewis, 1998):

$$P_R = \frac{P_T}{4\pi R_T^2} \quad (3.1)$$

where P_R is the power returned to the antenna from the ground surface, P_T is the transmitted power and R_T is the range to the target from the antenna.

However, SAR satellites focus their transmitted energy in the direction of the earth's surface, in a cone of solid angle Ω . Their focussing ability is known as gain, which was defined by Sullivan (2000, p.41) as "the ratio of the average power per steradian at the peak of the pattern to the average power per steradian of an isotropic antenna that emits the same overall power." The radar equation for backscatter when the transmitted energy is focussed in a certain direction is as given as follows by Campbell (2002), among others:

$$P_R = \frac{\sigma G^2 P_T \lambda^2}{(4\pi)^3 R^4} \quad (3.2)$$

where λ is the wavelength, G the antenna gain, and σ the radar cross-section. The radar cross-section is a function of the radar waves' interaction with the ground as they are absorbed (α) or isotropically reflected ($1-\alpha$) by the surface, with some gain in the direction of the sensor (g_s), and depends only on the characteristics of the target (A_s) and not those of the sensor (Henderson and Lewis, 1998; Sullivan, 2000).

$$\sigma = A_s (1 - \alpha) g_s \quad (3.3)$$

In remote sensing, the target of the radar is a distributed target, rather than a point. This means that the radar cross-section becomes radar scattering *per unit area* (σ^0). The total radar cross-section for a resolution cell of a radar satellite image is therefore scattering per unit area multiplied by the area of the cell (A), or $\sigma^0 A$, and the radar equation therefore becomes (Henderson and Lewis, 1998):

$$P_R = P_T (\sigma^0 A) \left(\frac{G^2 \lambda^2}{((4\pi)^3 R^4)} \right) \quad (3.4)$$

3.3 The European Remote-Sensing Satellites

The ERS satellites, operated by the European Space Agency (ESA), follow a sun-synchronous, near-polar orbit at an altitude of 785 km and an inclination of 98.516° , with each orbit lasting approximately 100 minutes and crossing the equator at approximately 10:30am local time. Each orbit of the ERS satellites is made up of 7200 equidistant nodes approximately 5 km apart, with 18 nodes between adjacent scenes. ERS-1 and ERS-2 have rectangular antennae measuring approximately ten metres by one metre and aligned with the flightpath, and the polarisation of both the transmitting and receiving antennae is vertical, or VV polarisation, which refers to the electrical component of the electromagnetic field. The incidence angle is 23° at the midrange, 19.35° at the near range, and 26.50° at the far range (Alaska SAR Facility, 1996), which Zebker *et al.* (1994b) point out is far from optimal because of causing significant layover for common terrain slopes (section 3.4.4) and Bamler and Hartl (1998) recommend an incidence angle of 45° in order to avoid this.

The radar footprint in the case of ERS-1 and ERS-2 is 80 by 4.8 km, as the size of the footprint is proportional to the wavelength and inversely proportional to the size of the antenna (Herzfeld, 2004). Images are acquired on both ascending and descending passes of the satellite, ascending being when the satellite is moving from south to north, and *vice versa*. The large volumes of data acquired by the ERS satellites means that data cannot be stored on board, and images must therefore be acquired within range of a ground station (Campbell, 2002). This limitation also means that not all possible scenes are acquired by the satellites, the effects of which are discussed further in section 4.2.

The ERS satellites are stripmap radars, which means that they image a strip parallel to the flightpath of the radar (Sullivan, 2000). SAR satellites are, by necessity, side-looking, in order to avoid ambiguity between targets at the same distance from the sensor but on opposite sides, and transmission is normal to the flight path rather than looking forward or backward. The ERS satellites look to the right of the nadir.

3.3.1 ERS SAR System

In the case of the ERS satellites, microwaves in the C-band of the electromagnetic spectrum are transmitted with a frequency of 5.3 GHz, or a wavelength of 5.66 cm (figure 3.1). The radar waves are transmitted in pulses, short periods of transmission known as chirps, with intervening, longer, periods of no transmission (Sullivan, 2000). ERS-1 and ERS-2 emit approximately 1700 pulses per second at regular intervals, the Pulse Repetition Frequency (PRF). As the ground track velocity of the satellites is 15,000 miles per hour (mph), which equates to 6.628 km s^{-1} , each pulse is between four and ten metres apart, and each point in view of the radar is pulsed approximately 1000 times (Alaska SAR Facility, 1996; European Space Agency, 2006a). The chirp duration for the ERS satellites is 37.1 microseconds, and the base frequency is 5.3 GHz (the speed of light, c , divided by the wavelength, 5.66 cm).

As a rule, radars must wait for the signal from one pulse to be returned before emitting the next pulse, in order to avoid the phase ambiguity that would occur if the radar was not able to tell which pulse of transmitted energy the received signal originated from. However, because of the complex nature of the chirp emitted by the ERS satellites (Sullivan, 2000), this rule does not apply, and pulses may therefore be transmitted closer together in time, thus improving the range resolution of the resulting images. However, the satellite must not move more than half the antenna length between pulses (Massonnet and Feigl, 1998).

SAR systems save the complete reflection history of the imaged scene, and use the Doppler shift, the change in frequency caused by relative motion between sensor and target, to allow the signal to be reconstructed as if the radar antenna were long, rather than shorter but moving (Franceschetti and Lanari, 1999) and to assign each of the patches of ground imaged to their correct position. Targets ahead of the sensor have a shift towards higher frequencies, while targets behind it have a shift to lower frequencies (Campbell, 2002), and the frequency of the received signal is compared to the known frequency of the transmitted signal. In the case of the ERS satellites, the satellite travels 4 km while each point on the ground is in view, which simulates the presence of a stationary antenna of

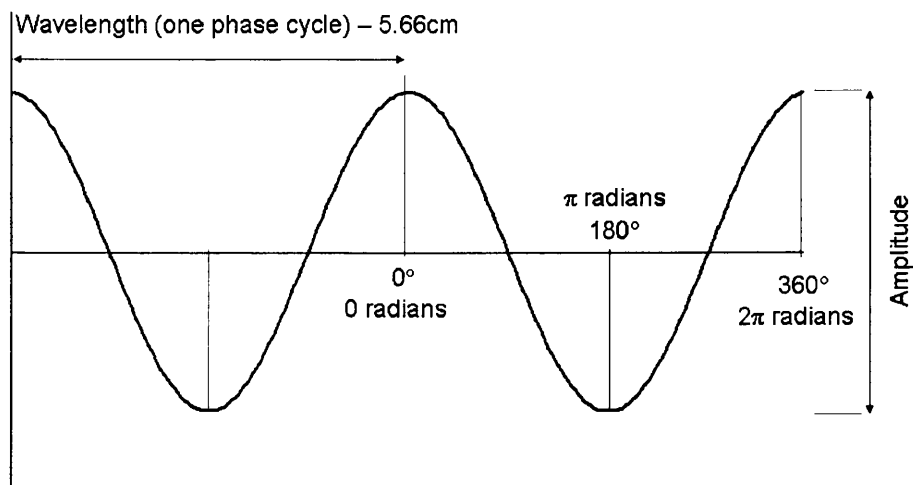


Figure 3.1: Amplitude, wavelength and phase.

that length. This, and the short wavelength, gives SAR fine spatial resolution in the azimuth direction. Resolution in the azimuth, along-track, direction is approximately five times that of the range, across-track, direction, although the two are independent. Resolution is discussed further in section 3.4.6.

SAR satellites measure three components of the returned signal: the intensity of the returned backscatter signal; the time taken for the signal to return, which gives the slant range distance to the target; and the phase of the returned wave (figure 3.1).

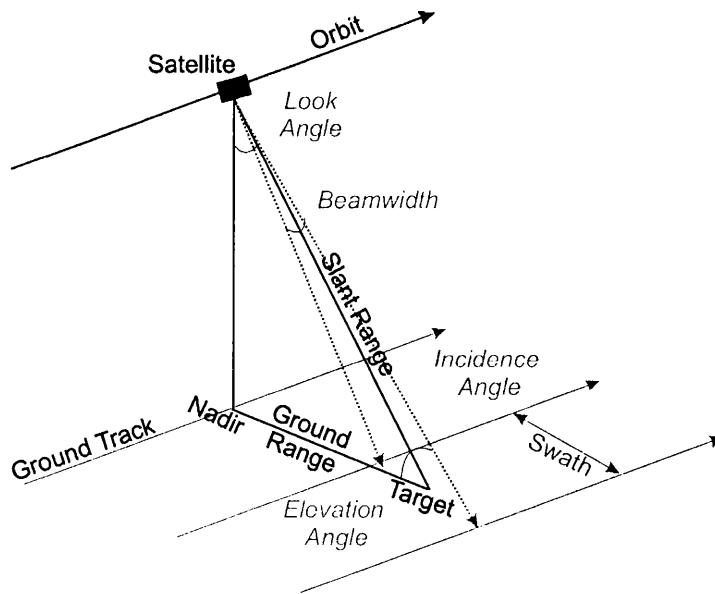


Figure 3.2: Imaging radar geometry.

3.4 Imaging

3.4.1 Backscatter

Backscatter is the proportion of the power of the transmitted wave which is returned directly to the sensor from the imaged surface. An important factor in determining the backscatter is the roughness of the surface. Surface scattering occurs when the transmitted pulse of energy interacts with the rough surface of the target (Herzfeld, 2004). It is surface scattering which dominates the signal from glacier ice, as it is dependent on the size of the roughness elements on the surface of the ice compared to the wavelength (Henderson and Lewis, 1998).

The local incidence angle θ , which approximates to the look angle (ω) for a flat surface but varies locally due to the topography of the scene being imaged, is also important in determining backscatter. The dielectric properties of the material also affect backscatter, but to a lesser extent than the other factors.

High backscatter in glacial environments is therefore produced by rough surfaces with a low content of liquid water, such as high density ice, firn with ice lenses, or exposed mountain ridges. Most imaging radars are calibrated so that brightness values from the images they produce can be related directly to backscatter values on the ground.

In some cases, backscatter may also show the properties of the near surface because of volume scattering, which occurs when the transmitted pulse partially penetrates the surface of the target before being reflected (Herzfeld, 2004).

3.4.2 Range

The slant range (R) is the distance from the sensor to the surface in the look direction of the radar, and the ground range is the distance from that same point on the surface to the point directly beneath the satellite, the nadir (figure 3.2). R is calculated by multiplying the speed of light (c) by the time taken for the transmitted signal to return (t), and dividing the product by two in order to account for two way travel time (Herzfeld, 2004).

$$R = \frac{ct}{2} \tag{3.5}$$

Some corrections for factors such as atmospheric effects must be applied to this simple equation in order to accurately calculate the range. However, interaction with the atmosphere will have less of an effect for Antarctica than elsewhere, as transmission through the atmosphere is less attenuated in the polar regions because the moisture content of the atmosphere is lower and the atmosphere itself thinner (Herzfeld, 2004).

3.4.3 Phase

The transmitted radar waveform originates from a stable local oscillator, a source which maintains the same frequency of transmission for each pulse, and as such the transmitted waveform is said to be coherent. This transmitted wave is the reference wave to which the phase of the returned signal can be compared. For a stable oscillator the reference wave is a cosine, and the returned wave is also compared to quadrature functions which are shifted by 90° from the reference wave, which means that by definition these are sine functions. SAR preserves the phase of the transmitted wave between pulses, which Real Aperture Radar (RAR) and Side Looking Airborne Radar (SLAR) do not.

For a coherent radar system, the ideal delay in phase $\Delta\phi$ between the transmitted and received waves is as follows (Sullivan, 2000):

$$\Delta\phi = -2\pi \cdot \frac{2R}{\lambda} = -\frac{4\pi R}{\lambda} \quad (3.6)$$

If, for example, two waves being compared, such as a transmitted wave and a received wave, were exactly the same, the phase difference would be 0 radians or 0 degrees, and they are said to be “in phase”. However, if the two waves are exactly in opposition, with the peak of one corresponding to the trough of the other, the phase difference would be π radians or 180 degrees, and the two are “out of phase” (figure 3.3). A phase shift of anything from 0 to 2π radians, or 0 to 360 degrees, may occur. Corresponding pixels from two satellite images collected from exactly the same location without any vertical or horizontal displacement occurring between the acquisition of the images would have equal phase. It is the phase of the returned signal which is important in the main method of this project, interferometry, as “If the phase difference can be attributed to a single cause, or a combination of well controlled causes, results on the dynamics of a glacier may be derived” (Herzfeld, 2004, p.18).

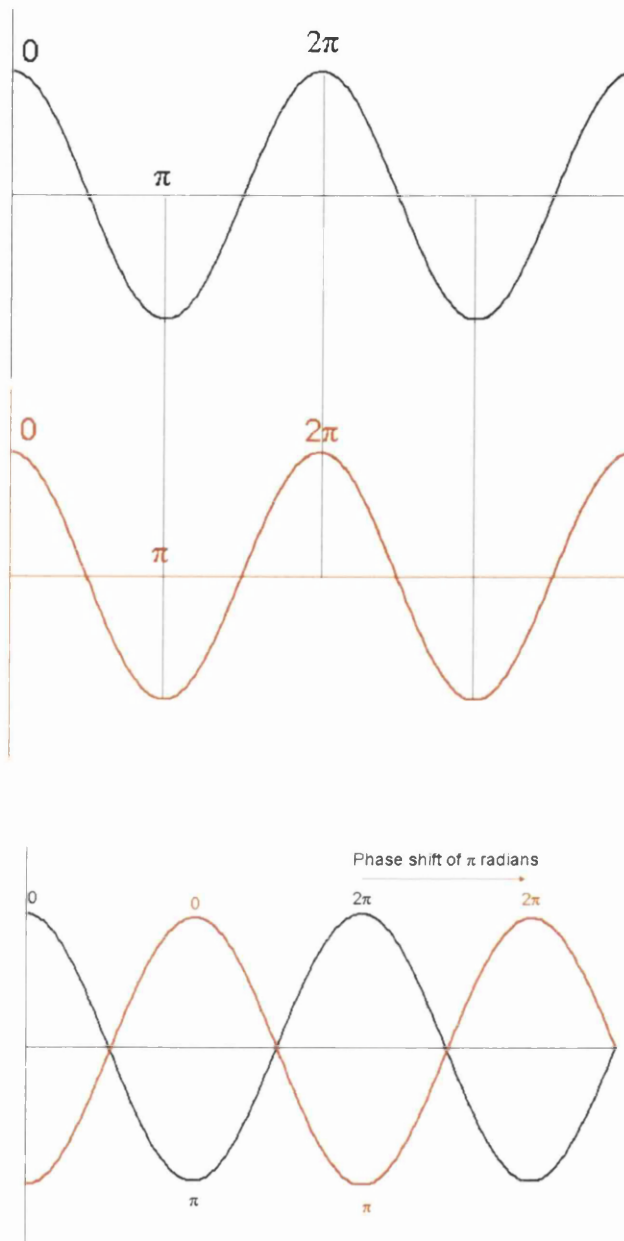


Figure 3.3: Correspondence between phase cycles. The top diagram shows two waves varying in phase, and the bottom diagram shows two waves out of phase, with a phase shift of 180 degrees, or π radians.

3.4.4 Limitations of SAR

SAR images may suffer a number of limitations, the three most widely documented of which are a result of the geometry between the imaging radar and the surface, and occur when slant range is converted to ground range for the purposes of constructing an image. Radar shadow is a limitation whereby certain areas of the scene which lie on the far side to the sensor of tall features such as mountains are not imaged, and occurs when terrain facing away from the radar has slope angles which exceed the incidence angle. Radar layover occurs when terrain facing towards the radar has slope angles exceeding the look angle, as two points which look to have the same range and relative velocity to the sensor will be placed at the same location in the SAR image (Sullivan, 2000). This distortion occurs for objects such as mountains with a high altitude, as the slant range distance to the top of the feature is less than that to the base of the feature, making the top of the feature appear closer to the sensor in the ground range. For similar reasons, slopes facing the radar appear steeper and shorter than those facing away, known as foreshortening. It is important to consider all these limitations when working with SAR images.

However, SAR satellites overcome some common limitations of other remote sensing platforms. Their nature as active sensors allows them to image independently of solar illumination which is especially important in a polar study area which is in darkness for several months at a time, and their wavelength allows them to penetrate clouds. Although it is widely known that wet weather conditions may affect the microwaves used in remote sensing on the way both to and from the surface, giving ambiguous phase changes, this applies mainly to wavelengths of less than 4 cm (Henderson and Lewis, 1998). Wet atmospheres are rare for Antarctica, which has low precipitation over its interior, and as such this is not an issue for the data used in this study.

3.4.5 SAR Images

The signal received by a SAR satellite is a sinusoidal wave with both phase and amplitude, which is digitised at the sensor and stored as a complex number, which is an efficient method of handling data with phase and amplitude components. This is represented as a two dimensional array of pixels which each have an amplitude V and phase ϕ to form a complex image. Power, which is the square of the amplitude, is proportional to the square of the magnitude of the voltage in both the signal and image domains, and as such the power image $V^2(x, y)$ can be displayed, in addition to the usual display of magnitude i.e. $V(x, y)$ (Henderson and Lewis, 1998; Sullivan, 2000). ERS SAR images are 100 by 100 km.

3.4.6 Resolution

Range resolution is given as follows (Gamma Remote Sensing, 2002):

$$\delta_r = \frac{c}{2B} \quad (3.7)$$

where c is the speed of light, and B the pulse bandwidth. The ERS satellites have a nominal chirp bandwidth of 15.55 MHz and as such the slant range resolution is 9.6 m (Gamma Remote Sensing, 2002).

The cross-range resolution (also known as azimuth resolution) of a SAR is given as follows by Sullivan (2000):

$$\delta_{cr} = \frac{\lambda}{2\Delta\mu} \quad (3.8)$$

where λ is the wavelength and $\Delta\mu$ the aperture angle of the SAR, which is equivalent to the two-way real aperture beamwidth of 3 dB for stripmap SAR (Gamma Remote Sensing, 2002; Sullivan, 2000).

However, as the physical beamwidth is approximately equal to the wavelength (λ) divided by the azimuthal length of the antenna (L), the nominal azimuth resolution, becomes (Gamma Remote Sensing, 2002; Sullivan, 2000):

$$\delta_{cr} \cong \frac{\lambda}{2\Delta\mu} \cong \frac{\lambda}{2(\frac{\lambda}{L})} \cong \frac{L}{2} \cong \delta_{az} \quad (3.9)$$

Through Doppler focussing, the azimuth resolution is therefore dependent on the angular beam width. Resolution improves as antenna length decreases, as the duration of the Doppler history is determined by beam width, which is in turn determined by antenna length, but it is also inversely proportional to Doppler frequency resolution (Gamma Remote Sensing, 2002).

Images may also have differing radiometric resolutions. Because each object (resolution cell) is pulsed 1000 times while in view of the satellite, an average of all the responses is taken to work out the object's radar cross-section (σ). When these averages are arranged into rows by Doppler shift and columns by range (section 3.5.5), this produces a Single Look Complex Image (SLCI). SLCI images are stored as float complex or short complex, pairs of floating points and integers respectively, with the latter being the case for the scenes used in this study. SLCIs produced from ERS images have a spatial ground range resolution of approximately 20 m in the range direction and 4 m in the azimuth direction.

3.5 The Interferometric Method

Satellite Radar Interferometry/Synthetic Aperture Radar Interferometry (SRI, known also as InSAR) is a technique which uses the phase of the returned backscatter signal of two or more images as a means of calculating relative and, with further processing, absolute values of elevation and/or displacement between coherent SAR images. Interferometry is comparable to stereoscopic photography, utilising radar geometry (Campbell, 2002).

Two Single Look Complex Images are coregistered (section 3.5.6) and the phase difference between them calculated (section 3.5.7), before the effects of the sensor position are removed to produce a flattened single difference interferogram (section 3.5.8). This shows contours of equal phase difference, scaled from 0 to 2π , known as fringes (section 3.5.7) which are the result of topography and displacement in the line-of-sight (LOS) direction of the satellite. Phase may be unwrapped (section 3.6), which adds the correct integer number of phase cycles to the fractional cycles represented by the fringes. Interferograms may then be differenced (section 3.8) to remove the effects of topography and leave only those of LOS displacement. This may be done through either simulating the topographic component of the phase from a Digital Elevation Model (DEM) (section 3.8.1) or creating a double difference interferogram representing only topographic phase (section 3.8.3), which is then unwrapped and Ground Control Points (GCPs) of known elevation are used to refine the baseline in order to simulate a height map (section 3.8.4). The simulated topographic phase from either the DEM or the height map is removed from the single difference interferogram, thus leaving only the displacement phase (section 3.8.6). Displacement maps may be produced based on the assumptions that all displacement is in the direction of the look vector, all displacement is vertical, or all displacement is in the horizontal plane on the ground corresponding to the look vector (section 3.8.8). Look vector displacement may finally be projected to ice flow direction through the use of a DEM (section 3.8.9).

3.5.1 The Gamma Software

Interferometry was carried out using the tools from Gamma Remote Sensing. The Gamma software is a series of five sets of C programs designed to achieve accurate SAR processing on a desktop computer (Gamma Remote Sensing, 2002). Gamma consists of a Modular SAR Processor (MSP) for converting raw SAR data into Single Look Complex (SLC) images; an Interferometric SAR Processor (ISP) for producing interferograms and height maps; Differential Interferometry and Geocoding (DIFF) software; Display software (DISP); and Land Application Tools (LAT) with functions such as filtering and classification. This software may be used with a number of airborne and spaceborne radar platforms. Gamma routines used are given throughout the text, in brackets where necessary.

3.5.2 Data Format

Some of the data used in this study arrived in raw format, rather than SLCI as requested, meaning different Gamma routines and additional stages of preprocessing had to be applied. These are discussed below. Preprocessing steps for both raw and SLCI format data are summarised in a flow chart (figure 3.4).

3.5.3 Parameter File Generation

Processing SAR data requires a parameter file for each scene, which is created from the leader file supplied with the data. In the case of ERS data the parameter generation programme for the appropriate Processing Archive Facility (PAF) must be selected - in our case, ESA/ESRIN. For data which came in SLCI format, the appropriate program was `par_ESA_ERS`, and for data which arrived raw, it was `ERS_proc_ESA`, which produce ISP and MSP parameter files respectively.

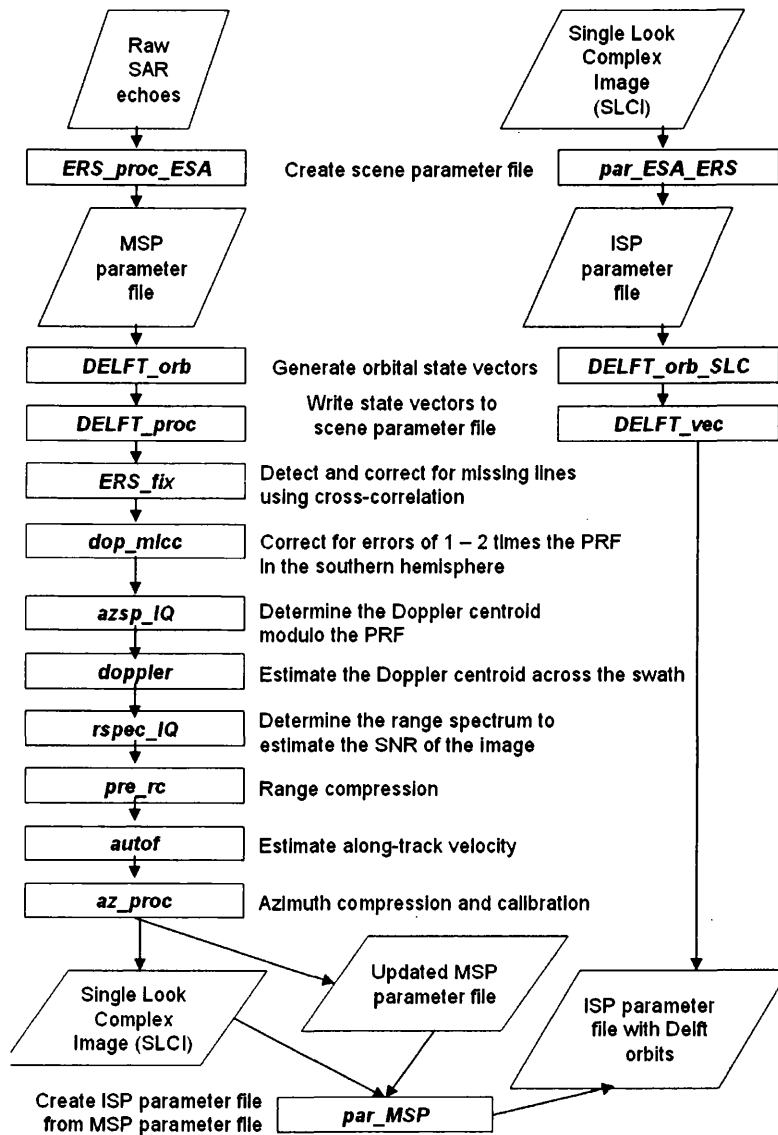


Figure 3.4: A flow chart to show the preprocessing steps required for data which arrived raw, and data which arrived in SLCI format.

3.5.4 Orbital State Vectors

Orbital state vectors giving the position and velocity of the satellite in three dimensions are provided by ESA for every image. More precise orbital positions are the Delft Orbits, which have a precision of 5-6 cm and are calculated using the DGM-E04 gravity model, Satellite Laser Ranging (SLR) and altimeter tracking data (Closa, 1998; Scharroo and Visser, 1998). These are inserted into the parameter file for each scene by the programs DELFT_orb_SLC and DELFT_vec for data which arrived as SLCI, and DELFT_orb and DELFT_proc for data which arrived raw. Five state vectors per image were used. The Delft Orbits are more recent and more accurate than the ESA Precision Orbits, and as such replace this information in the parameter file.

3.5.5 Processing Raw SAR Data

For data that arrived as SLCIs, the next stage is the calculation of offsets between paired images as discussed below in section 3.5.6, but additional stages of preprocessing given here were required for those scenes which arrived in raw format.

SAR data in their raw form are the complex values of each echo received by the radar as it moves along the flight path and must be calibrated and arranged into a two dimensional array of pixels in slant range/Doppler coordinates. Preprocessing raw SAR data makes use of two parameter files: one for the sensor, and one for the scene (Gamma Remote Sensing, 2002). The correct sensor parameter file must be identified from those that come with the Gamma software. Sensor parameters are those which remain the same for a particular satellite across all scenes and include antenna gain. The sensor parameter files for ERS-1 and ERS-2 are called, and the scene parameter files for each image updated, during most of the following stages.

Some scenes have missing data lines which may be corrected for if the problem is not too extensive. This is important as coherence may be completely lost if

even one line of data is missing from the raw file, and missing lines may not be apparent when examining the SLCI or Multilook Image (MLI) (Gamma Remote Sensing, 2002). The program `ERS_fix` is used to ascertain if lines are missing from the scene by looking at the satellite's binary line counter and cross-correlating consecutive lines, and then to correct the problem by duplicating the current line to fill in the gap, although the image signal-to-noise ratio (SNR) decreases as the number of missing lines increases. `ERS_fix` also detects and compensates for changes in the range gate, the slant range distance to the first line of the scene, which changes every thirty seconds along the flight track, and may be used to concatenate scenes of consecutive frames from the same satellite track together, if necessary.

Doppler History

Following this, the Doppler history of the image is reconstructed. The Doppler shift is exactly proportional to the relative velocity between the target and the radar and is given as follows by Sullivan (2000):

$$f_{doppler} = -\frac{2v_{rel}f}{c} = -\frac{2v_{rel}}{\lambda} \quad (3.10)$$

where v_{rel} is the relative velocity between the target and the radar (positive being increasing distance between sensor and target).

Zero Doppler shift is theoretically a surface in a plane perpendicular to the flight path. However, ambiguities exist because of the squinting of the antenna bore-sight away from the plane perpendicular to the flightpath, and a number of methods may be used to calculate these in order to correct for them. The Doppler centroid is defined as the Doppler frequency of points at the centre of the antenna beam. Both ERS satellites use yaw steering to keep the Doppler centroid within half of the PRF, and so their estimates of the Doppler centroid are unambiguous as the Nyquist criteria are satisfied. These criteria state that as long as the

bandwidth is less than the PRF, the original signal can be recovered if the correct multiple of the sampling frequency is known (Gamma Remote Sensing, 2002).

In the southern hemisphere, the ERS pointing algorithm makes errors where the actual Doppler centroid is 1 or 2 times the PRF away from the baseband (Gamma Remote Sensing, 2002), so an additional stage is required to estimate the Doppler ambiguity which is not required for scenes of the northern hemisphere. Two algorithms are available. The Multi-Look Cross-Correlation (MLCC) algorithm gives an unambiguous estimate of the Doppler centroid by producing an estimate of the Doppler centroid for different bands of the range chirp bandwidth with the phase of the correlation coefficient between echoes being directly proportional to the Doppler centroid. It was used in this study (`dop_mlcc`) as the Multi-Look Beat Frequency (MLBF) algorithm is more suitable for point targets in urban and suburban areas, although both algorithms work better when the scene is relatively featureless (Gamma Remote Sensing, 2002).

The fractional part of the Doppler centroid may be estimated from one of two methods: line to line complex correlation, or by finding the centroid of the azimuth power spectrum (`azsp_IQ`), the latter working well for ERS data which have a relatively constant centroid across their swath (Gamma Remote Sensing, 2002). However, although ERS data do not generally need their Doppler centroid to be estimated across the swath, Gamma Remote Sensing (2002) recommend this approach for data from the southern hemisphere because of the error in the pointing algorithm mentioned above, so the program `doppler` was used.

The estimated SNR of a scene is used in calibrating the SAR image with radiometric compensation for antenna gain, which applies only to the signal and not the noise. For complex data, this is done using the program `rspec_IQ`.

Range compression then applies a matched filter to the raw SAR data which compresses the energy from a given chirp into as narrow a time window as possible. The routine `pre_rc` estimates the raw data histogram, mean and standard deviation of each channel and the correlation between the real, in-phase component (I) and the imaginary, quadrature component (Q), and uses these to normalise

the output for the length of the transmitted chirp signal.

A properly focussed image may only be obtained after precise knowledge of the range and velocity of the radar platform is used to correct for deviations from the smooth curve parallel to the sphere approximating the Earth's surface, as otherwise blurred images are produced (Gamma Remote Sensing, 2002). The program `autof`, short for auto focus, cross-correlates images processed from different parts of the range and azimuth Doppler spectrum to improve the estimate of the radar's along-track velocity, as at a given Doppler centroid the azimuth shift as a function of time is related to velocity. The image offset caused because of the different velocities of subimages with different squint angles is used to refine the velocity over at least two iterations, but if the program cannot find correlation between the images produced it will revert to using the predicted velocity. Featureless ice sheets are often highlighted as problematic at this stage.

Finally, azimuth compression (`az_proc`) produces an SLCI from the range compressed data, using the sensor and scene parameter files and a range-Doppler algorithm. Compression is based on along-track velocity and slant range distance. Radiometric calibration is also included at this stage. Relative calibration ensures the noise power is uniform as a function of range. An absolute calibration factor of 49.7 dB was used for ERS-1, and 57.2 dB for ERS-2 for output in short complex format. Had the output been float complex, the calibration factors would have been -10.3 dB and -2.8 dB respectively (Gamma Remote Sensing, 2002). This is the stage where the SLCI is produced, the intensity of which is proportional to backscatter (Gamma Remote Sensing, 2002).

The MSP parameter file which was updated regularly throughout the preprocessing must finally be used to create an ISP parameter file for the next stages (`par_MSP`). The data that arrived in raw format and the data that arrived as SLCIs may be treated the same from this point in the processing chain forwards.

3.5.6 Offsets

In its simplest form, using one pair of images, interferometry works by subtracting the phase value of one image from that of another for exactly the same point on the ground. This means that the two SLCIs must firstly be coregistered to one another, and so the offset between them must be established. One image is assigned as the master image, and the other as the slave, and where necessary several slaves may be coregistered to one master. Coregistration is achieved by finding the point on the slave image which corresponds exactly to a given point on the master image (Franceschetti and Lanari, 1999). Accurate coregistration is paramount, as inaccuracies here affect the quality of all the outputs further down the processing chain (Zou *et al.*, 2007).

An offset parameter file is created for the pair (`create_offset`) before initial offsets are calculated from the orbit data contained in the scene parameter files (`init_offset_orbit`), which usually finds the offsets to within about five pixels (Gamma Remote Sensing, 2002). These offsets are then refined using a two dimensional cross-correlation analysis (`init_offset`). The offsets for a selected patch of the scene are calculated using Fast Fourier Transforms (FFTs) through an iterative process, in this case for 4 by 20 pixel multilooking (taking into account that the azimuth resolution is approximately five times finer than that of the range), then 2 by 10, and finally 1 by 1, after which an SNR greater than six indicates coregistration to within one tenth of a pixel (Gamma Remote Sensing, 2002). The centre of the window for calculating the initial offsets was always placed on slow-moving ice in the scene such as the Fletcher Promontory, Fowler Peninsula or Cape Zumberge (figure 1.1). The cross-correlation coefficient for two complex SAR images z_1 and z_2 is given as follows (Zou *et al.*, 2006):

$$\gamma = \frac{|E(z_1 z_2^*)|^2}{\sqrt{E(|z_1|^2)E(|z_2|^2)}} \quad (3.11)$$

There are several possible variations on the methods for calculating offsets. Once the solution is known to the nearest pixel from the previous stage, there are two methods of calculating the offsets for coregistration. Local correlation functions are calculated for small image patches and used to estimate the coefficients of the polynomials describing the warp between the two images in the range and azimuth directions. This is done on a patch by patch basis, by setting the size of the search window in the range and azimuth directions; the number of samples (windows) to be taken in the range and azimuth directions; and the threshold acceptable signal-to-noise ratio (SNR). Offsets maximising local correlation can be calculated by either cross-correlation of intensities (CCI) using the real valued data with the program `offset_pwr`, or by optimising the fringe visibility (FV) using the complex valued data with the program `offset_SLC`, which creates a small interferogram for each patch, takes a Fourier transform, and extracts the peak of the fringe spectrum. While FV is more accurate, CCI can calculate offsets for more patches of the image and may produce a better fit overall. For the CCI method, window sizes should be nominally square on the ground. CCI also has the advantage that images without interferometric coherence may be coregistered (Gamma Remote Sensing, 2002). The conjugate point on the slave image to the window on the master image is regarded as the centre of the window with the best match (Zou *et al.*, 2006, 2007).

The program `offset_fit` uses a least squares fit from the offsets of the patches to model the scene offset as bilinear polynomials describing the warp between the two images in the range and azimuth directions. A fourth order polynomial, the highest the software allows, is the norm (i.e. a second order polynomial in two dimensions), but for noisy data a third-order polynomial may be more appropriate (Gamma Remote Sensing, 2002). The polynomial is fitted through an iterative process to remove outliers and cull offsets which do not have a high enough SNR. SNR may be low for several reasons, such as too much change in the scene, too large a baseline, or a poor initial estimate of the offsets (Gamma Remote Sensing, 2002). An SNR threshold of 7 is appropriate for the CCI method, and 3 for FV (Gamma Remote Sensing, 2002). After this stage the standard deviations of fit in the range and azimuth directions should be checked to make sure they are less

than 0.5. The slave image must then be resampled to the geometry of the master, and coregistration is usually accurate to less than one tenth of a pixel.

Choosing appropriate window sizes and range and azimuth spacings is important. Zou *et al.* (2007) state that window sizes have usually been chosen by trial and error. While larger windows produce less noisy results, too large windows are computationally expensive, but too small windows may produce poor estimates of the parameters of the polynomial (Zou *et al.*, 2007). Zou *et al.* (2006) and Zou *et al.* (2007) investigated the optimum spacing for cross-correlation windows and optimum window size, and although they suggest 65 pixel by 65 pixel windows spaced approximately every 30 range and 200 azimuth pixels, their findings were scene-dependent and based on scenes of hilly terrain in Hong Kong. Gamma Remote Sensing (2002) suggest window sizes of 64 by 64 and spacings of 32 by 32 for `offset_pwr`, and 16 by 16 for both window size and spacing for `offset_SLC`. However, these recommendations are not specific to glaciated scenes. Patches of 256 by 1024 pixels and 128 by 256 pixels were used by Pritchard *et al.* (2003) and Luckman *et al.* (2003) respectively, while Bevan (2006) used a 64 by 64 pixel window spaced every 8 range and 40 azimuth pixels.

Areas which are known to be static, such as the Ellsworth Mountains, or almost static, such as the Fletcher Promontory, Fowler Peninsula, or Cape Zumberge, may be masked out (using the Gamma routine `polyras`) and used to create an offset polynomial without the effects of moving features using `slc_track`, a program created by Adrian Luckman, instead of `offset_pwr` or `offset_SLC`. However, this method is more vulnerable to the low SNR associated with a short temporal baseline and was affected by the Rutford and Evans Ice Streams largely filling their SAR frames, discussed later in section 7.3.2.

Initially in this study, both methods of calculating offsets (CCI and FV), both with and without a mask, were experimented with, with different window sizes, range and azimuth spacings, polynomial orders, and oversampling factors. In this study, offsets were calculated using method 1, intensity cross-correlation. The window size was 256 by 1024 pixels, with 80 samples in the range direction and 100 in the azimuth direction.

3.5.7 Interferograms

There are two options at this stage; coregistration and interferogram generation in separate stages, with the advantage of easy registration of several slave images to one master; or coregistration and interferogram generation in one stage, maximising efficiency and minimising disk use. This study used the latter, coregistering the images and generating interferograms in one step.

Interferometric phase is defined by the following equation (Henderson and Lewis, 1998):

$$\phi = \phi_2 - \phi_1 = \frac{2\pi}{\lambda} p(R_2 - R_1) \quad (3.12)$$

where $\phi_2 - \phi_1$ is the difference in phase for the same point on the ground, R_1 and R_2 are the ranges to the target on the first and second passes, and $p=2$ when the channels do not share the same transmitting antenna, otherwise $p=1$, the 1 and 2 indicating whether one-way or two-way propagation differences in the relative path apply.

The complex pixel values of one coregistered image (z_1) are multiplied by the complex conjugates of the other (z_2^*) and divided by the products of their respective amplitudes to produce an interferogram (equation 3.13), which is itself complex, in this case using the program `interf_SLC` (Gamma Remote Sensing, 2002).

$$\phi = \frac{(z_1 z_2^*)}{\sqrt{(z_1 z_1^*)(z_2 z_2^*)}} \quad (3.13)$$

Interferogram Phase

The phase difference between the two images making up the interferogram is caused by the change in path length to each point on the ground between images. This may be a result of elevation (as the scene topography is viewed from slightly different positions), motion of parts of the scene, or deformation. As such, at this stage, the total residual phase signal ϕ is a sum of the residual phase signals from geometry (ϕ_{geom} , equation 3.14, section 3.5.8), topography including the effects of B_{perp} (ϕ_{topo} , equation 3.15, section 3.5.8), translation because of the change in radial distance of a resolution cell between one satellite pass and the next due to ice movement, ΔR (ϕ_{trans} , equation 3.16, section 3.8.6) and phase noise (ϕ_{noise} , equation 3.17) (Fatland and Lingle, 1998). ϕ_{topo} , ϕ_{geom} and ϕ_{trans} are given below from Fatland and Lingle (1998), and ϕ_{noise} , the standard deviation of the phase, from Rodriguez and Martin (1992).

$$\phi_{geom} \approx \frac{2kB_{perp}}{R \tan \omega} \quad (3.14)$$

$$\phi_{topo} \approx \frac{2kB_{perp} \Delta e}{R \sin \omega} \quad (3.15)$$

$$\phi_{trans} \approx 2k \Delta R \quad (3.16)$$

$$\delta_{\phi} = \frac{1}{\sqrt{2N}} \frac{\sqrt{1 - \epsilon^2}}{\epsilon^2} \quad (3.17)$$

where k is the wavenumber of the radar (i.e. $2\pi/\lambda$), R the distance from the sensor to the scene centre, ω the look angle at the scene centre, Δe the elevation

of the resolution cell, ϵ the coherence (section 3.5.9) and N the number of looks to be averaged (Fatland and Lingle, 1998; Rodriguez and Martin, 1992).

Fringes

Interferometric phase represents the path difference, or phase shift, between the two images, expressed as a whole and fractional number of wavelengths. Interferograms show bands of colour known as fringes. One complete fringe cycle, which can be represented by one complete cycle of colour, represents a phase difference of one complete phase cycle from 0 to 2π radians, or 0 to 360 degrees. Fringes may be thought of as contours of equal phase difference, with each complete phase cycle representing a consistent amount of topography and/or displacement.

Phase Noise

Phase noise may be caused by receiver thermal noise, speckle noise (caused by the summation of different scatterers within each resolution cell) and noise from the effects of the antenna being in slightly different places for the acquisition of each image making up the interferogram (Goldstein *et al.*, 1988). Speckle noise may be reduced by multilooking.

Multilooking

Backscatter values may be averaged over a number of pixels to reduce phase noise for improved parameter estimation, or to improve the display and interpretability of backscatter images (Gamma Remote Sensing, 2002). Multilook Images (MLIs) are also produced at this stage (interf_SLC), one from each SLCI and both in the geometry of the master image. While SLCIs have the highest possible spatial resolution, the degree of speckle is also high. To overcome this, data are processed in subsets known as looks, which are averaged to produce the final, multilook image (MLI), stored in 4-byte float format, although radiometric resolution is

increased at the expense of spatial resolution. As the azimuth resolution is five times that of the range, multilooking is usually done at the ratio 1:5 range:azimuth looks. The MLIs used in this study were created by averaging 2 pixels in the range direction and 10 in the azimuth direction. Working with 1 by 5 multilooking was also investigated, but found to suffer from low coherence and largely increased processing time for stages such as phase unwrapping.

3.5.8 The Baseline

The baseline describes the difference in the time and position of the satellites between the acquisition of images (Franceschetti and Lanari, 1999). The baseline can be either spatial, if the two images were taken at the same time from different places, temporal, if the two images were taken from the same place at different times, or both, as is the case in this study.

The Temporal Baseline

The temporal baseline is the time elapsed between successive images of the same frame. This is an important consideration in selecting suitable scenes over a moving study area, and will be discussed in section 4.2.

The Spatial Baseline

The spatial baseline may be split into two components, perpendicular to and parallel to the satellite look direction. These are called B_{perp} and B_{para} respectively. Ideally the parallel baseline would be zero, and although this is not usually the case and must be accounted for, it is the perpendicular component of the baseline which is more critical for interferometry. Zebker *et al.* (1994a) approximate the parallel baseline to the difference in path lengths between the two scenes for spaceborne imaging geometries.

Short perpendicular baselines are good for producing interferograms showing displacement of the target surface relative to the satellite, but slightly longer baselines are needed to produce interferograms from which to derive topography. For the tandem mission of the ERS satellites (section 4.2), the orbits of ERS-1 and ERS-2 were deliberately offset in order to maintain a baseline of about 100 m so that topography could be derived (Bamler and Hartl, 1998), as when the spatial baseline is zero, there is no sensitivity to topography. However, the length of the baseline is a limiting factor in interpreting interferograms, as discussed in section 3.6.

The initial baseline is calculated by one of five possible methods (using the options 0 to 4 in the programme `base_init`): B_{para} and B_{perp} may both be calculated from orbit data; B_{para} and B_{perp} may both be calculated from registration offsets; B_{para} may be calculated from orbits while B_{perp} is calculated from the fringe rate; B_{para} may be calculated from the registration offsets while B_{perp} is calculated from the fringe rate, and; both B_{para} and B_{perp} may be calculated from the fringe rate. Because orbit data or registration offsets give better estimates of B_{para} , and the fringe rate gives a better estimate of B_{perp} (because the majority of the fringes are due to the flat earth effect caused by the distance between the sensor and different parts of the scene and the curvature of the earth), methods combining these are recommended. An accurate estimate of B_{perp} is paramount for interferometry, and fringe rate must be estimated from an area of the image the user knows to be flat, otherwise a residual phase trend may be left in an interferogram flattened using this baseline which leads to an inaccurate estimate of B_{perp} which will propagate through later stages of processing. The coordinate system for azimuth, look and pitch, in which the initial baseline and its rate of change are given, is Tangential Cross Normal (TCN). The initial baseline estimate and its rate of change are written to the baseline file for each interferometric pair.

In the first choice method used in this study the baselines were calculated using orbit data to calculate B_{para} and the fringe rate to calculate B_{perp} (method 2). Method 3 was used by Bevan (2006), but with the SAR scenes in this study, using this method led to estimates of the first component of the TCN baseline of zero, which affected the quality of flattening (discussed below) later on. The

window size of the area used for the FFT to estimate the fringe rate may be specified by the user and is a power of 2. A 128 by 128 window was used, after 2 by 10 multilooking, the same size window as used by Bevan (2006) after 4 by 20 multilooking. The default location is the scene centre but it is important to use a location on as flat a part of the image as possible, so this location was altered for each frame. Because the scenes used in this study have greatly varying topography, the option of estimating either component of the baselines with the fringe rate was considered very carefully. Using a small window (so that the window does not cover too large a range, which changes the fringe rate across the scene), placed on a flat area, was deemed accurate enough for some frames. However, for frames where the flattest areas had many fringes due to vertical displacement, the inaccuracies introduced to the baseline by using this method showed up clearly in poorly flattened interferograms further down the chain, and as such baseline method 0, calculating both components from orbit data, was chosen for these frames.

Flattening

The interferogram initially produced is a product not only of elevation and displacement, but also of the distance of different parts of the scene from the sensor, and of the curvature of the Earth over the area of the scene, and must be “flattened” to remove these effects by subtracting an approximately linear range component. This component of the phase, ϕ_{geom} , is mainly due to B_{perp} and the incidence angle θ , which varies across the scene and if the scene were completely flat, this is the component of the phase that would be left (Fatland and Lingle, 1998).

The flat earth phase trend, the geometric component of the phase, given by equation 3.14, is removed from the interferogram (ph_slope_base). However, errors in the perpendicular baseline may lead to an incorrect of flat earth phase trend being subtracted. The program base_perp is then used to show B_{para} and B_{perp} in metres for different lines and samples of the scene, as opposed to the TCN coordinates in which the baseline file is given. Following this stage,

an interferogram of a moving glaciated region with a non-zero perpendicular baseline has a phase equivalent to $\phi_{topo} + \phi_{trans} + \phi_{noise}$, the last of which may be discounted for now. An example of a flattened interferogram of the onset of the Rutford Ice Stream, and the same interferogram before flattening, is shown in figure 3.5 below.

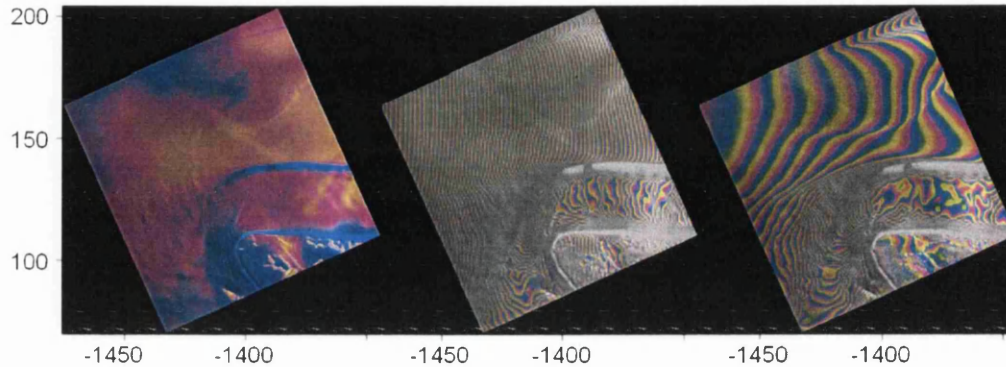


Figure 3.5: An example of a coherence image (left), a raw interferogram (centre) and a flattened interferogram (right) for frame 023_5265 of the onset region of the Rutford Ice Stream on 22nd and 25th January, 1994 (see section 4.2), with the ice flowing straight upwards from the bottom left corner of the image before turning 90° into the ice stream visible between the shear margins on the right of the image. This scene has a 3-day temporal baseline, a -11.3 m perpendicular baseline, and an altitude of ambiguity of 833 m (section 3.5.8). Coordinates are Polar Stereographic, in kilometres, with the origin at the South Pole. In the coherence image, pink represents high coherence and blue, low coherence. In the raw and flattened interferograms, one complete cycle of colour, or fringe (section 3.5.7) shows one complete phase cycle of phase difference between the two images making up the interferogram, from 0 to 2π radians. In the flattened interferogram (section 3.5.8), the component of the phase due to the differing distance between the sensor and different parts of the scene, ϕ_{geom} , has been removed, leaving only the phase difference due to scene topography, line-of-sight displacement of the surface, and the perpendicular baseline (section 3.5.7).

The Altitude of Ambiguity

Height sensitivity is given as follows, where H_s is the altitude of the sensor above the reference ellipsoid and R_1 the range from sensor to target, as the exact incidence angle (θ) depends on the altitude of the surface, e (Zebker *et al.*, 1994a; Zou *et al.*, 2006).

$$e = H_s - R_1 \cos \theta \quad (3.18)$$

One phase cycle represents the same change in elevation for each fringe, and the absolute value of this elevation change can be calculated from known parameters about the satellites and the perpendicular baseline of the interferogram. This constant elevation change is called the altitude of ambiguity, (δ_z), and is a function of radar wavelength, altitude, incidence angle, and the perpendicular baseline between the two images. As the wavelength, altitude and incidence angle of the ERS satellites are known and are constant, the altitude of ambiguity may be calculated by dividing 9416 by the perpendicular baseline (NPA Group, 2008). The numerator would change for different satellites with different wavelengths, altitudes and incidence angles.

$$\delta_z = \frac{9416}{B_{\text{perp}}} \quad (3.19)$$

3.5.9 Coherence

In order for successful interferometry to be carried out, the coherence, or correlation, between the two images must be high. Coherence is measured on a scale from 0, which means there is no correlation between the images, to 1, in which case a perfect interferogram would be produced. In this latter, theoretical, case, any differences between the phase of the two images can be accounted for by a change in elevation or by surface displacement, rather than phase noise, as the backscatter response of the scenes is constant. Image coregistration must be accurate to less than 0.2 pixels to avoid reducing coherence by more than 5%

Coherence is calculated from the two multilook images and the complex interferogram, by dividing the magnitude of the pixels in the interferogram by the product of the magnitudes of the pixels in the two images used to make the interferogram (Touzi *et al.*, 1999):

$$\epsilon = \frac{\sum_{i=1}^L z_{1i} z_{2i}^*}{\sqrt{\sum_{i=1}^L |z_{1i}|^2} \sqrt{\sum_{i=1}^L |z_{2i}|^2}} \quad (3.20)$$

where i is the sample number given L measurements and the magnitude of the coherence estimate is $|\epsilon|$. As with the offset, coherence is calculated for a window of pixels at a time, the default size of which for the Gamma tools is 5 by 5 pixels (`cc_wave`). The magnitude of the complex normalised interferogram corresponds to the interferometric correlation (Gamma Remote Sensing, 2002). A coherence image showing the degree of correlation between corresponding pixels in the two images may also be produced. An example of a coherence image is shown in figure 3.5.

Coherence between images may be lost for a number of reasons, such as long temporal and spatial baselines. Coherence is decreased by cryospheric factors causing

ice to undergo changes in reflection and scattering. Factors such as steep topography and surface displacement, which may be the intended subjects of study for interferometry, can cause loss of coherence when present in extreme amounts. When ice movement is especially complex, coherence between images will be lost entirely, completely excluding the possibility of interferometry (Herzfeld, 2004). Interferometry therefore requires a short temporal baseline in order for coherence between the two images to be maintained by avoiding temporal decorrelation due to changes in all of the above factors between the acquisition of the images. As Zebker *et al.* (1994b) state, although coherence decreases as the temporal baseline increases, the rate of this is not constant.

Although coherence images are mainly generated for visual inspection and confirmation of correlation, other applications are being developed, such as by Ichoku *et al.* (1998), who used Principal Components Analysis (PCA) on coherence images and found that the first channel produced an image with enough clarity for lithological mapping of their study area.

Filtering

Adaptive filtering was performed prior to phase unwrapping for both single and double difference interferograms, using the program *adf*. Filtering is used to overcome the limitations imposed by speckle noise which mean that backscatter values are poorly correlated to the physical properties of the imaged scene. Filtering to reduce noise improves both accuracy and phase unwrapping.

Adaptive filtering based on the power spectrum of the data may be used. Typical exponents are between 0.2 and 0.5 (0.5 being the default, which was used in this study). However, too strong filtering may eliminate some of the fringes so care must be taken, particularly when the phase is known to vary over the area used for filtering. The effectiveness of the filtering is assessed by looking at the phase standard deviation before and after filtering (Goldstein and Werner, 1998). However, filtering also reduces the spatial resolution of the height map produced (Gens and Van Genderen, 1996).

3.6 Phase Unwrapping

A single phase cycle of a SAR wave provides no information due to the relationship between the wavelength and the pixel spacing. As mentioned previously, phase is stored in the range from 0 to 2π radians, one complete phase cycle, with each complete cycle representing a relative change in topography or displacement, but the actual amount of phase change is made up of whole plus fractional phase cycles. In order to convert the fractional phase cycles represented by the interferogram fringes to relative, and, with further processing, absolute values of topography or displacement, the correct integer number of phase cycles must be added to the fractional cycles represented by the fringes. The true unwrapped phase of an interferogram may actually vary by hundreds of phase cycles (Massonnet and Feigl, 1998). This process is known as phase unwrapping.

Phase unwrapping assumes phase will not change by more than half a phase cycle from one pixel to the next, otherwise different solutions for unwrapped phase would occur depending on the integration path chosen (Goldstein *et al.*, 1988). There are two possible reasons for phase differences of greater than $\pm\pi$ between adjacent pixels. Topography-induced errors may occur due to either real discontinuities, such as cliff lines, or limitations such as layover and radar shadow, which may cause fringes to merge or end. Secondly, inconsistencies due to residues (local unwrapping errors, discussed below) from high phase noise, may hinder phase unwrapping, which becomes more likely with decreasing coherence (Bamler and Hartl, 1998). The latter may be partially overcome by filtering (section 3.5.9 and multi-looking (section 3.5.7), which Goldstein *et al.* (1988) found decreased the density of residues dramatically. Goldstein and Werner (1998), for example, found that 92% of an interferogram of Jakobshavn Isbræ, Greenland, could be unwrapped after filtering compared to 64% beforehand.

Phase unwrapping works best on areas which have relatively flat terrain and at least moderate coherence, and the steep incidence angle of the radar and low coherence in mountainous regions is known to cause problems in phase unwrapping (Gamma Remote Sensing, 2002). The spatial baseline between the images used

in repeat-pass interferometry must be less than 1100 metres, the critical baseline (Bamler and Hartl, 1998), in order for phase unwrapping to be possible, and if the baseline is relatively long within this limit, and therefore the fringe rate high, it is much more difficult to unwrap the phase reliably in terrain which is not flat (Zebker *et al.*, 1994a). Phase bulls-eyes due to vertical displacement of the surface, and ice stream shear margins are also likely locations for phase unwrapping errors (Joughin *et al.*, 1998).

Phase unwrapping is a two-step process. The phase gradient and a measure of its reliability must first be estimated, before this estimate is integrated, either in 1D, or in 2D using optional weighting according to the estimated reliability of the phase gradient (Bamler and Hartl, 1998).

3.6.1 Branch-cut Region Growing

The idea with branch-cut phase unwrapping is to allow only paths of integration leading to self-consistent solutions (Rosen *et al.*, 2000). Branch-cut region growing is applied to a filtered interferogram, and excludes areas of low coherence and residues, which are local unwrapping errors. `corr_flag` is used to mask out areas of low coherence prior to phase unwrapping. The flag file generated at this stage has other information added to it later. For single and double difference interferograms, initially the correlation threshold was set to 0.4. However, for some frames, a correlation threshold of only 0.25 had to be used, as higher thresholds masked out too much of the scene.

Neutrons are areas of high intensity and may be used to guide the unwrapping process, added to the flag file using the program `neutron`. They are treated as residues with no charge and are usually used to mask out areas of layover. The use of neutrons was experimented with in this study. However, this seemed to greatly increase processing time for negligible effect, so was rejected.

Residues

Residues may be defined as the end points of lines along which the phase gradient is more than $\pm\pi$ per pixel, i.e. branch cuts (Bamler and Hartl, 1998), and may propagate to form global errors in phase (Goldstein *et al.*, 1988). Branch cuts have a positive residue at one end and a negative residue at the other, although branch cuts due to decorrelation rather than terrain may only be one pixel long (Bamler and Hartl, 1998).

Residues are calculated by taking the sum of phase differences clockwise around four adjacent pixels. The result may be either zero, plus one cycle (a positive residue) or minus one cycle (a negative residue) (Goldstein *et al.*, 1988). If a path of integration encloses equal numbers of positive and negative residues, no phase inconsistency occurs. Placing branch cuts becomes more difficult as the density of residues increases (Bamler and Hartl, 1998). Areas of layover are characterised by a line of similarly charged residues on one side of the layover and opposite charged residues on the other side. Branch cuts are inserted to ensure paths of integration do not enclose net residues, but as phase discontinuities of more than half a phase cycle are introduced, minimising path length and therefore discontinuity is required.

`residue_cc` identifies these residues and writes them to the flag file, following which `tree_cc` is used to discharge residues through networks known as neutral trees. These trees cannot be crossed during unwrapping, which is done using the program `grasses`. Phase unwrapping starts by default at the image centre, but a user defined location may also be specified as it is important that phase unwrapping starts on a stable area (for example, Bevan (2006) used the centre of the ice cap Austfonna). In this study it was not always possible to place the starting point on bare rock (for example there is no bare rock in frames of the Evans Ice Stream), so areas of slow moving ice sometimes had to be used although these areas are not entirely stationary.

3.7 Geocoding

The inputs and outputs of the interferometry process are in a planar coordinate system of samples (in the x direction) and lines (in the y direction), usually representing slant range and azimuth respectively, although in some cases ground range and azimuth. As such, they may need geocoding to a map projection. Conversely, other data of the area such as DEMs may need geocoding into slant range/azimuth coordinates for processing, for example, for use in 2-pass differential interferometry (section 3.8.1).

Initially a `dem_par` file is created to define the parameters of the map projection (`create_dem_par`). Antarctica is usually mapped in the Polar Stereographic projection, a coordinate system which is based on the WGS84 ellipsoid, has its origin at the South Pole, its line of true scale at 71 degrees south, and units of metres. A posting of 50 m was chosen for geocoding in this study.

Geocoding begins by creating a lookup table showing the x and y coordinates of the image which correspond to each point of the geographic coordinate system (`gec_map`). This enables a many-to-one relationship between planar coordinates on multiple images and the map coordinate system, as the same lookup table can be used for each image to be geocoded. Lookup tables are in float complex format, with the real part corresponding to the x coordinate (i.e. slant range, easting or longitude), and the imaginary part to the y coordinate (i.e. azimuth, northing or latitude). There are two types of lookup table, one having the dimensions of an image in SAR coordinates and one having the dimensions of an image in map coordinates, depending on whether forward or backward geocoding is used. As the original lookup table is only accurate to within a few pixels because of uncertainties in the orbit data, the lookup table may then be refined using manually entered control points which are used to define a more accurate offset registration polynomial. However, this step was not used in this study due to the relatively low resolution of the DEMs (section 4.3.4) and because for frames with InSAR derived DEMs, geocoding was only for visualisation rather than a processing step.

One image is then resampled into the coordinates of the other. During resampling it is best to keep the image resolution approximately the same (Gamma Remote Sensing, 2002). Geocoding may be carried out either forwards, from the coordinates in which the lookup table is given in the dimensions of the lookup table using irregularly spaced samples (with the program `geocode`), or backwards, where the output data are in the same dimensions as the lookup table and geocoding is based on regular samples and therefore more efficient (`geocode_back`). Geocoded images may then be mosaicked together, using the Gamma routine `mosaic`.

Processing stages so far, picking up from where figure 3.4 left off, are summarised in table 3.1, along with the options used at each stage.

3.8 Differential Interferometry

In dynamic environments where phase changes between images occur because of surface displacement as well as elevation change, differential interferometry can be used to subtract two interferograms so that common topography is eliminated and therefore only phase change due to surface displacement, in this case ice movement, remains. Surface displacement in the line-of-sight (LOS) direction of the sensor may then be converted to ice stream flow velocity, or vertical change because of tidal displacements. Differential interferometry ideally requires two interferograms from an identical pair of positions. There are forms of differential interferometry possible using 2, 3 or 4 satellite passes.

Table 3.1: Summary of Gamma routines and options used in single difference interferometry, and geocoding, in this study.

Section	Routine	Options
Offsets		
3.5.6	create_offset	Method 1, intensity cross correlation
3.5.6	init_offset_orbit	Initial location set on stationary area
3.5.6	init_offset	4 by 20 multilooking
3.5.6	init_offset	2 by 10 multilooking
3.5.6	init_offset	1 by 1 multilooking
3.5.6	offset_pwr	80 by 100 windows size 256 by 1024, SNR threshold of 7
3.5.6	offset_fit	4th order polynomial
Single Difference Interferometry		
3.5.7	interf_SLC	Coregisters image and creates interferograms and MLIs in one stage
3.5.8	base_init	Estimates baseline using method 0 or 2, 128 by 128 FFT window placed on flat area
3.5.8	ph_slope_base	
3.5.8	base_perp	
3.5.9	cc_wave	5 by 5 window
3.5.9	adf	Adaptive filtering exponent 0.5
Phase Unwrapping		
3.6.1	corr_flag	Initial coherence threshold 0.4, used 0.25 where necessary
3.6.1	residue_cc	
3.6.1	tree_cc	
3.6.1	grasses	Place the start point for unwrapping on a stationary area of each frame
Geocoding		
3.7	create_dem_par	Polar Stereographic projection, 50 m resolution
3.7	gec_map	
3.7	geocode_back	
3.7	mosaic	

3.8.1 2-Pass Differential Interferometry

Two-pass differential interferometry requires one interferometric pair and an accurate DEM of an area. A reference interferogram is simulated based on the DEM, which must first be transformed into SAR image coordinates.

Appropriate sections of the DEMs were cut out, using corner coordinates from the geocoding (.polar.par) parameter files, and geocoded (using the program geocode, as opposed to geocode_back) into slant range/azimuth coordinates from Polar Stereographic or the ICESat projection (section 4.3.4) for each frame.

The unwrapped interferometric phase caused by topography only may then be simulated using the DEM, the reference SAR geometry, and the baseline model. phase_sim uses the elevations from the DEM resampled into SAR geometry to simulate the topographic component of the phase. This may either be subtracted from the complex, single difference, interferogram to give a complex differential interferogram, or from the unwrapped phase to give the unwrapped differential phase (section 3.8.6). As the flat earth component of the phase was not removed from the topographic phase, it must be added back to the unwrapped phase of the original interferogram (using the Gamma routine reramp). Gamma Remote Sensing (2002) find 2-pass differential interferometry more robust for areas of rugged terrain than methods involving unwrapping phase which is the result of both topography and displacement.

Two-pass differential interferometry leaves behind fringes caused by errors in the DEM, but these errors will be in the same geographic location on every interferogram processed with that DEM and so should be easily identified (Massonnet and Feigl, 1998).

3.8.2 3-Pass Differential Interferometry

Three-pass differential interferometry is suited to studying displacement events such as earthquakes, and requires an InSAR triplet, i.e. three SAR images from



the same track and frame. 3-pass differential interferometry was pioneered by Zebker *et al.* (1994a) investigating the Landers Earthquake, which occurred in June 1992. They created an interferogram from ERS-1 scenes from April and August, containing the effects of the displacement event, and a topography-only interferogram from the August scene paired with a scene from July. Scaling the phase of the topography-only interferogram to the ratio of the parallel baselines of the interferograms, and subtracting it from the phase of the interferogram containing the displacement event left an interferogram containing only the phase of the displacement in the line-of-sight (LOS) direction of the satellite caused during the earthquake.

Bearing in mind that the sensitivity to topography is inversely proportional to the perpendicular baseline, the reference interferogram should have the longer perpendicular baseline, although lengthening the baseline makes unwrapping more difficult.

Any differential interferometry using three images in this study was actually the combination of complex interferograms (section 3.8.3), but using three images, with the middle image used twice, rather than 3-pass interferometry in the more usual sense.

3.8.3 Combination of Complex Interferograms

In some of the literature this method is referred to as 4-pass differential interferometry (e.g. Gamma Remote Sensing (2002), Bevan (2006)). However, it may also be carried out with three satellite passes, with one image acting as a member of each interferometric pair, and is better termed double differencing. This is in contrast to the original interferograms created from pairs of images, which are single difference interferograms.

The combination of complex interferograms requires two interferometric pairs, which may be combined using integer phase scaling factors. Scaling the interferometric phase may be used to simulate the interferogram that would have been

produced with another baseline, for example to remove or enhance the sensitivity to topography by respectively reducing the simulated interferometric baseline and adding complex interferograms. It is important to note here that it is the unflattened interferograms, with the flat earth phase trend still present, that are combined. Filtering is recommended prior to combining interferograms to reduce problems from scaling the phase noise along with the wrapped phase (Gamma Remote Sensing, 2002).

As the two interferograms are in different geometries, the second must be resampled to the geometry of the first. `create_diff_par` takes in the offset files of both interferograms and uses these to create a parameter file on the difference between the positions of the two interferograms. The offsets between the two interferograms must then be calculated so that one may be resampled to the geometry of the other. The principles are the same for calculating offsets between multilook images for single difference interferometry, as discussed in section 3.5.6. The routines `init_offsetm`, `offset_pwr` and `offset_fitm` were used. The default settings (as used by Bevan (2006)) were 24 samples in the range and azimuth dimensions with a window size of 64 by 64. However, for the scenes used in this study, larger window sizes produced a higher number of accepted offsets, while still maintaining a low enough offset standard deviation, with 128 by 128 performing considerably better than 64 by 64 and 256 by 256 better still. The SNR threshold was 7. The offset polynomials are written to the `diff_par` file. `interp_cpx` is used to interpolate the second interferogram into the geometry of the first.

The two single difference interferograms are combined using `comb_interfs` with scaling factors of 1 and -1, which produces what is, in theory, a topography-only interferogram. Scaling factors of 1 and -1 are used to create an interferogram where the phase is the difference in phase between the two original interferograms (e.g. (Massonnet *et al.*, 1996)). The differential baseline is calculated by subtracting the perpendicular baseline of the second interferogram from that of the first (Fatland and Lingle, 1998).

The separation of topography and displacement phase was pioneered by Kwok

and Fahnestock (1996), who used a chain of four ERS SAR images, separated by 3 days each, of northeastern Greenland in January 1994. Differencing two 3-day interferograms removed the displacement phase, leaving only the topographic phase. However, this only works if displacement during the two 3-day periods is the same: the Constant Velocity Assumption (CVA), as discussed below in section 3.9. The phase of a topography-only interferogram (ϕ_{12}) created by subtracting the phases (ϕ_1 and ϕ_2) of two single difference interferograms is given as follows, where $a = 2k/R \sin \omega$ and $B_1 - B_2$ the differential baseline (Fatland and Lingle, 1998).

$$\phi_1 = 2k \Delta R_1 + a B_1 \Delta e \quad (3.21)$$

$$\phi_2 = 2k \Delta R_1 + a B_1 \Delta e \quad (3.22)$$

$$\phi_{12} = \phi_1 - \phi_2 \approx a (B_1 - B_2) \Delta e \quad (3.23)$$

The phase of a topography-only interferogram is therefore the sum of equations 3.14 and 3.15, which applies also to the phase of an interferogram produced from a static scene without moving features.

`ph_slope_base` is then used to remove the geometric component of the phase, i.e. the flat earth phase trend (section 3.5.8) using the combined baseline file. `cc_wave` estimates the coherence of the combined interferogram (section 3.5.9), which is used as a guide to phase unwrapping after the combined interferogram has been filtered using `adf` (section 3.5.9).

Using the Gamma tools, phase unwrapping may be carried out before the creation of the differential interferogram, resulting in unwrapped differential phase, or

after, resulting in a complex differential interferogram, which may subsequently be filtered and unwrapped (Gamma Remote Sensing, 2002). However, as phase unwrapping errors of the original interferograms introduce topographic errors into the combined interferogram (Massonnet and Feigl, 1998), in this study the combination of the original, wrapped, interferograms was used.

3.8.4 Height Map

An interferometrically derived height map is produced from the unwrapped phase of a topography-only interferogram. Zebker and Goldstein (1986) pioneered the method of creating height maps from interferograms. An accurate height map derived from a differential interferogram depends on the availability of accurate Ground Control Points (GCPs) distributed widely across the scene (Fatland and Lingle, 1998). Rignot (1996), for example, used 1400 tie points sampled from a DEM to refine the baseline when studying Petermann Gletscher, Greenland.

Calculating the baseline from orbit data or fringe frequency is accurate enough for removing the flat earth phase trend from a single difference interferogram. However, this information is not accurate enough to convert phases to topographic heights. A least squares fit for a number of ground control points of known topographic height is therefore required for refining the estimate of the baseline (Gamma Remote Sensing, 2002). Sources of ground control used in this study are discussed in section 4.3.

The coordinates of GCPs of known elevation are converted from map coordinates in Polar Stereographic projection or longitude and latitude to slant range and azimuth pixel coordinates in samples and lines on the multilooked images using `coord_to_sarpix`. `gcp_phase` is then used to extract the unwrapped phase at each control point and write this to the text file with the GCPs. Alternatively, if GCPs are taken from sampling from DEMs rather than from point data, the program `extract_gcp` is used, and this allows certain areas of the DEM to be masked out. `base_ls` then calculates a least squares estimate of the fit between the unwrapped phase of the GCPs and the expected phase using the initial baseline,

outputs statistics on the Root Mean Square Error (RMSE) of the fit, and writes the refined baseline, known as the precision baseline, to the combined baseline file.

Unsuccessful refinement of the baseline may be due to several factors such as a poor estimate of the initial baseline, poor control points, too small an area for averaging the phase, or too many free parameters in `base_ls`. A poor fit indicates that the baseline estimate needs to be improved, and this is done through an iterative process using least squares fitting until an acceptable RMS error is achieved (Fatland and Lingle, 1998). Refining the baseline may be difficult over featureless polar ice sheets, and it is limited by decorrelation between scenes and errors in the tie-points (Fatland and Lingle, 1998).

Following the accurate establishment of control points, the precision baseline and the unwrapped phase are used to produce a topographic height map (`hgt_map`). This map may then be geocoded from slant range and azimuth to map coordinates (Gamma Remote Sensing, 2002). Zebker *et al.* (1994b) state that it is possible to produce topographic maps with below 5 m RMS height error from ERS-1 data.

3.8.5 Simulation of Topographic Phase

Topographic phase is then simulated from the height map, in the case of double difference interferometry, or from the DEM in slant range/azimuth coordinates, in the case of 2-pass differential interferometry (`phase_sim`). In the first case, this gives the flattened, unwrapped topographic phase, which must have the geometric component added back to it using `reramp`. In the second case, whether the simulated phase is flattened or unflattened is specified when `phase_sim` is run. Unflattened phases are simulated for use in further processing, but, in this study, flattened phases were simulated for visualisation.

3.8.6 Separation of Topographic and Displacement Phase

The filtered single difference interferograms had the flat earth phase trend (ϕ_{geom}) added back to them at this stage. A least squares fit between the reramped phase of the single difference interferograms and the simulated topography-only phase was performed using `diff_ls_fit`, and `diff_ls_unwrap` is then used to subtract the topographic phase from the single difference interferograms to give the unwrapped differential phase in the reference geometry. This phase represents the change in slant range distance, i.e. displacement in the line-of-sight (LOS) direction of the satellite.

Scaling to B_1 or B_2 , allows the topographic component of the phase of the original interferogram (ϕ_{topo}) to be simulated so that it may be removed, leaving only ϕ_{trans} i.e. the phase due to displacement in the line-of-sight direction of the satellite (Fatland and Lingle, 1998). This is shown in the following two equations, for removing the topographic phase from the first and second single difference interferograms respectively.

$$\phi_{1-12} = \phi_1 - \left[\frac{B_1}{B_1 - B_2} \right] \phi_{12} \approx 2k\Delta R = \phi_{trans} \quad (3.24)$$

$$\phi_{2-12} = \phi_2 - \left[\frac{B_2}{B_1 - B_2} \right] \phi_{12} \approx 2k\Delta R = \phi_{trans} \quad (3.25)$$

As an assessment of the effectiveness of the removal of the topographic phase, pixels on static features should be examined to make sure they all have the same phase.

For some frames, when using 2-pass differential interferometry, subtraction of the topographic phase using `sub_phase` proved more effective than the above method.

3.8.7 Line-Of-Sight Velocities

Displacement in the LOS direction of the satellite is given as follows, where ΔT is the temporal baseline (Bevan, 2006).

$$Disp_{LOS} = \frac{\phi_{trans}}{2k\Delta T} \quad (3.26)$$

A 2π change in differential phase indicates a displacement in the LOS direction of the satellite of half the wavelength ($\lambda/2$), in this case, 2.83 cm (Franceschetti and Lanari, 1999).

Assuming topography has been removed, as is the case here, or the scene is flat, in the case of a single difference interferogram, each fringe in a flattened interferogram can be converted to horizontal velocity in the range direction as follows:

$$2\pi = 2.83/(\Delta T \sin\omega) \quad (3.27)$$

where ΔT is the temporal baseline, in days, and ω the look angle (Kwok and Fahnestock, 1996), or 2.3 cm day^{-1} for a 3-day ΔT . The fringe rate of fringes due to displacement phase increases linearly with the temporal baseline (Kwok and Fahnestock, 1996), as should be expected.

3.8.8 Displacement Maps

Displacement maps are produced using the program `dispmap`, which has three options: it may be assumed that all the displacement is in the direction of the look vector (bearing in mind the steep angle of the look vector to the scene); that all the displacement is vertical; or that all the displacement is in the horizontal plane corresponding to the look vector, assuming the surface is flat. This allows

researchers to examine different components of the 3-dimensional velocity vector of the scene studied.

3.8.9 Downslope Velocities

Following the removal of topographic phase, the translational phase needs to be projected into the flow direction to show the surface velocity vector. The flow direction is first derived for a horizontal plane, then the glacier slope is taken into account to add the z direction for surface parallel flow (Fatland and Lingle, 1998). Fatland and Lingle (1998) recommended drawing a centre-line for flow direction, although they were working with valley glaciers where flow could not be approximated to the downslope direction. Vectors may also be derived from connecting phase bulls eyes (Rignot *et al.*, 1995), concentric fringe patterns caused by ice flowing over bumps in subglacial topography, leading to vertical motion (Joughin *et al.*, 1995). LOS velocities may be converted to downslope velocities by the following equation (Burgess *et al.*, 2005):

$$Disp_{slope} = \frac{Disp_{LOS}}{(\cos \kappa \sin q \sin \theta) + (\sin \alpha \cos \theta)} \quad (3.28)$$

where κ is the surface slope, q the angle between the look direction and flow direction, and θ the incidence angle. For ice flowing more than 20 m a^{-1} , Burgess *et al.* (2005) found that when the flow direction was accurate to within $\pm 2^\circ$, errors in surface velocities were between 2 and 10 %. However, the largest errors in velocities from InSAR are due to baseline errors (Joughin *et al.*, 1998).

Displacements produced from `dispmmap` in the look vector direction and the horizontal were projected into the flow direction in a three stage process. `look_vector` calculates the local elevation and azimuth of the look vector to the surface, based on the InSAR DEM for double differencing methods and the input DEM for the 2-pass method. `dem_norm_vecs` was used to calculate the elevation and azimuth

of the plane normal i.e. at 90° to the DEM. The elevation therefore had to have $\pi/2$ radians (i.e. 90°) subtracted from it to represent the angle of the surface. The InSAR derived DEM does not need to be of absolute accuracy to determine flow directions (Bevan *et al.*, 2007). In this study, the slope and aspect of the DEMs used in 2-pass differential interferometry was also calculated in ArcMap as a comparison, using the Spatial Analyst. Finally, `dispmap_flow` was used in this study to project the look vector displacements into the flow direction, with areas masked out where the flow direction was more than 30° from the look direction due to the insensitivity of InSAR to displacement perpendicular to the look direction.

3.8.10 Dual Azimuth Interferometry

Dual azimuth interferometry was pioneered by Joughin *et al.* (1998). Dual azimuth interferometry takes interferograms of the same area from different orbital directions, ascending and descending. Joughin *et al.* (1998) state that interferometry using scenes from just one orbital track can provide only one component of the three dimensional velocity vector, and looking at the same area from three different orbital tracks would therefore be necessary in order to deduce the full velocity vector. Such an orbital configuration does not exist, as the ERS satellites have only two directions of pass and can only look north (Joughin *et al.*, 1998). However, by assuming surface parallel flow as one component of the velocity vector, interferometry on scenes of the same area from both ascending and descending orbital tracks can provide the other two components, and thus produce a three dimensional velocity field. However, the assumption of surface parallel flow is not usually valid, as ice flows slightly downward in the accumulation zone, as in the study area, and conversely flows slightly upward in the ablation zone (Joughin *et al.*, 1998). Indeed, Reeh *et al.* (2003) found vertical velocities in Storstrømmen, Greenland, needed to balance the ablation rate, were so large they led to errors of up to 20% in horizontal velocities derived from dual azimuth InSAR. However, Joughin *et al.* (1998) state that estimates of horizontal ice motion should not be affected by the failure of this assumption. Joughin *et al.*

(1998) recommend surface slope is averaged over 10 to 20 ice thicknesses prior to dual azimuth interferometry in order to approximate the flow direction with the direction of maximum surface slope, free of local perturbations.

Displacements in the flow direction from an ascending and a descending SAR frame and the frame DEM are used by the program `dispmap_3d` to show the velocity vector in three dimensions.

Processing stages so far, picking up from where table 3.1 left off, are summarised in table 3.2, along with the options used at each stage.

3.9 Constant Velocity Assumption

Forms of differential interferometry that use two interferograms rely on the validity of the Constant Velocity Assumption (CVA). The CVA applies to both three and four pass differential interferometry, and assumes that the rate of displacement between the images making up each interferometric pair is the same for both pairs used to create the differential interferogram. For this reason, it is better to select pairs spaced closely in time (Fatland and Lingle, 1998).

It is possible to calculate the errors introduced by failure of the CVA, once the combined perpendicular baseline of the topography-only interferogram has been established (section 3.8.3).

$$H_e = \frac{\delta_z}{2\pi/2k v_n} \quad (3.29)$$

where k is the wavenumber of the radar, δ_z the altitude of ambiguity, v_n the amount of non-constant velocity in metres per temporal baseline ($\text{m } \Delta T^{-1}$), and H_e the height error in metres. Failure of the Constant Velocity Assumption (CVA) proved important in this study, and is discussed further in section 7.3.4.

Table 3.2: Summary of Gamma routines and options used in differential interferometry in this study.

Section	Routine	Options
Combination of Complex Interferograms		
3.8.3	create_diff_par	
3.8.3	init_offsetm	3 by 3 multilooking
3.8.3	init_offsetm	2 by 2 multilooking
3.8.3	init_offsetm	1 by 1 multilooking
3.8.3	offset_pwrn	80 by 100 windows size 256 by 256, SNR threshold of 7
3.8.3	offset_fitm	4th order polynomial
3.8.3	interp_cpx	
3.8.3	comb_interfs	Phase scaling factors of 1 and -1
3.8.3	ph_slope_base	
3.8.3	cc_wave	5 by 5 window
3.5.9	adf	Adaptive filtering exponent 0.5
Refining the Baseline		
3.8.4	gcp_phase	Window size 3, using unwrapped phase
3.8.4	OR extract_gcp	
3.8.4	base_ls	
3.8.4	hgt_map	
Removal of Topography		
3.8.5	phase_sim	Using either the DEM segment or height map
3.8.6	reramp	
3.8.6	diff_ls_fit OR sub_phase	64 by 64 samples For some 2-pass
3.8.6	diff_ls_unwrap	Unless used sub_phase
Ice Flow		
3.8.9	look_vector	
3.8.9	dem_norm_vecs	Subsequently subtracted $\pi/2$
3.8.9	dispmap_flow	Excluding areas with $>30^\circ$ angle between look and flow direction

3.10 Grounding Zone Mapping

As mentioned in the previous chapter in section 2.6.1, interferometry may be used to map the hinge zones of ice streams. Interferometry, like most methods used to map the grounding zone, identifies the landward and seaward limits of tidal flexing, F and H (figure 2.3). The high phase gradient in the grounding zone, which occurs because of the change in vertical motion where the ice adjusts to hydrostatic equilibrium at H in figure 2.3, means the grounding zone is easily identifiable by its many closely spaced fringes (Rignot, 1998b). Interferometry cannot, therefore, identify the locations of G and I. Using 24-day repeat RADARSAT data from the Antarctic Mapping Mission (AMM), Forster *et al.* (1998) found that the grounding zone could also be identified from amplitude and coherence images. Gray *et al.* (2002) were able to map the grounding zone of Filchner Ice Shelf and the southeastern part of the Ross Ice Shelf to an estimated accuracy of 1-2km using 24-day repeat RADARSAT data from the AMM for interferometry, and Rignot (1998b) used double difference interferometry to map the hinge zone of the Rutford Ice Stream.

In Goldstein *et al.* (1993)'s groundbreaking interferometric study of the Rutford Ice Stream they were able to map the grounding zone to a precision of 0.5 km, but had to use an independent estimate of ice velocity to identify the displacement that was tidally related (Rignot, 1996). Rignot (1996) used quadruple difference interferometry to study tidal displacements of Petermann Gletscher, Greenland using a 3-day triplet of images from 1992, removing the topography using tie points from a DEM which had 0.005° resolution in latitude and 0.025° in longitude, and deriving control velocities from tracking crevasses.

Differential interferometry has previously been used by Rignot (1998b) to map the grounding zone of the Rutford Ice Stream. Topography and LOS displacement were separated using the standard approach of Zebker *et al.* (1994a) (section 3.8.3). A 5 km resolution DEM derived from ERS altimeter data (Bamber and Bindschadler, 1997), which is discussed in section 4.3.4, was found to provide more accurate topography on floating ice because of the difficulties in removing

the tidal signal from the interferometrically derived topography, and so this DEM was used to remove the topographic phase from the floating ice, leaving only tidal displacements. Tide only interferograms were created in Rignot (1998b)'s study by differencing two interferograms with equal temporal baselines which had had their topography removed using the DEM. However, this assumes that the CVA (section 3.9) is valid, so that the signal from creep flow, which limits the precision to which the grounding zone could be mapped to several hundred metres, would be the same for both interferograms.

Geocoded flattened interferograms were placed in a GIS in ArcMap, and the shape and width of the grounding zone digitised for each frame (figure 3.6). Vertical change in the grounding zone was examined from the maps. The ERS satellites are 2.4 times more sensitive to vertical displacement than horizontal displacement due to their steep look angle, 23° , and each fringe would represent approximately 2.6 cm of vertical displacement, if it was assumed all displacement was vertical. Fringes in the grounding zone were counted and the total vertical displacement compared to the tidal change between scenes as predicted by tidal models, as discussed in section 4.5.1 in the next chapter. The results are shown in section 6.3.

3.11 Application to Glaciology

Interferometry has previously been successfully applied to the cryosphere. Joughin *et al.* (1996) note that the slowly varying topography of ice sheets makes them particularly suited to interferometry. The following examples are by no means exhaustive of the literature, but aim to provide examples of different applications of interferometry to the cryosphere, and of work from different glaciated regions.

An early interferometric study of the cryosphere, by Goldstein *et al.* (1993), was discussed in section 2.8.1 in the previous chapter, as their chosen study area was the Rutford Ice Stream. In another early application of ERS SAR interferometry of the cryosphere, Joughin *et al.* (1995) used a 3-day pair of ERS-1 scenes to

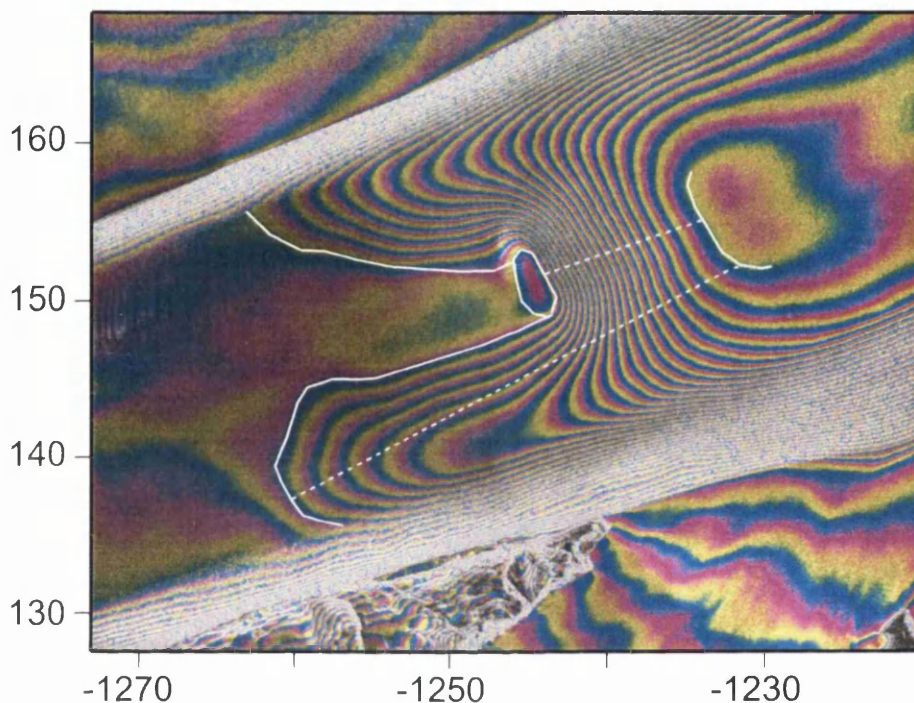


Figure 3.6: An example of grounding zone mapping for the Rutford Ice Stream from this study, using a flattened interferogram. Fringes (section 3.5.7) show one complete phase cycle of phase difference between the two images making up the interferogram, from 0 to 2π radians, and are the result of scene topography, line-of-sight displacement of the surface, and the perpendicular baseline (section 3.5.7). Dashed lines indicate where fringes were counted in interferograms and profiles of vertical displacement taken from displacement maps made following phase unwrapping. Coordinates are Polar Stereographic, in kilometres, with the origin at the South Pole.

produce interferograms of the ice margin in western Greenland, removed the topographic phase using a radar altimetry-derived DEM, and created a synthetic interferogram based on a model of ice motion.

Ice velocities may be derived over wide areas, some of which may have limited field measurements. Differential interferometry of Devon Ice Cap, Canada, was carried out by Burgess *et al.* (2005), who used both double differencing and 2-pass differential interferometry, and mosaicked together three displacement only interferograms which covered 98% of the ice cap. Rignot *et al.* (1995) derived velocities within 6% of those measured in the field in western Greenland. Storstrømmen, Greenland, was investigated using dual azimuth SAR interferometry by Mohr *et al.* (1998), who found good agreement between InSAR and GPS velocities.

Dual azimuth interferometry has also been previously applied to the cryosphere. Stenoien and Bentley (2000), for example, combined the velocities produced from interferometry of ascending and descending orbital tracks for the same area of Pine Island Glacier, West Antarctica, and removed the topographic component using a DEM derived from radar altimetry in order to produce velocity vectors, and Joughin *et al.* (1998) estimated the three dimensional velocity vector for Ryder Glacier, Greenland, using interferograms from ascending and descending passes and assuming surface parallel flow.

Velocities derived from InSAR may be used to examine several different phenomena. InSAR derived velocities may be compared to balance velocities in order to assess the current state of mass balance of an ice body. The mass balance of Glaciar Perito Moreno, Patagonia, was assessed with interferometry using Shuttle Imaging Radar (SIR) data along with velocity and ablation from stake measurements and bathymetry data on the lake into which the glacier calves (Stuefer *et al.*, 2007). The equilibrium line fluxes (the volume of ice flowing across the equilibrium line, where accumulation and ablation are equal, in a given time) of Austfonna, on Nordaustlandet in Svalbard, derived from InSAR velocities and RES ice thickness data were compared to balance fluxes (the flux required for the ice cap to maintain neutral mass balance), showing that the ice cap had a positive mass balance, and fluxes for each drainage basin were calculated to examine

surging behaviour (Bevan *et al.*, 2007; Bevan, 2006).

Interferometry has also been used to examine surging glaciers. The surge of Monacobreen, Svalbard, was investigated using eleven surface velocity maps derived from 36 ascending and descending ERS scenes from 1991 to 1997 using differential dual azimuth interferometry (Luckman *et al.*, 2002; Murray *et al.*, 2003b), and the surge of Fridtjovbreen, Svalbard, was studied using similar methods to produce ten surface velocity maps and 4 DEMs (Murray *et al.*, 2003a). Fatland and Lingle (1998) also used interferometry to examine the surge of Bering Glacier, Alaska. In some cases, the derivation of the DEM itself is an important stage of the research, for example, Pritchard *et al.* (2003) compared a map-derived DEM from before the surge of Sortebræe, Greenland, and an InSAR-derived DEM from afterwards. Joughin *et al.* (1996) also created interferometrically derived DEMs of Greenland, and found a relative accuracy of 2.5 m compared to airborne laser altimeter data.

InSAR may also be used to examine volcanic events beneath ice caps. Gudmundsson *et al.* (2002) used interferometrically derived 3D surface motion maps of Vatnajökull, Iceland, to study its recovery from a subglacial eruption and jökulhlaup which left a large depression on the surface, and were also able to estimate basal melting, and Magnússon *et al.* (2007) used tandem mission data to examine the same jökulhlaup using dual azimuth interferometry.

Interferometry of the cryosphere is not limited to grounded ice. It has also been used to study ice shelves such as Larsen B (Rack and Rott, 2004; Rack *et al.*, 1999). Rack *et al.* (1999), for example, found nunataks in the Larsen Ice Shelf were surrounded by concentric, closely spaced fringes corresponding to 0.34 to 0.35 m of vertical motion, agreeing well with a tidal model predicting a 0.36 m tidal height difference between the time of acquisition of both SAR images. Rignot *et al.* (2000) used differential interferometry to study the iceberg calving fronts of the Filchner and Ronne Ice Shelves, Antarctica. As mentioned previously in section 3.10, interferometry has previously been used to map ice stream grounding zones.

It is therefore clear from this wide range of previous work that there is great potential for interferometric applications in examining the cryosphere.

3.12 Summary

Remote sensing is an attractive method for studying polar regions due to their inaccessibility and large spatial extent. Synthetic Aperture Radar interferometry has previously been successfully applied to other glaciated regions, although case studies also highlight its errors and limitations. Numerous variations on the overall method of interferometry exist, and in this study interferometry was carried out from 2, 3 and 4 satellite passes, using the methods and Gamma software routines outlined in this chapter. The data used, including SAR scenes and sources of ground control, will be discussed in the next chapter, and the results of applying interferometry to the Rutford and Evans Ice Streams in chapter 5, which presents velocities and vertical displacements. These results, and the reliance of differential interferometry on either an accurate, high resolution DEM, or the validity of the Constant Velocity Assumption, are discussed in chapter 7.

Chapter 4

Data and Models

4.1 Introduction

This chapter will begin by cataloguing the satellite images used in this study and the reasons for their selection. During the process of interferometry a number of sources of ground control data were used, with varying degrees of success. Point data from Global Positioning Systems (GPS) and satellite radar and lidar altimetry will be discussed, as well as four Digital Elevation Models (DEMs) which were used to simulate topographic phase. Two balance velocity datasets, two tidal models, and an elastic beam model used in this study will also be described.

4.2 Satellite Data

Forty-seven SAR images were obtained through the VECTRA project. The ESA catalogue was interrogated for suitable combinations of scenes for carrying out interferometry, using the software descw. The high data rate of the ERS satellites and the necessity to regularly transmit data to ground stations, most of which are in Europe (Campbell, 2002), means that most of the scenes theoretically

visible from each orbit are not actually acquired, with images being acquired for a maximum of ten minutes per 100 minute orbit (European Space Agency, 2006b). As such, data availability was a major constraining factor.

The study area is at the southerly limit of coverage by the ERS satellites ERS-1 and ERS-2. This has the advantage that all the tracks converge on the area, in theory giving a large choice of scenes, but also the disadvantage that many frames, particularly of Rutford, are the first or last frame acquired in their track (depending on the respective ascending or descending heading of the orbit), and thus suffer from quality issues such as missing lines, which may occur for tens of kilometres and render some scenes acquired unusable.

Although meteorological observations of the area are sparse, the fact that the air temperature remains below zero all year round was taken into account when selecting scenes, as it meant there were no considerations of surface melting having occurred between the acquisition of the scenes making up each interferometric pair, as there are in similar studies in the Arctic (Bevan, 2006; Luckman *et al.*, 2002). Rates of accumulation are also low, with the Rutford Area Base of Ice Drilling (RABID) field party arriving on the ice stream in 2004 finding their depot, which had been left on the surface the previous season, under 0.5 m snow, about the amount they expected (Smith, 2006b), and so will not cause significant change in surface elevation between paired scenes. Although it is accepted that snowfall and the redistribution of snow by wind may cause some decorrelation between paired scenes, meteorological data were not available to allow this to be considered when selecting scenes.

Within these constraints, the most important factor was optimising the baseline for interferometry, beginning with the temporal baseline, which must be short enough to maintain coherence between the scenes making up an interferometric pair.

The ERS satellites have had orbital repeat periods of 3, 35, or 168 days, depending on the phase of the orbit (European Space Agency, 2005). Phases B and D of the orbit of ERS-1, the first and second ice phases, followed a 3-day repeat cycle, a

suitable temporal baseline for interferometry. Phase B lasted from 28 December 1991 to 2 April 1992 and Phase D from 23 December 1993 to 10 April 1994, with the track and frame numbers the same for both phases. Pairs with temporal baselines of multiples of three days were often available when 3-day pairs were not.

From 21 March 1995 onwards, one month prior to the launch of ERS-2, ERS-1 has been in phase G of its orbit, the second multi-disciplinary phase, following an orbit with a 35-day repeat. ERS-2 has also followed an orbit with a 35-day repeat since 21 April 1995, initially as a commissioning phase. The tandem mission, with ERS-2 following a 35-day repeat exactly 24 hours behind that of ERS-1, lasted from 17 August 1995 to 2 June 1996. This enabled sets of images known as tandem quads to be acquired, with a pair of images one day apart (a tandem pair), and then a 35-day gap, followed by another pair of images one day apart. This configuration optimises the temporal baseline for both interferometry, which requires the shortest possible baseline in order to maintain coherence, and feature tracking, which is hindered by low signal-to-noise ratio (SNR) when the temporal baseline is too short. The two one day pairs making up each quad can also be used for differential interferometry (section 3.8).

Suitably located frames of the Rutford and Evans Ice Streams were identified. For most of these, only one possible combination of scenes was available, particularly during the tandem mission. Once pairs with suitable temporal baselines had been identified, their perpendicular baselines were also examined to make sure they were well below the critical baseline for interferometry of approximately 1200 metres. However, although this turned out not to be an issue as baselines rarely exceeded 250 metres, even between ERS-1 and ERS-2 for tandem pairs. After these considerations, scenes were selected with the aim of maximising spatial and temporal coverage of the ice streams in the minimum number of scenes.

4.2.1 Scenes of Rutford Ice Stream

For the first ice phase, 3-day pairs were obtained for the ice stream onset and grounding line, and a 6-day pair for the middle section. For the second ice phase, images of Rutford were obtained for the same three track and frame numbers as for 1992, and in this case the middle section of the ice stream was covered by a 3-day rather than a 6-day pair. Tandem quads covering the ice stream from onset to grounding line were obtained for a period in early 1996 (figure 4.1, table 4.1).

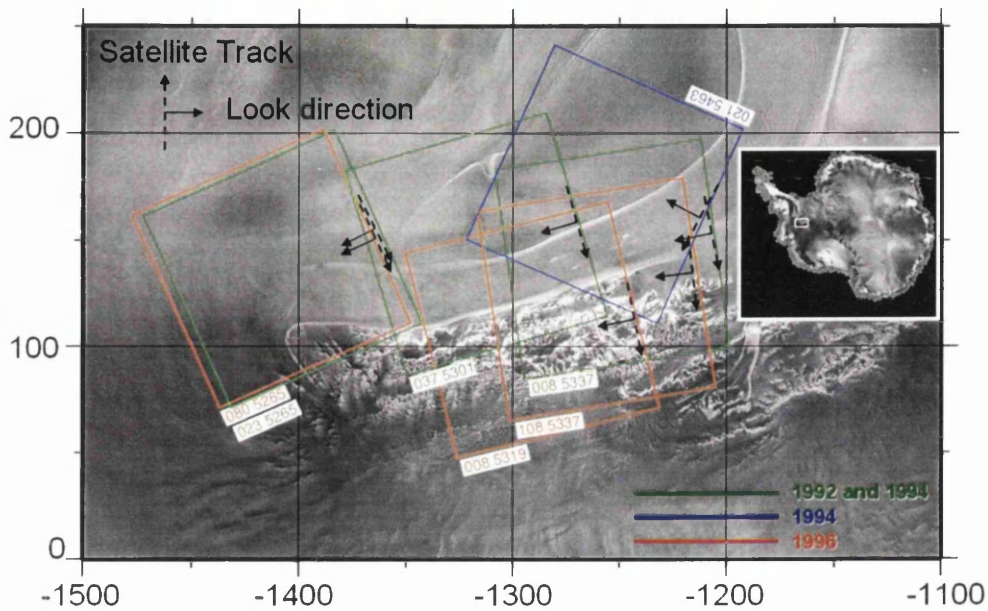


Figure 4.1: Frames of the Rutford Ice Stream. Numbers indicate track and frame respectively. Numbers below the scene represent descending orbits, and above, ascending. Scene look directions are shown. Ice stream flow in the main channel is from left to right. Coordinates are Polar Stereographic, in kilometres, with the origin at the South Pole.

Interestingly, the grounding line of the ice stream is covered by a 3-day triplet during the second ice phase - an image, then three days, then a second image, then three days, then a third image - which allows differential interferometry to

Table 4.1: SAR scenes for the Rutford Ice Stream.

Satellite	Orbit Phase	Orbit #	Date	Track #	Frame #	Direction
ERS-1	B	02814	29/01/92	008	5337	Descending
ERS-1	B	02857	01/02/92	008	5337	Descending
ERS-1	B	02972	09/02/92	037	5301	Descending
ERS-1	B	03044	14/02/92	023	5265	Descending
ERS-1	B	03058	15/02/92	037	5301	Descending
ERS-1	B	03087	17/02/92	023	5265	Descending
ERS-1	D	13165	21/01/94	008	5337	Descending
ERS-1	D	13178	22/01/94	021	5463	Ascending
ERS-1	D	13180	22/01/94	023	5265	Descending
ERS-1	D	13194	23/01/94	037	5301	Descending
ERS-1	D	13208	24/01/94	008	5337	Descending
ERS-1	D	13221	25/01/94	021	5463	Ascending
ERS-1	D	13223	25/01/94	023	5265	Descending
ERS-1	D	13237	26/01/94	037	5301	Descending
ERS-1	D	13251	27/01/94	008	5337	Descending
ERS-1	G	23543	15/01/96	008	5319	Descending
ERS-2	G	03870	16/01/96	008	5319	Descending
ERS-1	G	23615	20/01/96	080	5265	Descending
ERS-2	G	03942	21/01/96	080	5265	Descending
ERS-1	G	23643	22/01/96	108	5337	Descending
ERS-2	G	03970	23/01/96	108	5337	Descending
ERS-1	G	24044	19/02/96	008	5319	Descending
ERS-2	G	04371	20/02/96	008	5319	Descending
ERS-1	G	24116	24/02/96	080	5265	Descending
ERS-2	G	04443	25/02/96	080	5265	Descending
ERS-1	G	24144	26/02/96	108	5337	Descending
ERS-2	G	04471	27/02/96	108	5337	Descending

be carried out by using the middle of the three images as one member of each pair. Additionally, while all these images were acquired on descending passes of the satellites, a 3-day pair of the grounding line for an ascending orbit was also available for 1994. This scene overlaps with the descending 3-day triplet of the grounding line both spatially, giving coverage of the same section of the ice stream from two different look angles for almost the whole 100 km width of the frame, and temporally, with the 3-day pair from the ascending orbit falling entirely within the time period of the 3-day triplet from the descending orbit. This allows dual azimuth interferometry to be carried out for the grounding line of the ice stream (section 3.8.10).

4.2.2 Scenes of Evans Ice Stream

In the first ice phase, limited data of the Evans Ice Stream with short enough temporal baselines were available. Only one triplet of the confluence region where the five tributaries of the ice stream meet, made up of a 6-day and 3-day pair, was selected for 1992. A 3-day triplet for the same frame was selected for 1994, with two further 3-day triplets of the middle section and grounding zone also obtained for the second ice phase. Two tandem quads were obtained from ascending orbits for early 1996, covering the confluence region and the grounding zone (figure 4.2, table 4.2).

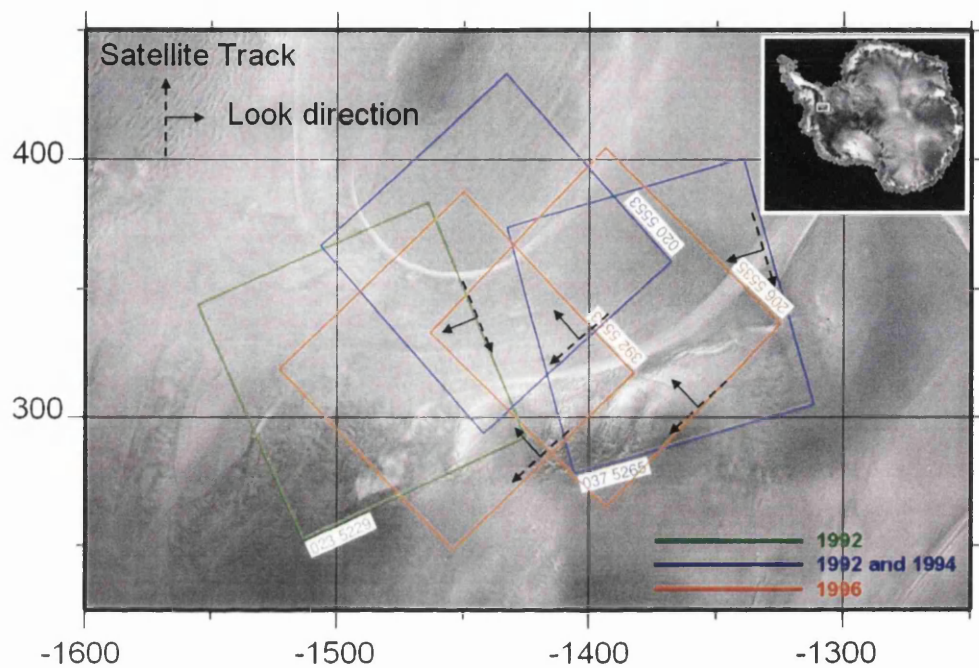


Figure 4.2: Frames of the Evans Ice Stream. Numbers indicate track and frame respectively. Numbers below the scene represent descending orbits, and above, ascending. Scene look directions are shown. Ice stream flow is from bottom left to top right in the main channel. Coordinates are Polar Stereographic, in kilometres, with the origin at the South Pole.

Table 4.2: SAR scenes for the Evans Ice Stream.

Satellite	Orbit Phase	Orbit #	Date	Track #	Frame #	Direction
ERS-1	B	02958	08/02/92	023	5229	Descending
ERS-1	B	03044	14/02/92	023	5229	Descending
ERS-1	B	03087	17/02/92	023	5229	Descending
ERS-1	D	13151	20/01/94	037	5265	Descending
ERS-1	D	13180	22/01/94	023	5229	Descending
ERS-1	D	13194	23/01/94	037	5265	Descending
ERS-1	D	13220	25/01/94	020	5553	Ascending
ERS-1	D	13223	25/01/94	023	5229	Descending
ERS-1	D	13237	26/01/94	037	5265	Descending
ERS-1	D	13263	28/01/94	020	5553	Ascending
ERS-1	D	13266	28/01/94	023	5229	Descending
ERS-1	D	13306	31/01/94	020	5553	Ascending
ERS-1	G	23741	29/01/96	206	5535	Ascending
ERS-2	G	04068	30/01/96	206	5535	Ascending
ERS-1	G	23927	11/02/96	392	5553	Ascending
ERS-2	G	04254	12/02/96	392	5553	Ascending
ERS-1	G	24242	04/03/96	206	5535	Ascending
ERS-2	G	04569	05/03/96	206	5535	Ascending
ERS-1	G	24428	17/03/96	392	5553	Ascending
ERS-2	G	04755	18/03/96	392	5553	Ascending

Table 4.3 shows the combinations of scenes used for differential interferometry. Throughout the rest of the study, image pairs, triplets and quads will be referred to by their track and frame number in the form track_frame, the track number alone being insufficient as in some cases two frames from the same track have been used. Furthermore, track 008 from the ice phases and track 008 from the tandem mission are not the same, and were referred to as tracks 008a and 008b respectively during processing.

Table 4.3: Image pairs, triplets and quads for differential interferometry. Scene footprints are shown in figure 4.1 for the Rutford Ice Stream and 4.2 for the Evans Ice Stream.

Ice stream	Year	track_frame	Dates	B_{perp} (metres)
Rutford	1992	008_5337	29/01/92 - 01/02/92	85.5
		023_5265	14/02/92 - 17/02/92	-17.1
		037_5301	09/02/92 - 15/02/92	85.5
	1994	008_5337	21/01/94 - 24/01/94	20.3
			24/01/94 - 27/01/94	-89.3
		021_5463	22/01/94 - 25/01/94	9.2
		023_5265	22/01/94 - 25/01/94	-11.3
		037_5301	23/01/94 - 26/01/94	-47.3
	1996	008_5319	15/01/96 - 16/01/96	-170.8
			19/02/96 - 20/02/96	-217.3
		080_5265	20/01/96 - 21/01/96	-219.6
			24/02/96 - 25/02/96	-169.1
		108_5337	22/01/96 - 23/01/96	-211.4
			26/02/96 - 27/02/96	-146.6
Evans	1992	023_5229	08/02/92 - 14/02/92	37.1
			14/02/92 - 17/02/92	-6.6
	1994	020_5553	25/01/94 - 28/01/94	-102.8
			28/01/94 - 31/01/94	-141.7
		023_5229	22/01/94 - 25/01/94	-17.6
			25/01/94 - 28/01/94	-150.0
		037_5265	23/01/94 - 26/01/94	24.0
			26/01/94 - 29/01/94	-51.6
	1996	206_5535	29/01/96 - 30/01/96	-143.1
			04/03/96 - 05/03/96	-177.1
		392_5553	11/02/96 - 12/02/96	-138.5
			14/03/96 - 15/03/96	-159.7

4.3 Ground Control

As discussed in section 3.8.4 in the previous chapter, accurate Ground Control Points (GCPs) are required to refine the interferometric baseline sufficiently to produce an accurate height map. In this study, ground control from both point sources and DEMs was used. Point data from three sources were considered: GPS stations, and satellite radar and lidar altimeter data. Each required different preprocessing before it could be used with Gamma routines to refine the baseline.

4.3.1 Global Positioning System (GPS) Data

Rutford Ice Stream GPS Data

In the 2004-2005 field season a network of seven GPS stations was maintained by the British Antarctic Survey's RABID (Rutford Area Base of Ice Drilling) project (figure 4.3) - five on the ice stream, one on the Fletcher Promontory and one in the Ellsworth Mountains; the location of the last was marked with a cairn for future use (Smith, 2006b). The station on the Fletcher Promontory was considered less accurate because of being on slowly moving ice and because of its long baseline to the rest of the network (Smith, 2006b). Data were obtained from T. Murray and G. Aðalgeirsdóttir (pers. comm., 2005), both of Swansea University (figure 4.3).

Using these GPS stations to refine the baseline was an interesting experiment at a time when not much other ground control data had been obtained. However, the limitations of this dataset were acknowledged from the outset. GCPs should be spaced throughout the frame, and Gamma Remote Sensing (2002) recommend using 20 control points at various altitudes: this dataset only had seven GCPs, five of which were very close together in altitude on the flat ice stream.

The ideal case with these data would be to use the Fletcher and Tolly's Heel stations with one of the ones on the ice stream, as a minimum of three control points are required for the program to run (although four control points are

required to refine the baseline and its rate of change accurately (Joughin *et al.*, 1996)); however, this combination of GPS stations did not all fall within the same frame for most of the scenes used in this study, with only frame 037_5301 containing all seven points.

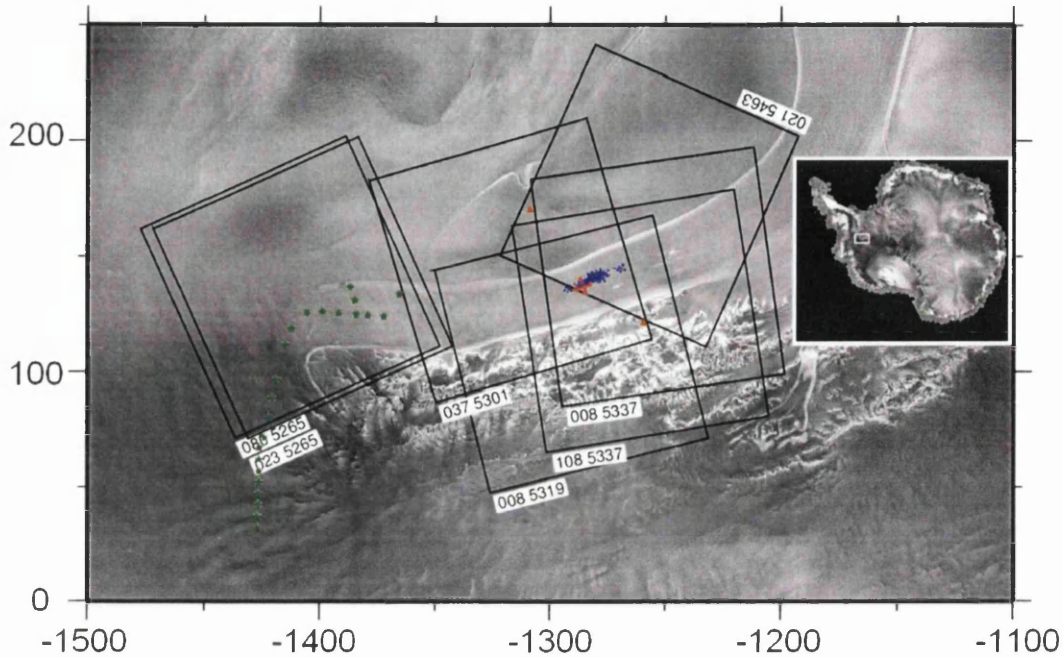


Figure 4.3: GPS stations on and around the Rutford Ice Stream. Red = RABID field party, 2004-2005 field season. Blue = H. Gudmundsson (H. Pritchard pers. comm., 2007) Green = A. Jenkins and E. King (H. Pritchard pers. comm., 2007). Coordinates are Polar Stereographic, in kilometres, with the origin at the South Pole.

Two more extensive sets of GPS data were also used. These came from Hamish Pritchard of BAS. One dataset covered the onset region and was collected by Adrian Jenkins and Ed King, and the other covered the main trunk upstream of the grounding line and was collected by Hilmar Gudmundsson. Figure 4.3 shows the distribution of these GCPs in relation to the SAR frames used in this study. Jenkins and King's data fall within frames 023_5265 during the ice phases and 080_5265 during the tandem phase, and Gudmundsson's data within all five of

the other frames used for the Rutford Ice Stream.

Evans Ice Stream GPS Data

GPS data of the Evans Ice Stream were obtained from Liz Morris of the Scott Polar Research Institute. These data came from the 1994-1995 BAS field season. Two points are located on the floating part of the Evans Ice Stream, and two at Haag Nunataks on Fowler Peninsula (figure 4.4).

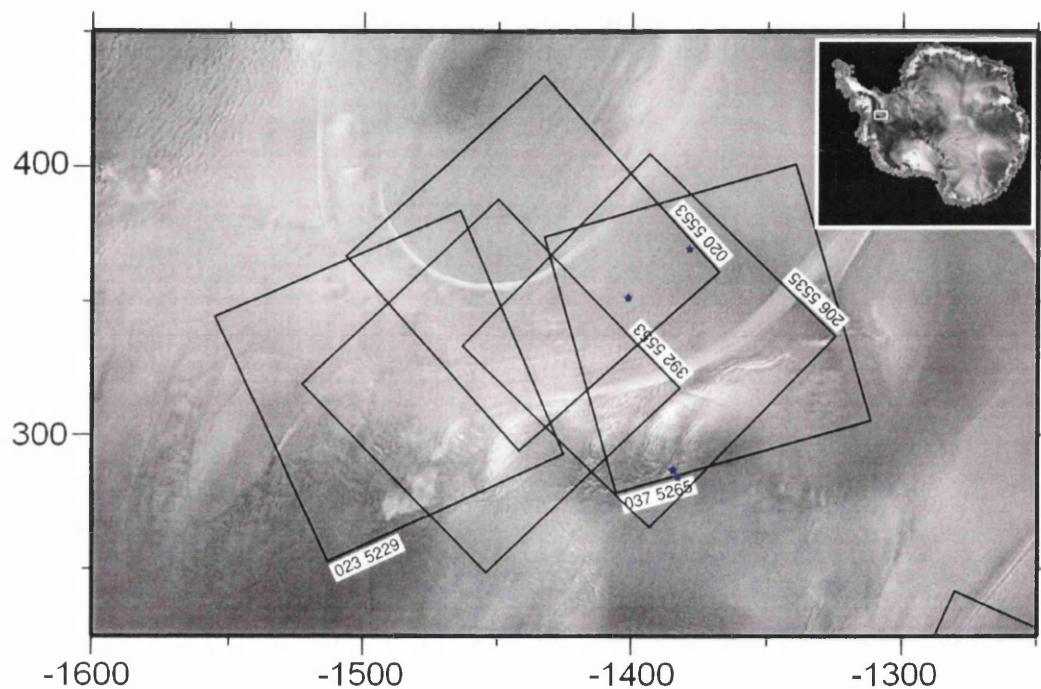


Figure 4.4: GPS stations in the Evans Ice Stream area in the 1994-1995 field season (E. Morris pers. comm., 2007). Coordinates are Polar Stereographic, in kilometres, with the origin at the South Pole.

Originally GPS stations were planned for the grounded part of the ice stream, but adverse conditions in the field prevented the field party getting to the intended sites. The two points on the ice shelf fall within frame 020_5553 during the ice

phases, and both these points and one at Haag Nunataks also fall within frame 037_5263. All four points fall within frame 206_5535 during the tandem phase.

4.3.2 Altimetry

Satellite altimetry uses the two-way travel time between the transmission and reception of an EM signal to calculate the range to the target on the ground, knowing that EM waves travel at the speed of light. Two sources of altimeter data were used in this study: radar altimeter data from the ERS satellites, and lidar altimeter data from ICESat. Altimeter data were obtained from Helen Fricker at the Scripps Institute of Oceanography. Satellite altimetry has the advantage that density increases at higher latitudes as orbital tracks converge, but the disadvantage that its accuracy is highly dependent on terrain slope angle, because the range of elevations within the altimeter's footprint increases the steeper the terrain surface.

ERS Altimetry

The Radar Altimeter (RA) aboard the ERS satellites is a Ku band (13.8 GHz) nadir-pointing sensor (European Space Agency, 2006b). Altimeter data was collected during the geodetic phase (phase E) and the shifted geodetic phase (phase F), which together lasted from 10 April 1994 to 21 March 1995. The satellite was placed in a 168-day orbit, which was then followed by a second 168-day orbit shifted by 8 km (European Space Agency, 2005). At a latitude of 70° this led to track spacing of 2 km. Along-track spacing of measurements was 335 m (Bamber and Bindschadler, 1997). Of the 184 tracks originally investigated for the FRIS area, 29 tracks covered the Rutford Ice Stream, and 27 tracks the Evans Ice Stream (figure 4.5). Data were obtained as .sav files, intended for use with Interactive Data Language (IDL), and converted to tab delimited text for use with Gamma.

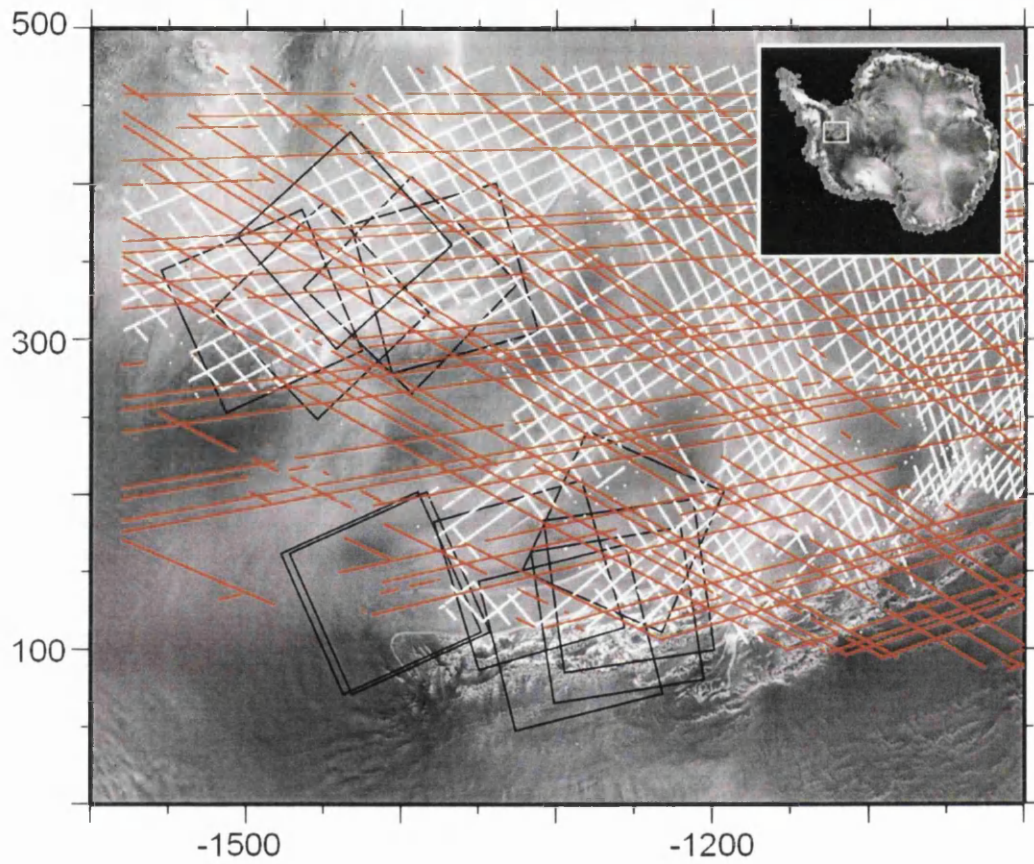


Figure 4.5: Altimetry data of the study area. Tracks of white points represent ERS tracks, and red points, ICESat. Coordinates are Polar Stereographic, in kilometres, with the origin at the South Pole.

ICESat Altimetry

ICESat (Ice, Cloud and land Elevation SATellite) is a lidar satellite launched in January 2003. The Geoscience Laser Altimeter System (GLAS) on board transmits 40 1064 nm pulses per second from an orbit 600 km in altitude. The centres of each 60 m spot illuminated on the ground fall 172 m apart (Schutz *et al.*, 2006; Zwally *et al.*, 2002). Along track resolution is therefore very good, but there can be gaps of tens of kilometres between tracks. Accuracy, based on orbital crossovers, is ± 14 cm, and precision 2.1 cm (Shuman *et al.*, 2006). As a lidar sensor, ICESat is hampered by the presence of cloud, especially affecting large parts of the study area which are prone to cloud much of the time, such as the Fletcher Promontory and the whole of the Evans Ice Stream. ICESat coverage of the study area is shown in figure 4.5.

4.3.3 Point Data Preprocessing

Control point data files must be in text format for use with Gamma, with four columns: control point number, range pixel, azimuth line, and elevation in metres. As with chapter 3, Gamma routines used are given in brackets. Preprocessing was done using gawk, and the stages are shown in a flowchart in figure 4.6.

The FRIS area was cut out of the altimeter datasets to make them a more manageable size, between a minimum of (-1600000, 0) at the bottom left, using Polar Stereographic coordinates, and a maximum of (-1000000, 450000) at the top right. These were the coordinates used for all subsetting of large datasets throughout this study.

Elevation values were dealt with first. As some of the GPS data were records from the same receivers at several points in time, several values of latitude, longitude and elevation were given for each receiver for the datasets of both Jenkins/King and Morris. In both cases, an average value of location and elevation was taken for each receiver. A 30 cm correction for the height of the GPS antennae bases was also applied to Jenkins and King's data.

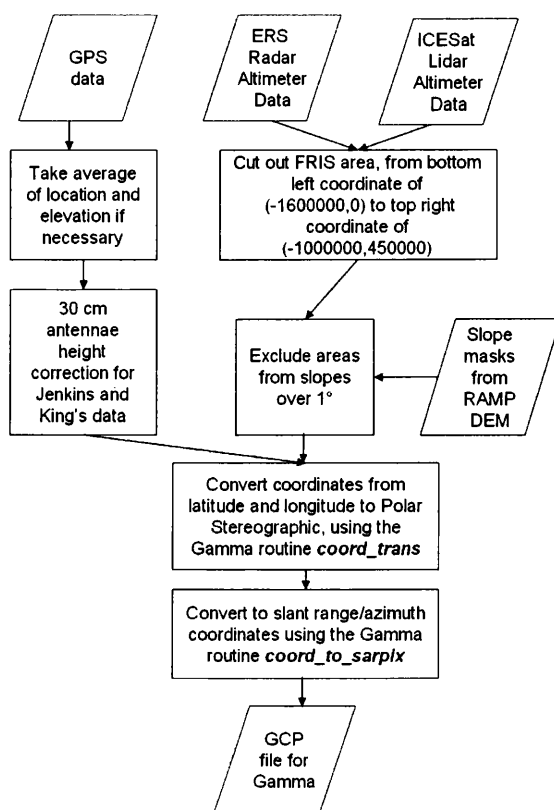


Figure 4.6: A flow chart to show the steps taken in preprocessing Ground Control Point data for use in interferometry.

Many elevation datasets for Antarctica are given relative to both the WGS84 ellipsoid and the OSU91A geoid. An ellipsoid is a simpler representation of the Earth's surface, which takes only an equatorial and polar radius, whereas a geoid is a more complex representation of what mean sea level would be if the oceans extended through locations that are currently land. Mean sea level in the Antarctic is actually 1.5 m below the geoid, because of currents in the Southern Ocean (Liu *et al.*, 1999). In the Antarctic, the geoidal undulation ranges from -67 to +42 m (Liu *et al.*, 1999). In this thesis, all elevation data were taken as WGS84 due to it being a standard used for map projections such as Polar Stereographic, and due to some datasets coming in WGS84 without the correction to OSU91A

available.

Elevations of ICESat points needed to be corrected from the OSU91A ellipsoid to the WGS84 geoid, the datum used in the rest of the study, but this was straightforward as the differences between the ellipsoid and geoid heights were given with the original data.

Altimeter data from steep areas of terrain were excluded. The effects of surface slope and irregularities on altimeter data over ice sheets are widely recognised (Ekholm, 1996): even a slope of 0.5° , for example, leads to a 30 m overestimation of height because the ERS altimeter measures the range to the closest part of the footprint and not the nadir. More seriously, major errors exist in altimeter data when the sensor loses lock over a slope, but is delayed in registering that lock has been lost, and continues recording elevation values (Bamber and Bindenschadler, 1997).

Altimeter data were cut out for areas with a slope of less than 1° . Slopes were calculated from the RAMP DEM in ArcGIS, using the D8 algorithm. However, derivatives from a DEM amplify its errors: the RMS error of the slope derived from the RAMP DEM, for example, is directly proportional to the RMS errors in elevation (Wilson and Gallant, 2000), discussed in section 4.3.4 below. ERS-1's altimeter has a beam width of 1.3° degrees, and although Ekholm (1996) felt that altimeter measurements may only be relied upon for slopes of up to half this angle, a threshold of 1° was chosen because it was felt that the RAMP DEM, used for calculating the slope, was not precise enough to be working in fractional degrees (see section 4.3.4), and noticeably more data were left to work with when using this slightly higher threshold. Shuman *et al.* (2006) found that, when analysing the accuracy of ICESat data using crossover analysis, the steepest category of slopes, greater than 1.25° , had standard deviations of over 25 cm and the fewest observations and, interestingly, they also noted differences between the residuals over grounded and floating ice. As surface elevations given by ICESat are the mean over the footprint area, they also become less representative with increasingly sloping terrain. Liu *et al.* (1999), for example, when compiling the RAMP DEM (section 4.3.4), only used altimeter data for slopes of less than 0.8° ,

or on slopes of up to 1° in the absence of any alternatives.

Coordinates of all the GPS and altimeter datasets were originally given in latitude and longitude, and were converted to Polar Stereographic using `coord_trans`. The Polar Stereographic coordinates were used to cut out control points for each frame, using the parameter files produced during geocoding (section 3.7) to calculate the extent of each frame from the coordinates of the top left, the resolution, and the number of rows and columns. Control point coordinates for each frame were converted to slant range/azimuth coordinates (`coord_to_sarpix`) before they could be used with Gamma.

DEM Creation

Initially, creating DEMs from the altimeter data, and sampling GCPs from them, was considered. DEM creation is a three stage process involving data collection, topological structuring, and model interpolation (Stocks and Heywood, 1994). Points were created from the original text files of the ERS and ICESat altimeter data in Mapinfo, and exported to ArcGIS as .e00 files. Different methods of interpolation were considered. Interpolation methods are selected on whether they are global or local; gradual or abrupt; exact or approximate; and deterministic or stochastic (Heywood *et al.*, 2002). Inverse Distance Weighted (IDW), a form of Spatially Moving Average (SMA) with spatial autocorrelation, was selected. This method is local, which is suitable for surfaces with large variation; gradual, which is suitable for continuous data; exact, which honours the datapoints and is suitable when points are considered sufficiently accurate; and deterministic, which does not introduce an element of randomness as a stochastic method would. The option of creating contour data prior to DEM creation was rejected because DEMs created from contours show an overrepresentation of the heights at which contours occur. This is more of a problem in flat areas such as on the ice streams than, for example, the Fletcher Promontory.

The idea of dividing the altimeter data in half, after areas with a slope greater than 1° were removed, and using half to create a DEM and half to validate it,

was considered. However, this was eventually rejected as the datasets would not be independent. Because of the spatial distribution of the source data, which are not evenly spaced across the scene, instead being in linear tracks with large gaps in between, the idea of creating a DEM was eventually rejected, as interpolated values far from the satellite tracks were too speculative. Although on the gently varying terrain of the ice stream this is less of a problem, and more varied terrain such as the Ellsworth Mountains were masked out due to its steepness anyway, it was decided to use only the altimeter data directly as control points for greater accuracy.

4.3.4 Digital Elevation Models

Digital Elevation Models have two uses in interferometry: they may either be used to simulate the topographic component of the phase, which is then removed in 2-pass differential interferometry (section 3.8.1), or they may be sampled for GCPs for use in refining the baseline (section 3.8.4). They can also be used for 3D visualisation of the study area. A number of DEMs are available for Antarctica. However, DEMs of Antarctica all suffer from a lack of input data and are therefore usually available at lower resolution than for other regions.

RAMP DEM

The RAMP DEM was compiled in a Geographical Information System (GIS) from many available data sources for use in processing with the RAMP mosaic of Jezek and the RAMP Product Team (2002). Data from the Antarctic Digital Database (ADD), satellite radar altimetry, airborne radar and maps from the United States Geological Survey (USGS) and Australian Antarctic Division (AAD), dating from the 1940s to 1990s, were combined into a DEM of the whole of Antarctica from 60 degrees south (Liu *et al.*, 1999; National Snow and Ice Data Center, 2001). Versions of the RAMP DEM were produced at resolutions of 200, 400 and 1000 m. However, it is important to note that the source data in some areas of the continent were far sparser than this (Liu *et al.*, 1999). In this study,

the 200 m resolution version of the DEM was used as it is the best resolution DEM available for the study area.

The Ellsworth Mountains were noted as a particularly problematic area during error assessment of the RAMP DEM, which Liu *et al.* (1999) carried out using local and global statistical analyses of the ARC/INFO coverages of the data. Contours from the ADD had positional offsets of 3 to 5 km compared to an orthorectified Landsat image and a RADARSAT image, probably due to inaccurate ground control and navigation at the time topographic maps of the area were produced in the 1960s. Liu *et al.* (1999) were able to correct the problem by warping the DEM using tie points.

The geolocational accuracy of the DEM is governed by that of the data, but is assumed to be better than the resolution (National Snow and Ice Data Center, 2001). The vertical accuracy of the RAMP DEM varies by terrain type, ranging from ± 1 m for ice shelves to ± 100 m in mountainous areas, with ± 7.5 m for gently sloping areas of interior ice sheet (Liu *et al.*, 1999; National Snow and Ice Data Center, 2001). Errors were assessed through global statistics, cross-validation of overlapping datasets, visual inspection, image simulation and spatial autocorrelation. Nowhere in interior Antarctica is the surface elevation of the ice or exposed rock at or below zero metres above sea level, although the bed elevation, of course, dips to many thousands of metres below sea level. The minimum value of the RAMP DEM data of -67 is due to the correction between the WGS84 ellipsoid and the OSU91A geoid, in which the minimum is 0 m, representing the coast.

BEDMAP DEM

It is worth noting here that the BEDMAP DEM uses an older version of the same data as the RAMP DEM, the Liu *et al.* (1999) data (Lythe *et al.*, 2001), but at far lower resolution, 5000 m. As such, there is nothing to be gained from further investigating the BEDMAP DEM as a source of ground control.

ERS DEM

A 5000 m resolution DEM was produced by Bamber and Bindschadler (1997) from ERS RA data acquired during the geodetic phase of ERS-1 as discussed in section 4.3.2. The DEM was acquired from the National Snow and Ice Data Center, and as heights were given in the OSU91A geoid, rather than the WGS84 ellipsoid, a correction, supplied with the data for each elevation value, was applied.

A number of artifacts exist in the DEM for the study area, which were not present in the test area used by Bamber and Bindschadler (1997) on the Siple Coast, and are discussed further in sections 5.3.2 and 7.3.6. Bamber and Bindschadler (1997) themselves highlighted the need to filter out anomalous height measurements, and found that after using 14 different tests they needed to remove 27% of the data which was in error because of loss of lock over surfaces of high relief. Similar issues were present in a 2 km resolution DEM of Greenland (Ekholm, 1996).

ICESat DEM

In early 2007, a 500 m resolution DEM created from ICESat data became available (DiMarzio *et al.*, 2007). This DEM was in a slightly different projection to usual, which seems unique to ICESat, with the latitude of true scale being -70° instead of the usual -71° used in Polar Stereographic projections of the Antarctic.

The ICESat DEM did not suffer from the artifacts of the ERS DEM, but did not capture the variability of the terrain as well. Vinson Massif, the highest mountain in Antarctica, is located in the Ellsworth Mountains and has a height of 4897 m (Swithinbank, 1988), but the highest point on the ICESat DEM for the Rutford/Evans cut out area is less than 3000 m.

4.3.5 DEM Preprocessing

Several stages of preprocessing were required for the DEMs before they could be used in interferometry, and the stages of this are shown in a flow chart in figure 4.7. The study area was cut out of each DEM for a rectangular area with a bottom left coordinate, in Polar Stereographic, of $(-1600000, 0)$ and a top right coordinate of $(-1000000, 450000)$. All DEMs were resampled to 50 m resolution (`dem_trans`) using bilinear interpolation, which was the same resolution used for any geocoded products from interferometry.

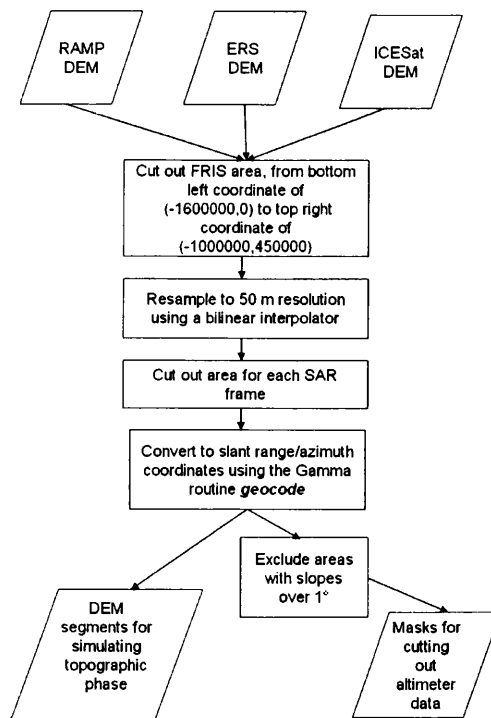


Figure 4.7: A flow chart to show the steps taken in preprocessing DEM data for use in interferometry.

DEMs were cut out for each frame for use in 2-pass differential interferometry (section 3.8.1) using the Polar Stereographic coordinates from the parameter files generated during geocoding. These cut out DEMs were then geocoded into slant range/azimuth coordinates (geocode) before the topographic phase could be simulated. Because sampling GCPs from DEMs may be problematic in steep areas due to layover, versions of the DEMs with slopes greater than 1° masked out were created in Arc, and these were used when extracting GCPs (section 3.8.4).

4.4 Balance Velocity Data

Velocities derived from InSAR will be compared to published balance velocities from Bamber *et al.* (2000c) and Wu and Jezek (2004), with the results presented in section 5.6 and discussed further in section 7.2.2. The balance velocity is the “depth averaged velocity required at any point to maintain the ice sheet in a state of balance, given a specified distribution of mass flux” (Bamber *et al.*, 2000c, p.1248). Depth-averaged velocities are usually 80-90% of the surface velocity (Paterson, 1994).

Balance velocities are calculated from ice thickness, surface slope and mean net surface mass balance and therefore an accurate calculation depends on accurate knowledge of all of these. Bamber *et al.* (2000c) used ice thicknesses taken from 1970s radar data, and a DEM from ERS RA (Bamber and Bindschadler, 1997) and terrestrial data, which they smoothed over 20 ice thicknesses to remove short wavelength undulations to calculate balance velocities using a 2D finite difference method. They state 25% errors in their balance velocities. Although they estimated a 20% error in their ice thickness grid, balance velocity calculations are more dependent on an accurate surface DEM, and the inaccuracy of the DEM on which the one used by Bamber *et al.* (2000c) to calculate balance velocities were based has been discussed in section 4.3.4, and is further highlighted in section 5.3.2. Inaccuracies in the input data therefore propagate into calculated balance velocities, and these must be treated with caution.

Wu and Jezek (2004) used the Ohio State University DEM of Antarctica, ice thickness data from BEDMAP, and flowlines digitised from satellite data in areas of low or complex slope where the ice is assumed to be in equilibrium. They compared their balance velocity model to observations such as InSAR velocities for selected outlet glaciers, and found good agreement. Errors in balance velocity increase downstream from the ice divide, from tens of metres per year on the interior ice sheet to hundreds at the outer ends of ice streams and outlet glaciers (Wu and Jezek, 2004).

In Greenland, Bamber *et al.* (2000b) and Bamber *et al.* (2000a) found that balance velocities became unreliable near the margins of ice streams because of errors in the ice thickness, slope and ablation rate, and in fact one ice stream was missed out entirely due to model limitations. Although Bamber *et al.* (2000c)'s bed elevations for Antarctic balance velocities were based on a 20 km resolution interpolated dataset, some of the measurements were actually more than 500 km apart (Lythe *et al.*, 2001). A comparison between balance velocities and observed velocities from GPS on Lambert Glacier, East Antarctica, showed both flowline and finite difference methods for estimating the balance velocities overestimated velocity compared to GPS, partly due to ice sheet sliding which causes the ratio between surface and depth-averaged velocities to be closer to 1. Balance velocities calculated using the finite difference method increased when the resolution of the input DEM was finer (Testut *et al.*, 2003). These limitations must be considered when comparing InSAR derived velocities to balance velocities.

The original Bamber *et al.* (2000c) data (J. Bamber pers. comm., 2005), were a 1121 by 1121 grid at 5000 m resolution. The Wu and Jezek (2004) data (X. Wu pers. comm., 2008) were a 574 by 494 grid at 10,000 m resolution. In this study, both datasets were imported into ArcGIS and the Bamber *et al.* (2000c) data were set to Antarctic Polar Stereographic projection, with a latitude of true scale at -71° , the projection used throughout the rest of this study and which the Wu and Jezek (2004) data were already in. The difference between the two balance velocity datasets was calculated. Geocoded interferograms and displacement maps were added to the GIS, and InSAR and balance velocities were compared for both ice streams and across the width of each ice stream at

its grounding line. The results are presented in section 5.6.

4.5 Tidal Model

Results from the first stage of interferometry, discussed in the next chapter, showed the need to model the tide at the grounding lines of the ice streams. Although “tides provide the major short-period signal that will be detected by satellite-based techniques such as SAR and laser altimetry”, the potential of SAR data cannot be fully explored while its accuracy is so much greater than that of tidal models (Padman *et al.*, 2002, p.252).

Gudmundsson (2006) highlights the need for caution in interpreting ice stream velocities from interferometry because of the variations in velocity caused by the spring-neap tidal cycle, which has a greater length than the usual time separation between interferometric pairs of satellite scenes (discussed in section 4.2). The tidal signal is usually separated in order to remove it from the overall signal. However, in this case it is more appropriate to separate the tidal signal in order to study it in its own right.

4.5.1 Tidal Modelling

Tidal forcing is modelled using classic harmonic analysis, separating the sinusoids of the different components from the overall broad, low-frequency power spectrum. Two tidal models were run in Matlab to calculate the tidal height at appropriate locations in the Rutford and Evans Ice Stream grounding zones, both for the periods covered by the SAR scenes, and at the exact time of acquisition of each individual scene, in order to calculate the difference in tidal height for each interferometric pair.

CATS02.01 Model

The Circum-Antarctic Tidal Simulation CATS02.01 model, a forward model with approximately 10 km resolution (1/4 degree by 1/12 degree), gives four diurnal components (O_1 , K_1 , P_1 and Q_1), four semidiurnal components (M_2 , S_2 , K_2 and N_2), and two longer period components, (M_f and M_m , which are approximately fortnightly and monthly respectively) (Padman *et al.*, 2002). These ten components were shown in table 2.2. Although the Circum-Antarctic Data Assimilation CADA10 model, developed by the same team, also assimilates satellite radar altimetry and tide gauge data, the models' developers consider the CATS02.01 model better because of the out-of-date coastline and bathymetry files used in CADA10 (Padman, 2005). The accuracy of the CATS02.01 model is considered good, with an error of 10 cm between the model and InSAR data of the shelf front of the Filchner-Ronne Ice Shelf (FRIS) (Padman *et al.*, 2002). In a study using GPS data from 15 Antarctic sites and observations from the Gravity Recovery and Climate Experiment (GRACE) satellite to validate numerous tidal models, it was generally found that models which focussed on specific regions agreed best with GPS data, but CATS02.01 (and CADA00.10) also performed well (King *et al.*, 2005).

For the Evans Ice Stream, these ten components were extracted for -76.75° latitude and -76.00° longitude (figure 4.8). As the Evans grounding zone is a complex shape (discussed further in section 7.4.2), the components were initially extracted for a grid of points spaced every 1/4 degree latitude and 1/2 degree longitude in the area, but this was found to make little difference, typically millimetres in amplitude and less than one degree in phase. It was not possible to extract the components for a coordinate closer to the published grounding lines shown in figure 7.5 due to the model's bathymetry grid, which meant that such points were not recognised as water and the model output null values (also discussed further in section 7.4.2). These ten components were then used in the `t_tide` model.

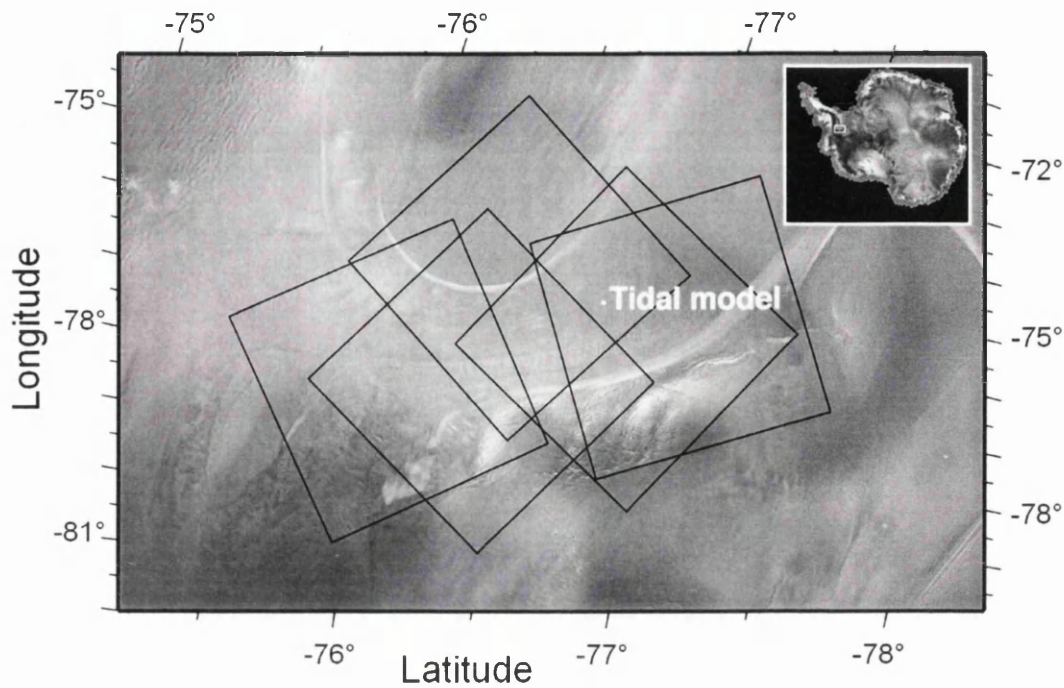


Figure 4.8: The location where the tidal model was run for the Evans Ice Stream. SAR frames are shown in black.

t_{tid} Model

The t_{tid} model uses the phase and amplitude of different tidal constituents (section 2.6.3) to calculate the tidal height for a given time and place. The t_{tid} model has been described as “classical harmonic analysis with nodal corrections” (Pawlowicz *et al.*, 2002, p.930) and works with 45 astronomical and 101 shallow water constituents. As the model works by calculating the signal from the middle of the input time series, the 1992, 1994 and 1996 runs were done with the time of acquisition of the images in the middle of the time over which the model ran.

For the pinning point of the the grounding line of the Rutford Ice Stream, the model in its simplest form worked with the four components which explained the majority of the tidal signal observed by tiltmeter and gravimeter data, as used by Smith (1991): O_1 , K_1 , M_2 and S_2 (table 2.2). Entering the latitude of the

predictions is important for nodal corrections which account for the 18.6-year variations in the Moon's orbit (Open University Course Team, 1999). Originally a latitude of -78.5° was used, the latitude of the pinning point at the grounding line (figure 4.9).

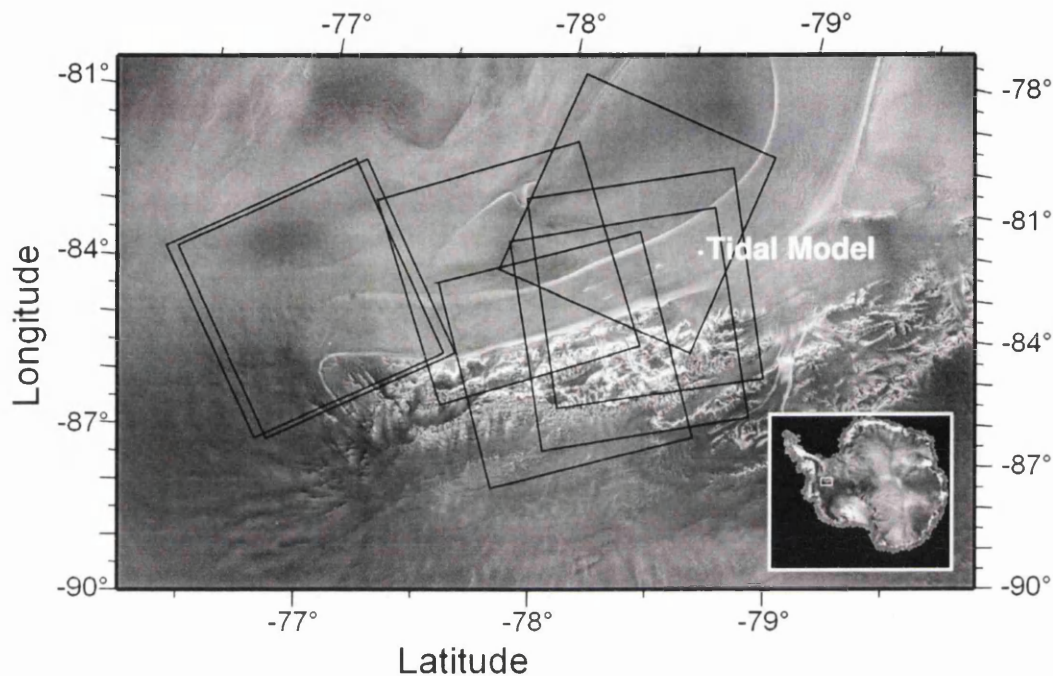


Figure 4.9: The location where the tidal model was run for the Rutford Ice Stream. SAR frames are shown in black.

Increasing the number of constituents increases the accuracy of the predictions, so a second run of the Rutford model was carried out including the eight principal semidiurnal and diurnal tidal components derived from data from GPS positioned at the grounding line (K. Makinson pers. comm., 2005, M. King pers. comm., 2005). The final, ten component model, additionally includes the M_f and M_m components from the CATS02.01 model at a latitude of -78.6472° and longitude of -82.6671° (M. King pers. comm., 2005) (figure 4.9). Using this latitude for the four component model, or the original latitude, -78.5° , for the eight and ten component models, made a difference of only millimetres in the tidal height

predictions.

Out of interest, all ten components for the Rutford Ice Stream were also extracted from CATS02.01 and run through `t_tide`, and the results compared to those using the GPS data. Discrepancies between the phases of tidal constituents extracted from CATS02.01 for this study and by M. King (pers. comm. 2005) were assumed to be because of the more recent version of the CATS02.01 model used in this study, which included bug fixes in nodal corrections and constituents interpolated near the coast. The amplitudes remained the same. In any case, the maximum difference in tidal height predictions between M_f and M_m from the old and new versions, when used with the 8 components from GPS, was only 1.5 cm.

For the Evans Ice Stream, all ten components from the CATS02.01 model were run through `t_tide` at the same latitude the CATS02.01 model was run, -76.75° . For the Rutford Ice Stream, the final tidal heights given were taken from the model using 8 components from GPS and M_f and M_m from the latest run of the CATS02.01 model, because of the perceived greater accuracy of the GPS data and more recent CATS02.01 model. The latitude for all Rutford model runs was taken as -78.6472° for consistency. The results of the tidal modelling are presented in section 6.3.

4.6 Elastic Beam Model

An elastic beam model from Vaughan (1995) was used to model the width of the hinge zones of both ice streams downstream of the grounding line. An elastic material such as the ice shelf at the hinge zone deforms when stress is applied, but returns to its original shape after the stress is removed, as long as the stress does not exceed the elastic limit of the material. For the Rutford Ice Stream grounding zone, Jenkins *et al.* (2006) found that strain was proportional to tidal elevation, and so assumed an elastic response was valid. The vertical displacement of the ice shelf from its mean position ($w(x)$) was modelled along an x axis perpendicular to and downstream of the grounding line, which, in the model, was clamped in

place at $x=0$. The beam was of uniform thickness. The hinge zone lies between the conditions where w , $\partial w/\partial x$ and $x = 0$ (at the grounding line) and $w = A_0(t)$ (figure 4.10). It is given by the following equation (Vaughan, 1995):

$$w = A_0(t)[1 - e^{-\beta x}(\cos\beta x + \sin\beta x)] \quad (4.1)$$

$A_0(t)$ is instantaneous sea level, i.e. the deviation from mean sea level, at a given time, and is half the tidal range (Smith, 1991). It would be the height of the ice shelf surface were it floating in hydrostatic equilibrium. The spatial wavenumber β is given by the following equation (Vaughan, 1995):

$$\beta^4 = 3 \rho_{sea} g \frac{1 - \nu^2}{Eh^3} \quad (4.2)$$

where ρ_{sea} is the sea water density, g is the gravitational acceleration, E is the elastic (Young's) modulus, ν is Poisson's ratio and h the ice shelf thickness. β has a non-linear dependence on h , because changing the ice thickness changes the rigidity of the beam, but is relatively insensitive to E and ν (Reeh *et al.*, 2003; Vaughan, 1995). Various values of E and ν were taken from the literature. ρ_{sea} was taken as 1030 kg m^{-3} (Smith, 1991).

E is the ratio of stress to strain, the tensile stress divided by tensile strain in Nm^{-2} (or Pascals, Pa). Runs of the model were done with several values of E : 1.1 GPa, as used by Smith (1991); 0.88 GPa, derived empirically by Vaughan (1995) from analysis of tiltmeter data for several sites in Antarctica including the grounding line and shear margins of Rutford; and 9 GPa, as used by Stephenson (1984), similar to laboratory derived values of E of 9.3 GPa (Reeh *et al.*, 2003), although Stephenson (1984) had to use an ice thickness about half the real value with this value of E , and these were the data that were revisited by Smith (1991).

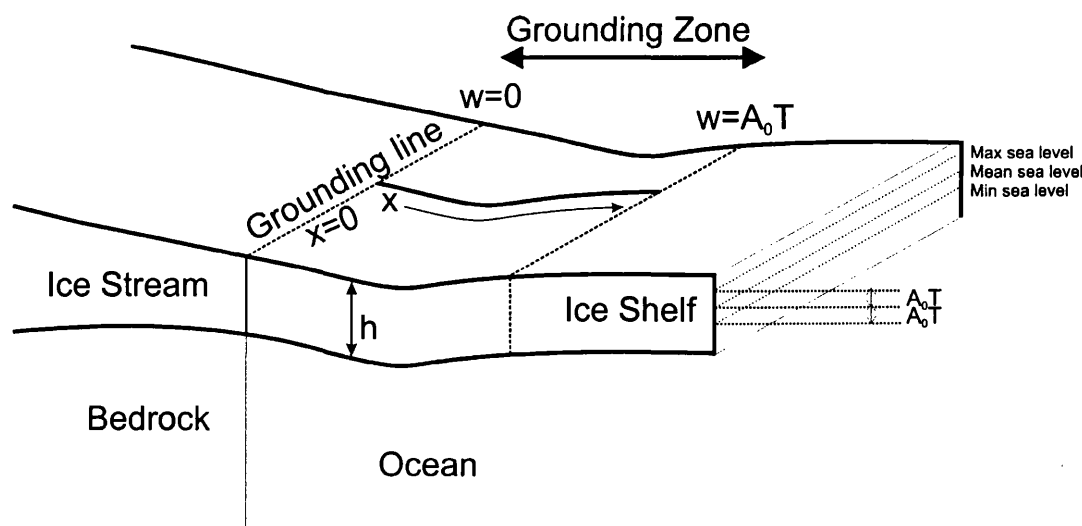


Figure 4.10: Schematic representation of the elastic beam model, adapted from Smith (1991) and Vaughan (1995).

v is transverse contraction strain divided by longitudinal extension strain in the direction of the stretching force, and is a measure of how much a material which is being stretched in one dimension contracts in the other two dimensions. Values of v of 0.3 (Smith, 1991; Stephenson, 1984; Vaughan, 1995) and 0.5 (Jenkins *et al.*, 2006) were used. 0.3 is the usual value of v given for ice, but Jenkins *et al.* (2006) found a value of v of close to 0.5 fitted their measured horizontal and vertical strains. Interestingly, 0.5 is the maximum theoretical value of v for a stable material, in order to maintain positive values of the shear modulus and bulk modulus of the material, and assumes the material, in this case the ice shelf, is incompressible.

Other input parameters were specific to the study sites and were selected following the mapping of the grounding zones of both ice streams, which is presented in section 6.2 and the completion of the tidal models, which are presented in section 6.3. The ice thickness h was taken from BEDMAP (Lythe *et al.*, 2001): 1648 m for Rutford, at the pinning point (figure 6.1); 1929 m for Rutford at the upstream extent of the hinge zone as mapped from interferometry on the east side of the ice stream (figure 6.1); 1955 m for Rutford at the upstream extent of the hinge

zone as mapped from interferometry on the west side of the ice stream (figure 6.1); 1017 m for Evans at the location the CATS02.01 model was run (figure 6.3); and 1913 m for Evans at the hinge zone as mapped from the interferograms, much further upstream (figure 6.3). Values of $A_0(t)$ came from the results of the t_tide model and were taken as half the typical maximum tidal amplitude at both spring and neap tides for the study period: 3.2 m and 0.75 m respectively for the Rutford Ice Stream, and 2.35 m and 0.62 m for Evans. The model was run in Matlab and the hinge zone width calculated to the nearest 100 m. The results of the different runs of the model, with different values of h , v , E and $A_0(t)$, are presented in section 6.4 and discussed further in section 7.6.

4.7 Summary

SAR images of the Rutford and Evans Ice Streams are available with suitable spatial coverage and temporal baselines to carry out differential interferometry of these areas. Although there are GCPs and DEMs available for the study area, they have issues with resolution, coverage and accuracy, the effects of which are seen in the next chapter and discussed in chapter 7, along with results from tidal and elastic beam modelling of the ice streams presented in chapter 6.

Chapter 5

Ice Stream Displacements

5.1 Introduction

Differential interferometry was carried out for the Rutford and Evans Ice Streams. This chapter presents interferogram mosaics of these ice streams, showing their main features in terms of topographic and displacement phase. Topography interferograms from double differencing and simulated from DEMs are presented. The effects of topography were removed from the single difference interferograms presented in the mosaics to give ice displacements in the horizontal plane corresponding to the look vector, and vertical displacements, which may be projected into the flow direction. Ice velocities for both ice streams are presented, used to estimate the discharge of both ice streams through the study period, and compared to published balance velocities.

5.2 Interferogram Mosaics

Interferograms were produced using the methods described in section 3.5, and mosaicked together for the Rutford and Evans Ice Stream areas for each time period. This showed the main features of both study areas in terms of topographic

and displacement phase.

Frames of the Rutford Ice Stream correspond to those in figure 4.1 and tables 4.1 and 4.3. Frames of the Evans Ice Stream correspond to those in figure 4.2 and tables 4.2 and 4.3. In all cases, coordinates are Polar Stereographic, in kilometres, with the origin of at the South Pole. Complete cycles of colour, or fringes, were discussed in section 3.5.7, and each represent one complete phase cycle of difference between the two images making up the interferogram, from 0 to 2π radians. In the flattened single difference interferograms presented throughout section 5.2, fringes are the result of both scene topography (ϕ_{topo} , section 3.5.7) and line-of-sight (LOS) displacement (ϕ_{trans} , section 3.5.7), which means that a higher fringe rate, i.e. more closely spaced fringes, results from either steeper topography or greater ice motion.

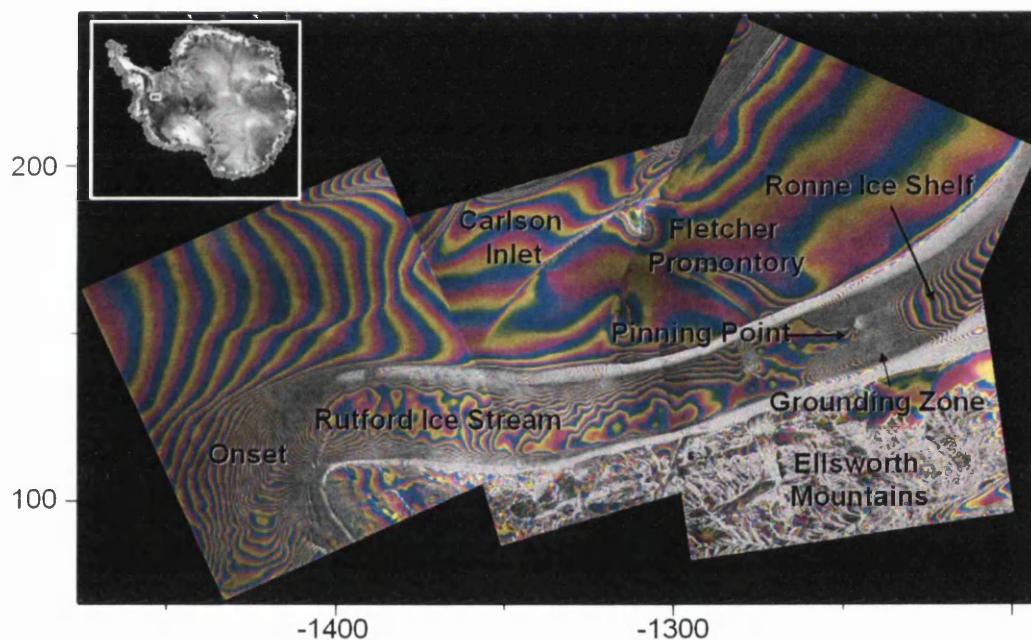


Figure 5.1: Interferogram mosaic of the Rutford Ice Stream for frames 023_5265, 037_5301, 008_5337 and 021_5463 for 1994, showing the main features of the study area. Coordinates are Polar Stereographic, in kilometres, with the origin at the South Pole.

Figure 5.1 shows the main features of the Rutford Ice Stream area. Interferograms of the Rutford Ice Stream showed closely spaced fringes in the Ellsworth Mountains, which are due to the steep topography, and topographic fringes on the Fletcher Promontory, which rises to elevations several hundred metres higher than those of the ice stream. The ice stream itself exhibits fringes due to both topography and displacement. The line-of-sight direction is almost exactly upstream for descending frames of the grounding zone and main trunk, at an approximately 45° angle upstream for frame 021_5463, and varies from directly upstream to completely perpendicular to the flow direction for the most upstream frames, 023_5265 and 080_5265, due to the 90° bend in the flow direction of the ice stream as it rounds the Ellsworth Mountains. However, the most striking feature of the interferograms of the Rutford Ice Stream was its clearly defined grounding zone, the high fringe rate being due to vertical displacement of the ice between the time of acquisition of the first and second SAR scenes making up each interferometric pair as shown in sections 5.4 and 6.3.3. Figures 5.2 to 5.6 show mosaics of interferograms of Rutford for each study period. The two 1996 mosaics from the tandem period exhibit greater sensitivity to topography because of longer perpendicular baselines and therefore lower altitudes of ambiguity (section 3.5.8; table 4.3). This is particularly evident for frame 080_5265, the most upstream frame in the 1996 study period, compared to frame 023_5265, the most upstream frame in the 1992 and 1994 study periods (figure 4.1). The gap in the 1996 mosaic occurs because two frames of the upstream section of the ice stream that would not have left gaps were unsuitable because of data quality issues as discussed in section 4.2, and frame 080_5265 was the third choice.

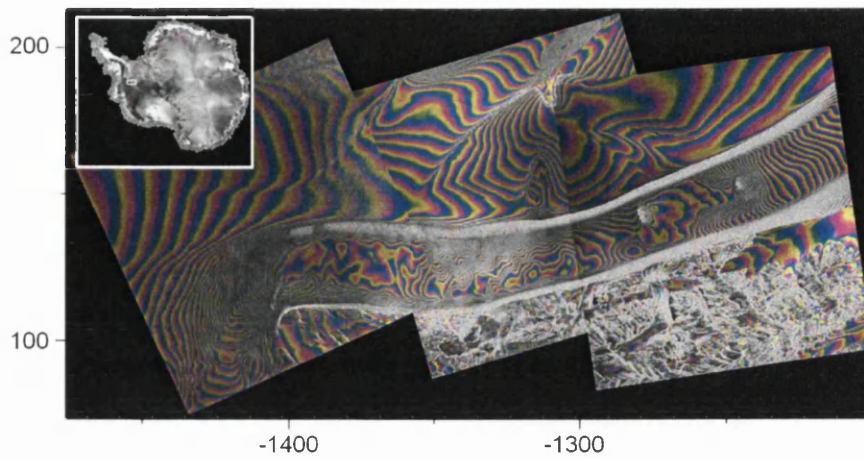


Figure 5.2: Interferogram mosaic of the Rutford Ice Stream for frames 023_5265, 037_5301, and 008_5337 for 1992. Coordinates are Polar Stereographic, in kilometres, with the origin at the South Pole.

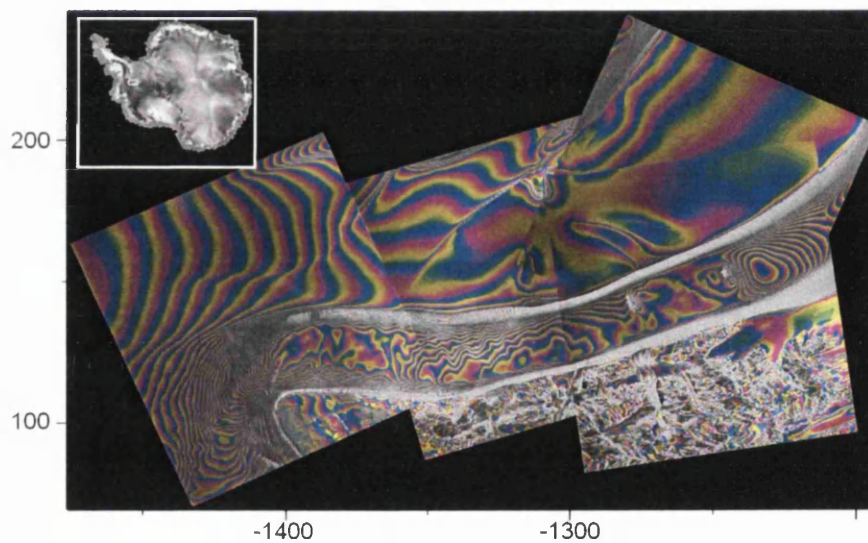


Figure 5.3: Interferogram mosaic of the Rutford Ice Stream for frames 023_5265, 037_5301, and 008_5337 for 1994 using the first pair from frame 008_5337. Coordinates are Polar Stereographic, in kilometres, with the origin at the South Pole.

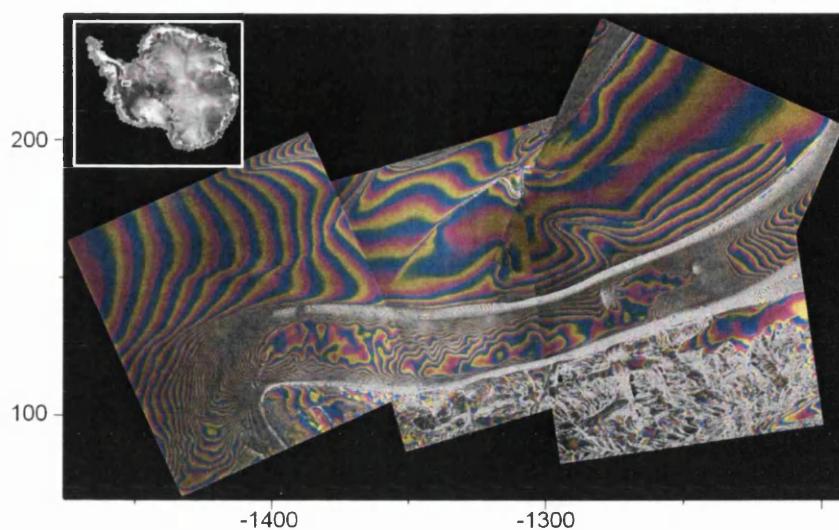


Figure 5.4: Interferogram mosaic of the Rutford Ice Stream for frames 023_5265, 037_5301, and 008_5337 for 1994 using the second pair from frame 008_5337. Coordinates are Polar Stereographic, in kilometres, with the origin at the South Pole.

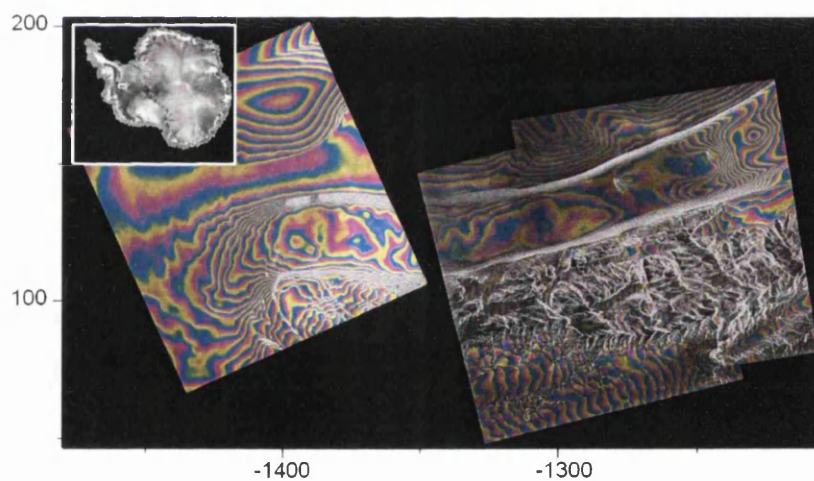


Figure 5.5: Interferogram mosaic of the Rutford Ice Stream for frames 080_5265, 008_5319 and 108_5337 for 1996 using the first tandem pairs of each frame. Coordinates are Polar Stereographic, in kilometres, with the origin at the South Pole.

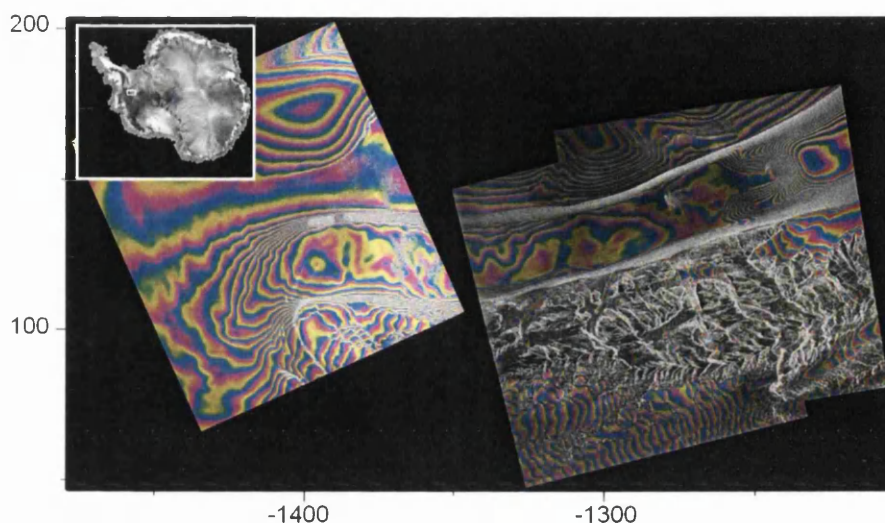


Figure 5.6: Interferogram mosaic of the Rutford Ice Stream for frames 080_5265, 008_5319 and 108_5337 for 1996 using the second tandem pairs of each frame. Coordinates are Polar Stereographic, in kilometres, with the origin at the South Pole.

Figure 5.7 shows the main features of the Evans Ice Stream area. Topographic fringes on the Fowler Peninsula and Cape Zumberge were clearly visible, as was the regular pattern of fringes displayed on the Ronne Ice Shelf in the extensive floating area downstream. Fringes on the Evans Ice Stream itself were more difficult to interpret. Complex patterns of displacement were observed because of the convergence in flow from the five tributaries (the eastern group having already begun to converge outside the extent of the SAR frames used in this study). The effects of this on interferograms are especially apparent in figure 5.8, where the lefthand example has twice the temporal baseline of the righthand example, and as such has twice as many fringes due to displacement. There was, however, a clearly visible grounding zone (see especially figure 5.9). Mapping the grounding zones of both ice streams from interferometry is discussed further in section 6.2.

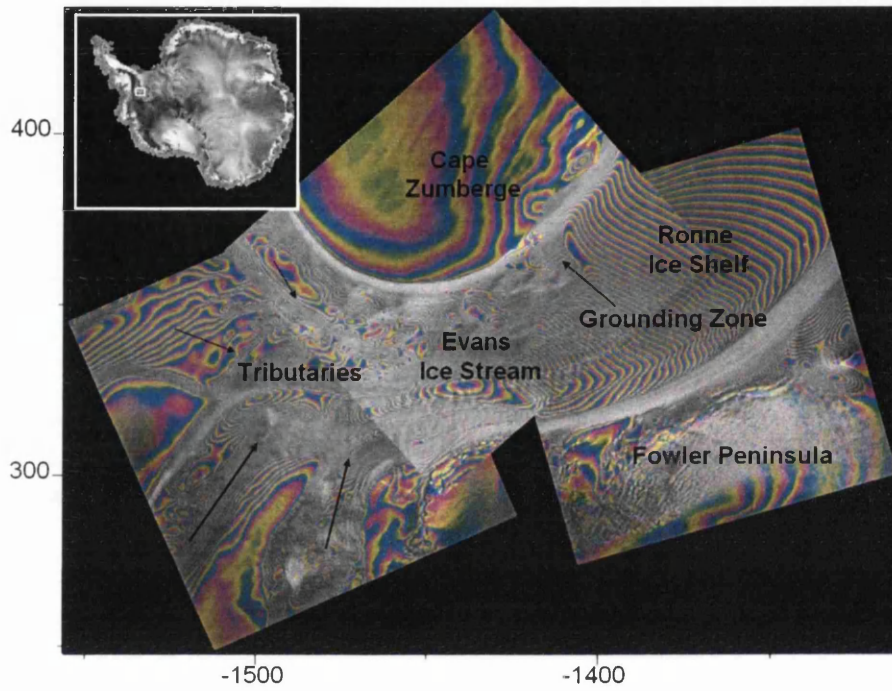


Figure 5.7: Interferogram mosaic of the Evans Ice Stream for frames 023_5229, 020_5553 and 037_5265 for 1994 using the pairs with the shortest baselines (table 4.3), showing the main features of the study area. Coordinates are Polar Stereographic, in kilometres, with the origin at the South Pole.

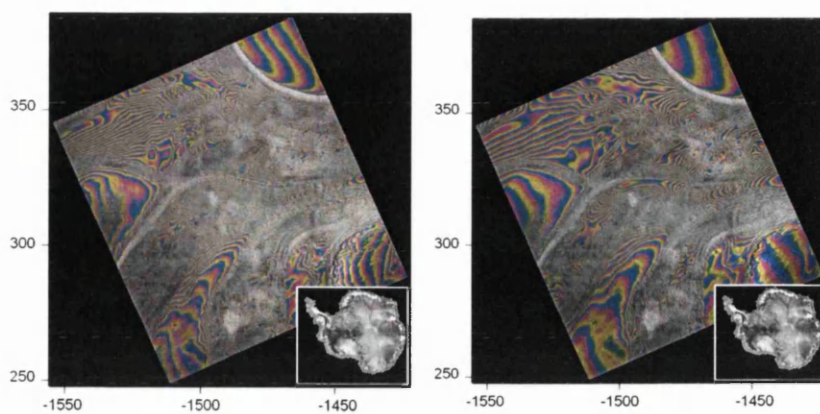


Figure 5.8: Interferograms of frame 023_5229 for the Evans Ice Stream, the only frame for 1992. On the left, the first, 6-day pair, and on the right, the second, 3-day pair. Coordinates are Polar Stereographic, in kilometres, with the origin at the South Pole.

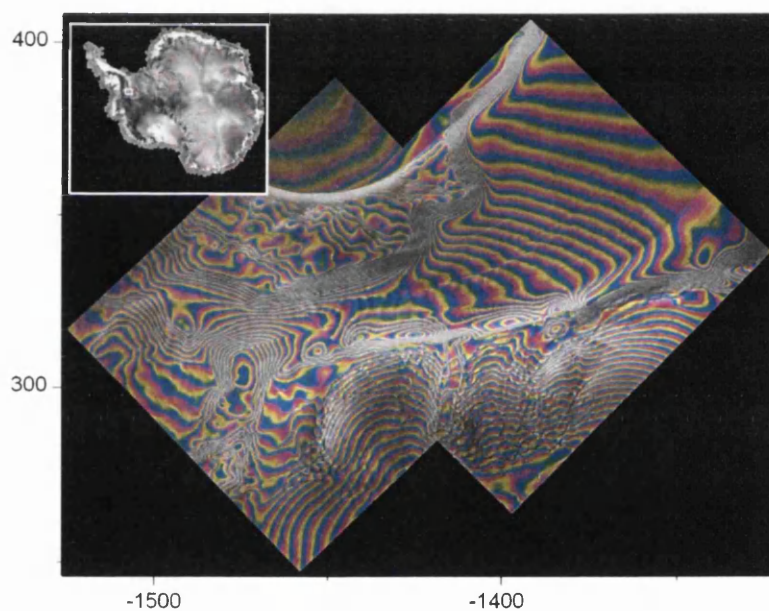


Figure 5.9: Interferogram mosaic of the Evans Ice Stream for frames 392_5553 and 206_5535 for 1996 using the pairs with the shortest baselines (table 4.3). Coordinates are Polar Stereographic, in kilometres, with the origin at the South Pole.

5.3 DEM Creation

Following the creation of single difference interferograms as presented above, the next stage in the derivation of ice stream velocities is to combine these interferograms into double difference, topography-only interferograms (section 3.8), although not all SAR frames had scenes in suitable combinations for this procedure (see tables 4.1, 4.2 and 4.3). Of those that did, creating a topography-only interferogram was only successful for one frame: 080_5265, the most upstream frame of Rutford in 1996, for which a tandem quad had been obtained (section 4.2). The reasons for this are discussed in section 7.3.4.

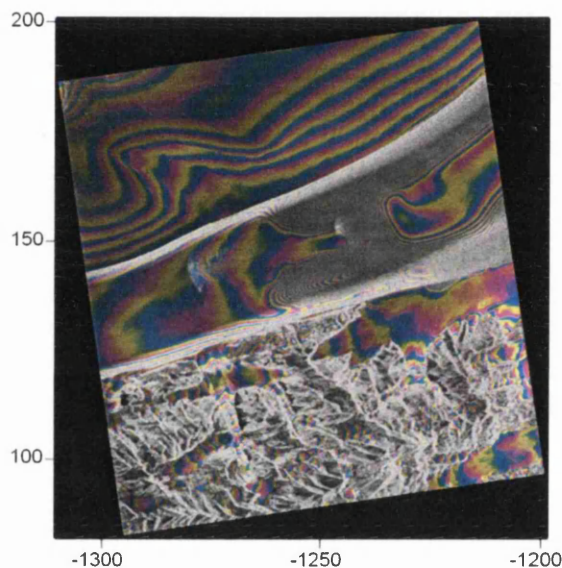


Figure 5.10: A “topography-only” interferogram for the 1994 triplet of frame 008_5337 of the Rutford Ice Stream derived using methods as described in section 3.8, clearly showing non-topographic fringes in the grounding zone. The combined baseline is 110 m and the combined altitude of ambiguity 86 m. Coordinates are Polar Stereographic, in kilometres, with the origin at the South Pole.

Figures 5.10 and 5.11 show typical examples of attempts to produce topography-only interferograms for the Rutford and Evans Ice Streams respectively. It is clear that displacement fringes are present in the grounding zones of both ice streams.

For Rutford, only the most upstream frames for each study period were free from this effect: 023_5265 in 1992 and 1994, for which combinations of scenes suitable for double differencing were not available in this study, and 080_5265 in 1996. In the case of the Evans Ice Stream, all frames were affected, even frame 023_5229 which was the furthest upstream. This meant that further processing with these double difference interferograms was not possible, as the next stages rely on these interferograms containing only topographic phase. This is also discussed further in section 7.3.4. The topography-only interferogram of frame 080_5265 is shown in figure 5.12.

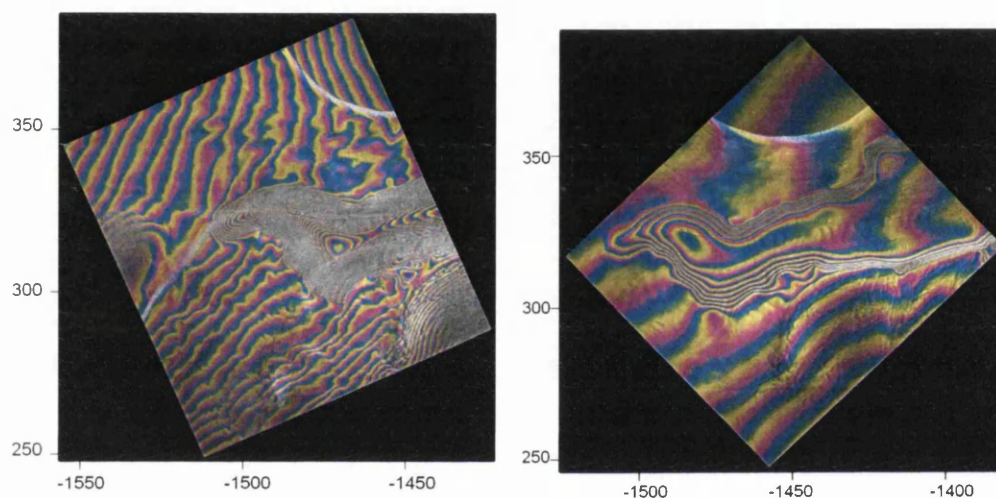


Figure 5.11: “Topography-only” interferograms for the 1994 triplet of frame 023_5229 (left) and the 1996 tandem quad of frame 392_5553 (right) of the Evans Ice Stream derived using methods as described in section 3.8, clearly showing non-topographic fringes in the grounding zone. For frame 392_5553 the combined baseline is 21.2 m and the combined altitude of ambiguity 444 m. Frame 023_5229 could not be adequately flattened (section 3.5.8 and section 7.3.4) but was included to show that even the most upstream frame of the Evans Ice Stream was affected. Coordinates are Polar Stereographic, in kilometres, with the origin at the South Pole.

5.3.1 Ground Control

The baseline of an unwrapped topography-only interferogram must be refined using GCPs before a height map can be produced (section 3.8.4). Frame 080_5265 was covered by three point datasets with the potential to be used for ground control: GPS points; ERS radar altimetry; and ICESat lidar altimetry, as shown in figures 4.3 and 4.5. All of these datasets and sampling of control points from all three DEMs (section 4.3.4) was experimented with. The quality of the baseline refinement is assessed through the Root Mean Square Error (RMSE) of the fit between the simulated and actual phase of the GCPs, which is shown for the point datasets in table 5.1. However, the quality of the baseline refinement was also assessed by examining the simulated height maps and how closely they matched the topography-only interferogram, and examining the combined baseline file for the quad, as the initial and precision baselines should be close. The control point dataset that performed the best all round in refining the baseline was created by combining all 3 GCP datasets. Figure 5.12 shows the topography-only interferogram for frame 080_5265, along with the height map produced. This is discussed further in section 7.3.6.

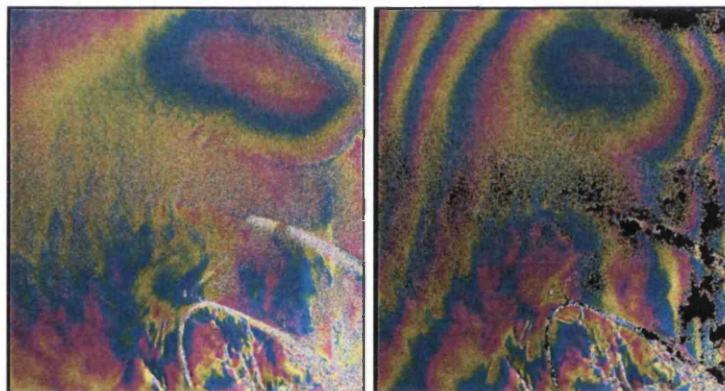


Figure 5.12: Topography-only interferogram for frame 080_5265 of the Rutford Ice Stream, with an altitude of ambiguity of 190 m, and a height map simulated after the baseline was refined with GCPs (section 3.8.4), displayed with 190 m per colour cycle. Frame location is shown in figure 4.1.

Table 5.1: RMS errors of control points used to refine the baseline of the topography-only interferogram of frame 080_5265.

Dataset	No. of points	No. of points with unwrapped phase	RMSE (m)
GPS (section 4.3.1)	15	13	14.892
ERS Radar Altimeter(section 4.3.2)	93	82	129.362
ICESat Lidar Altimeter (section 4.3.2)	1709	578	135.033
GPS and ERS	107	96	131.125
GPS, ERS and ICESat	1816	675	190.301

5.3.2 Simulation of Topographic Phase from DEMs

Other frames were examined using 2-pass differential interferometry, either because they had only had pairs of scenes, rather than triplets or quads, or more usually because of the effects seen earlier in this section. DEMs geocoded into slant-range/azimuth geometry (section 4.3.5) were used to simulate the topographic phase (ϕ_{topo} , section 3.5.7) for each frame which can be subtracted from single difference interferograms in the same way as that simulated from a height map produced from a double difference, topography-only, interferogram (see section 3.8), in order to leave only line-of-sight displacement.

Three DEMs were considered for the simulation of topographic phase. The RAMP DEM (section 4.3.4) was the highest resolution DEM available but was quickly ruled out due to issues of accuracy, as discussed further in section 7.3.5. The Bamber and Bindschadler (1997) ERS DEM (section 4.3.4) was the only other DEM that had been obtained at the time. Figure 5.13 shows the topographic phase for frame 008_5319 simulated from this DEM, flattened using the baseline of the velocity pair, i.e. the pair with the shorter baseline. Note that the flattened topographic phase is not used in the processing chain, but the simulated topographic phase was flattened for visualisation and ease of interpretation. It is clear that the Bamber and Bindschadler (1997) DEM was hindered by its low resolution. The topographic variation in the Ellsworth Mountains has clearly not been captured, as shown by the straight lines of the fringes in this area, running

mainly from left to right. The low resolution also means that the edges of the ice stream are located only to the edge of the nearest 5 km resolution cell, rather than in their correct locations. This DEM is also hindered by artifacts such as that in the centre at the top, which shows a very high fringe rate in a square pattern which would represent an unrealistically high change in elevation in a shape unlikely to occur naturally. Other similar artifacts were found in other frames of the study area. This DEM was not a good option for simulating topographic phase.

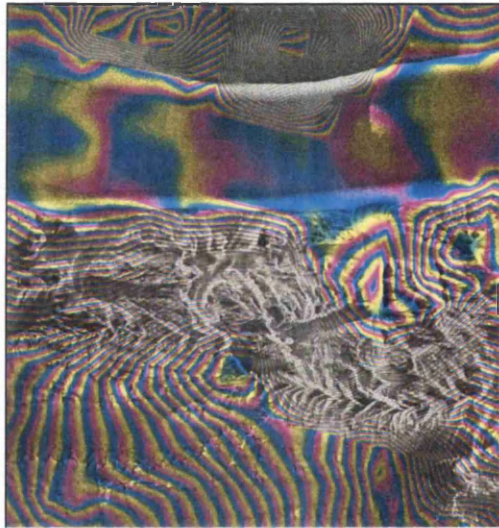


Figure 5.13: Simulated topographic phase using the ERS DEM, flattened using the velocity pair baseline, for frame 008_5319, the location of which is shown in figure 4.1.

The ICESat DEM (section 4.3.4) became available partway through this study, and was also used to simulate topographic phase. Figure 5.14 shows an example of the flattened topographic phase simulated from the ICESat DEM for frame 108_5337. This DEM proved more effective: for example, the topography of the Fletcher Promontory to the top of the image has been represented well, and compares to that shown in actual interferograms of the same area such the bottom right frame of figure 5.4.

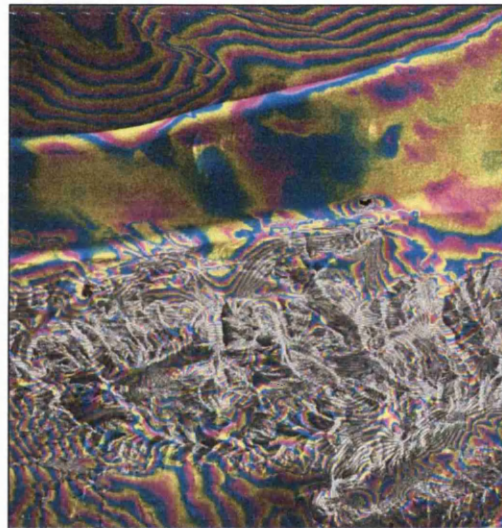


Figure 5.14: Simulated topographic phase using the ICESat DEM, flattened using the velocity pair baseline, for frame 108_5337, the location of which is shown in figure 4.1.

5.4 Displacements

Displacement maps were created as described in section 3.8.8, the topographic phase having been either simulated from the height map created from double differencing for frame 080_5265, or from the slant range/azimuth geocoded DEMs, for other frames, and removed from the filtered single difference interferograms.

5.4.1 Rutford Ice Stream

The onset region of the Rutford Ice Stream was the only part of the study area for which a displacement map could be produced from double differencing. Figure 5.15 shows displacement maps in the horizontal plane corresponding to the look vector for 1992, 1994 and 1996. Look directions and locations of all frames of the Rutford Ice Stream were shown in figure 4.1.

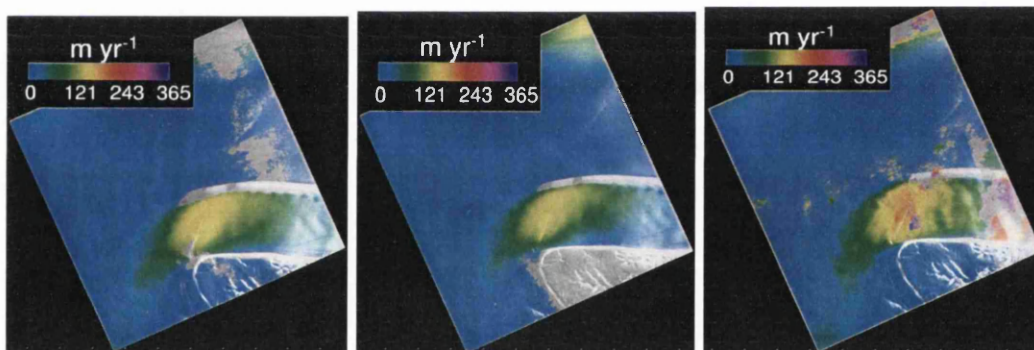


Figure 5.15: Displacement maps in the horizontal plane beneath the look vector for the onset region of the Rutford Ice Stream for frame 023_5265 in 1992 (left) and 1994 (centre) and frame 080_5265 in 1996 (right). Locations and look directions of all frames of the Rutford Ice Stream are shown in figure 4.1

Displaying the displacement maps projected into the flow direction proved ineffective as their patchiness made them difficult to interpret (section 7.3.8). However, the pixel values of the data were interrogated manually and their histograms

examined. The maximum displacement in the flow direction for each of these frames, and its equivalent in metres per year, is shown below in table 5.2. Figure 5.15 and table 5.2 suggest there has not been a significant trend in downslope velocity in this area over the study period, but velocity may have decreased in 1994 and recovered to its 1992 level by 1996.

Table 5.2: Downslope velocities for the onset region of the Rutford Ice Stream from 1992 to 1996.

Year	Frame	Maximum displacement (m)	Temporal baseline (days)	Downslope Velocity (m a^{-1})
1992	023_5265	1.53	3	186
1994	023_5265	1.33	3	162
1996	080_5265	0.52	1	190

The middle section of the ice stream proved much more difficult to derive velocities for. Possible reasons for this are discussed in section 7.3.8. Figure 5.16 shows the displacement map in the horizontal for frame 008_5319 on 15th and 16th January 1996. In this case the look direction was directly parallel to the flow direction. Displacements on the ice stream appear to be typically 1.35 m day^{-1} which equates to 475 m a^{-1} . However, the Fletcher Promontory would appear to be moving at a consistent speed of approximately 0.5 m day^{-1} . Clearly, this is not the case in reality, and this is most likely a function of inaccuracies in the DEM, meaning that an incorrect amount of topographic phase has been removed. It would be more sensible to assume the real horizontal ice stream velocity is the difference between this false velocity of the Fletcher Promontory and the velocity derived for the ice stream, and therefore about 310 m a^{-1} . This shows an increase in velocity compared to the onset, which is what should be expected. Velocity consistently increases downstream across the frame, which is also what would be expected. The edge of the grounding zone is visible at the righthand side of the frame. This appears as an increase in velocity compared to the rest of the ice stream because the tide was higher when the second image was acquired, meaning the ice surface had risen and moved closer to the sensor. The results of tidal modelling of the ice streams are shown in section 6.3 and the effects

of changing tidal heights on interferometric representations of ice velocity are discussed further in section 7.5.1.

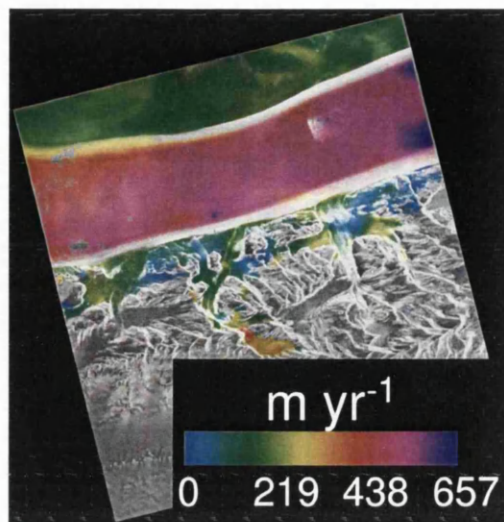


Figure 5.16: Displacement in the horizontal plane beneath the look vector for frame 008_5319 for 15th and 16th January 1996. Locations and look directions of all frames of the Rutford Ice Stream are shown in figure 4.1.

Displacement maps of the grounding zone region proved much more complex, as they contained the effects of both ice velocity and vertical ice stream motion due to the tide, which is investigated further in the next chapter. Figure 5.17 shows both horizontal and vertical displacement maps for the grounding zone of the Rutford Ice Stream based on the same interferogram, that from frame 008_5337 on 24th and 27th January 1994. Horizontal velocities increased towards the grounding zone, from approximately 380 m a^{-1} at the upstream extent of the frame to over 400 m a^{-1} at the grounding zone. Displacements projected to the flow direction also reached a maximum of over 400 m a^{-1} for both the 1992 and 1994 frames in this location. This shows an increase in velocity compared to the middle section, which would again be expected.

However, downstream of the grounding zone it would appear that the ice stream has negative horizontal velocity, i.e. is moving backwards. This effect occurs because the ice surface at the righthand side of the frame has moved downward

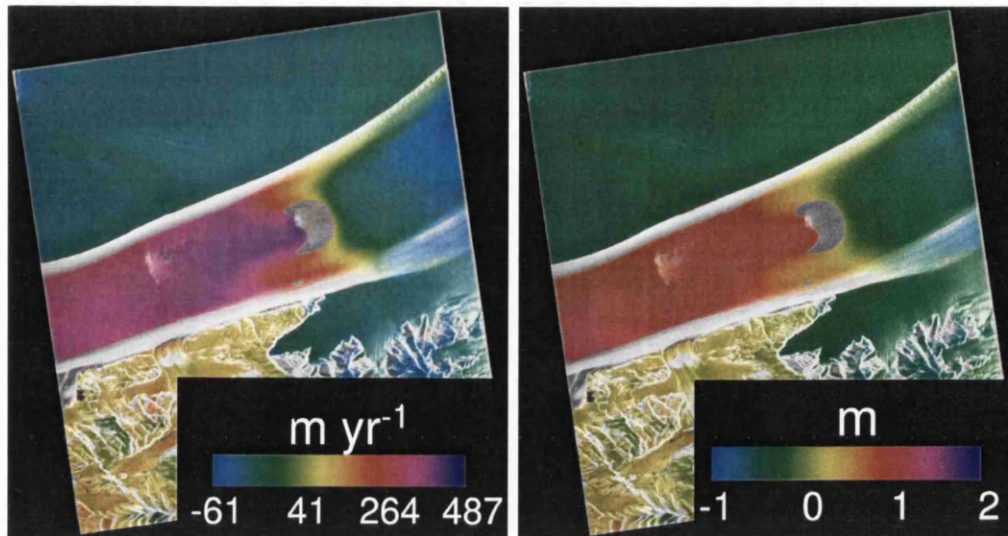


Figure 5.17: Horizontal and vertical displacements for frame 008_5337 for 24th and 27th January 1994. Locations and look directions of all frames of the Rutford Ice Stream are shown in figure 4.1.

between scenes due to a lower tidal elevation, as shown by the vertical displacement map, so has a greater slant range distance to the sensor. The appearance of upward vertical motion of the main trunk of the ice stream in the righthand figure is because of its forward motion as it moves towards the sensor. It is clear that vertical motion can dominate the displacement phase of a differential interferogram and make the derivation of velocity and the interpretation of displacement maps difficult. These effects are discussed further in section 7.5.1, following the presentation of the tidal height differences for each interferogram in section 6.3.

Vertical displacements were visible in other frames of the ice stream grounding zone. Figure 5.18 shows a vertical displacement map of frame 108_5337 from 26th and 27th February 1996, with the colour scale chosen to minimise the effects of horizontal ice stream flow on the main trunk of the ice stream. The grounding zone of the ice stream is clearly visible and upward vertical motion of the floating ice downstream of here has taken place.

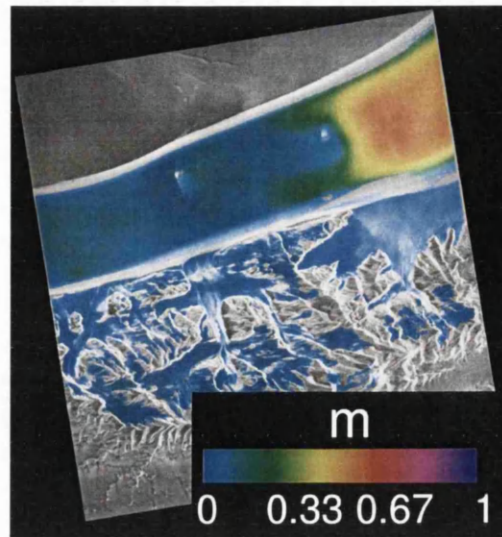


Figure 5.18: Vertical displacement for frame 108_5337 for 26th and 27th February 1996. Locations and look directions of all frames of the Rutford Ice Stream are shown in figure 4.1.

In summary, interferometry of the the Rutford Ice Stream shows an increase in speed from approximately 180 m a^{-1} where it rounds the Ellsworth Mountains to approximately 400 m a^{-1} at its grounding zone. There is no indication of a change in flow velocity between 1992 and 1996. When flow is towards the sensor, as is the case here, upward vertical motion of the ice shelf makes flow velocities appear higher than they really are, and downward motion, lower.

5.4.2 Evans Ice Stream

The picture is even more complicated for the Evans Ice Stream, where no frames are free of the influence of the grounding zone and the look directions are usually not as favourable (figure 4.2). However, the most upstream frame for the 1992 and 1994 study periods, 025_5229 had an ideal look direction and displacement maps in the horizontal plane corresponding to the look direction are shown in figure 5.19 below.

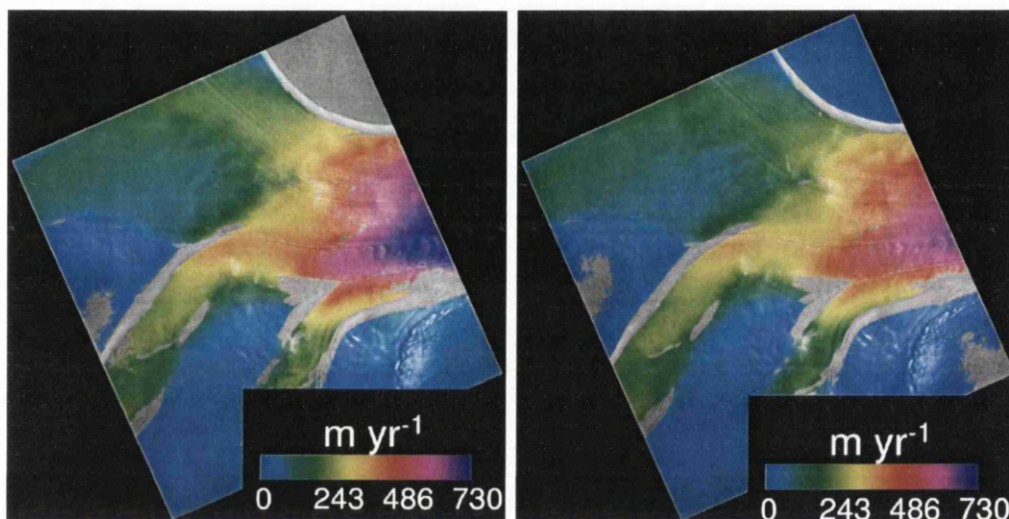


Figure 5.19: Horizontal displacements for frame 023_5229 for 14th and 17th January 1992 (left) and 22nd and 25th January 1994 (right). Locations and look directions of all frames of the Evans Ice Stream are shown in figure 4.2.

Downstream of where the five tributaries of the Evans Ice Stream meet, horizontal velocities higher than those of Rutherford are reached. Velocities when projected into the flow direction reached almost 750 m a^{-1} for this frame for 1992 and 625 m a^{-1} for 1994. This would suggest that the ice stream slowed over this period, especially as tidal influence, if present, would cause 1994 horizontal velocities to appear greater than those in 1992 (section 7.5.1). It would appear that the western tributaries (towards the bottom of figure 5.19) have higher velocities than the eastern tributaries (towards the top).

The middle section of the ice stream, shown in figure 5.20 below, appears slower than the upper section, but this is a consequence of the less favourable look direction compared to frame 023_5229. When displacements were projected into the flow direction, velocities reached 687 m a^{-1} , an increase on the speed on the upstream section for the same time period, January 1994. The grey area through the middle of the scene is the grounding zone, which could not be unwrapped for this particular image pair as it fell below the coherence threshold (section 3.6), and the ice above this in figure 5.20 (i.e. to the east of the grounding zone) is grounded, and below this in figure 5.20 (i.e. to the west of the grounding zone), floating, as discussed further in section 6.2. As with the Rutford Ice Stream, the influence of vertical motion is present in displacement fields, with the floating section at the bottom of the image appearing to have a large increase in horizontal velocity downstream of the grounding line which is actually caused upward vertical motion of the surface of the floating ice.

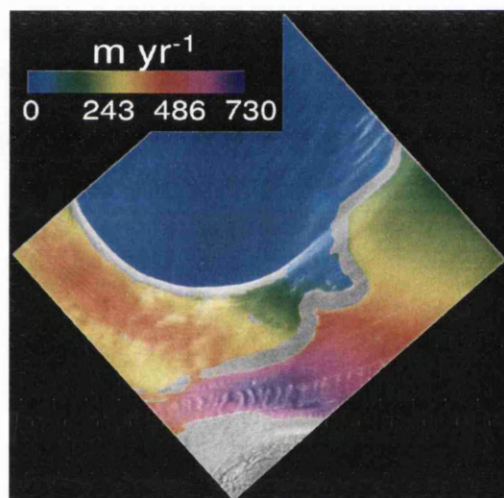


Figure 5.20: Horizontal displacements for frame 020_5553 for 25th and 28th January 1994. Locations and look directions of all frames of the Evans Ice Stream are shown in figure 4.2.

It was more difficult to get a clear picture of ice velocities in 1996 as both frames are affected by vertical motion and had less favourable look directions compared to the flow direction (figure 4.2). The grounded side of the ice stream (towards the

top of the figures) shows horizontal velocities of over 500 m a^{-1} , and velocities when projected into the flow direction were slightly higher than this, approximately 540 m a^{-1} . However, both these frames show falsely low velocities on floating areas because of downward vertical motion. For frame 206_5553 further downstream, the vertical motion cancels out the signal from the ice velocity to the extent that velocities appear negative, as with frame 008_5337.

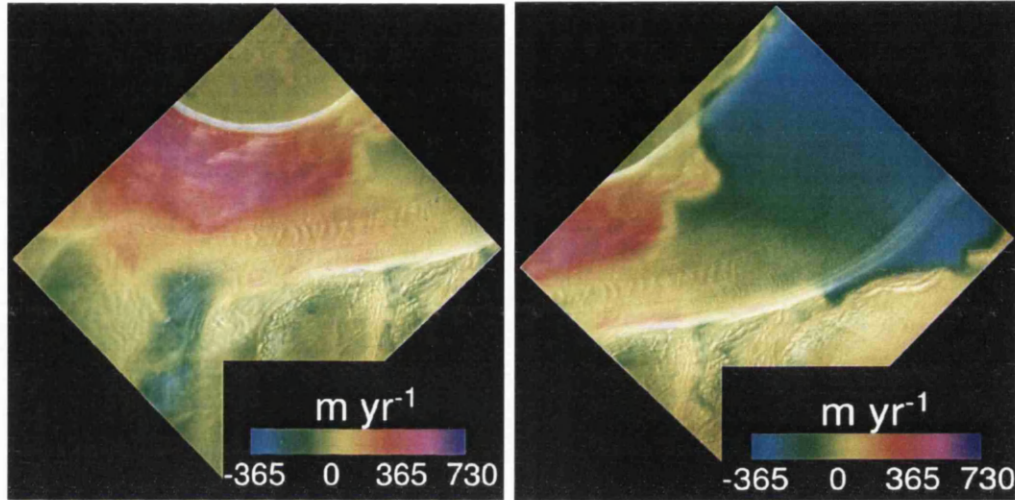


Figure 5.21: Horizontal displacements for frames 392_5553 for 11th and 12th February 1996 (left) and 206_5553 for 29th and 30th January 1996 (right). Locations and look directions of all frames of the Evans Ice Stream are shown in figure 4.2.

Downward vertical motion was also exhibited by frame 037_5265 (figure 5.22). This frame is almost entirely floating so it was not possible to derive ice velocities in the flow direction this far downstream.

In summary, interferometry shows that the Evans Ice Stream flows faster than Rutford, with speeds reaching 750 m a^{-1} . It appears to have slowed down to approximately 540 m a^{-1} from 1992 to 1996, and displacement fields from interferometry are affected by vertical motion in the same way as those of the Rutford Ice Stream.

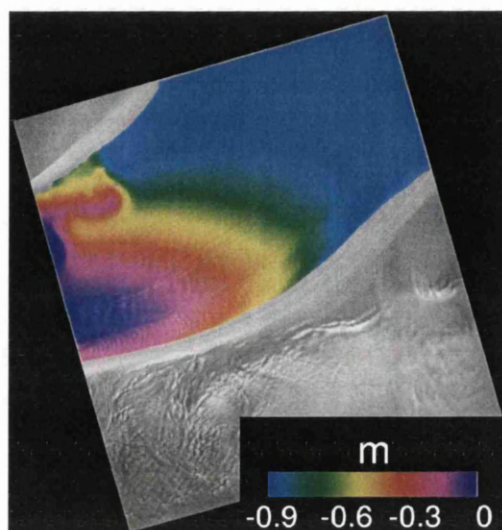


Figure 5.22: Vertical displacements for frame 037_5265 for 26th and 29th January 1994. Locations and look directions of all frames of the Evans Ice Stream are shown in figure 4.2.

5.5 Estimated Ice Stream Discharge

There is no evidence that the Rutford Ice Stream changed speed throughout the study period. Taking an ice velocity of 400 m a^{-1} at the grounding zone, a width of 30 km and an average ice thickness across the width (based on a profile from BEDMAP (Lythe *et al.*, 2001)) of 1700 m, this gives a discharge of $20.4 \text{ km}^3 \text{ a}^{-1}$ across the grounding line, or 18.7 Gt a^{-1} , taking ice density as 917 kg m^{-3} (Benn and Evans, 1998).

The velocity of the Evans Ice Stream appears to have decreased from approximately 750 m a^{-1} to 540 m a^{-1} between 1992 and 1996. Taking an ice stream width of 65 km and average thickness of 1100 m across the ice stream (again based on a profile from BEDMAP (Lythe *et al.*, 2001)), this would give a discharge of $53.6 \text{ km}^3 \text{ a}^{-1}$ in 1992 and $38.6 \text{ km}^3 \text{ a}^{-1}$ in 1996. This represents a decrease from 46.1 Gt a^{-1} in 1992 to 35.4 Gt a^{-1} in 1996, a significant decrease. This is discussed further in section 7.2.

5.6 Comparison to Balance Velocities

Published balance velocities from Bamber *et al.* (2000c) and Wu and Jezek (2004) have been compared to the InSAR derived velocities presented here. Balance velocities were taken for profiles across the ice stream, as discussed in section 7.2.2.

Using Bamber *et al.* (2000c)'s balance velocities, the average balance velocity at the approximate location of the Rutford Ice Stream grounding line is 364 m a^{-1} , suggesting that Rutford does not deviate too far from its balance velocity, but that mass balance may be slightly negative if anything. For the Evans Ice Stream, the average balance velocity across the ice stream at the approximate downstream extent of the grounding zone is 797 m a^{-1} . This suggests that the ice stream was close to balance at the start of the study period, but that mass balance became positive as the ice stream slowed between 1992 and 1996. This would suggest that this area of the ice sheet is gaining considerable mass.

These findings are, however, contradicted by comparing InSAR velocities to balance velocities from Wu and Jezek (2004). Their balance velocities for both ice streams are considerably lower than those of Bamber *et al.* (2000c). The highest balance velocity in the vicinity of the Evans Ice Stream is 297 m a^{-1} , and in the vicinity of the Rutford Ice Stream is 260 m a^{-1} .

Comparing the average balance velocities across the approximate locations of the ice stream grounding lines to InSAR velocities for the same locations suggests that both ice streams have negative mass balance, Evans more so than Rutford. Even taking into account that Wu and Jezek (2004) give errors in their balance velocities of 20 to 50 m a^{-1} for the relevant location on the Rutford Ice Stream and 50 to 100 m a^{-1} for the relevant location on the Evans Ice Stream, the findings are still contradictory to those from comparing InSAR velocities to Bamber *et al.* (2000c)'s. Taking the upper limits of these errors would give balance velocities of Rutford and Evans of 310 m a^{-1} and 497 m a^{-1} respectively. This discrepancy cannot be resolved without more information, and the differences between these two datasets are discussed further in section 7.2.2.

5.7 Summary

The Rutford and Evans Ice Streams were examined with differential interferometry. The Rutford Ice Stream increases in speed from approximately 180 m a^{-1} at the 90° bend downstream of the onset, to 400 m a^{-1} at the grounding line. There is nothing to suggest the ice stream changed speed throughout the study period between 1992 and 1996. The Evans Ice Stream has a higher velocity than Rutford, and seems to have decreased in velocity throughout the study period from approximately 750 m a^{-1} to 540 m a^{-1} . Comparing InSAR velocities to balance velocities proved inconclusive because of discrepancies between two balance velocity datasets used. Differential interferometry of this study area was complicated by one important factor: vertical tidal motion of floating areas. This prohibited the use of double difference interferometry for most frames due to the failure of the Constant Velocity Assumption, discussed further in section 7.3.4, leading to supposedly “topography-only” interferograms containing many fringes due to displacement in their grounding zones, and complicated the interpretation of the displacement signal from interferometry by changing the slant range distance between the sensor and the ice surface, in some cases leading to apparent backward motion of the ice stream, discussed further in section 7.5.1.

Chapter 6

The Grounding Zone

6.1 Introduction

As seen in results presented in the previous chapter, and discussed in the next chapter, single and double difference interferograms of both ice streams exhibited different amounts of vertical change in their grounding zones, which complicated the process of interferometry. These displacements did, however, allow the grounding zones of both ice streams to be mapped from interferometry which was particularly useful for the Evans Ice Stream, whose grounding zone has not been previously well established (section 7.4.2). Observations of different amounts of vertical change in the grounding zone of both ice streams at this stage led to tidal models being run to predict the tidal height difference between the scenes making up each interferometric pair. This allowed the observed and expected vertical changes to be compared. An elastic beam model was used to model the width of the grounding zones, varying different parameters, and the results at different locations around the grounding zones of both ice streams will be presented here and compared to the width as mapped from interferometry.

6.2 Mapping the Grounding Zone

The grounding zone of an ice stream is a major control on its stability, and must be accurately located for a number of reasons which were discussed previously in section 2.6. From the first results of this project, it was apparent that there is no such thing as the “grounding line” of either the Rutford or Evans Ice Streams. SAR interferometry showed that both ice streams had vertical motion in a clearly defined grounding zone up to tens of kilometres wide in which tidal change was important.

Interferograms made from pairs of images of the Rutford Ice Stream for frames 008_5337, 008_5319, 021_5463 and 108_5337 showed interesting tidal effects, with a horseshoe-shaped grounding zone with a high fringe rate surrounding a central pinning point (figure 6.1). The western side of the horseshoe shape extended approximately 20 km upstream and the eastern side 15 km. The pinning point corresponds to a subglacial topographic high in the BEDMAP dataset (Lythe *et al.*, 2001), with that 5 km cell having a bed elevation hundreds of metres higher than its neighbours. The BEDMAP water column data also show water tens of metres deep in the cells either side of the pinning point, deepening quickly downstream, with shallower water in the middle of the ice stream and deeper water outside of that, showing that the W-shape of the trough in which the Rutford Ice Stream sits is preserved downstream. The grounding zone shape matched between frames where the frames overlapped, with two exceptions. The first 3 day pair from frame 008_5337 in 1994 did not show the horseshoe shaped area, but instead showed a second concentric pattern of fringes immediately downstream of that at the pinning point. The first tandem pair of frame 108_5337 in 1996 is the only other interferogram to show this second concentric pattern, although it is much less pronounced than in the previous case, and although it also shows the horseshoe shaped grounding zone, this is also much less pronounced than for all the other frames where the horseshoe shape is present. These two interferograms, and an example of a more typical interferogram showing the grounding zone, are shown in figure 6.2 and discussed further in section 6.3.3, in the context of the results of the tidal model.

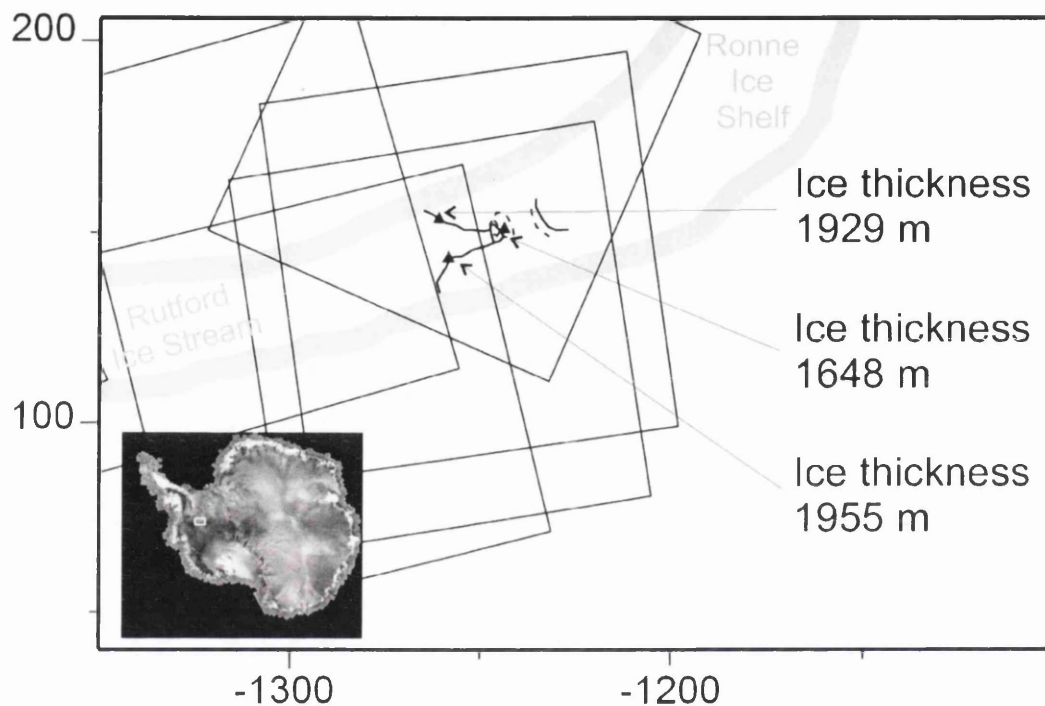


Figure 6.1: The grounding zone of the Rutford Ice Stream, as mapped from interferometry. Dashed lines indicate the grounding zone as mapped from the first 3-day pair of frame 008_5337 in 1994, and solid lines that mapped from all other frames. The locations of ice thicknesses used in the elastic beam model are marked as black triangles. Grey areas represent ice stream shear margins. SAR frames are shown in black. Coordinates are Polar Stereographic, in kilometres, with the origin at the South Pole.

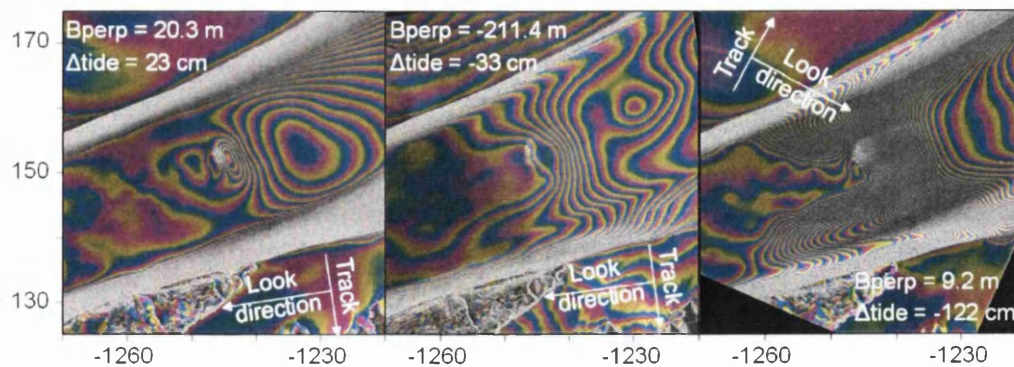


Figure 6.2: Interferograms of the Rutford Ice Stream showing different grounding zone features. Left: frame 008_5337, 21st and 24th January 1994. Centre: frame 108_5337, 15th and 16th January 1996. Right: frame 021_5463, 22nd and 25th January 1994. All are 50 by 50 km subsets of flattened interferograms, with a top left Polar Stereographic coordinate of -1270000, 175000. Map coordinates are Polar Stereographic, in kilometres, with the origin at the South Pole.

For the Evans Ice Stream, the grounding zone was mapped from interferograms of four SAR frames (020_5553, 037_5265, 206_5535 and 392_5553), and found to match where the frames overlapped (figure 6.3), which is significant as there has been previous disagreement over its location. Interferograms showed a complex shaped area with a high fringe rate comparable to the horseshoe shaped area on Rutford (for example, running downwards from the top right of figure 5.9), although narrower, with a usual width of about 8 km. The grounding line runs parallel to the direction of the main trunk for approximately 120 km on the east side of the ice stream. The upstream end of this part of the grounding zone lies adjacent to an area of slow moving ice, probably frozen to its bed, which divides the eastern and western groups of tributaries. A major flowline, visible in both SAR intensity images and interferograms, extends downstream from here, dividing the flow regimes from the two groups of tributaries, and that section of the grounding zone runs parallel to and east of this. The grounding zone to the west of this flowline is perpendicular to the direction of the main trunk and considerably wider than that on the east side. As such, for much of the length of the main trunk, the east side of the ice stream is grounded and the west side

floating. This is discussed further in section 7.4.2.

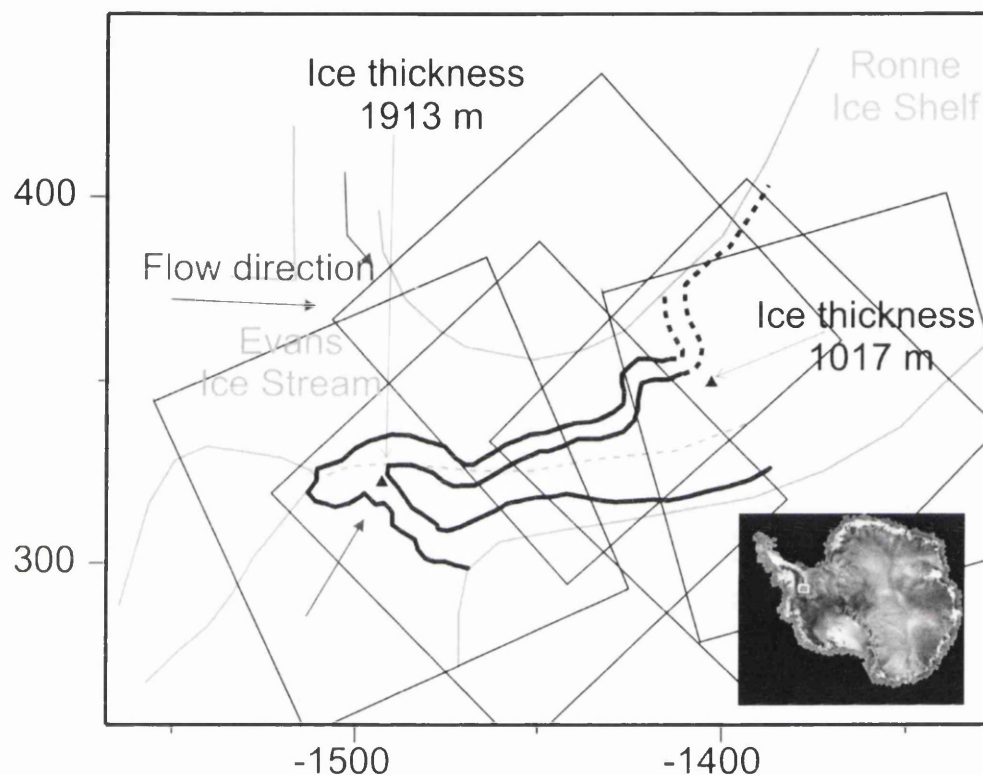


Figure 6.3: The grounding zone of the Evans Ice Stream, as mapped from interferometry. Dotted lines indicate mapping from frame 206_5535, which also fitted interferograms from frames 020_5553 and 037_5265; solid lines indicate mapping from frame 392_5553 further upstream. The locations of ice thicknesses used in the elastic beam model are marked as black triangles. SAR frames are shown in black. The dashed grey line indicates a major flowline. Coordinates are Polar Stereographic, in kilometres, with the origin at the South Pole.

6.3 Tidal Model Results

It is clear from the high fringe rate in the clearly defined grounding zones of both ice streams that in both cases the grounding zone area was undergoing a change in vertical motion over time. Although the grounding zone locations agreed between different frames of each ice stream, the fringe rate in the grounding zone differed between flattened interferograms of different scenes, which was probably due to their different vertical tidal displacements, after taking the perpendicular baseline and therefore the altitude of ambiguity into account. These observations were further investigated with the use of tidal models, as described in section 4.5.1, which were used to predict the tidal height at the time of acquisition of each SAR image, and therefore the difference in tidal height for each interferometric pair, in order to examine the amount of vertical change that might be expected.

6.3.1 Rutford Ice Stream

Figures 6.4, 6.5, 6.6 and 6.7 show plots of tidal height over the three study periods (the 1996 period divided in two for clarity), with the times of the images marked. Table 6.1 shows the height of the tide at the time of acquisition for each image of the grounding zone of the Rutford Ice Stream, and table 6.2 the difference in tidal height for each interferometric pair.

As discussed in section 4.5.1, different sources of data were used to derive the components for reconstructing the tide of the Rutford Ice Stream. The final model settled on here used 8 diurnal and semi-diurnal constituents derived from GPS, and the two longer period constituents derived from the CATS02.01 model. As a comparison, `t_tide` was also run with all ten constituents extracted from CATS02.01. Differences of up to 30 cm, or about 5% of the total tidal range, were found between these two sets of predictions. However, it was assumed that the constituents extracted from GPS were more accurate due to being based on actual observed measurements and being specific to this ice stream, unlike the models. This comparison is shown in figure 6.8.

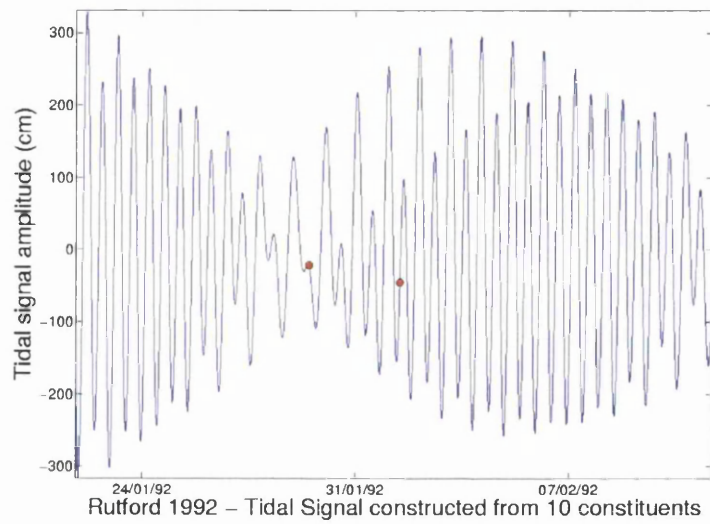


Figure 6.4: Tidal signal for the Rutford Ice Stream during the 1992 study period. Times of the SAR images from frame 008_5337 are marked as red points.

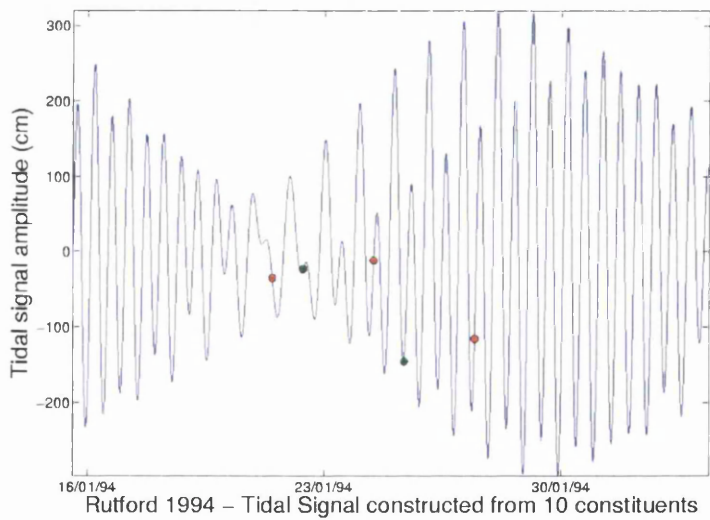


Figure 6.5: Tidal signal for the Rutford Ice Stream during the 1994 study period. Times of the SAR images from frame 008_5337 are marked as red points and from frame 021_5463 as green points.

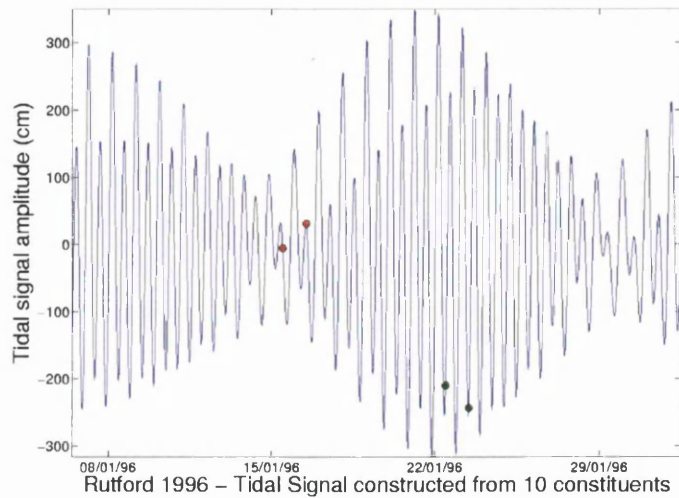


Figure 6.6: Tidal signal for the Rutford Ice Stream during the earlier part of the 1996 study period. Times of the SAR images from frame 008_5319 are marked as red points and from frame 108_5337 as green points.

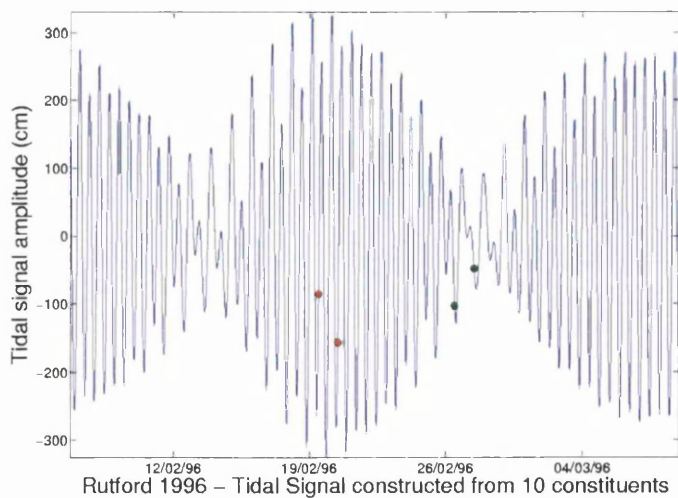


Figure 6.7: Tidal signal for the Rutford Ice Stream during the later part of the 1996 study period. Times of the SAR images from frame 008_5319 are marked as red points and from frame 108_5337 as green points.

Table 6.1: Tidal heights at the time of acquisition of each SAR image of the Rutford Ice Stream.

Image track_frame	Image Date	Image Time (GMT)	Tidal Height (m)
008_5337	29/01/92	11:04:20	-0.21
008_5337	01/02/92	11:04:20	-0.45
037_5301	09/02/92	11:37:19	-2.14
023_5265	14/02/92	12:10:22	0.02
037_5301	15/02/92	11:37:23	0.29
023_5265	17/02/92	12:10:21	0.66
008_5337	21/01/94	11:04:26	-0.35
021_5463	22/01/94	08:52:14	-0.23
023_5265	22/01/94	12:10:24	-0.18
037_5301	23/01/94	11:37:25	0.06
008_5337	24/01/94	11:04:24	-0.11
021_5463	25/01/94	08:52:13	-1.45
023_5265	25/01/94	12:10:23	0.39
037_5301	26/01/94	11:37:24	-0.21
008_5337	27/01/94	11:04:25	-1.16
008_5319	15/01/96	11:27:59	-0.05
008_5319	16/01/96	11:28:00	0.32
108_5337	22/01/96	11:08:09	-2.09
108_5337	23/01/96	11:08:10	-2.43
008_5319	19/02/96	11:28:03	-0.85
008_5319	20/02/96	11:28:03	-1.57
108_5337	26/02/96	11:08:11	-1.03
108_5337	27/02/96	11:08:10	-0.48

Table 6.2: Tidal height differences between scenes making up interferometric pairs, triplets and quads of the Rutford Ice Stream.

Year	Pair track_frame	Tidal Height Difference (m)		
		Image 1 to 2	Image 2 to 3	Image 3 to 4
1992	008_5337	-0.24		
1994	008_5337	0.23	-1.04	
	021_5463	-1.22		
1996	108_5337	-0.33		0.55

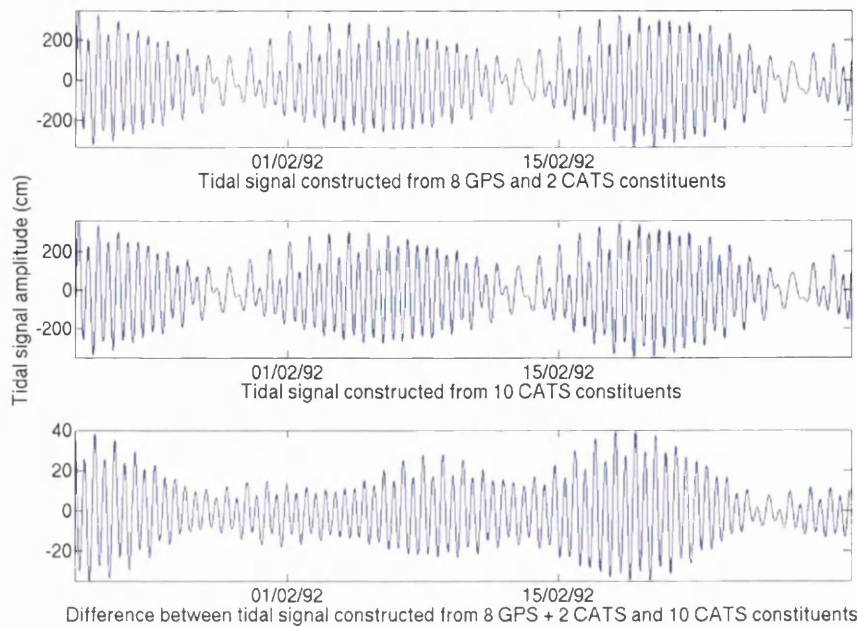


Figure 6.8: A comparison between the tidal signal reconstructed for the Rutford Ice Stream for 1992 with 8 components from GPS and 2 from CATS02.01 (top), and all ten components extracted from CATS02.01 (middle). Note the different scale on the Y axis for the comparison (bottom).

6.3.2 Evans Ice Stream

Figures 6.9, 6.10, 6.11 and 6.12 show plots of tidal height over the three study periods (the 1996 period divided in two for clarity), with the times of the images marked. Table 6.3 shows the height of the tide at the time of acquisition for each image of the grounding zone of the Evans Ice Stream, and table 6.4 the difference in tidal height for each interferometric pair.

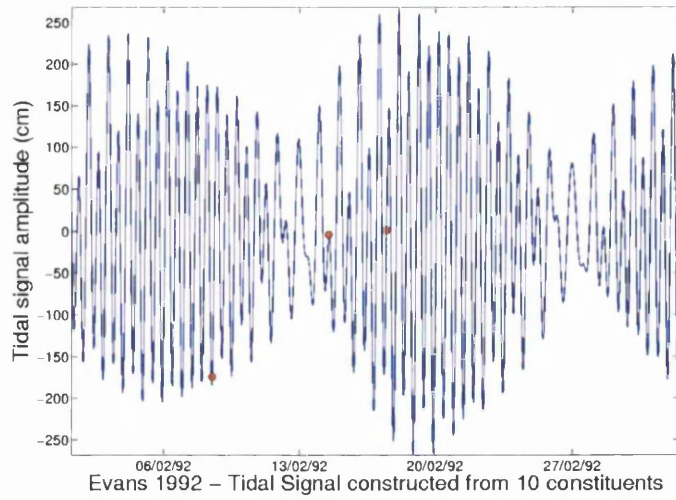


Figure 6.9: Tidal signal for the Evans Ice Stream during the 1992 study period. Times of the SAR images from frame 023_5229 are marked as red points.

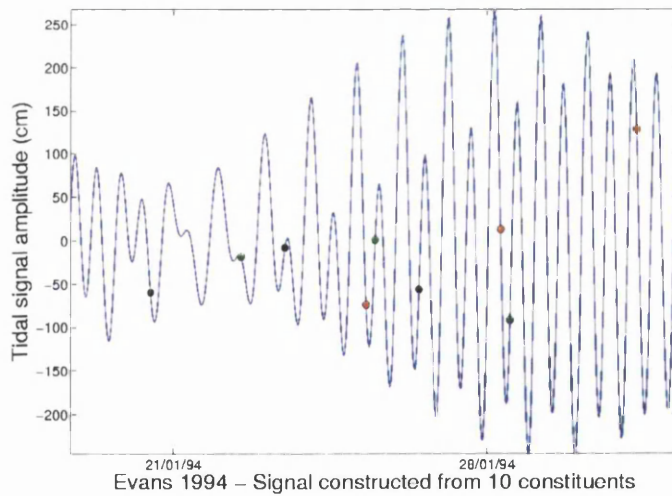


Figure 6.10: Tidal signal for the Evans Ice Stream during the 1994 study period. Times of the SAR images from frame 020_5553 are marked as red points, 023_5229 as green points and 037_5265 as black.

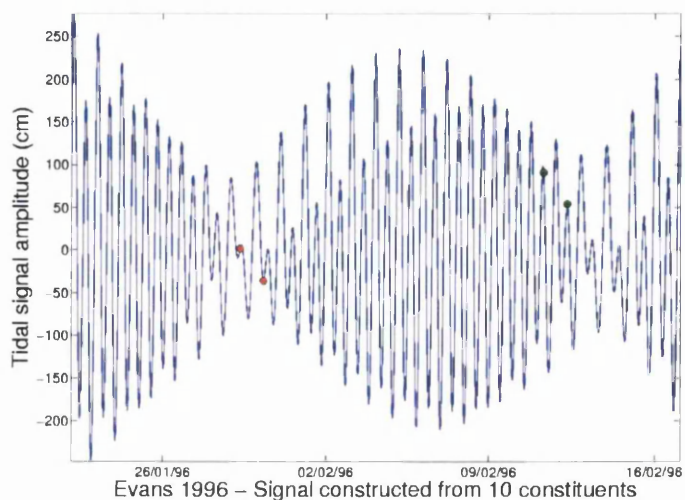


Figure 6.11: Tidal signal for the Evans Ice Stream during the earlier part of the 1996 study period. Times of the SAR images from frame 206_5535 are marked as red points and from frame 392_5553 as green points.

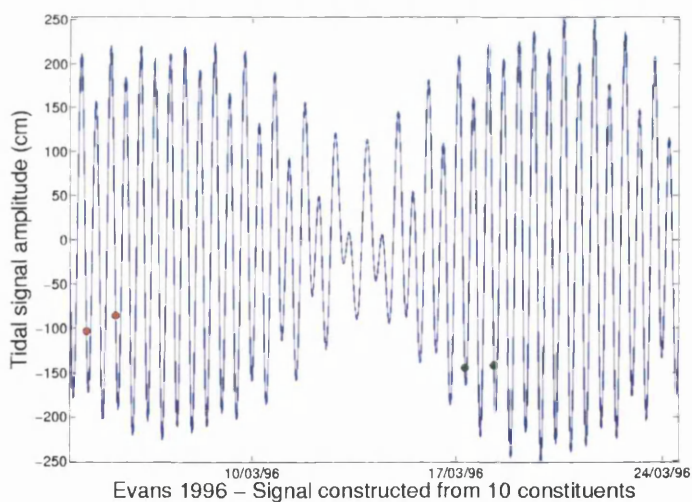


Figure 6.12: Tidal signal for the Evans Ice Stream during the later part of the 1996 study period. Times of the SAR images from frame 206_5535 are marked as red points and from frame 392_5553 as green points.

Table 6.3: Tidal heights at the time of acquisition of each SAR image of the Evans Ice Stream.

Image track_frame	Image Date	Image Time (GMT)	Tidal Height (m)
023_5229	08/02/92	12:09:48 PM	-1.74
023_5229	14/02/92	12:09:52 PM	-0.04
023_5229	17/02/92	12:09:51 PM	0.01
037_5265	20/01/94	11:36:55 AM	-0.60
023_5229	22/01/94	12:09:54 PM	-0.19
037_5265	23/01/94	11:26:54 AM	-0.08
020_5553	25/01/94	07:13:00 AM	-0.74
023_5229	25/01/94	12:09:53 PM	0.01
037_5265	26/01/94	11:36:54 AM	-0.56
020_5553	28/01/94	07:13:00 AM	0.13
023_5229	28/01/94	12:09:53 PM	-0.92
020_5553	31/01/94	07:13:01 AM	1.28
206_5535	29/01/96	07:29:37 AM	0.01
206_5535	30/01/96	07:29:38 AM	-0.36
392_5553	11/02/96	07:21:15 AM	0.91
392_5553	12/02/96	07:21:17 AM	0.54
206_5535	04/03/96	07:29:37 AM	-1.04
206_5535	05/03/96	07:29:37 AM	-0.86
392_5553	17/03/96	07:21:08 AM	-1.44
392_5553	18/03/96	07:21:10 AM	-1.42

Table 6.4: Tidal height differences between scenes making up interferometric pairs, triplets and quads of the Evans Ice Stream.

Year	Pair track_frame	Tidal Height Difference (m)		
		Image 1 to 2	Image 2 to 3	Image 3 to 4
1992	023_5229	1.70	0.05	
1994	020_5553	0.20	-0.93	
	023_5229	0.87	1.15	
	037_5265	0.52	-0.48	
1996	206_5535	-0.38		0.18
	392_5553	-0.37		0.02

6.3.3 Vertical Tidal Displacement

Tidal modelling showed that the maximum tidal range for the Evans Ice Stream grounding zone is over 5 metres and for the Rutford Ice Stream over 6 metres, which are both unusually high for the Antarctic (section 7.5).

Clearly, for both ice streams, pairs of images exist with small and large changes in tidal height between their acquisition. Vertical displacement observed in the interferograms (such as that shown in section 5.2) was compared to the modelled tidal height differences. It would be expected that interferograms from pairs with the largest tidal changes would show the greatest vertical displacement. As discussed in section 3.10, if it was assumed that all displacement shown in an interferogram was vertical, then each fringe would represent 2.6 cm of displacement due to the 23° look angle of the ERS satellites. Table 6.5 shows the number of fringes across the grounding zone of each interferogram of the grounding zone of the Rutford Ice Stream, and the amount of vertical displacement this would represent if it were assumed that all displacement is vertical (section 3.5.7, section 3.8.8). Table 6.6 shows the same for the Evans Ice Stream. Figure 6.13 shows the relationship between the number of fringes in the grounding zones of the ice streams, and tidal height change.

It is important to examine at this stage to what extent fringes are due to vertical displacement. Following the first stage of interferometry, using pairs of images, fringes in each interferogram are due to topography, line-of-sight displacement, and the perpendicular baseline, as discussed in section 3.5.7. For both ice streams, on the relatively flat topography of the ice shelf, fringes due to the perpendicular baseline could be discounted because of the relatively high altitudes of ambiguity (table 6.5, table 6.6). For the Evans Ice Stream, although some fringes can be accounted for by LOS displacement, the changing orientation of the grounding zone and range of flow directions from the tributaries means that for most of the area the flow direction is orientated approximately perpendicular to the LOS, meaning the majority of the fringes can be explained by vertical motion. For the Rutford Ice Stream, interferograms from frames other than 021_5463 are more sensitive to LOS displacement than the Evans interferograms, as look

directions are oriented directly upstream, but frame 021_5463's look direction is at approximately a 45° angle to the flow direction and is therefore less sensitive to displacement in the flow direction i.e. ice velocity. In any case, interferometry is more sensitive to vertical than horizontal displacement, as discussed in sections 3.10 and 7.5.1.

Table 6.5: Altitudes of ambiguity for each pair and vertical change, assuming all change is vertical, for the Rutford Ice Stream. Fringes were counted outwards from the centre of the pinning point in the downstream direction, and across the horseshoe-shaped area as shown on figure 3.6, and the number was found to be a close match.

Frame	Dates	Perpendicular baseline (m)	Altitude of ambiguity (m)	Tidal height change (m)	Grounding zone fringes	Grounding zone fringes * 0.026 (m)
008_5337	29/01/92 - 01/02/92	85.5	110.13	-0.24	16	0.416
008_5337	21/01/94 - 24/01/94	20.3	463.84	0.23	9	0.234
021_5463	22/01/94 - 25/01/94	9.2	1023.48	-1.22	49	1.274
008_5337	24/01/94 - 27/01/94	-89.3	105.44	-1.04	44	1.144
108_5337	22/01/96 - 23/01/96	-211.4	44.54	-0.33	9	0.234
108_5337	26/02/96 - 27/02/96	-146.6	64.23	0.55	19	0.494

Table 6.6: Altitudes of ambiguity for each pair and vertical change, assuming all change is vertical, for the Evans Ice Stream.

Frame	Dates	Perpendicular baseline (m)	Altitude of ambiguity (m)	Tidal height change (m)	Grounding zone fringes	Grounding zone fringes * 0.026 (m)
020_5553	25/01/94 - 28/01/94	-102.8	91.60	0.87	27	0.702
037_5265	23/01/94 - 26/01/94	-51.6	182.48	-0.48	10	0.260
206_5535	29/01/96 - 30/01/96	-143.1	65.80	-0.38	12	0.312
392_5553	11/02/96 - 12/02/96	-138.5	67.99	-0.37	8	0.208

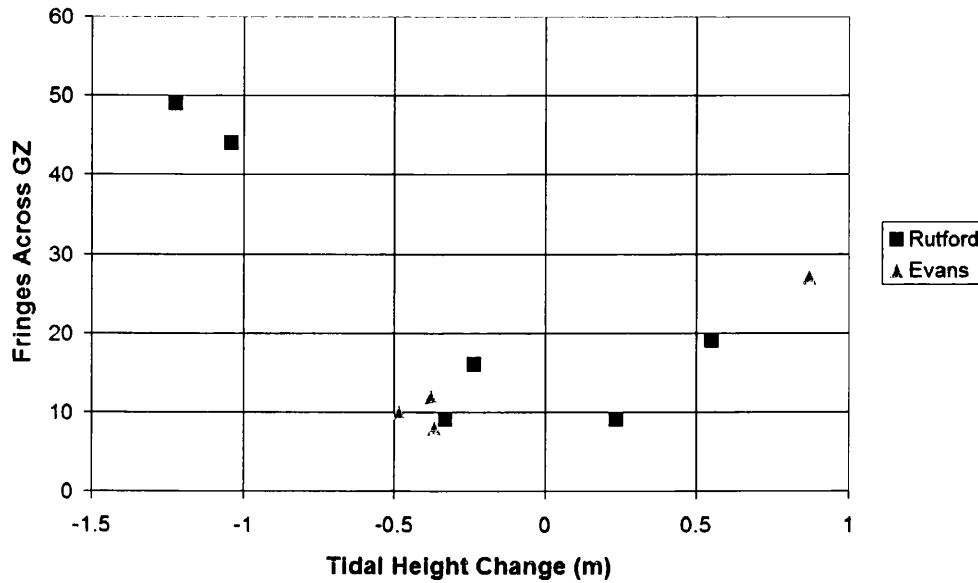


Figure 6.13: Vertical displacements from interferometry as shown by the number of fringes in the grounding zone (GZ) compared to modelled tidal height changes for the Rutford and Evans Ice Streams. Squares represent frames of Rutford, and triangles frames of Evans.

For the Rutford Ice Stream, vertical change as shown by the number of fringes was a surprisingly close match to tidal height change, especially given the sensitivity of the frames to LOS displacement, although frame 008_5337 in 1992 overestimates the vertical change by a factor of two, with a tidal height change of -24 cm and 16 fringes in the grounding zone. It is not known why this is the case, particularly with other interferograms of the same frame being a better match. For the Evans Ice Stream, the vertical displacement from the number of fringes is a closer match to that predicted from the tidal model for frames 020_5553 and 206_5535, which are ascending frames located in similar places in 1994 and 1996 respectively, and have look directions perpendicular to the ice stream flow direction, making them especially insensitive to horizontal displacement. In the case of the frame 020_5553 interferogram, additional fringes may have been present in the grounding zone had the scene extended further north. It is therefore clear that the grounding zone is being affected by vertical motion

proportional to changing tidal height.

6.4 Elastic Beam Model Results

Observations from mapping the width of the grounding zones using interferometry led to the width of the hinge zone being modelled using an elastic beam model, as described in section 4.6. The width of the hinge zone, as modelled using different values of h , ν and E , is shown in tables 6.7 and 6.8 for the Rutford and Evans Ice Streams respectively. Figures 6.14, 6.15 and 6.16 show the hinge zone for the Rutford Ice Stream modelled with different values of E and ν , at three different locations with different ice thicknesses as marked on figure 6.1: the pinning point (ice thickness 1648 m); the upstream extent of the grounding zone on the east side of the ice stream (ice thickness 1929 m); and the upstream extent of the grounding zone on the west side of the ice stream (ice thickness 1955 m) respectively. Figures 6.17 and 6.18 show the same for the Evans Ice Stream with two different ice thicknesses used for different locations as marked on figure 6.3; the location where the CATS02.01 tidal model was run, which was constrained by the landward extent of its bathymetry grid (ice thickness 1017 m), and the highest ice thickness within the grounding zone as mapped from interferometry (ice thickness 1913 m) respectively.

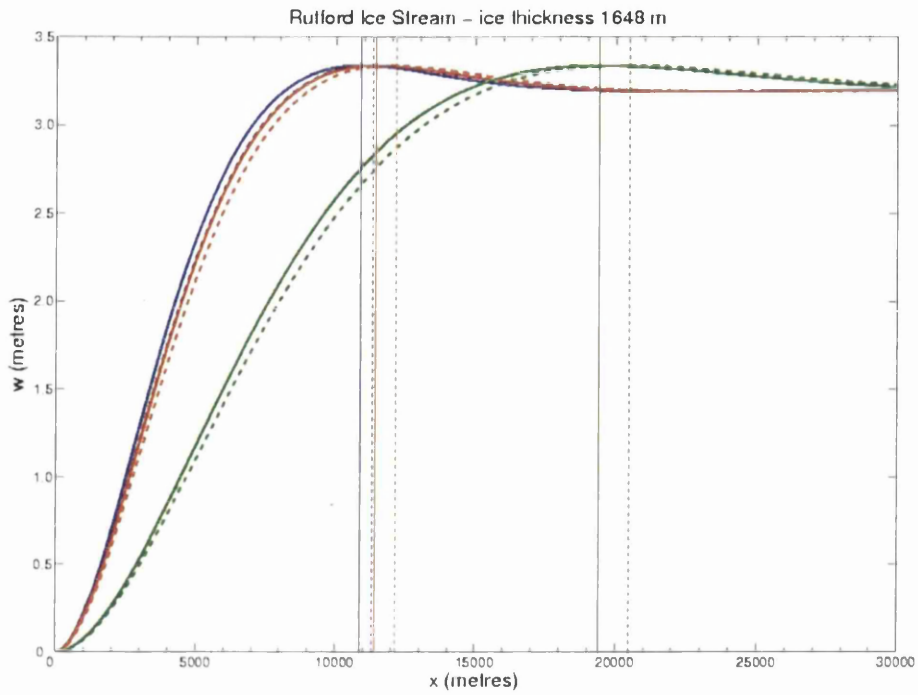


Figure 6.14: Grounding zone width modelled by an elastic beam for the Rutford Ice Stream using an ice thickness of 1648 m. Blue lines indicate a Young's Modulus of 0.88 GPa; red indicate 1.1 GPa; and green indicate 9 GPa. Solid lines indicate a Poisson's ratio of 0.3; dashed lines, 0.5. Correspondingly coloured dashed/solid vertical lines indicate grounding zone width.

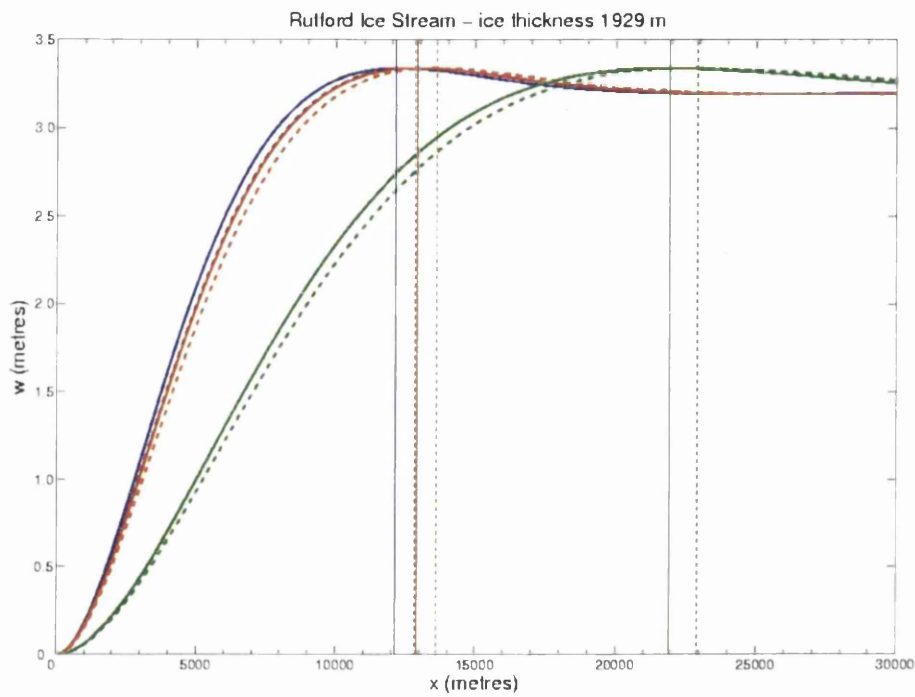


Figure 6.15: Grounding zone width modelled by an elastic beam for the Rutford Ice Stream using an ice thickness of 1929 m. Blue lines indicate a Young's Modulus of 0.88 GPa; red indicate 1.1 GPa; and green indicate 9 GPa. Solid lines indicate a Poisson's ratio of 0.3; dashed lines, 0.5. Correspondingly coloured dashed/solid vertical lines indicate grounding zone width.

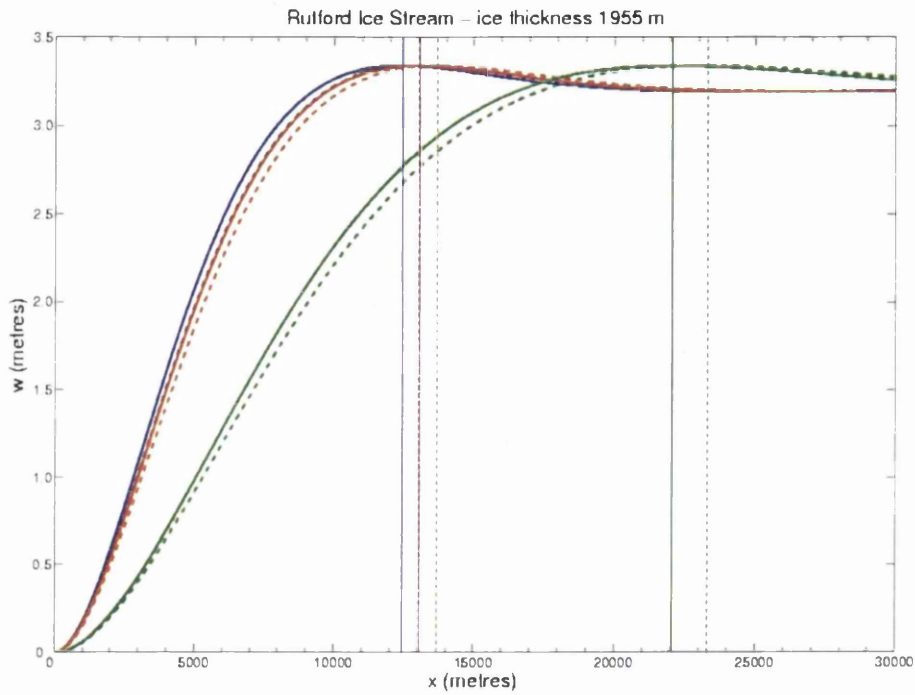


Figure 6.16: Grounding zone width modelled by an elastic beam for the Rutford Ice Stream using an ice thickness of 1955 m. Blue lines indicate a Young's Modulus of 0.88 GPa; red indicate 1.1 GPa; and green indicate 9 GPa. Solid lines indicate a Poisson's ratio of 0.3; dashed lines, 0.5. Correspondingly coloured dashed/solid vertical lines indicate grounding zone width.

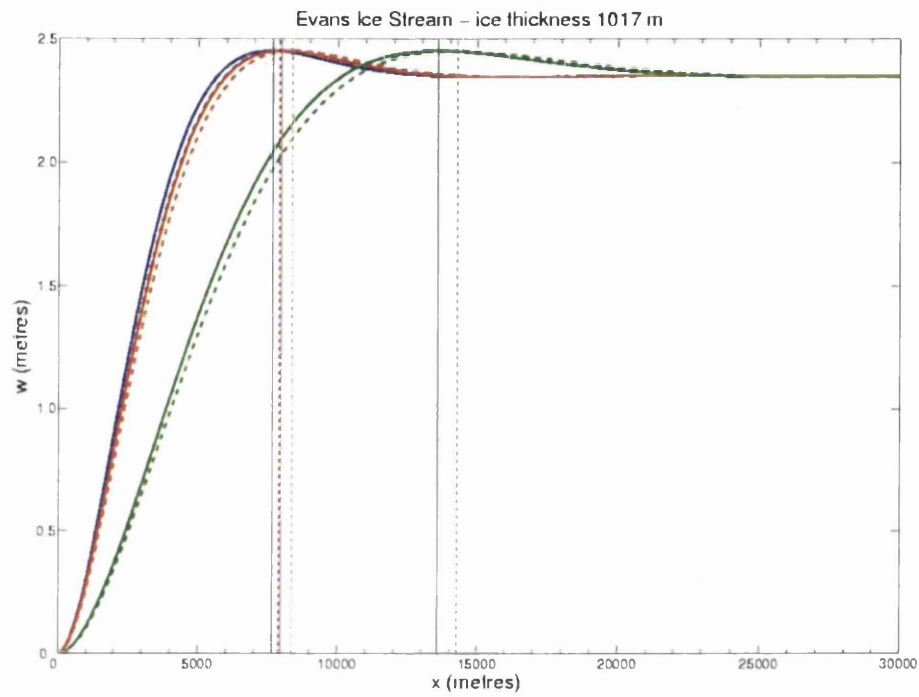


Figure 6.17: Grounding zone width modelled by an elastic beam for the Evans Ice Stream using an ice thickness of 1017 m. Blue lines indicate a Young's Modulus of 0.88 GPa; red indicate 1.1 GPa; and green indicate 9 GPa. Solid lines indicate a Poisson's ratio of 0.3; dashed lines, 0.5. Correspondingly coloured dashed/solid vertical lines indicate grounding zone width.

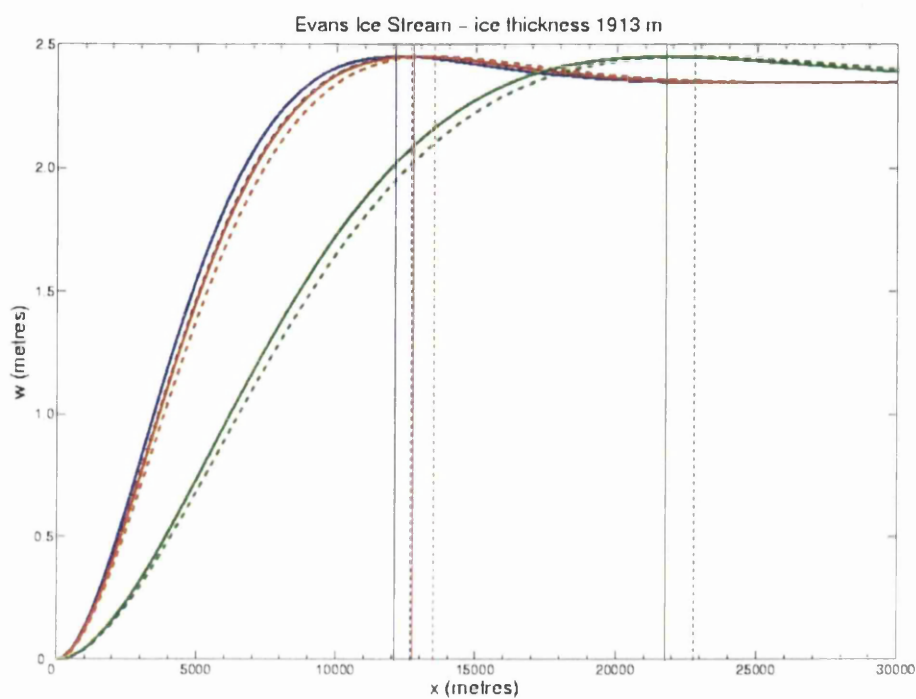


Figure 6.18: Grounding zone width modelled by an elastic beam for the Evans Ice Stream using an ice thickness of 1017 m. Blue lines indicate a Young's Modulus of 0.88 GPa; red indicate 1.1 GPa; and green indicate 9 GPa. Solid lines indicate a Poisson's ratio of 0.3; dashed lines, 0.5. Correspondingly coloured dashed/solid vertical lines indicate grounding zone width.

Table 6.7: The width of the grounding zone of the Rutford Ice Stream as modelled using an elastic beam, showing the distance from the landward limit of tidal flexing to both the inflection point and the seaward limit of tidal flexing, in km (F to I and F to H respectively in figure 2.3).

Ice thickness (m)	Young's modulus (GPa)	F to I		F to H	
		Grounding zone width (km)		Grounding zone width (km)	
		$v=0.3$	$v=0.5$	$v=0.3$	$v=0.5$
1648	0.88	10.9	11.4	19.0	20.0
	1.1	11.5	12.1	20.1	21.1
	9	19.4	20.4	33.9	35.7
1929	0.88	12.2	12.8	21.4	22.5
	1.1	12.9	13.6	22.6	23.7
	9	21.9	22.9	38.2	40.1
1955	0.88	12.3	13.0	21.6	22.6
	1.1	13.1	13.7	22.8	24.0
	9	22.1	23.2	38.7	40.5

Table 6.8: The width of the grounding zone of the Evans Ice Stream as modelled using an elastic beam, showing the distance from the landward limit of tidal flexing to both the inflection point and the seaward limit of tidal flexing, in km (F to I and F to H respectively in figure 2.3).

Ice thickness (m)	Young's modulus (GPa)	F to I		F to H	
		Grounding zone width (km)		Grounding zone width (km)	
		$v=0.3$	$v=0.5$	$v=0.3$	$v=0.5$
1017	0.88	7.6	7.9	13.2	13.9
	1.1	8.0	8.4	14.0	14.7
	9	13.5	14.2	23.7	24.9
1913	0.88	12.1	12.7	21.2	22.3
	1.1	12.8	13.5	22.5	23.6
	9	21.7	22.8	38.0	39.9

Clearly, changing the values of E , v and h affects the modelled width of the grounding zone. Increasing values of E , h and v lead to an increase in the modelled width, with increases in h leading to the most pronounced increases in modelled width. Using Stephenson (1984)'s value of E , 9 GPa, the grounding zones are modelled up to 17 km wider than with the other values (the difference increasing with ice thickness). Taking E as 1.1 GPa, a more realistic value (section 4.6), the width of the grounding zone of the Evans Ice Stream, from F to I, at the hinge zone as mapped from the interferograms where the ice thickness is 1913 m, is 12.8 km, and further downstream, corresponding to the location where the CATS02.01 model was run, where the ice thickness is 1017 m, the grounding zone width from F to I is 8 km. Corresponding values of the grounding zone width from F to H are 22.5 km and 14.0 km respectively. For the Rutford Ice Stream, taking the ice thickness at the pinning point (1648 m), the hinge zone is 11.5 km wide with an E of 1.1. For ice thicknesses from the east and west sides of the horseshoe shape (1929 m and 1955 m respectively), the grounding zone is 12.9 km and 13.1 km wide respectively. The corresponding grounding zone widths from F to H were 20.1 km, 22.6 km and 22.8 km for ice thicknesses of 1648 m, 1929 m and 1955 m respectively.

The choice of input tidal amplitude A_0T does not affect the calculated width of the hinge zone, which is consequently the same for spring and neap tides as shown by figure 6.19, which uses the largest ice thickness to best illustrate the difference between the two. Figures 6.14 to 6.18 are shown using the spring tide results to best illustrate the differences between model runs using different values of E , h and v , which become more pronounced with increasing A_0T . The grounding zone mapped from interferometry also remained the same width throughout the tidal cycle.

The mapped width of the grounding zone was compared to that modelled using an elastic beam. The grounding zone of the Evans Ice Stream as mapped from interferometry (figure 6.3), from F to H, varied between approximately 6 km and 23 km, with increasing grounding zone width corresponding to increasing ice thickness according to BEDMAP. For Evans, the grounding zone nearest to where the tidal model was run, where the ice thickness was 1017 m, was found

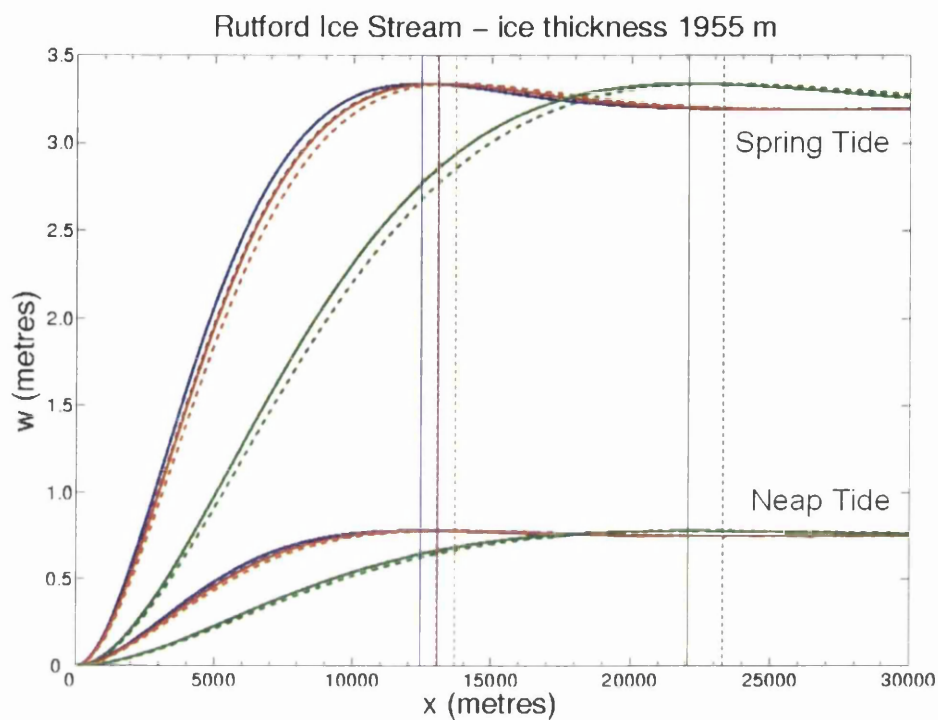


Figure 6.19: Spring and neap tidal ranges used to model the width of the grounding zone of the Rutford Ice Stream for an ice thickness of 1955 m. Blue lines indicate a Young's Modulus of 0.88 GPa; red indicate 1.1 GPa; and green indicate 9 GPa. Solid lines indicate a Poisson's ratio of 0.3; dashed lines, 0.5. Correspondingly coloured dashed/solid vertical lines indicate grounding zone width.

to best fit a model using an E of 0.88 and ν of 0.3. This was the case for most of the rest of the grounding zone. However, much further upstream, at the mapped grounding zone where the maximum ice thickness was 1913 m, the mapped width best fits an E of 1.1 and a ν between 0.3 and 0.5. Using values of ν for ice other than 0.3 should therefore be considered in future work.

The width of the grounding zone downstream of the Rutford pinning point as mapped from interferometry was 11 km (figure 6.1), and from the centre of the pinning point to the downstream extent of the grounding zone it was 12 km. As such, the model here best fits the lowest values of E and ν , although these still overestimate the width of the grounding zone from F to H. Modelling the width of the Rutford grounding zone at the sides of the ice stream using realistic values of E is a reasonable fit to that mapped from the interferograms, as the mapped grounding zone is approximately 29 km wide on the east side of the ice stream, where the ice thickness is 1929 m, and 34 km on the west side of the ice stream, where the ice thickness was 1955 m. The observed grounding zone widths lie between the values calculated from F to H using an E of 1.1 and a ν of 0.5, and an E of 9 and a ν of 0.3, although the latter value of E is not realistic. Compared to the modelled width using an E of 1.1 and a ν of 0.5, increasing the values of either the ice thickness, Young's modulus or Poisson's ratio would cause the model output to match the observed width of the grounding zone. Increasing the ice thickness is unrealistic: although the ice thicknesses are taken from BEDMAP and may therefore be affected by the 5 km resolution of the dataset, they are close to (and indeed derived from) ice thicknesses used by other authors in this region. Vaughan (1995), for example, used an ice thickness of 1550 m and Smith (1991) used 1800 m, from Stephenson and Doake (1982), who measured ice thickness with Radio Echo Sounding (RES). For the west side of the ice stream, where the grounding zone is modelled downstream of the extent of the horseshoe shaped area (downstream of where their ice thicknesses were taken from), widths using an elastic modulus of 9 GPa are actually closer to the width of the grounding zone as mapped from interferometry. However, this is not to suggest that this value of E applies in reality, as the grounding zone width is clearly affected by the central pinning point, whereas the model does not take bed topography into

account. It may also be that the Evans Ice Stream grounding zone is also affected by local pinning points which are not represented by the BEDMAP data due to their interpolation over wide areas from sparse data.

Elastic beam modelling therefore shows that the width of ice stream grounding zones can be modelled quite accurately with values of E between 0.88 and 1.1 and values of ν between 0.3 and 0.5, as long as ice thickness is known. As suspected, using an E of 9 vastly overestimates the width of the grounding zone and thus laboratory derived values of E for ice are unsuitable for use in this type of work.

6.5 Summary

The grounding zones of both the Rutford and Evans Ice Streams have been mapped using SAR interferometry and found to be several kilometres wide. Rutford's grounding zone is affected by a major pinning point in the centre of the ice stream, while Evans' grounding zone is shaped such that the east side of the ice stream is grounded and the west side floating for much of the length of the main trunk. While the grounding zones mapped from different SAR frames generally coincide, the vertical displacement represented by each interferogram differs because of differing amounts of tidal change between the scenes making up each interferometric pair, which were calculated using models. The width of the grounding zones could be accurately modelled using an elastic beam model with values of Young's Modulus (E) between 0.88 and 1.1 and Poisson's Ratio (ν) between 0.3 and 0.5, as long as the ice thickness is known and even if the tidal range is not. These results are discussed further in the next chapter.

Chapter 7

Discussion

7.1 Introduction

This chapter presents interpretation of the results of this study discussed in chapters 5 and 6, making use of the glaciological literature. Ice velocities and discharges derived here are compared to those of other authors, and the contradiction between the two balance velocity datasets used in this study is examined. There are a number of stages where errors and uncertainties may be introduced in interferometry, and these are discussed in turn. By far the most important error is the failure of the Constant Velocity Assumption (CVA), which is in itself a significant finding. The height errors that would be introduced to topography-only interferograms by non-constant displacement due the large tidal ranges of both ice streams are quantified. The accuracy of DEMs and GCPs used in this study and its effect on processing is also investigated. The grounding zones mapped from interferometry are compared to published sources for both ice streams. Finally, the effects of vertical tidal displacement on ice velocities derived from interferometry are examined.

7.2 Ice Stream Velocities

Many WAIS ice streams have shown marked changes in velocity over the period since the beginning of their study. From the velocities derived in section 5.4, it would seem that the Rutford Ice Stream maintained speed throughout the study period, while the Evans Ice Stream may have slowed down.

Velocities derived by InSAR for the Rutford Ice Stream match published velocities, which are summarised in table 7.1. This match includes velocities for the present day (section 2.8.1). This extends Frolich and Doake (1998)'s observation of no significant change in velocity from 1978 to 1992 through to 1996, and, taken with recent velocities such as from papers such as Murray *et al.* (2007), suggests that there has been no significant trend in the velocity of the Rutford Ice Stream in the past thirty years, since the beginning of its study. There may, however, have been shorter term fluctuations, such as that observed at the upstream end of the ice stream between 1992 and 1996 (section 5.4.1).

Table 7.1: Published velocities for the Rutford and Evans Ice Streams.

	Location	Velocity (m a^{-1})	Method	Authors
Rutford	For at least 130 km upstream of grounding line	300	Ground surveys with geodetic control from satellite tracking	Doake <i>et al.</i> (1987) and Frolich <i>et al.</i> (1989)
	Grounding line	Up to 400	Ground surveys in 1978-9 and 1979-80 field seasons	Stephenson and Doake (1982) and Doake <i>et al.</i> (1987)
	40 km upstream of grounding line	377.3	Differential GPS in 2003-4 field season	Murray <i>et al.</i> (2007)
	40 km upstream of grounding line	Up to 380	Differential GPS	Aðalgeirsdóttir <i>et al.</i> (2008)
Evans	No published velocities, other than as part of maps of wide areas, with inadequate keys for reading off velocities			

The Evans Ice Stream, on the other hand, appears to have slowed down between 1992 and 1996. Published velocities of this ice stream such as by Joughin and Bamber (2005) are in the form of maps, as part of a wider area, and so determining precise velocities for the Evans Ice Stream is not possible. However, velocities derived for the Evans Ice Stream in this study for 1992 are higher than the

published velocities appear to be, and published velocities appear close to what was observed in 1996. This suggests that the Evans Ice Stream is capable of flowing at higher velocities than previously thought, has done so in the recent past, and therefore may do so again. To determine the conditions under which this might take place is one of many reasons why the Evans Ice Stream merits further investigation.

7.2.1 Ice Stream Discharge

The discharge calculated for the Rutford Ice Stream, 18.7 Gt a^{-1} , is close to that given by Doake *et al.* (2001) and Rignot (1998b) (section 2.8.1), and to that estimated by Joughin and Bamber (2005) using flux gate methods at the shelf front. For the Evans Ice Stream, the discharge calculated from the lower velocities at the end of the study period, in 1996, is close to and within the error estimate of that estimated by Joughin and Bamber (2005) (section 2.8.2). This supports the validity of the assumptions used to estimate ice stream discharge in this study, including the higher estimate of discharge for Evans at the start of the study period.

This does, however, highlight one of the disadvantages of the study period being 1992 to 1996, which were the only phases in the lifetimes of the ERS satellites with orbital repeat periods short enough for interferometry, as discussed in section 4.2: it has not been possible to determine in this study how the ice streams have behaved in the last fourteen years. Presumably the slowdown of the Evans Ice Stream and decrease in its discharge either did not continue after 1996, or decreased further but recovered to 1996 levels before the ice stream was next studied by Joughin and Bamber (2005). Further observations of the Evans Ice Stream through the 1992 to 1996 period, using additional SAR frames, would be required to confirm the slowdown of the ice stream seen here.

As Evans has the highest discharge of any ice stream feeding the FRIS, changes in the discharge of the Evans Ice Stream could have a profound effect on the flow of the ice shelf. Section 2.7.1 showed how the collapse of Larsen B was triggered

by rupturing in suture zones between flow units on the ice shelf (Glasser and Scambos, 2008). Changes in the flow of any of the ice streams feeding the FRIS could therefore have serious consequences in terms of the stability of the FRIS.

7.2.2 Comparison to Balance Velocities

Balance velocities have a lot of associated errors and uncertainties, as discussed in section 4.4, but comparing InSAR derived velocities to them was interesting nonetheless. As Rutford and Evans between them drain an area greater than $150,000 \text{ km}^2$, or more than 8% of the $1,809,760 \text{ km}^2$ grounded area of the WAIS (Drewry *et al.*, 1982; Joughin and Bamber, 2005), whether or not they are in balance has a profound effect on the stability of the ice sheet.

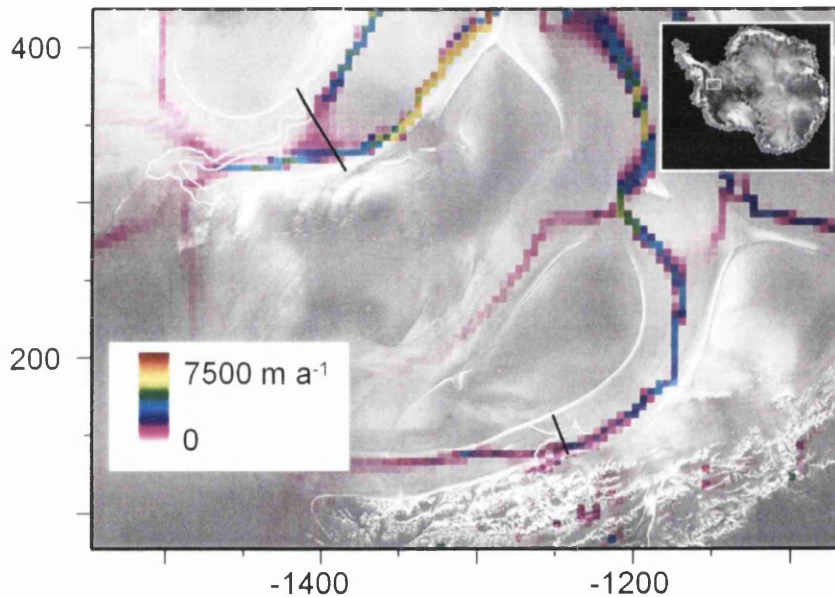


Figure 7.1: Balance velocities for the Rutford and Evans Ice Stream area, taken from Bamber *et al.* (2000c). The grounding zones derived in this study are shown in white. Coordinates are Polar Stereographic, in kilometres, with the origin at the South Pole.

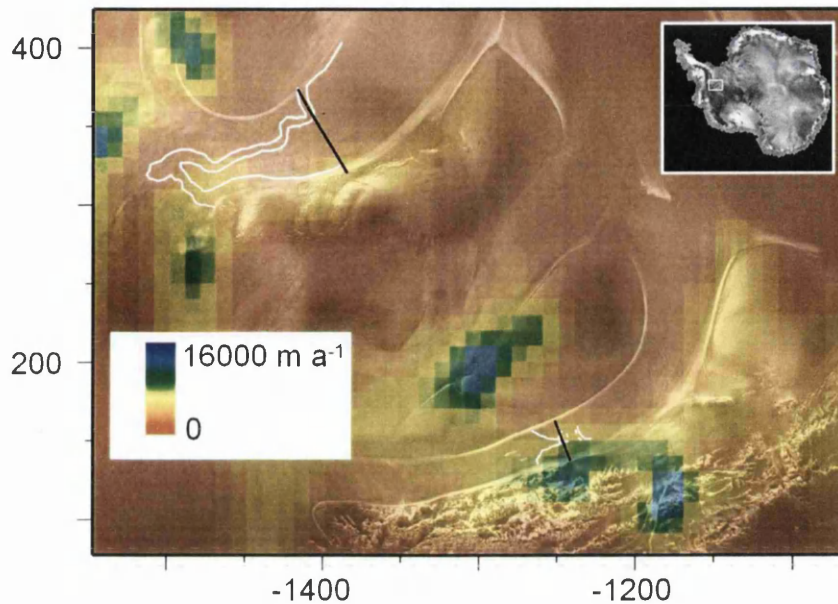


Figure 7.2: Balance velocities for the Rutford and Evans Ice Stream area, taken from Wu and Jezek (2004). The grouting zones derived in this study are shown in white. Coordinates are Polar Stereographic, in kilometres, with the origin at the South Pole.

Figures 7.1 and 7.2 show the balance velocities for both the Bamber *et al.* (2000c) and Wu and Jezek (2004) datasets for the study area, overlaid with the RAMP mosaic, with the locations of the profiles taken for the Rutford and Evans Ice Streams. The average balance velocities for these profiles are also shown in table 7.2. It is clear that the resolution of the balance velocity models used in this study means that the Rutford and Evans Ice Streams have not been captured fully. The Rutford Ice Stream shows up in Bamber *et al.* (2000c)'s model, for example, as only one 5 km pixel wide, whereas the ice stream is actually about 30 km wide. As such, some balance velocities which fall within the margins of the ice streams are similar to those values for slow moving ice frozen to its bed, tens of metres or less.

Bamber *et al.* (2000c)'s balance velocities reach more than 2200 m a^{-1} for the Rutford Ice Stream, although this value occurs some distance downstream of

Table 7.2: Average balance velocities across both ice streams from Bamber *et al.* (2000c) and Wu and Jezek (2004).

Ice Stream	Average balance velocity (Bamber <i>et al.</i> , 2000c) in m a^{-1}	Average balance velocity (Wu and Jezek, 2004) in m a^{-1}
Rutford	364	49.38
Evans	797	151.75

the grounding line and outside the extent of the SAR frames used in this study. Bamber *et al.* (2000c)'s balance velocities also reach more than 5000 m a^{-1} for the Evans Ice Stream. Taking the average balance velocity across the width of both ice streams at different points was seen as more representative than relying on the concentrated balance velocities in the narrow flow units. The average balance velocity at the Rutford grounding line as marked on figure 7.1 was 364 m a^{-1} , and at the Evans grounding line 797 m a^{-1} .

The difference between Bamber *et al.* (2000c) and Wu and Jezek (2004)'s balance velocities was examined. It was found to be negligible for slow moving areas of ice. However, Wu and Jezek (2004)'s balance velocities for ice streams and outlet glaciers were on average considerably lower and much less variable than those of Bamber *et al.* (2000c). This is the case for both the Rutford and Evans Ice Streams (table 7.2). Interestingly, Carlson Inlet has a higher balance velocity in Wu and Jezek (2004)'s dataset than either Rutford or Evans, reaching balance velocities of up to 344 m a^{-1} .

Because of the discrepancies between these two datasets, comparisons between published balance velocities and InSAR velocities proved inconclusive (section 5.6). High resolution, accurate balance modelling of all the ice streams draining the WAIS (and indeed the EAIS and Greenland) is therefore required before a more accurate assessment of the mass balance of these ice sheets can be made using this method.

Joughin and Bamber (2005) estimated the mass balance of all the catchments feeding the FRIS using a different method, by comparing discharge to accumu-

lation rather than by comparing ice stream velocities to balance velocities. Although they found slightly negative mass balance for Rutford and slightly positive for Evans, their figures were subject large errors caused by significant uncertainties in accumulation. For both ice streams, mass balances well within the error estimates could change the sign of the imbalance. It is clear that the mass balance of the ice streams feeding the FRIS requires a lot more investigation.

7.2.3 Implications

The complex nature of the drainage of the WAIS was established in chapter 2. The Rutford Ice Stream is in the minority of WAIS ice streams that are maintaining speed. The Evans Ice Stream appears to have undergone a deceleration, but its present behaviour is unknown. As seen in section 2.5, other WAIS ice streams, such as Mercer and Whillans, are also decelerating. Modelling suggests that basal temperatures may not be high enough to sustain streaming flow of those ice streams, and this should therefore be investigated for the Evans Ice Stream as well. However, one extremely important unknown about the behaviour of the Evans Ice Stream is the nature of its subglacial hydrological system. Other ice streams showing stagnation or deceleration are part of a larger ice-water-till system, such as that beneath Whillans, Kamb and Bindschadler ice streams or Rutford Ice Stream and Carlson Inlet. These systems each have a stagnant ice stream because its subglacial water is being diverted elsewhere (section 2.5). Deceleration of the Evans Ice Stream could have occurred because of a loss of subglacial water which is required to lubricate the bed, and whether the Evans Ice Stream is part of the same hydrological system as Rutford Ice Stream and Carlson Inlet should also be investigated, particularly to ascertain if the possibility exists that subglacial water diverted from the Evans Ice Stream might restart the flow of Carlson Inlet.

In the context of concern about climate change and rising sea levels, it is encouraging that neither the Rutford or Evans Ice Streams shows signs of acceleration or conclusive evidence of negative mass balance during the study period.

7.3 The Interferometric Method

Although the principles of Satellite Radar Interferometry are well established, “SAR interferometry is a relatively simple image-processing concept made complex in practice by the the exigencies of the data” (Fatland and Lingle, 1998, p.533). Rees (2006, p.205) states that “InSAR is technically difficult to implement, and cannot be described as a wholly predictable technique” and that it places “considerable technical demands on both the agency operating the SAR and the user processing the data” (Rees, 2006, p.74). All of this has held true in this study!

7.3.1 Uncertainties in Velocity

There are a number of potential sources of uncertainty about the velocities derived in this study, and in interferometry there are a large number of stages where errors and uncertainties can be introduced. These are discussed in the following sections. An accurate velocity field from interferometry relies on accurate calculation of the offsets between the scenes (section 7.3.2), an accurate baseline model, which in turn depends on accurate orbit information and a good assessment of the fringe rate (section 7.3.2), and correct phase unwrapping. Double difference interferometry relies also on precise coregistration of the single difference interferograms and good ground control for refining the baseline (section 7.3.6). Two-pass differential interferometry relies upon the accuracy of the DEM used to simulate the topographic phase (section 7.3.5) and that it has been correctly geocoded into slant range/azimuth coordinates. Errors and uncertainties in any of these contribute to errors in the velocities derived.

7.3.2 Interferometric Pairs

Offsets

The sheer size of the glaciological features examined in this study was always going to lead to problems when calculating the offsets between the SLCIs of each pair (section 3.5.6). The Evans Ice Stream can fill the whole width and/or height of a SAR frame, leaving only a small proportion of the scene composed of slow moving ice frozen to its bed. As the calculation of offsets is based on the assumption that the tracks have slowly converged or diverged as the satellite moves in the azimuth direction, offsets based on windows distributed throughout the whole image are required to produce an accurate polynomial. Authors studying smaller ice features note steps that can be taken to avoid a patch used to calculate offsets lying on an entirely moving area and thus having a high enough SNR to be accepted, such as the use of large patches (section 3.5.6). However, for the Evans Ice Stream, and the entire range width of some scenes of the Rutford Ice Stream for certain azimuths, avoiding this is impossible. Masking out fast moving areas for calculating offsets is also not feasible, as for some frames 90% of the frame or worse would be excluded (e.g. frame 023_5229, figure 4.2).

Bevan (2006) used this type of offset calculation. However, Bevan (2006)'s scenes of Austfonna, Svalbard, were different in nature to the scenes of the Rutford and Evans Ice Streams used in this study, as in the former case, each frame is mainly made up of slow moving ice, with fast moving outlet glaciers making up a comparatively small part of the scene, whereas in the latter case for this study, the frames are largely filled by the fast moving ice streams. Calculating the offsets based only on static parts of the images using `slc_track`, as Bevan (2006) did, was experimented with but found to produce far worse results in this case, particularly for the Evans Ice Stream which is considerably wider than Rutford and as such left a smaller stationary area per frame. Far more of the offset estimates were culled for having an unacceptable SNR, and the offset standard deviations were much higher. The effects of these less accurate offsets were seen clearly when comparing coherence images between different methods of calculating the offsets

and so this method of calculating offsets, masking out areas using `slc_track`, was rejected.

Frames examined with 6-day pairs were more difficult to work with than those with 1-day or 3-day pairs. As more horizontal displacement had occurred between the SAR images, calculating offsets was more difficult because parts of the image had moved more between scenes than would be the case for shorter temporal baselines.

Baselines

Two different methods of calculating baselines were used in this study: one based on orbit data, and one which based the parallel baseline on orbit data and the perpendicular baseline on the fringe rate (section 3.5.8). While the latter method is usually more accurate, it relies on the fringe rate being estimated for an area of the scene which is as flat as possible, but stationary. For some scenes of Rutford and all scenes of Evans, no such area exists, and if this method was used to calculate the baseline estimates were inaccurate when compared to baseline catalogues and other methods and led to poorly flattened interferograms.

Gabriel *et al.* (1989) state that processing must be the same for all images so that any phase errors introduced here will be the same for all images cancel out during phase differencing. Similarly, Massonnet and Feigl (1998) highlight that a small difference in the processing of once scene can have a much worse effect on the quality of an interferogram than a major error applied to both scenes. In this study, processing was kept consistent within each pair, triplet or quad, but in some cases different processing was used for different frames. Other researchers undertaking similar work should also select processing parameters on a frame by frame basis, as was done here, especially when their scenes differ in nature such as including varying amounts of slow- and fast-moving ice, bare rock and floating areas, rather than relying on a standard approach for all scenes.

Out of interest, for each pair of scenes, the ERS baseline catalogue (at <http://earth.esa.int/ers/sar/baselines>), the baselines estimated by the ESA

software descw, which was used to select the scenes used in this study (section 4.2), and baselines at the scene centre as calculated by base_perp, using several methods as discussed in section 3.5.8, were compared in a spreadsheet. Differences of up to 297 m in the perpendicular baselines were found, although differences were more typically tens of metres. This is a cautionary tale for users selecting suitable pairs of scenes for interferometry by their baselines (section 4.2), particularly when selecting interferometric pairs with the intention of optimising the baseline for either deriving topography (a baseline of tens to hundreds of metres) or being free from the effects of topography (a baseline close to zero), or when the the perpendicular baseline is approaching the critical baseline for interferometry (section 3.6).

Coherence

Coherence would be expected to be worse for Evans than Rutford because of its higher accumulation, and because its weather conditions make it more susceptible to aeolian redistribution of snow, and this was indeed the case. Coherence for the most upstream frame of the Rutford Ice Stream was also lower than for further downstream, which again would be expected because of its closer proximity to the Bellingshausen Sea coast leading to higher precipitation and accumulation.

7.3.3 Differential Interferometry

In this study, interferometry with triplets actually follows the methods of four pass differential interferometry with one scene in common, rather than three pass differential interferometry in the traditional sense spanning a displacement event (section 3.8.2).

In double differencing, the effects of flow on supposedly topography-only interferograms can be minimised by choosing interferograms whose baselines have opposite signs (Mohr *et al.*, 2003). However, as mentioned previously in section 4.2, for many suitably located frames only one possible combination of scenes for

differential interferometry was available for each time period, and as such being selective about baselines to that extent could not be afforded.

The first choice method for this project would have been to use double difference interferometry for all frames, and indeed scenes were ordered with a view to this (section 4.2). However, through the course of the project it became clear that one of the fundamental assumptions upon which double difference interferometry is based, the Constant Velocity Assumption, had been violated.

7.3.4 Failure of the Constant Velocity Assumption

By far the most important feature of the differential interferometry used in this study was the effects of the failure of the Constant Velocity Assumption (section 3.9), upon which forms of differential interferometry using 3 or 4 satellite passes rely. However, this assumption fails for the both the Rutford and Evans Ice Streams. The Constant Velocity Assumption should more accurately be called the Constant Displacement Assumption (CDA), as it applies to both horizontal and vertical displacements, and in the case of this study area, the failure of the CVA/CDA appears to be due to tidal effects in the grounding zones of both ice streams.

The effects of this failure manifest as false topographic fringes in supposedly “topography-only” interferograms, as seen in chapter 5 when showing the derivation of ice stream displacements. Figure 5.10 illustrated this phenomenon for frame 008_5337 over the three day triplet from 1994 (table 4.1). The two original interferograms, containing topographic and displacement phase, were shown as the righthand frames of figures 5.3 and 5.4. Vertical change in the grounding zone is clearly shown in the same position as for the original interferograms (the single difference interferogram of the first pair of this frame being the exception due to its low tidal range). In other parts of the interferogram the topographic fringes appear as expected. The high fringe rate in the Ellsworth Mountains is due to their steepness, the topography of the Fletcher Promontory is apparent and so is the more gentle downward slope of the ice stream from northwest to

southeast, i.e. the left of the frame to the right.

Figure 5.11 showed two similar examples from the Evans Ice Stream. The failure of the CVA/CDA for the Evans Ice Stream had the benefit that its grounding zone was actually easier to map from supposedly “topography-only” interferograms, as the pattern of displacement fringes could be quite complex in the original interferograms (section 5.2). If these interferograms were genuinely topography-only, then the grounding zones would not be visible in this manner.

The violation of the CVA/CDA occurs because the vertical displacements in the pairs of interferograms used to create the topography-only interferograms were not constant. These two interferograms combined into figure 5.10 contain different tidal height changes, 0.23 m for the first compared to -1.04 m for the second (table 6.2), and so the difference between the tidal height changes of the first and second interferograms is 1.27 m. For the righthand example of figure 5.11, the tidal height changes for the first and second pairs are -0.37 m and 0.02 m respectively (table 6.4), giving a difference of -0.39 m. These examples are typical of frames located over the grounding zone of either ice stream. It is clear that the CVA/CDA is dramatically untrue for the grounding zones of both ice streams, and this is seemingly a much more important effect for ice stream grounding zones than differing horizontal displacement.

The effects of the failure of the CVA, which has been better termed the CDA, on supposedly “topography-only” interferograms have also been noted by other authors. For example, Fatland and Lingle (1998), when looking at Bering Glacier, Alaska, found two concentric fringe patterns which they termed “phase bulls-eyes,” concentric circular patterns of fringes, in a nominally topography-only differential interferogram. With 3-day temporal baselines, a 9-day separation between the reference images and a differential baseline of 28 m, they would represent 1600 m of topography each. They ruled out atmospheric effects due to the localised nature of the phase bulls-eyes and their location over what was thought to be the deepest part of the icefield. The most likely explanation was a 0.20 m rise of the surface over 3 days, due to a hydrological event. Further investigation found phase bulls-eyes were 0.5 to 4 km in diameter, and represented both bumps and

dips on the surface and were associated with pressurisation and depressurisation events due to changes in subglacial water volume of interferometric timescales of 1 to 3 days (Fatland and Lingle, 2002). Similar phase bulls eye effects are observed in this study surrounding the pinning point at the centre of the Rutford Ice Stream (such as those visible in figures 5.1 and 6.2).

The difference between the Constant Velocity Assumption and the Constant Displacement Assumption is an important distinction to make. It is important to reiterate that the CVA refers to a constant rate of displacement in the LOS direction of the satellite, rather than constant ice velocity in the flow direction as the term velocity might suggest. In this case it is the vertical component of the velocity vector that is by far the most important, and this has been termed displacement to help differentiate it from ice movement in the flow direction. Because the grounding zones of the Rutford and Evans Ice Streams have a much higher than average tidal range than other ice shelves surrounding the Antarctic (sections 6.3 and 7.5), the effects of non-constant vertical displacement on “topography-only” interferograms would be expected to be worse here than for ice shelves with lower tidal ranges. However, even the 1-2 m tidal displacements common for Antarctic ice shelves would be expected to introduce similar effects, but to a lesser extent, and this must be taken into account when using differential interferometry of ice sheet grounding zones, tidewater glaciers and similar.

Height Errors

It is possible to calculate the effects of non-constant vertical displacement on topography-only interferograms (equation 3.29). Bevan (2006) states that to introduce a 10 m height error into a topography-only interferogram with an altitude of ambiguity of 80 m, non-constant velocity of 0.35 cm day^{-1} would be required for a tandem quad. In many study areas even this would be unlikely, and Fatland and Lingle (1998) state that for valley glaciers most failures of the CVA are less than 1 cm day^{-1} . However, non-constant displacements in ice stream grounding zones may theoretically be orders of magnitude greater than this. It must be kept in mind that non-constant displacement in this case need not be sustained

between scenes, as vertical displacements follow the cyclical nature of the tidal signal. A 1 m difference in LOS displacement, for example, which is entirely reasonable for this study area due to the large tidal ranges, would introduce errors in topography-only interferograms of the order of thousands of metres.

This phenomenon is illustrated by taking frame 023_5229 as the most extreme example from this study area. Although tidal height change may not be exactly equal to vertical displacement of the ice surface it is a good approximation for these purposes as shown in section 6.3.3. For the triplet of images of this frame the first, 6-day pair had a tidal height change of 1.70 m and the second, 3-day pair had a tidal height change of 0.05 m (table 6.4). This equates to non-constant vertical displacement of 1.65 m, or non-constant LOS displacement of 1.52 m. The “topography-only” interferogram of this frame was presented in figure 5.11 and a large number of fringes were present in the grounding zone. However, this interferogram could not be correctly flattened, probably because of the difficulties in establishing the correct offset between the original two interferograms (section 7.3.2) and having no suitable area to assess the fringe rate using an FFT (section 7.3.2), so the number of fringes cannot be interpreted in terms of the amount of displacement they represent. The combined altitude of ambiguity (calculated from the combined baseline) was 215 m. Given this, a non-constant LOS displacement of 1.52 m would lead to a height error of 11,575 m, an astonishing amount. Frame 008_5319 of the Rutford Ice Stream also showed extreme non-constant displacement. The two 1-day interferograms of this frame had a combined altitude of ambiguity of 202 m, and difference of 1.09 m in the amount of vertical displacement between them. This is equivalent to a difference of 0.97 m in LOS displacement between the two pairs. The height error introduced by this into a topography-only interferogram would therefore be 7120 m. There are other similar but less extreme examples from the study area. Frame 008_5337 in 1994, for example, although having a non-constant vertical displacement of 1.27 m, had a lower height error than frame 008_5319 because of its much lower combined altitude of ambiguity (lower being relative, as the height error would still have been 3560 m). Because the tidal range of this study area is so high compared to the rest of the Antarctic (section 7.5), it may be that failures of the CVA/CDA

to this extent are unprecedented, and evidence of failures of similar magnitude could not be found in the literature.

These findings suggest that it would be a good idea for researchers wishing to undertake interferometry of parts of the cryosphere with large or unknown tidal ranges to run a tidal model or obtain GPS surface height measurements of their study area prior to interrogating the ESA catalogue (or its future equivalents for new sensors with short enough temporal baselines) for suitable combinations of SAR scenes. It may, theoretically, be possible for users to select combinations of scenes in which the pairs making up the triplets or quads that would be used in differential interferometry have similar tidal effects present. However, errors and uncertainties in the tidal models as discussed in section 7.5 are likely to complicate this and the extreme sensitivity of SRI to vertical displacements mean that even small violations of the CVA/CDA have major effects on differential processing. An even greater constraint is the availability of such combinations of SAR scenes. As mentioned in section 4.2, many SAR frames have only one triplet or quad available for each of the three phases with suitable temporal baselines, and therefore one could not afford to be selective of scenes by their tidal displacements as well as all the usual considerations because it would quite likely leave no options for scene selection at all. Instead, researchers working in such areas should investigate the existence of a suitably accurate DEM which could be used to remove topography with 2-pass differential interferometry prior to selecting scenes, as this does not rely on the CVA/CDA and conducting forms of differential interferometry other than 2-pass is therefore inadvisable for ice stream or tidewater glacier grounding zones with vertical displacements of even a few centimetres.

In this study, this issue was overcome by using 2-pass differential interferometry to investigate SAR frames of both ice streams which proved unsuitable for 3- or 4-pass differential interferometry, along with frames for which only pairs of scenes had been obtained, as described in section 3.8.1. The results of this were presented in section 5.4.

Some frames which were only partially composed of the grounding zone and

floating areas could possibly have been used to derive velocities through double difference methods by taking a subset of the image excluding these areas, or masking out these areas in order to derive velocities for grounded areas. However, for many frames, the amount of the frame that would have been left was a very small proportion, and as the option of the alternative method of 2-pass differential interferometry was available this did not seem necessary. As the project progressed, the vertical motion observed in the grounding zones of both ice streams became the intended subject of study and therefore masking out grounding zones and floating areas would have defeated the object.

7.3.5 Comparison Between DEMs

The accuracy of the DEMs used in this study was a limiting factor, and became more important than anticipated once it became apparent most frames would have to be investigated using 2-pass rather than double difference interferometry because of the failure of the CVA/CDA (section 7.3.4). Three DEMs of Antarctica were considered in this study (section 4.3.4). The georegistered ERS, ICESat and RAMP DEMs were put into a GIS in ArcMap, corrected to WGS84 where necessary and resampled to 50 m resolution using a bilinear interpolator (section 4.3.5). Some major differences between the DEMs were found for the study area.

Taking the difference between the ICESat and RAMP DEMs, the two highest resolution DEMs, as an example (figure 7.3), differences of up to over 200 m occur for the Rutford Ice Stream, while the Evans Ice Stream fares slightly better with differences rarely exceeding 30 m. The difference between the RAMP and ERS DEMs also yielded similar values, although with the larger differences occurring more frequently for the Rutford Ice Stream. The differences between the ICESat and ERS DEMs were generally less than this, although this was affected by the low resolution of the ERS DEM with pixels closer to the ice stream margins having larger differences between DEMs. For steeper areas such as slow moving ice and mountains differences between all combinations of DEMs are far greater and the DEMs were not trusted in these areas (section 4.3.4). Although some

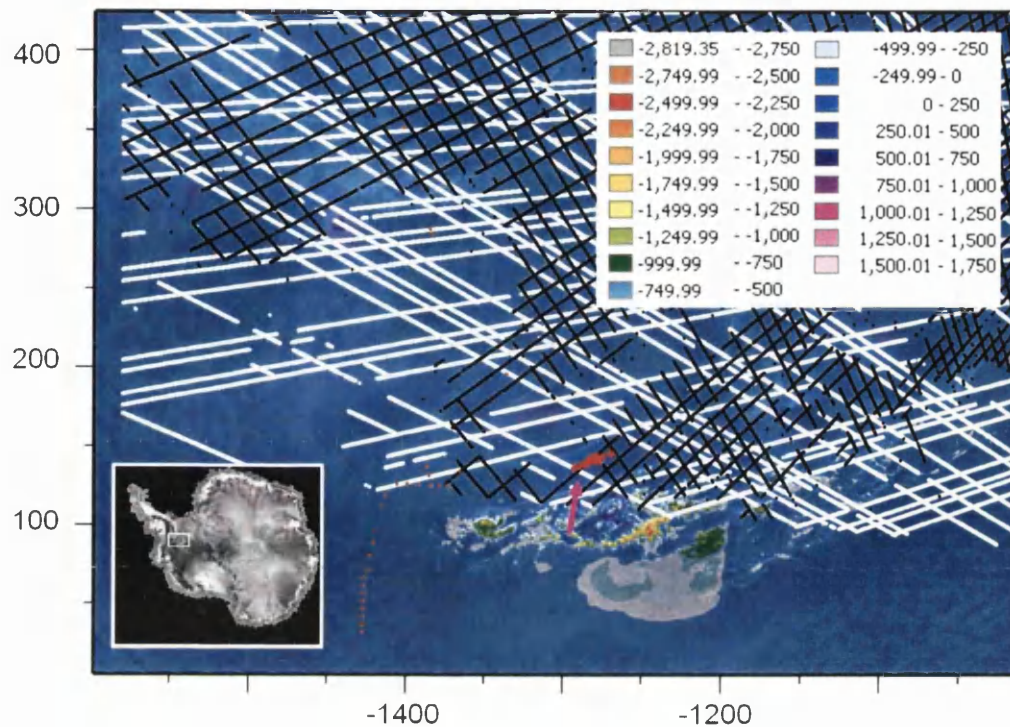


Figure 7.3: A classified map to show the difference between the ICESat and RAMP DEMs for the study area, in metres. Positive numbers indicate that the elevation of the ICESat DEM is greater. GCP datasets used in this study are also marked: GPS data in red, ICESat data in white and ERS data in black. Coordinates are Polar Stereographic, in kilometres, with the origin at the South Pole.

of the differences may be explained by differences in resolution, the fact that the DEMs needed to be sampled at precisely defined point locations meant that this was nonetheless unhelpful. Because of the sparse input data used in DEMs of the Antarctic (section 4.3.4), particularly compared to DEMs of many other regions, it is perhaps unsurprising that their accuracy is generally insufficient for this type of work.

7.3.6 Ground Control

The availability of ground control data for a remote study area such as Antarctica may be limited and it is telling that most data used as ground control in this study actually came from spaceborne sensors rather than field measurements. However, GCP data, even where available, could only be utilised for areas where topography-only interferograms could be derived (section 5.3; section 7.3.4).

Adding the GCP data to the same GIS as the DEMs gave even more discrepancies, with typical differences of up to tens of metres between a GCP and the DEMs for the same location. For the ice streams, GCP elevations were closer to those of the ICESat DEM than the other DEMs. Taking as an example the location marked with an arrow on figure 7.3, where an ERS track and ICESat track cross within approximately 2500 m of a GPS observation on the relatively flat topography of the main trunk of the Rutford Ice Stream, the elevations given are 293 m, 288 m and 307 m respectively. The ICESat and ERS DEMs both also give elevations of around 290 m in that area, while the RAMP DEM underestimates elevation dramatically (table 7.3).

Table 7.3: Comparison of elevations from different datasets for the location marked with arrow on figure 7.3 on the Rutford Ice Stream. DEMs had been resampled to 50 m resolution using a bilinear interpolator (section 4.3.5.)

Dataset	Elevation (m)
GPS	307
ERS Radar Altimeter	293
ICESat Lidar Altimeter	288
ERS DEM (Bamber and Bindshadler, 1997)	284
ICESat DEM (DiMarzio <i>et al.</i> , 2007)	289
RAMP DEM (Liu <i>et al.</i> , 1999)	193

More general errors with GCPs must also be taken into account, such as considering the size of the points in comparison to InSAR resolution. Altimetry measurements from ICESat, for example, are an average over the whole footprint area, and the footprint is the size of many SAR pixels even following geocoding.

There may also be genuine differences in surface elevation between GCPs and their corresponding locations on interferograms because of the time elapsed between the acquisition of the SAR images and the acquisition of the GCP datasets.

It is important that GCP datasets used to refine the baseline of a topography-only interferogram in order to produce a height map are not only accurate, but extend into all corners of the SAR frame. For the one frame for which more than two scenes had been obtained and which was far enough upstream to be free of vertical tidal motion in the grounding zone, 080_5265, three GCP datasets had to be combined to get adequate coverage of the scene. Coverage of GPS and altimeter data within this frame was shown in figures 4.3 and 4.5 respectively. Even so, the outer edges of the scene suffered from a lack of GCPs, the effects of which were apparent in the height map simulated from the topographic phase following the refinement of the baseline. The top left of the height map shown in figure 5.12 shows a false phase trend introduced because of a lack of GCPs in this area of the interferogram. Height maps produced using other datasets also contained this effect but to a far worse extent. Although the RMSE was best for the GPS points (table 5.1) this obviously applied to only the small part of the frame where the GPS points were located and it would be misleading to use the RMSE alone as an indicator of the effectiveness of the baseline refinement, as the height map produced using this dataset bore no resemblance to the topography of the scene. The RMSE alone should not be relied upon for assessing the quality of the fit. Examining the relationship between the original and precision baselines also gives an indication of the effectiveness of refining the baseline as these two baselines should not differ greatly in the combined baseline file. Sampling from DEMs (after resampling to slant range/azimuth coordinates) ensures that GCPs are spaced throughout the scene. However, this is affected by DEM resolution and accuracy, issues with which have been noted above.

Some point datasets did not end up being used as GCPs during interferometry, as the areas where they were located were covered by scenes which proved unsuitable for double difference interferometry. This applies to the two more downstream sets of GPS data for Rutford (section 4.3.1) and the Evans GPS data (section 4.3.1). However, these data still proved useful in assessing the accuracy (or oth-

erwise) of the DEMs.

7.3.7 Implications

The ICESat DEM was therefore chosen as the primary DEM for 2-pass differential interferometry (section 5.3.2) due to its superior accuracy compared to the RAMP DEM and its superior resolution compared to the ERS DEM.

It is clear that the accuracy of DEMs of large parts of Antarctica is a hindrance to processing. While satellite coverage is reasonably extensive, especially north of 81.5° , ground truthing is sparse, and, in some areas, non-existent. This highlights the importance of remote sensing in looking at these remote areas of the planet. Other authors working with DEMs of remote areas with little ground truthing should be wary of data quality, accuracy, resolution and consistency and should spend time investigating this.

Summarising section 7.3 so far, table 7.4 below summarises the desirable characteristics of SAR data, and the limitations arising from the nature of the SAR data used during this study.

7.3.8 Displacement Maps

It is important to reiterate that when displacement maps are produced (section 3.8.8) in either the look vector, the horizontal or the vertical this procedure does not separate the effects of displacements in these three directions, but merely assumes that all the displacement that has taken place within the scene is in one of these planes. They are always represented as positive numbers being towards the sensor.

Displacement maps produced once look vector displacements had been projected into the flow direction (section 3.8.9) were very patchy due to the nature of the DEMs, because areas where the flow direction was within 30° of normal

Table 7.4: Desirable characteristics of SAR data, and actual characteristics of the SAR data used in this study.

Desirable	Actual
Large number of available scenes with suitable temporal baselines	Usually only one pair or quad for each frame during each mission phase Available only for 1992-1996
Static areas within frames for offset calculation	Frames filled entirely by the Evans Ice Stream
Accurate baseline model: Good orbit information Good assessment of fringe rate	Good orbit information Not enough flat, stationary areas for good assessment of fringe rate
Accurate ground control for refining baseline	Inconsistencies between datasets
Accurate DEMs for simulation of topographic phase	Inconsistencies between datasets
Correct phase unwrapping	
Constant velocity	Tidal motion

to the look direction were masked out, and because areas which fell below the coherence threshold had not been unwrapped. Although these data were not effectively displayed as figures, they nonetheless provided useful information from their histograms and typical pixel values in different parts of each scene. This is another area of differential interferometry where the resolution and accuracy of DEMs used has a major effect. The patchiness of the displacement maps in the flow direction and the accuracy and resolution of the DEMs also prevented dual azimuth interferometry from being carried out. As all the areas where this would have been possible given the combination of scenes available in this study were areas where the signal from ice stream flow was complicated by that from vertical displacement the effectiveness of this method would have been limited in any case.

For Rutford, it is unsurprising that the only SAR frame for which the first choice method, double differencing, was possible, frame 080_5265, came out with the most sensible velocities, along with the other only frame which was free of tidal motion, 023_5265. It was comparatively easy to produce velocities for the Evans

Ice Stream, which was completely unexpected. The single difference interferograms were more complex than those of Rutford, there was no bare rock to use as a start point for phase unwrapping, no frames were suitable for double difference interferometry as no frames were unaffected by the vertical tidal motion of the grounding zone, and the grounding zone itself is a more complex shape, further complicating the interpretation of displacement. However, unwrapping was much easier for frames of Evans than of Rutford, with fewer residues, which is probably because the terrain of the Evans area is much less complex than that of the Rutford area. For this reason, it may also be that the DEM of the Evans area was more accurate than for Rutford and therefore the amount of topographic phase removed was more precise.

The frame that was by far the most significant in showing changing velocities was frame 023_5229 of the convergence of the five tributaries of the Evans Ice Stream in 1992 and 1994. The largest source of error in 2-pass differential interferometry, as used here, is inaccuracies in the input DEM. However, as this comparison between 1992 and 1994 was made using the same frame it was also made using the same segment of the DEM, and therefore any error from the DEM introduced into one frame would be introduced to the other (section 3.8.1). The seed point for phase unwrapping was also the same for 1992 and 1994. The two interferograms may contain different errors from their different offset fields, baseline models, and unwrapping solutions, but as the observed change in velocity was large, over 100 m a^{-1} , this signal would be greater than that introduced by any such errors and as such it can be confidently assumed that the significant change observed was real, especially compared to if the change had been observed from different frames in the same location at different times.

7.4 The Grounding Zone

It is now widely recognised that the previously held view of an ice sheet “grounding line” is an oversimplification (section 2.6), and instead study of the area where the ice starts to float should focus on the grounding zone between the landward and seaward limits of tidal flexing, F and H, as defined in section 2.6 and figure 2.3. Locating the grounding zone of an ice stream correctly is important for a number of reasons. Velocity data are likely to contain tidal modulation of the signal downstream of F, although more subdued tidal modulation of velocity may also occur considerable distances upstream of F (section 2.6.3). Recent literature has also shown that ice thickness and vertical strain rates may also contain tidal modulation downstream of F, as Jenkins *et al.* (2006) found on the Rutford Ice Stream. Monitoring grounding zone migration in order to assess the overall stability of the WAIS is also reliant on the initial location of the grounding zone, and its apparent variability between different data sources from different times, being correctly identified, as is the accuracy of models using grounding line location as a boundary condition. Accurate knowledge of the location, width and vertical forcing of ice stream grounding zones is paramount.

7.4.1 The Rutford Ice Stream Grounding Zone

The grounding zone mapped from interferometry for the Rutford Ice Stream is corroborated by previous work. Grounding lines used by, for example, Vaughan *et al.* (2003), Jenkins *et al.* (2006) and derived by Rignot (1998b), all of which were derived from SAR interferometry, agreed well with the grounding zone mapped using interferometry in this study (figure 7.4). However, it is also important to compare the mapped grounding zone derived here to that defined using methods other than interferometry. It was not possible to geocode some published versions of the Rutford grounding line and add them to the Rutford GIS as they lacked sufficient (or in some cases, any) map coordinates or other suitable features to be used as control points for georegistration. However, examining the mapped grounding zones of Stephenson and Doake (1982) and Stephenson (1984) (also

used by Doake *et al.* (1987) and Vaughan (1994)), which were derived using tiltmeters, seemed to corroborate the one derived in this study for the west side of the ice stream and the pinning point; Stephenson and Doake (1982)'s grounding line on the east side of the ice stream is further downstream than ours (although it is possible that the position of the grounding line changed between 1982 and the present study), and Stephenson (1984)'s figure does not extend that far east. This affirms the validity of the method used to map the grounding zone in this study, which was also applied to the Evans Ice Stream, for which no known maps of the grounding zone exist.

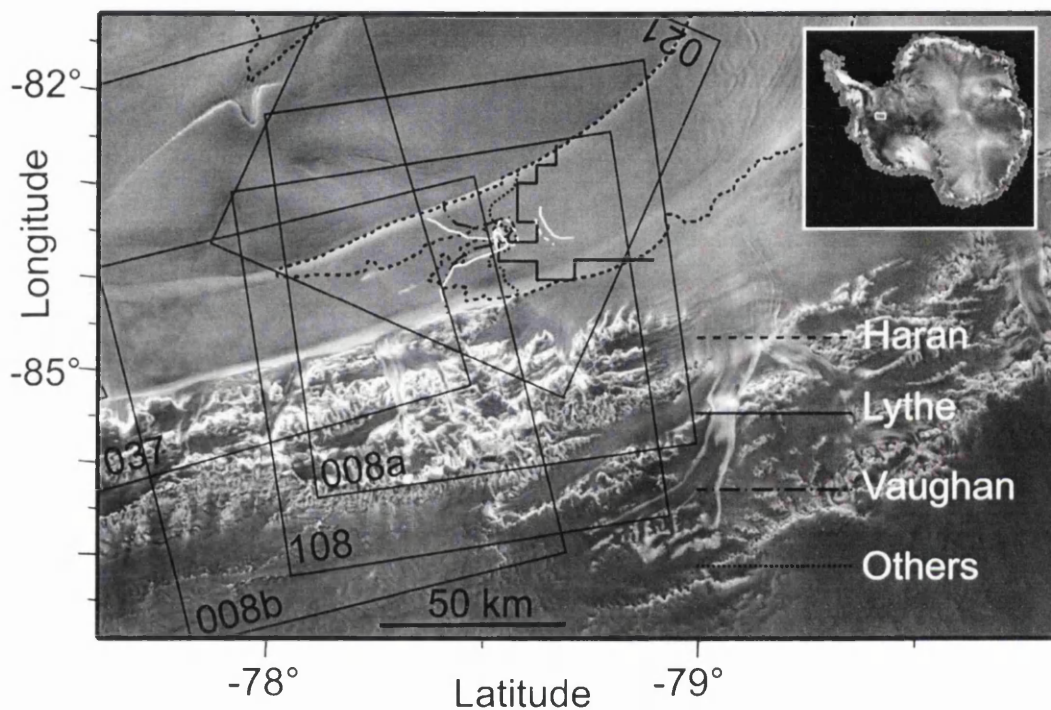


Figure 7.4: Published versions of the grounding line of the Rutford Ice Stream taken from Haran *et al.* (2006), Lythe *et al.* (2001), Vaughan *et al.* (2003) and other sources whose grounding lines coincide, such as Gudmundsson (2006) and Smith *et al.* (2007), with the grounding zone derived in this study shown in white.

A definition of the Rutford grounding line used by several papers published by authors at the British Antarctic Survey (for example Gudmundsson (2006) and

Smith *et al.* (2007), marked as 'Others' on figure 7.4) coincides with that derived in this study at the pinning point but lies farther downstream at the sides of the ice stream. However, it is not known what method was used to derive this grounding line, and it is probable that it was created using a method which identifies either G or I, since it lies within the grounding zone derived using interferometry, which identifies F and H (figure 2.3).

Several widely used datasets of the Antarctic define the Rutford Ice Stream's grounding line in a slightly different place to that mapped here (figure 7.4). However, this is discussed in the following section along with the Evans Ice Stream, where the problem is much more severe.

7.4.2 The Evans Ice Stream Grounding Zone

One of the reasons the Evans Ice Stream was chosen as the second study site was to investigate its grounding zone. The second order of SAR data, the scenes of Evans, were chosen after the initial results from the Rutford Ice Stream had been obtained and the tidal model run. It was known that published versions of the grounding line for the Evans Ice Stream (and versions defined within several widely used datasets of Antarctica such as BEDMAP) were very different, and that the grounding zone had a complex shape, and it was felt this merited further investigation.

The grounding lines from Vaughan *et al.* (2003) and Joughin *et al.* (2006)'s papers and from the BEDMAP data of Lythe *et al.* (2001) were digitised and added to a GIS, along with the grounding line from the MODIS mosaic (Haran *et al.*, 2006), which had been supplied as a shape file (NSIDC pers. comm. 2007). The Lythe *et al.* (2001) and Haran *et al.* (2006) grounding lines were similarly added to the Rutford GIS. Figure 7.5 shows the difference between the four grounding lines. It is clear that the Vaughan *et al.* (2003) and the Joughin *et al.* (2006) versions are quite close together, with differences of up to 9 km. The Haran *et al.* (2006) version is much farther downstream, up to 93 km from the other grounding lines. Other definitions of the Evans grounding line have clearly been used in other

published datasets: the BEDMAP dataset, for example, defines the grounding line even farther downstream than the Haran *et al.* (2006) grounding line, by as much as 37 km, as shown by the seaward limit of the grounded bed layer and the landward limit of the water depth layer. These two grounding lines are clearly on the floating ice shelf compared to the grounding zone mapped from interferometry (section 6.2). The Haran *et al.* (2006) grounding line for Rutford suffers the opposite problem and extends slightly too far upstream on the east side of the ice stream. The Lythe *et al.* (2001) grounding line for Rutford is correct at the pinning point but slightly too far downstream for the outer part of the ice stream. This imprecision clearly affects any work using the BEDMAP dataset as an input.

Similarly, for the Evans Ice Stream, the landward limit of the bathymetry grid in the CATS02.01 model, which is in a similar place to the grounding line of Lythe *et al.* (2001), meant that tidal components used in this study were extracted from the CATS02.01 model at a latitude of -76.75° and a longitude of -76.00° (figure 7.5) rather than for a coordinate closer to the mapped grounding zone, as mentioned previously in section 4.5.1. Whether the ice thickness used for the elastic beam model came from this location or from the mapped grounding zone made a difference of up to 9 km in the modelled width of the hinge zone using an elastic beam, for realistic values of E (section 6.4). Balance velocities from Wu and Jezek (2004) are also affected in the same way. The profile across the Evans Ice Stream taken for the Bamber *et al.* (2000c) balance velocities was located across the ice stream at the downstream extent of the hinge zone on the east side of the ice stream (figure 7.1). However, as Wu and Jezek (2004) calculated balance velocities for only grounded areas of the ice sheet, no balance velocities were available for the east side of the Evans ice stream that far downstream for comparison, so balance velocities from approximately 30 km further upstream were examined. Many more examples of imprecise location of ice stream grounding lines affecting the results of investigating ice streams using different methods are to be expected.

The locations of the grounding lines may differ because they were derived using different methods. Vaughan *et al.* (2003)'s Evans grounding line was proba-

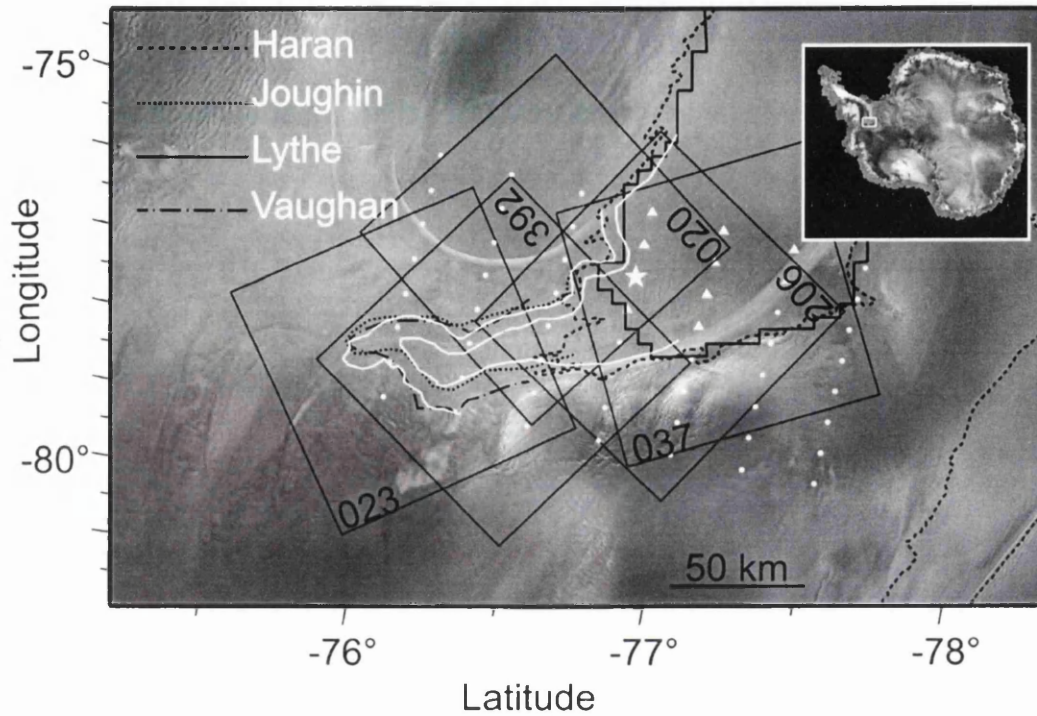


Figure 7.5: Published versions of the grounding line of the Evans Ice Stream taken from Haran *et al.* (2006), Joughin *et al.* (1996), Lythe *et al.* (2001) and Vaughan *et al.* (2003), with the grounding zone derived in this study shown in white. White triangles represent where the CATS02.01 model would run, with the white star showing the location for which the tidal components were extracted, and white circles indicate locations where it would not run due to its bathymetry grid not extending that far upstream.

bly digitised from an interferogram of Eric Rignot's (D. Vaughan pers. comm. 2007), which is presumably unpublished, and was described as the "current best estimate" only (Vaughan *et al.*, 2003, p.226). It is not known how Joughin *et al.* (2006)'s Evans grounding line was derived, although interferometry seems a safe assumption due to the nature of most of Joughin's work. Haran *et al.* (2006)'s grounding line was derived from identifying the slope break between grounded and floating ice by flicking between the MOA and RAMP mosaic in the Environment for Visualizing Images (ENVI), after stretching the image to improve contrast (NSIDC pers. comm. 2007). However, the grounding line of the MOA is intended, in future, to be reconciled with that of Joughin *et al.* (2006) (NSIDC pers. comm. 2007). It is not the case that the three grounding lines differ due to picking out different combinations of F, G, I and H, as were shown in figure 2.3. As previously stated, interferometry maps the zone between F and H, so methods locating either G or I would locate their grounding lines within the hinge zone as mapped from interferometry, and locating either F or H would match the upstream or downstream extent of the grounding zone as mapped from interferometry.

The Vaughan *et al.* (2003) and Joughin *et al.* (2006) grounding lines would be expected to be more accurate as they were defined for the Evans Ice Stream specifically, whereas Haran *et al.* (2006)'s grounding line is from a dataset of the whole of Antarctica, the MODIS mosaic, so would be expected to be at a much coarser resolution. BEDMAP and CATS also cover the whole of Antarctica, and the limits of their bathymetry grids would also be expected to be at a much coarser resolution than datasets defined for a specific ice stream.

The Evans ice stream grounding line has previously proved difficult to map using interferometry (Vaughan *et al.*, 2003, p.227), which is attributed to its complexity and "subdued subglacial topography." Figure 6.3 showed the grounding zone derived from interferometry in this study. Grounding lines by Vaughan *et al.* (2003) and Joughin *et al.* (2006) overlap with the grounding zone derived here. However, in 1992, 1994 and 1996 the Evans Ice Stream grounding zone was up to 100 km from its location in the BEDMAP dataset, a significant discrepancy even for an ice stream the size of Evans. Imprecise or incorrect location of the

grounding line also affects how other results have been interpreted and described. The five tributaries of the Evans Ice Stream are said by Vaughan *et al.* (2003) to converge 50 to 100 km upstream of the grounding line, for example, but this of course depends on where the grounding line is defined.

Although ice thickness and basal topography are known to affect grounding zone width (Fricker and Padman, 2006), in the case of the Evans Ice Stream this may also apply to its shape. On the eastern side of the main trunk, where the hinge zone is further downstream, the bed is shallower than on the western side (as shown using data from BEDMAP), with depths of, for example, 1249 m compared to 1546 m. The ice surface elevation is only slightly higher on the eastern side, for example, 235 m compared to 201 m. As such, on the part of the main trunk where the eastern side is grounded and the western side floating, the floating ice is thicker, for example, 1787 m compared to 1475 m (Lythe *et al.*, 2001), leading to a wider grounding zone.

The two most notable features about the Evans Ice Stream are its network of five tributaries and the complex shape of its grounding line, and it would seem that these two features are linked. The two more westerly tributaries of the Evans Ice Stream have higher velocities than the easterly group (e.g. figure 5.19). This may be because of the shape of the grounding zone, as these tributaries converge close to the grounding zone and therefore have far less buttressing from the ice shelf than the tributaries entering the east side of the ice stream whose grounding line is much further downstream.

7.4.3 Are These Grounding Zones Typical?

An important consideration is whether the grounding zones of the Rutford and Evans ice streams are typical of those of other WAIS ice streams, and whether they are similar to simplified theoretical models of ice stream grounding zones on which many assumptions about ice stream behaviour are based, and as such to what extent the features of these two grounding zones shown by this investigation are applicable elsewhere.

The Rutford grounding zone is unusual because of its pinning point. Smith (1997b) also felt that the Rutford grounding line is atypical for this reason and the surface crevassing the pinning point causes. However, the grounding zone of the Rutford Ice Stream has perhaps had more extensive field study than any other ice stream grounding zone. It may be that some things that seem atypical about it in fact apply to other ice streams, but have not yet been discovered. When the sinusoidal nature, the curved shape, of the Rutford grounding zone was first discovered by Stephenson and Doake (1982) they found it surprising, having assumed a simple hinge line, and the discovery of grounding zone more complex than previously thought may also be the case for other ice streams when they are investigated further. Evans, on the other hand, occupies a much wider and shallower basin than Rutford, without any obvious pinning points, but may be atypical because of its shape, particularly on the main trunk where the east side is grounded and the west side floating. Johnson and Smith (1997) also found overdeepening in the mouths of both Evans and Rutford ice streams (the area slightly upstream of where the ice stream opens out into the ice shelf) which may affect their grounding zones in a way that does not occur for ice streams without this overdeepening, and other ice streams should therefore be investigated to find out whether such overdeepening is present.

The current investigation of an ice stream grounding zone has shown that even locating it correctly in the first place may be problematic when different sources of information disagree, and although the grounding zone is easily located from single and double difference interferograms, this relies on appropriately located SAR frames being selected in the first place. Frame 037_5265, for example, proved to be mostly floating and as such was not very useful, although this was not known at the time the SAR scenes were ordered as the location of the grounding zone upstream from here had not been established. Correctly locating the grounding zone is an important prerequisite for further work investigating its nature and behaviour. 50% of the Antarctic coastline is made up of tidewater glaciers (Benn and Evans, 1998) and where possible, each should be examined using remote sensing methods to determine the correct location for the grounding zone. Using ERS interferometry to do this is not possible for those ice streams

grounded south of 81.5° , and for ice streams which have extremely low tidal ranges such that the grounding zone area with the high fringe rate would be much less distinguishable from the rest of the ice stream. However, in the latter case the effects of tidal forcing in the grounding zone would also be less.

In any case, it is clear that the traditionally held view of an ice stream “grounding line” is a gross oversimplification. Even if each ice stream’s unique characteristics mean that findings have only limited generalisability to other ice streams, knowledge of the behaviour of each of the ice streams draining the WAIS is necessary for an accurate assessment of its present and future mass balance and contribution to sea level rise.

7.5 The Tide

Both the Rutford and Evans Ice Streams have tidal ranges much higher than usual for the Antarctic. The usual tidal range for the ice shelves surrounding Antarctica is 1-2 m, and for the FRIS, 3 m (Doake, 1992; Padman *et al.*, 2002). Tidal effects on the Rutford and Evans Ice Streams may therefore be expected to be greater than on other ice streams because of their larger vertical forcing, over 6 m and 5 m respectively.

Tidal height change between the scenes making up each interferogram led to vertical motion of floating areas. The effects of this on the interpretation of ice displacements from InSAR are discussed in section 7.5.1 below. This effect also led to a high fringe rate in the grounding zone where the ice undergoes the transition from negligible vertical motion where it is grounded, to being freely floating in hydrostatic equilibrium. This led to the grounding zone being clearly defined in interferograms, enabling it to be mapped.

Tidal height change also explains the different grounding zone features present for the Rutford Ice Stream when the grounding zone is mapped from different frames. In figure 6.2, the left hand interferogram represented only a 0.23 m change in tidal height, and as such vertical change in the horseshoe shaped area is not

shown as there has been such a small amount of it. The right hand example represented 1.22 m of tidal height change, and clearly shows the vertical change in the grounding zone. The centre example showed a tidal height change of 0.33 m and showed the beginnings of the horseshoe shaped area. It is possible that a 0.23 to 0.33 m tidal height change is a threshold for vertical change in the grounding zone area. However, it is important to remember that the tide will have undergone several cycles between the acquisition of the images making up each interferometric pair, and the ice stream may be responding with a lag to these tidal changes. In any case, relatively small changes in tidal height can have a major effect on the way the grounding zone appears in interferometry.

In figure 6.2 the absence of the horseshoe-shaped part of the Rutford Ice Stream grounding zone in the lefthand example and its less defined nature in the centre example is not to suggest that the grounding line has moved tens of kilometres downstream with the tide, but rather that the amount of tidal height change for that interferometric pair is not sufficient for this feature to be visible.

The anomaly where frame 008_5337 for 1992 appears from the interferogram to have more tidal height change than was modelled may be a result of inaccuracies in the tidal models predicting a lower amount of tidal height change for that pair than actually took place, or because of the ice stream responding to the daily tidal range increasing throughout the three day pair from a neap tide towards a spring tide; the second 3-day pair of frame 008_5337 in 1994 and the pair from frame 021_5463 also occurred under those conditions but with much higher tidal height ranges.

A number of sources of error exist in the tidal model predictions. Errors in the CATS model, used as part of the Evans Ice Stream reconstruction, may originate from simplified model physics, errors in forcing, and errors in the water column thickness grid (Padman *et al.*, 2002). The inverse barometer effect means that the surface elevation of an ice shelf is depressed by 1 cm for a drop in pressure of 1 hPa (or 1 millibar). There are no meteorological data available for the time of acquisition of the SAR images used in this study (K. Makinson pers. comm., 2005) and therefore the inverse barometer effect is not part of the tidal reconstruction.

However, the tidal models used in this study reconstructed the observed vertical change well.

7.5.1 Vertical Ice Stream Motion

It was pleasing that the results of the tidal models correlated so well with observed vertical motion of the ice streams, particularly for Rutford (section 6.3.3).

It is clear that InSAR velocities of grounding zones and floating ice are contaminated by vertical tidal motion. Vertical motion of 0.425 m gives the same phase signal as a 1 m displacement in the horizontal flow direction corresponding to the look vector. This ratio occurs because of the 23° incidence angle (θ) of the ERS satellites, although the ratio varies as the local incidence angle varies due to terrain slope. Assuming a flat surface, such as an ice shelf, 1 m of displacement in the LOS is equivalent to 2.56 m displacement in the horizontal or 1.09 m of vertical displacement.

When horizontal and vertical displacements occur in opposite directions (i.e. towards versus away from the sensor) within a scene they may cancel each other out. This was the case for frame 008_5337 as shown in figure 5.17. The ice stream was flowing horizontally towards the sensor at approximately 400 m a^{-1} at the grounding zone, equivalent to about 3.3 m horizontal displacement for the 3-day temporal baseline, but the tide fell 1.04 m between scenes (table 6.2), equivalent to 2.45 m of ice flow upstream. By the edge of the frame, the ratio of downward vertical motion to forward velocity was such that the phase change due to the downward vertical motion dominated, giving the appearance of negative velocities, i.e. upstream flow. This effect manifests itself as an extreme gradient in flow velocity across the grounding zone of the displacement map, which is obviously entirely false.

Frames 392_5553 and 206_5535 of the Evans Ice Stream also exhibited this. These two displacement maps are presented in figure 5.21 using the same colour scale for direct comparison. These two interferograms had very similar tidal

displacements, -0.37 m and -0.38 m respectively, which is equivalent to approximately 0.87 m of flow away from the sensor in the horizontal, i.e. about 270° from the flow direction for frame 392_5553 and 225° from the flow direction for frame 206_5535 (figure 4.2). Frame 392_5553 appears to lose considerable velocity downstream of the grounding line, while frame 206_5535 appears to have negative velocity by the most downstream extent of the frame. In both cases, this is because the phase signal from ice velocity has been cancelled out by that from vertical motion to a lesser or greater extent. Figure 5.22 also shows an example of vertical ice motion away from the sensor, in this case corresponding to a tidal height change of -0.48 m.

When horizontal and vertical displacement occur in the same direction (i.e. both towards or both away from the sensor) the signal is amplified. This was the case for the edge of the Rutford grounding zone to the extreme right of figure 5.16, as the ice stream was flowing towards the sensor at approximately 1 m day^{-1} and the tide rose 0.37 m between scenes, equivalent to another 0.87 m day^{-1} of horizontal displacement in the flow direction, making velocities in this area appear much higher than they really are. Figures 5.18 also shows an example of upward ice motion towards the sensor, corresponding to a tidal height change of 0.58 m. The good correspondence between observed vertical motion from interferometry and tidal height change allowed good confidence in the performance of the tidal models.

The expected signal from vertical tidal motion should always be calculated for velocity fields derived for ice stream grounding zones, and preferably corrected for, especially as it may not always be immediately noticeable on visual inspection as it is in these extreme cases.

The sensitivity of interferograms to this effect is dependent on two main factors (in addition to the velocities and vertical displacements specific to a given ice stream): the angle between the look direction and the flow direction, and the temporal baseline. Because InSAR is sensitive to displacement in its LOS direction, it is most sensitive to ice flow in the plane parallel to the look vector, and not at all sensitive to ice flow perpendicular to the look vector, but equally sensitive

to vertical motion whatever the flow direction. As such, if vertical motion is the intended subject of study it may be better to select scenes where ice flow is perpendicular to the look direction in order to remove the effects of ice velocity on phase, which would be counterproductive for most interferometric applications of the cryosphere. For a given ice velocity and tidal range, interferograms with longer temporal baselines would be less sensitive to a given vertical displacement as the ratio between that and the horizontal displacement would increase. For example, an ice stream flowing at 1 m day^{-1} in the horizontal towards the sensor, a downward vertical displacement of 0.425 m would cancel out the signal from ice velocity giving an apparent displacement of zero. However, a 6-day interferogram of ice moving at the same velocity with a downward vertical displacement of 0.425 m would still appear to have moved 5 m of the 6 m it would actually have moved (this is not to suggest that equal vertical displacement is likely, due to the nature of the tidal signal, and in some circumstances depending on the combination of scenes and their position in the tidal cycle it would not even be possible). However, selecting pairs of scenes with longer temporal baselines over fast flow features may not be advisable and may cause coherence to be lost.

Examining the vertical displacements of the ice stream through counting fringes proved to be a valid method of assessing vertical ice stream displacement, compared to vertical displacements from unwrapped differential phase and the amount of vertical change expected from the tidal models. However, caution must be exercised when using this method for interferograms with long perpendicular baselines, i.e. low altitudes of ambiguity. Other authors have ignored altitudes of ambiguity of similar magnitudes to the ones in this study in previous work examining vertical ice displacements, for example, Rack *et al.* (1999) neglected a 26 m perpendicular baseline when studying the Larsen Ice Shelf using SAR interferometry. As the sensitivity of differential phase to displacement is independent of the baseline, the altitude of ambiguity does not affect the number of displacement fringes present.

7.6 Elastic Beam Modelling

Elastic beam modelling proved a useful way of predicting the width of an ice stream grounding zone, provided the input parameters are realistic. As the Rutford Ice Stream has been well studied and its values of E and ν established using field methods, if its grounding zone width could be accurately reconstructed with the model then the predictions of the model could be relied upon for the Evans Ice Stream which lacks such information.

As, in several locations, using a ν of 0.5 produced a better fit between the modelled and observed grounding zone width, it is clear that using values of ν for ice higher than the usual 0.3 should therefore be considered in future work, especially since Jenkins *et al.* (2006)'s work suggesting the ν of 0.5 from their observed horizontal and vertical strain data took place in the exact location being modelled downstream of the grounding line of the Rutford Ice Stream. Using higher values of E close to laboratory derived values of E for ice (section 4.6) do not produce accurate results, severely overestimating the width of the grounding zone, and should therefore be avoided in elastic beam modelling of grounding zones.

Taking the ice thickness from the correct location is extremely important, as changing this had a major effect on the results, as shown by the large differences in predicted grounding zone width for the Evans Ice Stream when ice thicknesses were 900 m different (section 4.6, table 6.8). For example, taking an E of 1.1 and a ν of 0.3, the modelled grounding zone width from F to H was 14.0 km for the ice thickness taken from further downstream, 1017 m, and 22.5 km for the ice thickness taken from further upstream, 1913 m, a difference of 8.5 km (greater than the width of some parts of the grounding zone), although both are based on valid ice thicknesses from the grounding zone of the same ice stream. This highlights another reason for establishing the correct location of the grounding zone in the first place in order to take ice thickness from the correct location here.

Comparing modelled and observed grounding zone widths using different values of the model parameters was by no means an attempt to infer ice properties. The grounding zone widths modelled using an E of 0.88 with a ν of 0.5 were so close

to those using an E of 1.1 and a ν of 0.3 that even if this were the intention it would be impossible to tell which of these combinations applied for any given observed grounding zone width. This does, however, legitimise the use of values of E between 0.88 and 1.1 and values of ν between 0.3 and 0.5 in elastic beam modelling of ice stream grounding zones.

7.7 Summary

The Rutford and Evans Ice Streams have many interesting glaciological characteristics which were investigated in this study. The Rutford Ice Stream appears to have maintained a steady speed over the last thirty years, making it unusual in West Antarctica. The Evans Ice Stream appears to have decelerated in the mid 1990s, and this clearly requires much more investigation. There is no evidence that either ice stream is significantly out of balance. InSAR is clearly a useful method for deriving ice velocities, but its limitations must also be considered. DEMs and ground control must be of sufficient quality and resolution and some datasets of this study area contradicted each other. The tidal ranges of both ice streams are significantly above average for Antarctica and cause significant vertical tidal motion in the grounding zones of both ice streams. This makes velocities from InSAR difficult to interpret as displacement signals from ice flow and vertical tidal height change may either amplify each other or cancel each other out. However, the most significant effect of the tidal range on interferometry is the failure of the Constant Velocity Assumption, which has been better termed the Constant Displacement Assumption, and non-constant displacements observed in this study and the errors they would introduce to double difference interferograms, due to the large tidal displacements, may be unprecedented.

Chapter 8

Conclusions and Further Work

8.1 Introduction

This chapter summarises the main findings of this thesis. The research aims and objectives discussed in section 1.3 have been met, and findings relating to both the glaciology of the Rutford and Evans Ice Streams, and to the remote sensing and modelling methods employed, will be presented. Recommendations for further research will also be made, based on the discoveries and shortcomings of this study, and in the context of the glaciological literature and new developments in satellite technology.

8.2 Summary of Results

8.2.1 Ice Stream Velocities

Ice stream velocities were derived using differential SRI using scenes from the SAR satellites ERS-1 and ERS-2. The Rutford Ice Stream increases in speed from approximately 180 m a^{-1} at the head of the main trunk to 400 m a^{-1} at the grounding line, and velocity does not appear to have changed throughout the study period. When considered with velocities taken from the literature, it appears flow has been steady from 1978 to the present. Estimated ice discharge, using ice thicknesses taken from the BEDMAP dataset of Lythe *et al.* (2001), is 18.7 Gt a^{-1} , similar to values from the literature such as Joughin and Bamber (2005)'s value of $17.8 \pm 1.8 \text{ Gt a}^{-1}$.

The Evans Ice Stream has a higher velocity than Rutford, and velocity appears to have decreased throughout the study period. Velocities reached up to 750 m a^{-1} where the five tributaries converge in 1992, but had decreased to 625 m a^{-1} in the same location in 1994. Displacements were more difficult to interpret for 1996 but velocity appears to be about 540 m a^{-1} . The western tributaries have higher velocities than those on the east. Discharge decreased from 46.17 Gt a^{-1} in 1992 to 35.40 Gt a^{-1} in 1996, the latter being similar to the published value of $35.7 \pm 3.6 \text{ Gt a}^{-1}$ (Joughin and Bamber, 2005).

While some WAIS ice streams have shown increases in velocity which may be as a result of climatic warming, particularly through decreased back pressure due to the loss of buttressing ice shelves, neither the Rutford or Evans Ice Streams have shown this, which is reassuring when examining the stability of the WAIS and its potential contribution to future sea level rise. However, further investigation is required, particularly as the velocities derived in this study were for 1996 at the latest because of the limited availability of satellite scenes with suitably short temporal baselines for interferometry.

Although comparing InSAR velocities to balance velocities was investigated, no consistent conclusions were found due to large differences between the two balance

velocity datasets considered. This highlights the issue of inconsistency between datasets of Antarctica, discussed further below, which often occurs because of sparse data and lack of ground truthing due to the inaccessible nature of the Antarctic continent.

The velocities derived in this study are all, however, subject to a number of uncertainties introduced during the method of interferometry.

8.2.2 Interferometry

Interferometry is a powerful tool for deriving ice velocities over large areas such as ice streams hundreds of kilometres in length, and in this study also proved useful for investigating vertical displacements. However, the availability of scenes with temporal baselines suitable for interferometry was a severe constraint on the method, particularly because the only periods in the lifetimes of the ERS satellites with suitable temporal baselines occurred during 1992-1996, i.e. at least twelve years ago.

The Constant Displacement Assumption

Double difference interferometry was prevented for many of the frames in this study due to failure of the Constant Velocity Assumption (CVA), which is paramount to differential interferometry. The CVA states that two interferograms which are differenced to produce a “topography-only” interferogram should contain the same phase due to displacement, in order for this to be removed when one is subtracted from the other. However, for both the Rutford and Evans Ice Streams, differing amounts of vertical motion took place due to changing tidal height, causing dramatic failure of the CVA. The CVA should be better called the Constant Displacement Assumption (CDA), to emphasise that velocity in the CVA means the three dimensional velocity vector, including vertical displacement, and not just ice displacement in the flow direction. Vertical displacement can have a much more significant effect because magnitudes of non-constant displacement can be

much greater than non-constant velocities and because interferometry is 2.3 times more sensitive to displacement in this direction compared to displacement in the horizontal plane corresponding to the look direction.

The failure of the CDA introduced large numbers of fringes in the grounding zones of supposedly “topography-only” interferograms, and for the Evans Ice Stream it actually proved easier to map the grounding zone from double difference than single difference interferograms. The amount of non-constant displacement observed in this study, because of the large tidal ranges of both ice streams, would introduce errors of thousands of metres into topography-only interferograms. This magnitude of non-constant displacement may be unprecedented in SRI of glaciated regions because of the extreme tidal range of the study area, and examples of a similar magnitude could not be found in the literature.

Failure of the CDA is something which must be considered by other researchers wishing to apply SAR interferometry to grounding zones with even modest tidal ranges. However, the failure of the CDA leading to bands of closely spaced fringes in the grounding zone of “topography-only” interferograms due to non-constant vertical tidal motion did have the advantage of making the grounding zone very easy to map.

Ground Truthing

Accurate Ground Control Points (GCPs) or Digital Elevation Models (DEMs) are also paramount for successful differential interferometry. GCPs are required to refine the interferometric baseline in double difference interferometry, and DEMs may either provide such GCPs or be geocoded into SAR coordinates and used to simulate the topographic phase in 2-pass differential interferometry. The accuracy of the simulated topographic phase, which is removed from single difference interferograms to leave displacement, is dependent on the accuracy of the DEM, and inaccuracies in the DEM therefore lead to errors in ice velocities. Inconsistencies between GCP and DEM datasets of remote areas is an issue which should be further investigated.

8.2.3 Grounding Zones

The investigation into the grounding zones of both ice streams, particularly, provided an equally useful insight into both the methods used in this study, and the characteristics of the study area.

The position of the grounding zone of the Rutford Ice Stream was constant between 1992 and 1996. For the Evans Ice Stream, it remained in the same place between 1994 and 1996, but the only SAR frame obtained for 1992 was too far upstream to say where the rest of the grounding zone was in that year. The position of the grounding zone does not migrate with the tide; that is to say, the landward and seaward limits of tidal flexing remain in the same place, but the behaviour of the limit of flotation and the inflection point cannot be determined from interferometry.

Neither the Rutford or Evans Ice Streams can be said to have a “grounding line” as such, instead having a grounding zone several kilometres wide which is clearly affected by changing tidal heights. The Rutford grounding zone has a central pinning point and extends up to 20 km upstream of this at the sides of the ice stream. The Evans Ice Stream has a complex shaped grounding zone which may be governed by its bed topography.

The grounding zones of both ice streams were mapped using SRI, and were easier to map from double difference interferograms which were free from the effects of ice stream flow. The Rutford grounding zone was mapped in a similar place to the grounding line as mapped by other authors, which confirms the validity of the method used. SAR interferometry maps the Evans grounding zone up to 100 km upstream of its location in some other widely used datasets.

The width of the grounding zone could be accurately modelled using an elastic beam when realistic values of Young’s modulus and Poisson’s ratio were used, as long as the ice thickness was known. Modelling the width of the grounding zone with an elastic beam does not depend on the tidal range being known.

8.2.4 The Tide

Both ice streams have high tidal ranges for Antarctica, with Rutford having a tidal range greater than 6 m and Evans greater than 5 m. This leads to extensive vertical motion of floating areas, including both the grounding zones of both ice streams, and the Ronne Ice Shelf farther downstream.

Tidal motion complicates the interpretation of velocities derived from interferometry. The displacements measured by InSAR are changes in the slant range distance between scenes, which may occur either due to ice flow or due to upward or downward vertical tidal motion. For an ice stream with a flow direction parallel to the look direction of the satellite, 1 m of ice flow produces the same phase change as 42.5 cm of vertical motion. As vertical displacements in both study areas may be far greater than this, downward vertical motion of the ice shelf can cancel out the signal from forward velocity to the extent that velocities appear negative, i.e. the ice stream appears to be flowing backwards. Similarly, upward vertical motion can cause velocities to appear much greater than they really are as the ice moves towards the sensor both forwards and upwards. Great care must be taken when interpreting InSAR velocities over grounding zones and floating areas, and this highlights the importance of correctly locating ice stream grounding zones and establishing their tidal ranges.

8.3 Further Work

There is a great deal of interesting further work to be done in this area. As a direct extension to this study, obtaining further SAR frames of the tributaries of the Evans Ice Stream and the onset region of Rutford and carrying out double differencing for both ice phases and the tandem phase (section 4.2) would be an interesting step. This would extend the velocity fields derived in this study further upstream, and allow investigation of whether the tributaries of the Evans Ice Stream underwent a change in velocity prior to or linked to the deceleration of the main trunk.

Extending the velocity fields of the Rutford and Evans Ice Streams to the present day could be achieved through SAR feature tracking. ERS-2 remains in a 35-day repeating orbit up to the present day, and the ESA satellite ENVISAT also follows this pattern. While this repeat period is too long to maintain coherence for interferometry, the short temporal baselines in interferometry are actually a hindrance to feature tracking because of the low signal-to-noise ratio (SNR) they cause. This was indeed found to be the case in this study, when feature tracking was experimented with early on, for scenes of the Rutford Ice Stream. Feature tracking may also be carried out on pairs of images where the temporal baseline would be short enough for interferometry, but coherence is low for reasons other than temporal decorrelation, such as fast flow speed. However, theoretically, feature tracking is not as accurate as interferometry.

Both ice streams have an above average tidal range for Antarctica, and as such the effects of tidal forcing on grounding zone processes and ice stream flow would be expected to be more pronounced here than elsewhere and should be further investigated. Excitingly, the British Antarctic Survey have a field campaign planned to study the grounding zone of the Evans Ice Stream with GPS, in order to derive the tidal constituents in a similar way to what has been done for Rutford, as Gudmundsson (2007) expected the Evans Ice Stream to show similar fortnightly tidal variations in velocity to Rutford, and the one tributary of Evans which has been studied has biweekly flow variations similar to Rutford. GPS receivers will be installed in January 2009, and the data will be collected one year later (H. Gudmundsson pers. comm. 2008).

Other ice streams feeding into the Filchner-Ronne Ice Shelf (FRIS) would benefit from similar studies using interferometry, tidal modelling and elastic beam modelling. Institute and Bailey Ice Streams, and Slessor Glacier, which drain into the FRIS from East Antarctica, and Jutulstraumen Glacier, at 0° longitude, were also considered for the second study site. However, Evans Ice Stream was chosen because it was felt working on the same coast as Rutford made the most sense. It would still be interesting to work on these sites, especially in the light of more recent work on the characteristics of these ice streams published in the intervening time. Jutulstraumen Glacier is a fast flow feature in an area shown

by the GRACE (Gravity Recovery and Climate Experiment) satellite to be losing mass (Chen *et al.*, 2008). Recent work using Radio Echo Sounding (RES) of Institute and Möller Ice Streams by Bingham *et al.* (2007) found that they were similar to the Siple Coast ice streams. However, Möller and Foundation Ice Streams and Support Force Glacier are all too far south for ERS coverage. Although RADARSAT's Antarctic Mapping Missions covered these areas, they collected data with a 24-day repeat, which is too long a temporal baseline to maintain coherence over ice moving at more than approximately 100 m a^{-1} (Joughin, 2002).

Totten Glacier, which has the largest discharge in East Antarctica, would also be an interesting area for a similar study. It has a similar grounding zone to Pine Island Glacier, with a 120 km confined ice shelf, and would be vulnerable to similar changes. It is already known to be thinning and suffering negative mass balance (Rignot, 2006) and so would merit further investigation.

The launch of two new SAR satellites, TerraSAR-X in June 2007, which has 11-day repeat coverage as far south as 82.6° , and RADARSAT-2 in December 2007, which has 24-day repeat coverage as far south as 81.4° , opens up new possibilities. It is surely impossible to assess the future of the FRIS, and in turn its effect on the stability of the WAIS (and indeed the EAIS) when so little is known about what several of the ice streams feeding into it are doing.

8.4 Final Remarks

The Rutford and Evans Ice Streams were chosen as the study areas for this thesis for opposite reasons: Rutford because of the large amount of previous work, data, research interest and understanding, and Evans because it lacked all of those. It is clear that remote sensing and modelling methods can not only provide mutual verification of and support for field measurements, but allow a great deal to be learnt about ice streams which have not had extensive field campaigns, and which indeed may not be able to have them because of adverse conditions on the ground.

As such, lack of field and ground truthing data should not exclude ice streams as study sites for remote sensing and modelling as much as it perhaps has done in the past.

References

- ADALGEIRSDÓTTIR, G., MURRAY, T., SMITH, A., KING, M., MAKINSON, K., NICHOLLS, K. and BEHAR, A., 2008, Tidal influence on Rutford Ice Stream, West Antarctica: Observations of surface flow and basal processes from closely-spaced GPS and passive seismic stations. *Journal of Glaciology*, **in press**.
- ALASKA SAR FACILITY, 1996, ERS-1 and ERS-2 SAR images. <http://www.asf.alaska.edu/reference/general/ERSproducts.pdf>, last viewed May 1, 2008.
- ALLEY, R., ANANDAKRISHNAN, S., DUPONT, T. and PARIZEK, B., 2004, Ice streams - fast, and faster?. *C.R. Physique*, **5**, 723–734.
- ALLEY, R. and BINDSCHADLER, R., 2001, The West Antarctic Ice Sheet and sea-level change. In *The West Antarctic Ice Sheet: Behavior and Environment* (American Geophysical Union), pp. 1–11.
- ALLEY, R., CLARK, P., HUYBRECHTS, P. and JOUGHIN, I., 2005, Ice-sheet and sea-level changes. *Science*, **310**, 456–460.
- ANANDAKRISHNAN, S. and ALLEY, R., 1997, Tidal forcing of basal seismicity of ice stream C, West Antarctica, observed far inland. *Journal of Geophysical Research*, **102(B7)**, 15,183–15,196.
- ANANDAKRISHNAN, S., ALLEY, R., JACOBEL, R. and CONWAY, H., 2001, The flow regime of ice stream C and hypotheses concerning its recent stagnation. In *The West Antarctic Ice Sheet: Behavior and Environment* (American Geophysical Union), pp. 283–296.

- ANANDAKRISHNAN, S., BLANKENSHIP, D., ALLEY, R. and STOFFA, P., 1998, Influence of subglacial geology on the position of a West Antarctic ice stream from seismic observations. *Nature*, **394**, 62–65.
- ANANDAKRISHNAN, S. and WINBERRY, J., 2004, Antarctic subglacial sedimentary layer thickness from receiver function analysis. *Global and Planetary Change*, **42**, 167–176.
- ANDERSON, J., 1999, *Antarctic Marine Geology* (Cambridge: Cambridge University Press).
- ANDERSON, J. and SHIPP, S., 2001, Evolution of the West Antarctic Ice Sheet. In *The West Antarctic Ice Sheet: Behavior and Environment* (American Geophysical Union), pp. 45–57.
- ARTHERN, R. and HINDMARSH, R., 2006, Determining the contribution of Antarctica to sea-level rise using data assimilation methods. *Philosophical Transactions of the Royal Society of London, Series A*, **364**, 1841–1865.
- BAMBER, J. and BINDSCHADLER, R., 1997, An improved elevation dataset for climate and ice-sheet modelling: validation with satellite imagery. *Annals of Glaciology*, **25**, 439–444.
- BAMBER, J., EKHOLM, S. and KRABILL, W., 2001, A new, high-resolution digital elevation model of Greenland fully validated with airborne laser altimeter data. *Journal of Geophysical Research*, **108(B4)**, 6733–6745.
- BAMBER, J., HARDY, R., HUYBRECHTS, P. and JOUGHIN, I., 2000a, A comparison of balance velocities, measured velocities and thermomechanically modelled velocities for the Greenland ice sheet. *Annals of Glaciology*, **30**, 211–216.
- BAMBER, J., HARDY, R. and JOUGHIN, I., 2000b, An analysis of balance velocities over the Greenland ice sheet and comparison with synthetic aperture radar interferometry. *Journal of Glaciology*, **46**, 67–74.
- BAMBER, J., VAUGHAN, D. and JOUGHIN, I., 2000c, Widespread complex flow in the interior of the Antarctic ice sheet. *Science*, **287**, 1248–1250.

- BAMLER, R. and HARTL, P., 1998, Synthetic Aperture Radar Interferometry. *Inverse Problems*, **14**, R1–R54.
- BELL, R., BLANKENSHIP, D., FINN, C., MORSE, D., SCAMBOS, T., BROZENA, J. and HODGE, S., 1998, Influence of subglacial geology on the onset of a West Antarctic ice stream from aerogeophysical observations. *Nature*, **394**, 58–62.
- BELL, R., STUDINGER, M., SHUMAN, C., FAHNESTOCK, M. and JOUGHIN, I., 2007, Large subglacial lakes in East Antarctica at the onset of fast-flowing ice streams. *Nature*, **445**, 904–907.
- BENN, D. and EVANS, D., 1998, *Glaciers and Glaciation* (London: Arnold).
- BENTLEY, C., 1998, Rapid sea level rise from a West Antarctic Ice-Sheet collapse - a short term perspective. *Journal of Glaciology*, **44**, 157–163.
- BENTLEY, C., 2004, Chapter 12: Mass balance of the Antarctic ice sheet: observational aspects. In *Mass balance of the Cryosphere* (Cambridge: Cambridge University Press), pp. 459–490.
- BEVAN, S., LUCKMAN, A., MURRAY, T., SYKES, H. and KOHLER, J., 2007, Positive mass balance during the late 20th century on Austfonna, Svalbard. revealed using satellite radar interferometry. *Annals of Glaciology*, **46**, 117–122.
- BEVAN, S., 2006, The spatial distribution of mass balance on Austfonna in Svalbard determined using satellite radar interferometry. PhD thesis, School of the Environment and Society, University of Wales Swansea.
- BINDSCHADLER, R., 2006, The environment and evolution of the West Antarctic ice sheet: setting the stage. *Philosophical Transactions of the Royal Society of London, Series A*, **364**, 1583–1605.
- BINDSCHADLER, R., BAMBER, J. and ANANDAKRISHNAN, S., 2001, Onset of streaming flow in the Siple Coast region, West Antarctica. In *The West Antarctic Ice Sheet: Behavior and Environment* (American Geophysical Union), pp. 123–136.

- BINDSCHADLER, R. and VORNBERGER, P., 1998, Changes in the West Antarctic Ice Sheet since 1963 from declassified satellite photography. *Science*, **279**, 689–692.
- BINDSCHADLER, R. and CHOI, H., 2007, Increased water storage at ice-stream onsets: a critical mechanism?. *Journal of Glaciology*, **53**, 163–171.
- BINDSCHADLER, R., KING, M., ALLEY, R., ANANDAKRISHNAN, S. and PADMAN, L., 2003, Tidally controlled stick-slip discharge of a West Antarctic ice stream. *Science*, **301**, 1087–1089.
- BINGHAM, R., SIEGERT, M., YOUNG, D. and BLANKENSHIP, D., 2007, Organized flow from the South Pole to the Filchner-Ronne ice shelf: An assessment of balance velocities in interior East Antarctica using radio echo sounding data. *Journal of Geophysical Research*, **112**, F03S26 doi:10.1029/2006JF000556.
- BLANKENSHIP, D., MORSE, D., FINN, C., BELL, R., PETERS, M., KEMPF, S., HODGE, S., STUDINGER, M., BEHRENDT, J. and BROZENA, J., 2001, Geologic controls on the initiation of rapid basal motion for West Antarctic ice streams: a geophysical perspective including new airborne radar sounding and laser altimetry results. In *The West Antarctic Ice Sheet: Behavior and Environment* (American Geophysical Union), pp. 105–121.
- BORNS, H., 2001, The glacial geologic terrestrial record from West Antarctica with emphasis on the last glacial cycle. In *The West Antarctic Ice Sheet: Behavior and Environment* (American Geophysical Union), pp. 59–74.
- BOUGAMONT, M. and TULACZYK, S., 2003, Glacial erosion beneath ice streams and ice-stream tributaries: constraints on temporal and spatial distribution of erosion from numerical simulations of a West Antarctic ice stream. *Boreas*, **32**, 178–190.
- BROMWICH, D. and RODGERS, A., 2001, The El Niño Southern Oscillation modulation of West Antarctic precipitation. In *The West Antarctic Ice Sheet: Behavior and Environment* (American Geophysical Union), pp. 91–103.

- BURGESS, D., SHARP, M., MAIR, D., DOWDESWELL, J. and BENHAM, T., 2005, Flow dynamics and iceberg calving rates of Devon Ice Cap, Nunavut, Canada. *Journal of Glaciology*, **51**, 219–230.
- CAMPBELL, J., 2002, *Introduction to Remote Sensing* (London: Taylor and Francis).
- CATANIA, G., CONWAY, H., RAYMOND, C. and SCAMBOS, T., 2006, Evidence for floatation or near floatation in the mouth of Kamb Ice Stream, West Antarctica, prior to stagnation. *Journal of Geophysical Research*, **111**, F01005 doi:10.1029/2005JF000355.
- CHEN, J., WILSON, C., TAPLEY, B., BLANKENSHIP, D. and YOUNG, D., 2008, Antarctic regional ice loss rates from GRACE. *Earth and Planetary Science Letters*, **266**, 140–148.
- CHURCH, J. and WHITE, N., 2006, A 20th century acceleration in global sea-level rise. *Geophysical Research Letters*, **33**, L01602 doi:10.1029/2005GL024826.
- CLARKE, G., 1987, Fast glacier flow: Ice streams, surging and tidewater glaciers. *Journal of Geophysical Research*, **92(B9)**, 8835–8841.
- CLOSA, J., 1998, The Influence of Orbit Precision in the Quality of ERS SAR Interferometric Data. http://earth.esa.int/ers/sysutil/ORB_QL.html, last viewed Apr 28, 2008.
- COLBECK, S., 1980, *Dynamics of Snow and Ice Masses* (London: Academic Press).
- CONWAY, H., CATANIA, G., RAYMOND, C., GADES, A., SCAMBOS, T. and ENGELHARDT, H., 2002, Switch of flow direction in an Antarctic ice stream. *Nature*, **419**, 465–467.
- CONWAY, H., HALL, B., DENTON, G., GADES, A. and WADDINGTON, E., 1999, Past and future grounding-line retreat of the West Antarctic Ice Sheet. *Science*, **286**, 280–283.

- COOK, A., FOX, A., VAUGHAN, D. and FERRIGNO, J., 2005, Retreating glacier fronts on the Antarctic Peninsula over the past half-century. *Nature*, **308**, 541–544.
- DAVIS, C., LI, Y., MCCONNELL, J., FREY, M. and HANNA, E., 2005, Snowfall-driven growth in East Antarctic Ice Sheet mitigates recent sea-level rise. *Science*, **308**, 1898–1901.
- DE ANGELIS, H. and SKVARCA, P., 2003, Glacier surge after ice shelf collapse. *Science*, **299**, 1560–1562.
- DIMARZIO, J., BRENNER, A., SCHUTZ, R., SHUMAN, C. and ZWALLY, H., 2007, GLAS/ICESat 500m laser altimetry digital elevation model of Antarctica. National Snow and Ice Data Center, Boulder, Colorado. (Digital media).
- DOAKE, C., 1992, Gravimetric tidal measurements on Filchner Ronne Ice Shelf. In *Proceedings of the Filchner-Ronne Ice Shelf Programme Report*, 6, pp. 34–39.
- DOAKE, C., CORR, H., JENKINS, A., MAKINSON, K., NICHOLLS, K., NATH, C., SMITH, A. and VAUGHAN, D., 2001, Rutford Ice Stream, Antarctica. In *The West Antarctic Ice Sheet: Behavior and Environment* (American Geophysical Union), pp. 221–235.
- DOAKE, C., CORR, H., NICHOLLS, K., GAFFIKIN, A., JENKINS, A., BERTIGER, W. and KING, M., 2002, Tide-induced lateral movement of Brunt Ice Shelf, Antarctica. *Geophysical Research Letters*, **29**, doi:10.1029/2001GL014606.
- DOAKE, C., FROLICH, R., MANTRIPP, D., SMITH, A. and VAUGHAN, D., 1987, Glaciological studies on Rutford Ice Stream, Antarctica. *Journal of Geophysical Research*, **92(B9)**, 8951–8960.
- DREWRY, D., JORDAN, S. and JANKOWSKI, E., 1982, Measured properties of the Antarctic ice sheet: surface configuration, ice thickness, volume and bedrock characteristics. *Annals of Glaciology*, **3**, 83–91.

- DUPONT, T. and ALLEY, R., 2005, Assessment of the importance of ice-shelf buttressing to ice-sheet flow. *Geophysical Research Letters*, **32**, L04503 doi:10.1029/2004GL022024.
- EKHOLM, S., 1996, A full coverage, high-resolution, topographic model of Greenland computed from a variety of digital elevation data. *Journal of Geophysical Research*, **101(B10)**, 21,961–21,972.
- ENGELHARDT, H. and KAMB, B., 1997, Basal hydraulic system of a West Antarctic ice stream: constraints from borehole observations. *Journal of Glaciology*, **43**, 207–230.
- ENGELHARDT, H. and KAMB, B., 1998, Basal sliding of Ice Stream B, West Antarctica. *Journal of Glaciology*, **44**, 223–230.
- EUROPEAN SPACE AGENCY, 2005, ERS-1 and ERS-2 Mission Phase Summary. <http://earth.esa.int/rootcollection/eo/missionphasesum.html>, last viewed Dec 19, 2007.
- EUROPEAN SPACE AGENCY, 2006a, ASAR FAQ. <http://envisat.esa.int/object/index.cfm?fobjectid=3772&contentid=3829>, last viewed Apr 28, 2008.
- EUROPEAN SPACE AGENCY, 2006b, ESA Earthnet: ERS instruments. <http://earth.esa.int/object/index.cfm?fobjectid=3978>, last viewed Dec 19, 2007.
- FAHNESTOCK, M. and BAMBER, J., 2001, Morphology and surface characteristics of the West Antarctic Ice Sheet. In *The West Antarctic Ice Sheet: Behavior and Environment* (American Geophysical Union), pp. 13–27.
- FATLAND, D. and LINGLE, C., 1998, Analysis of the 1993-95 Bering Glacier (Alaska) surge using differential SAR interferometry. *Journal of Glaciology*, **44**, 532–546.
- FATLAND, D. and LINGLE, C., 2002, InSAR observations of the 1993-95 Bering Glacier (Alaska, U.S.A.) surge and a surge hypothesis. *Journal of Glaciology*, **48**, 439–451.

- FORSTER, R., JEZEK, K., GYOO SOHN, H., GRAY, A. and MATTER, K., 1998, Analysis of flow dynamics from preliminary RADARSAT InSAR data of the Antarctic Mapping Mission. In *Proceedings of the Geoscience and Remote Sensing Symposium. IGARSS '98*, pp. 2225–2227.
- FRANCESCHETTI, G. and LANARI, R., 1999, *Synthetic Aperture Radar Processing* (Boca Raton, Florida: CRC Press).
- FRICKER, H. and PADMAN, L., 2002, Tides on Filchner-Ronne Ice Shelf from ERS radar altimetry. *Geophysical Research Letters*, **29**, doi:10.1029/2001GL014175.
- FRICKER, H. and PADMAN, L., 2006, Ice shelf grounding zone structure from ICESat laser altimetry. *Geophysical Research Letters*, **33**, L15502 doi:10.1029/2006GL026907.
- FRICKER, H., SCAMBOS, T., BINDSCHADLER, R. and PADMAN, L., 2007, An active subglacial water system in West Antarctica mapped from space. *Science*, **315**, 1544–1548.
- FROLICH, R. and DOAKE, C., 1988, Relative importance of lateral and vertical shear on Rutford Ice Stream, Antarctica. *Annals of Glaciology*, **11**, 19–22.
- FROLICH, R. and DOAKE, C., 1998, Synthetic Aperture Radar Interferometry over Rutford Ice Stream and Carlson Inlet, West Antarctica. *Journal of Glaciology*, **44**, 77–92.
- FROLICH, R. and MACAYEAL, D., 1990, Numerical modelling of Rutford Ice Stream, Antarctica. *Annals of Glaciology*, **14**, 336–336.
- FROLICH, R., VAUGHAN, D. and DOAKE, C., 1989, Flow of Rutford Ice Stream and comparison with Carlson Inlet, Antarctica. *Annals of Glaciology*, **12**, 51–56.
- GABRIEL, A., GOLDSTEIN, R. and ZEBKER, H., 1989, Mapping small elevation changes over large areas: differential radar interferometry. *Journal of Geophysical Research*, **94**(B7), 9183–9191.

- GAMMA REMOTE SENSING, *Gamma Reference Manual*, Bern, Switzerland 2002.
- GENS, R. and VAN GENDEREN, J., 1996, Review Article: SAR interferometry - issues, techniques, applications. *International Journal of Remote Sensing*, **17**, 1803–1835.
- GLASSER, N. and SCAMBOS, T., 2008, A structural glaciological analysis of the 2002 Larsen B ice shelf collapse. *Journal of Glaciology*, **54**, 3–16.
- GOLDSTEIN, R., ENGELHARDT, H., KAMB, B. and FROLICH, R., 1993, Satellite Radar Interferometry for monitoring ice-sheet motion: Application to an Antarctic ice stream. *Science*, **262**, 1525–1530.
- GOLDSTEIN, R. and WERNER, C., 1998, Radar interferogram filtering for geophysical applications. *Geophysical Research Letters*, **25**, 4035–4038.
- GOLDSTEIN, R., ZEBKER, H. and WERNER, C., 1988, Satellite radar interferometry: Two-dimensional phase unwrapping. *Radio Science*, **23**, 713–720.
- GRAY, L., SHORT, N., BINDSCHADLER, R., JOUGHIN, I., PADMAN, L., VORNBERGER, P. and KHANANIAN, A., 2002, RADARAT interferometry for Antarctic grounding-zone mapping. *Annals of Glaciology*, **34**, 269–276.
- GREGORY, J. and HUYBRECHTS, P., 2006, Ice-sheet contributions to future sea-level change. *Philosophical Transactions of the Royal Society of London, Series A*, **364**, 1709–1731.
- GUDMUNDSSON, G., 2006, Fortnightly variations in the flow velocity of Rutford Ice Stream, West Antarctica. *Nature*, **444**, 1063–1064.
- GUDMUNDSSON, G., 2007, Tides and the flow of Rutford Ice Stream, West Antarctica. *Journal of Geophysical Research*, **112**, F04007 doi:10.1029/2006JF000731.
- GUDMUNDSSON, S., GUDMUNDSSON, M., BJÖRNSSON, H., SIGMUNDSSON, F., ROTT, H. and CARSTENSEN, J., 2002, Three-dimensional glacier surface motion maps of the Gjálþ eruption site, Iceland, inferred from combining InSAR and other ice-displacement data. *Annals of Glaciology*, **34**, 315–322.

- HARAN, T., BOHLANDER, J., SCAMBOS, T., PAINTER, T. and FAHNESTOCK, M., 2006, MODIS mosaic of Antarctica (MOA) image map. National Snow and Ice Data Center, Boulder, Colorado. (Digital media).
- HARLAND, W., ARMSTRONG, R., COX, A., CRAIG, L., SMITH, A. and SMITH, D., 1990, *A Geologic Timescale 1989* (Cambridge: Cambridge University Press).
- HEINERT, M. and RIEDEL, B., 2007, Parametric modelling of the geometrical ice-ocean interaction in the Ekstroemisen grounding zone based on short time-series. *Geophysical Journal International*, **162**, 407–420.
- HENDERSON, F. and LEWIS, A. (Eds) , 1998, *Principles and Applications of Imaging Radar* (New York: Wiley).
- HERZFELD, U., 2004, *Atlas of Antarctica: Topographic Maps from Geostatistical Analysis of Satellite Radar Altimeter Data* (Berlin: Springer-Verlag).
- HEYWOOD, I., CORNELIUS, S. and CARVER, S., 2002, *An Introduction to Geographical Information Systems* (Harlow: Prentice Hall).
- HINDMARSH, R., 2006, The role of membrane-like stresses in determining the stability and sensitivity of the Antarctic ice sheets: back pressure and grounding line motion. *Philosophical Transactions of the Royal Society of London, Series A*, **364**, 1733–1767.
- HODGE, S. and DOPPELHAMMER, S., 1996, Satellite imagery of the onset of streaming flow of ice streams C and D, West Antarctica. *Journal of Geophysical Research*, **101(C3)**, 6669–6677.
- HOOKE, R.L., 2005, *Principles of Glacier Mechanics* (Cambridge: Cambridge University Press).
- HORGAN, H. and ANANDAKRISHNAN, S., 2006, Static grounding lines and dynamic ice streams: Evidence from the Siple Coast, West Antarctica. *Geophysical Research Letters*, **33**, L18502 doi:10.1029/2006GL027091.

- HUGHES, T., 1973, Is the West Antarctic Ice Sheet disintegrating?. *Journal of Geophysical Research*, **78**, 7884–7910.
- HULBE, C., JOUGHIN, I., MORSE, D. and BINDSCHADLER, R., 2000, Tributaries to West Antarctic ice streams: characteristics deduced from numerical modelling of ice flow. *Annals of Glaciology*, **31**, 184–190.
- HULBE, C. and PAYNE, A., 2001, The contribution of numerical modelling to our understanding of the West Antarctic Ice Sheet. In *The West Antarctic Ice Sheet: Behavior and Environment* (American Geophysical Union), pp. 201–219.
- HULBE, C., WANG, W., JOUGHIN, I. and SIEGERT, M., 2003, The role of lateral and vertical shear in tributary flow toward a West Antarctic ice stream. *Annals of Glaciology*, **36**, 244–250.
- HUYBRECHTS, P., 1990a, A 3-D model for the Antarctic Ice Sheet: a sensitivity study on the glacial-interglacial contrast. *Climate Dynamics*, **5**, 79–92.
- HUYBRECHTS, P., 1990b, The Antarctic Ice Sheet during the last glacial-interglacial cycle: a three-dimensional experiment. *Annals of Glaciology*, **14**, 115–119.
- HUYBRECHTS, P., 1992, The Antarctic Ice Sheet and environmental change: a three-dimensional modelling study. *Berichte zur Polarforschung*, **99**, 1–241.
- HUYBRECHTS, P., 2004, Chapter 13: Antarctica: Modelling. In *Mass balance of the Cryosphere* (Cambridge: Cambridge University Press), pp. 491–523.
- ICHOKU, C., KARNIELI, A., ARKIN, Y., CHOROWICZ, J., FLEURY, T. and RUDANT, J.P., 1998, Exploring the utility potential of SAR interferometric coherence images. *International Journal of Remote Sensing*, **19**, 1147–1160.
- INTERGOVERNMENTAL PANEL ON CLIMATE CHANGE: FOURTH ASSESSMENT REPORT, “Climate Change 2007: Synthesis Report. Longer Report”, 2007.
- IPCC WORKING GROUP I, “Intergovernmental Panel on Climate Change Fourth Assessment Report: Working Group I: Summary for Policy Makers”, 2007.

- JACOBSON, H. and RAYMOND, C., 1998, Thermal effects on the location of ice stream margins. *Journal of Geophysical Research*, **103(B6)**, 12,111–12,122.
- JENKINS, A., CORR, H., NICHOLLS, K., STEWART, C. and DOAKE, C., 2006, Interactions between ice and ocean observed with phase-sensitive radar near an Antarctic ice-shelf grounding line. *Journal of Glaciology*, **52**, 325–346.
- JEZEK, K. and THE RAMP PRODUCT TEAM, 2002, RAMP AMM-1 SAR image mosaic of Antarctica. Alaska Satellite Facility in association with the National Snow and Ice Data Center. (Digital media).
- JOHNSON, M. and SMITH, A., 1997, Seabed topography under the southern and western Ronne Ice Shelf, derived from seismic surveys. *Antarctic Science*, **9**, 201–208.
- JOUGHIN, I., 2002, Ice-sheet velocity mapping: A combined interferometric and speckle tracking approach. *Annals of Glaciology*, **34**, 195–201.
- JOUGHIN, I. and BAMBER, J., 2005, Thickening of the ice stream catchments feeding the Filchner-Ronne Ice Shelf, Antarctica. *Geophysical Research Letters*, **32**, L17503 doi:10.1029/2005GL023844.
- JOUGHIN, I., BAMBER, J., SCAMBOS, T., TULACZYK, S., FAHNESTOCK, M. and MACAYEAL, D., 2006, Integrating satellite observations with modelling: basal shear stress of the Filchner-Ronne ice streams, Antarctica. *Philosophical Transactions of the Royal Society of London, Series A*, **364**, 1795–1814.
- JOUGHIN, I., GRAY, L., BINDSCHADLER, R., PRICE, S., MORSE, D., HULBE, C., MATTAR, K. and WERNER, C., 1999, Tributaries of West Antarctic ice streams revealed by RADARSAT interferometry. *Science*, **286**, 283–286.
- JOUGHIN, I., KWOK, R. and FAHNESTOCK, M., 1998, Interferometric estimation of three-dimensional ice-flow using ascending and descending passes. *IEEE Transactions on Geoscience and Remote Sensing*, **36**, 25–37.
- JOUGHIN, I. and PADMAN, L., 2003, Melting and freezing beneath Filchner-Ronne Ice Shelf, Antarctica. *Geophysical Research Letters*, **30**, doi:10.1029/2003GL016941.

- JOUGHIN, I. and TULACZYK, S., 2002, Positive mass balance of the Ross Ice Streams, West Antarctica. *Science*, **295**, 476–480.
- JOUGHIN, I., TULACZYK, S., BINDSCHADLER, R. and PRICE, S., 2002, Changes in west Antarctic ice stream Velocities: Observation and analysis. *Journal of Geophysical Research*, **107**(B11), doi:10.1029/2001JB001029.
- JOUGHIN, I., TULACZYK, S. and ENGELHARDT, H., 2003, Basal melt beneath Whillans Ice Stream and Ice Streams A and C, West Antarctica. *Annals of Glaciology*, **36**, 257–262.
- JOUGHIN, I. and VAUGHAN, D., 2004, Marine ice beneath the Filchner-Ronne Ice Shelf, Antarctica: a comparison of estimated thickness distributions. *Annals of Glaciology*, **39**, 511–517.
- JOUGHIN, I., WINEBRENNER, D., FAHNESTOCK, M., KWOK, R. and KRABILL, W., 1996, Measurement of ice-sheet topography using satellite-radar interferometry. *Journal of Glaciology*, **42**, 10–22.
- JOUGHIN, I., WINEBRENNER, D. and FAHNESTOCK, M., 1995, Observations of ice-sheet motion in Greenland using satellite radar interferometry. *Geophysical Research Letters*, **22**, 571–574.
- KAMB, B., 2001, Basal zone lubrication of the West Antarctic ice streams and its role in lubrication of their rapid motion. In *The West Antarctic Ice Sheet: Behavior and Environment* (American Geophysical Union), pp. 157–199.
- KING, E., WOODWARD, J. and SMITH, A., 2004, Seismic evidence for a water-filled canal in deforming till beneath Rutford Ice Stream, West Antarctica. *Geophysical Research Letters*, **31**, L20401 doi:10.1029/2004GL020379.
- KING, E., WOODWARD, J. and SMITH, A., 2007, Seismic and radar observations of subglacial bed forms beneath the onset zone of Rutford Ice Stream, Antarctica. *Journal of Glaciology*, **53**, 665–672.
- KING, M., PENNA, N., CLARKE, P. and KING, E., 2005, Validation of ocean tide models around Antarctica using onshore GPS and gravity data. *Journal of Geophysical Research*, **110**, B08401 doi:10.1029/2004JB003390.

- KWOK, R. and FAHNESTOCK, M., 1996, Ice sheet motion and topography from radar interferometry. *IEEE Transactions on Geoscience and Remote Sensing*, **34**, 189–200.
- LARA STEERING COMMITTEE, “LARA - Scientific opportunities for a long range aircraft for research in Antarctica”, 2005.
- LAROUB, E., RIGNOT, E., JOUGHIN, I. and AUBRY, D., 2005, Rheology of the Ronne Ice Shelf, Antarctica, inferred from satellite radar interferometry data using an inverse control method. *Geophysical Research Letters*, **32**, L05503 doi:10.1029/2004JB003390.
- LETRÉGUILLY, A., REEH, N. and HUYBRECHTS, P., 1991, The Greenland Ice Sheet through the last glacial - interglacial cycle. *Global and Planetary Change*, **4**, 385–394.
- LIU, H., JEZEK, K. and LI, B., 1999, Development of an Antarctic digital elevation model by integrating cartographic and remotely sensed data: A geographical information system based approach. *Journal of Geophysical Research*, **104**(B10), 23,199–23,213.
- LUCKMAN, A., MURRAY, T., JISKOOT, H., PRITCHARD, H. and STROZZI, T., 2003, ERS SAR feature-tracking measurement of outlet glacier velocities on a regional scale in East Greenland. *Annals of Glaciology*, **36**, 129–134.
- LUCKMAN, A., MURRAY, T. and STROZZI, T., 2002, Surface flow elevation throughout a glacier surge measured by satellite radar interferometry. *Geophysical Research Letters*, **29**, doi:10.1029/2001GL014570.
- LYTHE, M., VAUGHAN, D. and THE BEDMAP CONSORTIUM, 2001, BEDMAP: A new ice thickness and subglacial topographic model of Antarctica. *Journal of Geophysical Research*, **106**(B6), 11,335–11,351.
- MAGNÚSSON, E., ROTT, H., BJÖRNSSON, H. and PÁLSSON, F., 2007, The impact of jökulhlaups on basal sliding observed by SAR interferometry on Vatnajökull, Iceland. *Journal of Glaciology*, **53**, 232–240.

- MASSONNET, D. and FEIGL, K., 1998, Radar interferometry and its application to changes in the Earth's surface. *Reviews of Geophysics*, **36**, 441–500.
- MASSONNET, D., VADON, H. and ROSSI, M., 1996, Reduction of the need for phase unwrapping in radar interferometry. *IEEE Transactions on Geoscience and Remote Sensing*, **34**, 489–497.
- MCGIBBON, K. and SMITH, A., 1991, New geophysical results and preliminary interpretation of crustal structure between the Antarctic Peninsula and Ellsworth Land. In *Geological Evolution of Antarctica* (Cambridge: Cambridge University Press), pp. 475–479.
- MCINTYRE, N., 1985, The dynamics of ice-sheet outlets. *Journal of Glaciology*, **31**, 99–107.
- MEIER, M., DYURGEROV, M., RICK, U., O'NEEL, S., PFEFFER, W., ANDERSON, R., ANDERSON, S. and GLAZOVSKY, A., 2007, Glaciers dominate eustatic sea level rise in the 21st century. *Science*, **317**, 1064–1067.
- MERCER, J., 1978, West Antarctic ice sheet and CO₂ greenhouse effect: a threat of disaster. *Nature*, **271**, 321–325.
- MOHR, J., REEH, N. and MADSEN, S., 1998, Three-dimensional glacier flow and surface elevation measured with radar interferometry. *Nature*, **391**, 273–276.
- MOHR, J., REEH, N. and MADSEN, S., 2003, Accuracy of three-dimensional glacier surface velocities derived from radar interferometry and ice-sounding radar measurements. *Journal of Glaciology*, **49**, 210–222.
- MORRIS, E. and VAUGHAN, D., 2003, Spatial and temporal variation of surface temperature on the Antarctic Peninsula and the limit of viability of ice shelves. In *Antarctic Peninsula Climate Variability - Historical and Paleoenvironmental Perspectives* (Washington D.C.: American Geophysical Union), pp. 61–68.
- MURRAY, T., LUCKMAN, A., STROZZI, T. and NUTALL, A.M., 2003a, The initiation of glacier surging at Fridtjovbreen, Svalbard. *Annals of Glaciology*, **36**, 110–116.

- MURRAY, T., SMITH, A., KING, M. and WEEDON, G., 2007, Ice flow modulated by tides at up to annual periods at Rutford Ice Stream, West Antarctica. *Geophysical Research Letters*, **34**, L18503 doi:10.1029/2007GL031207.
- MURRAY, T., STROZZI, T., LUCKMAN, A., JISKOOT, H. and CHRISTAKOS, P., 2003b, Is there a single surge mechanism? Contrasts in dynamics between glacier surges in Svalbard and other regions. *Journal of Geophysical Research*, **108(B5)**, doi:10.1029/2002JB001906.
- NATIONAL SNOW AND ICE DATA CENTER, 2001, Radarsat Antarctic Mapping Project Digital Elevation Model Version 2. http://nsidc.org/data/docs/daac/nsidc0082_ramp_dem_v2.gd.html, last viewed Jan 21, 2008.
- NG, F. and CONWAY, H., 2004, Fast-flow signature in the stagnated Kamb Ice Stream, West Antarctica. *Geology*, **32**, 481–484.
- NPA GROUP, 2008, A Brief Guide to SAR Interferometry (InSAR). http://www.npagroup.co.uk/insar/whatisinsar/insar_simple.htm, last viewed Apr 28, 2008.
- OPEN UNIVERSITY COURSE TEAM, 1999, *Waves, Tides and Shallow Water Processes* (Oxford: Butterworth-Heinemann).
- OPPENHEIMER, M., 1998, Global warming and the stability of the West Antarctic Ice Sheet. *Nature*, **393**, 325–332.
- PADMAN, L., 2005, Tide Model Driver (TMD) Manual. http://www.esr.org/polar_tide_models/README_TMD.pdf, last viewed May 29, 2008.
- PADMAN, L., FRICKER, H., COLEMAN, R., HOWARD, S. and EROFEEVA, L., 2002, A new tide model for the Antarctic ice shelves and seas. *Annals of Glaciology*, **34**, 247–254.
- PARIZEK, B., ALLEY, R. and HULBE, C., 2003, Subglacial thermal balance permits ongoing grounding-line retreat along the Siple Coast of West Antarctica. *Annals of Glaciology*, **36**, 251–256.

- PATERSON, W., 1994, *The Physics of Glaciers* (Oxford: Butterworth-Heinemann).
- PATTYN, F., HUYGHE, A., DE BRABANDER, S. and DE SMEDT, B., 2006, Role of transition zones in marine ice sheet dynamics. *Journal of Geophysical Research*, **111**, F02004 doi:10.1029/2005JF000394.
- PAWLOWICZ, R., BEARDSLEY, B. and LENTZ, S., 2002, Classical tidal harmonic analysis including error estimates in MATLAB using T_TIDE. *Computers & Geosciences*, **28**, 929–937.
- PAYNE, A., 1999, A thermodynamical model of ice flow in West Antarctica. *Climate Dynamics*, **15**, 115–125.
- PRITCHARD, H., MURRAY, T., STROZZI, T., BARR, S. and LUCKMAN, A., 2003, Surge-related topographic change of the glacier Sortebrae, East Greenland, derived from Synthetic Aperture Radar interferometry. *Journal of Glaciology*, **49**, 381–390.
- PRITCHARD, H. and VAUGHAN, D., 2007, Widespread acceleration of tidewater glaciers on the Antarctic Peninsula. *Journal of Geophysical Research*, **112**, F03S29 doi:10.1029/2006JF000597.
- RABUS, B. and LANG, O., 2003, Interannual surface velocity variations of Pine Island Glacier, West Antarctica. *Annals of Glaciology*, **36**, 205–214.
- RACK, W. and ROTT, H., 2004, Pattern of retreat and disintegration of the Larsen B ice shelf, Antarctic Peninsula. *Annals of Glaciology*, **39**, 505–510.
- RACK, W., ROTT, H., SIEGEL, A. and SKVARCA, P., 1999, The motion field of northern Larsen Ice Shelf, Antarctic Peninsula, derived from satellite imagery. *Annals of Glaciology*, **29**, 261–266.
- RAYMOND, C., 1996, Shear margins in glaciers and ice sheets. *Journal of Glaciology*, **42**, 90–102.
- RAYMOND, C., 2000, Energy Balance of Ice Streams. *Journal of Glaciology*, **46**, 665–674.

- RAYMOND, C., ECHELMMEYER, K., WHILLANS, I. and DOAKE, C., 2001, Ice stream shear margins. In *The West Antarctic Ice Sheet: Behavior and Environment* (American Geophysical Union), pp. 137–155.
- REEH, N., CHRISTENSEN, E., MAYER, C. and OLESEN, O., 2003, Tidal bending of glaciers: a linear viscoelastic approach. *Annals of Glaciology*, **37**, 83–89.
- REES, W., 2006, *Remote Sensing of Snow and Ice* (Boca Raton, Florida: Taylor & Francis).
- RETZLAFF, R., LORD, N. and BENTLEY, C., 1993, Airborne radar studies: ice streams A, B and C. West Antarctica. *Journal of Glaciology*, **39**, 495–506.
- RIGNOT, E., 1996, Tidal motion, ice velocity and melt rate of Petermann Gletscher, Greenland, measured from radar interferometry. *Journal of Glaciology*, **42**, 476–485.
- RIGNOT, E., 1998a, Fast Recession of a West Antarctic Glacier. *Science*, **281**, 549–551.
- RIGNOT, E., 1998b, Radar interferometry detection of hinge-line migration on Rutford Ice Stream and Carlson Inlet, Antarctica. *Annals of Glaciology*, **27**, 25–32.
- RIGNOT, E., 2001, Evidence for rapid retreat and mass loss of Thwaites Glacier, West Antarctica. *Journal of Glaciology*, **47**, 213–222.
- RIGNOT, E., 2006, Changes in ice dynamics and mass balance of the Antarctic ice sheet. *Philosophical Transactions of the Royal Society of London, Series A*, **364**, 1637–1655.
- RIGNOT, E., BAMBER, J., VAN DEN BROEKE, M., DAVIS, C., LI, Y., VAN DE BERG, W. and VAN MEIJGAARD, E., 2008, Recent Antarctic ice mass loss from radar interferometry and regional climate modelling. *Nature Geoscience*, **1**, 106–110.
- RIGNOT, E., CASASSA, G., GOGINENI, P., KRABILL, W., RIVERA, A. and THOMAS, R., 2004a, Accelerated ice discharge from the Antarctic Peninsula

- following the collapse of Larsen B ice shelf. *Geophysical Research Letters*, **31**, L18401 doi:10.1029/2004GL020697.
- RIGNOT, E., JEZEK, K. and SOHN, H., 1995, Ice flow dynamics of the Greenland Ice Sheet from SAR interferometry. *Geophysical Research Letters*, **22**, 575–578.
- RIGNOT, E., PADMAN, L., MACAYEAL, D. and SCHMELTZ, M., 2000, Observation of ocean tides below the Filchner and Ronne Ice Shelves, Antarctica, using synthetic aperture radar interferometry: Comparison with tide model predictions. *Journal of Geophysical Research*, **105(C8)**, 19,615–19,630.
- RIGNOT, E. and THOMAS, R., 2002, Mass balance of polar ice sheets. *Science*, **297**, 1502–1506.
- RIGNOT, E., THOMAS, R., KANAGARATNAM, P., CASASSA, G., FREDERICK, E., GOGINENI, S., KRABILL, W., RIVERA, A., RUSSELL, R., SONNTAG, J., SWIFT, R. and YUNGEL, J., 2004b, Improved estimation of the mass balance of glaciers draining into the Amundsen Sea sector of West Antarctica from the CECS/NASA 2002 campaign. *Annals of Glaciology*, **39**, 231–237.
- RIPPIN, D., BAMBER, J., SIEGERT, M., VAUGHAN, D. and CORR, H., 2006, Basal conditions beneath enhanced-flow tributaries of Slessor Glacier, East Antarctica. *Journal of Glaciology*, **52**, 481–490.
- RODRIGUEZ, E. and MARTIN, J., 1992, Theory and design of interferometric synthetic aperture radars. *Radar and Signal Processing, IEE Proceedings F*, **139**, 147–159.
- ROSEN, P., HENSLEY, S., JOUGHIN, I., LI, F., MADSEN, S., RODRIGUEZ, E. and GOLDSTEIN, R., 2000, Synthetic Aperture Radar Interferometry. *Proceedings of the IEEE*, **88**, 333–382.
- SCAMBOS, T., BOHLANDER, J., SHUMAN, C. and SKVARCA, P., 2004, Glacier acceleration and thinning after ice shelf collapse in the Larsen B Embayment, Antarctica. *Geophysical Research Letters*, **31**, L18402 doi:10.1029/2004GL020670.

- SCAMBOS, T., NERESON, N. and FAHNESTOCK, M., 1998, Detailed topography of Roosevelt Island and Siple Dome, West Antarctica. *Annals of Glaciology*, **27**, 61–67.
- SCHARROO, R. and VISSER, P., 1998, Precise orbit determination and gravity field improvement for the ERS satellites. *Journal of Geophysical Research*, **103(C4)**, 8113–8127.
- SCHMELTZ, M., RIGNOT, E., DUPONT, T. and MACAYEAL, D., 2002, Sensitivity of Pine Island Glacier, West Antarctica to changes in ice-shelf and basal conditions: a model study. *Journal of Glaciology*, **48**, 552–558.
- SCHOOFF, C., 2007, Ice sheet grounding line dynamics: Steady states, stability and hysteresis. *Journal of Geophysical Research*, **112**, F03S28 doi:10.1029/2006JF000664.
- SCHUTZ, B., ZWALLY, H., SHUMAN, C., HANCOCK, D. and DIMARZIO, J., 2006, Overview of the ICESat Mission. *Geophysical Research Letters*, **32**, L21S01 doi:10.1029/2005GL024009.
- SHAPIRO, N. and RITZWOLLER, M., 2004, Inferring surface heat flux distributions guided by a global seismic model: particular application to Antarctica. *Earth and Planetary Science Letters*, **223**, 213–224.
- SHEPHERD, A., WINGHAM, D. and RIGNOT, E., 2004, Warm ocean is warming West Antarctic Ice Sheet. *Geophysical Research Letters*, **31**, L23402 doi:10.1029/2004GL021106.
- SHEPHERD, A., WINGHAM, D., MANSLEY, J. and CORR, H., 2001, Inland thinning of Pine Island Glacier, West Antarctica. *Science*, **291**, 862–864.
- SHUMAN, C., ZWALLY, H., SCHUTZ, B., BRENNER, A., DIMARZIO, J., SUCHDEO, V. and FRICKER, H., 2006, ICESat Antarctic elevation data: Preliminary precision and accuracy assessment. *Geophysical Research Letters*, **33**, L07501 doi:10.1029/2005GL025227.
- SIEGERT, M. and BAMBER, J., 2000, Subglacial water at the heads of Antarctic ice-stream tributaries. *Journal of Glaciology*, **46**, 702–706.

- SKVARCA, P., RACK, W. and ROTT, H., 1999, 34 year satellite time series to monitor characteristics, extent and dynamics of Larsen B Ice Shelf, Antarctic Peninsula. *Annals of Glaciology*, **29**, 255–260.
- SMITH, A., 1991, The use of tiltmeters to study the dynamics of Antarctic ice-shelf grounding lines. *Journal of Glaciology*, **37**, 51–58.
- SMITH, A., 1997a, Basal conditions on Rutford Ice Stream, West Antarctica, from seismic observations. *Journal of Geophysical Research*, **102(B1)**, 543–552.
- SMITH, A., 1997b, Seismic investigations on Rutford Ice Stream, West Antarctica. PhD thesis, Open University.
- SMITH, A., 1997c, Variations in basal conditions on Rutford Ice Stream, West Antarctica. *Journal of Glaciology*, **43**, 245–255.
- SMITH, A., 2006a, Microearthquakes and subglacial conditions. *Geophysical Research Letters*, **33**, L24501 doi:10.1029/2006GL028207.
- SMITH, A., “RABID: Basal conditions on Rutford Ice Stream, West Antarctica: Hot-water drilling and down-hole instrumentation. Field Report 2004/2005 season”, 2006b.
- SMITH, A. and DOAKE, C., 1994, Sea-bed depths at the mouth of Rutford Ice Stream, Antarctica. *Annals of Glaciology*, **20**, 353–356.
- SMITH, A. and MURRAY, T., 2008, Bedform topography and basal conditions beneath a fast-flowing West Antarctic ice stream. *Quaternary Science Reviews*, **in review**.
- SMITH, A., MURRAY, T., NICHOLLS, K., MAKINSON, K., ADALGEIRSDÓTTIR, G., BEHAR, A. and VAUGHAN, D., 2007, Rapid erosion, drumlin formation, and changing hydrology beneath an Antarctic ice stream. *Geology*, **35**, 127–130.
- SOLOMON, S., QIN, D., MANNING, M., ALLEY, R., BERNTSEN, T., BINDOFF, N., CHEN, Z., CHIDTHAISONG, A., GREGORY, J., HEGERL, G., HEIMANN,

- M., HEWITSON, B., HOSKINS, B., JOOS, F., JOUZEL, J., KATTSOV, V., LOHMANN, U., MATSUNO, T., MOLINA, M., NICHOLLS, N., OVERPECK, J., RAGA, G., RAMASWAMY, V., REN, J., RUSTICUCCI, M., SOMERVILLE, R., STOCKER, T., WHETTON, P., WOOD, R. and WRATT, D., 2007, Technical Summary. In *Climate Change 2007: The Physical Science Basis. Contribution of Working Group I to the Fourth Assessment Report of the Intergovernmental Panel on Climate Change* (Cambridge, United Kingdom and New York, USA: Cambridge University Press), pp. 19–92.
- STEARNS, L., JEZEK, K. and VAN DER VEEN, C., 2005, Decadal-scale variations in ice flow along Whillans Ice Stream and its tributaries, West Antarctica. *Journal of Glaciology*, **51**, 147–157.
- STEIG, E., FASTOOK, J., ZWECK, C., GOODWIN, I., LICHT, K., WHITE, J. and ACKERT, R., 2001, West Antarctic Ice Sheet elevation changes. In *The West Antarctic Ice Sheet: Behavior and Environment* (American Geophysical Union), pp. 75–90.
- STENOIEN, M. and BENTLEY, C., 2000, Pine Island Glacier, Antarctica: A study of the catchment using interferometric synthetic aperture radar measurements and radar altimetry. *Journal of Geophysical Research*, **105(B9)**, 21,761–21,779.
- STEPHENSON, N. and DOAKE, C., 1986, Strain rates of Rutford Ice Stream, Antarctica. *Annals of Glaciology*, **8**, 207–207.
- STEPHENSON, N., 1984, Glacier flexure and the position of grounding lines: measurements by tiltmeter on Rutford Ice Stream, Antarctica. *Annals of Glaciology*, **5**, 165–169.
- STEPHENSON, S. and DOAKE, C., 1982, Dynamic behaviour of Rutford Ice Stream. *Annals of Glaciology*, **3**, 295–299.
- STOCKS, A. and HEYWOOD, D., 1994, Terrain modelling for mountains. In *Mountain Environments and Geographic Information Systems* (London: Taylor and Francis), pp. 25–40.

- STUEFER, M., ROTT, H. and SKVARCA, P., 2007, Glaciar Perito Moreno, Patagonia: climate sensitivities and glacier characteristics preceding the 2003/4 and 2005/6 damming events. *Journal of Glaciology*, **53**, 3–16.
- SULLIVAN, R., 2000, *Microwave Radar: Imaging and Advanced Concepts* (Boston: Artech House).
- SWITHINBANK, C., 1988, *Satellite Image Atlas of Glaciers of the World: Antarctica* (United States Geological Survey).
- TAKEDA, A., COX, S. and PAYNE, A., 2002, Parallel numerical modelling of the Antarctic Ice Sheet. *Computers & Geosciences*, **28**, 723–734.
- TESTUT, L., HURD, R., COLEMAN, R., RÉMY, F. and LEGRÉSY, B., 2003, Comparison between computed balance velocities and GPS measurements in the Lambert Glacier basin, East Antarctica. *Annals of Glaciology*, **37**, 337–343.
- THOMAS, R., RIGNOT, E., KANAGARATNAM, P., KRABILL, W. and CASASSA, G., 2004, Force-perturbation analysis of Pine Island Glacier, Antarctica, suggests cause for recent acceleration. *Annals of Glaciology*, **39**, 133–138.
- TOUZI, R., LOPES, A., BRUNIQUEL, J. and VACHON, P., 1999, Coherence estimation for SAR imagery. *IEEE Transactions on Geoscience and Remote Sensing*, **37**, 135–149.
- TULACZYK, S., SCHERER, R. and CLARK, C., 2001, A ploughing model for the origin of weak tills beneath ice streams: a qualitative treatment. *Quaternary International*, **86**, 59–70.
- VAN DER VEEN, C., JEZEK, K. and STEARNS, L., 2007, Shear measurements across the northern margin of Whillans Ice Stream. *Journal of Glaciology*, **53**, 17–29.
- VAN DER VEEN, C., 1999, *Fundamentals of Glacier Dynamics* (Rotterdam: Balkema).
- VAUGHAN, D., 1994, Investigating tidal flexure on an ice shelf using kinematic GPS. *Annals of Glaciology*, **20**, 372–376.

- VAUGHAN, D., 1995, Tidal flexure at ice shelf margins. *Journal of Geophysical Research*, **100**(B4), 6213–6224.
- VAUGHAN, D., CORR, H., SMITH, A., PRITCHARD, H. and SHEPHERD, A., 2008, Flow-switching and water piracy between Rutford Ice Stream and Carlson Inlet, West Antarctica. *Journal of Glaciology*, **54**, 41–48.
- VAUGHAN, D. and DOAKE, C., 1989, Comparison between SPOT and Landsat imagery of Rutford Ice Stream, Antarctica. *Annals of Glaciology*, **12**, 217–217.
- VAUGHAN, D., SMITH, A., CORR, H., JENKINS, A., BENTLEY, C., STENOIEN, M., JACOBS, S., KELLOGG, T., RIGNOT, E. and LUCCHITTA, B., 2001, A review of Pine Island Glacier, West Antarctica: Hypotheses of instability vs. observations of change. In *The West Antarctic Ice Sheet: Behavior and Environment* (American Geophysical Union), pp. 237–256.
- VAUGHAN, D., SMITH, A., NATH, P. and LE MEUR, E., 2003, Acoustic impedance and basal shear stress beneath four Antarctic ice streams. *Annals of Glaciology*, **36**, 225–232.
- VAUGHAN, D. and SPOUGE, J., 2002, Risk estimation of collapse of the West Antarctic Ice Sheet. *Climatic Change*, **52**, 65–91.
- VIELI, A. and PAYNE, A., 2005, Assessing the ability of numerical ice sheet models to simulate grounding line migration. *Journal of Geophysical Research*, **110**, F01003 doi:10.1029/2004JF000202.
- VOGEL, S., TULACZYK, S. and JOUGHIN, I., 2003, Distribution of basal melting and freezing beneath tributaries of Ice Stream C: implication for the Holocene decay of the West Antarctic ice sheet. *Annals of Glaciology*, **36**, 273–282.
- WEERTMAN, J., 1974, Stability of the junction of an ice sheet and an ice shelf. *Journal of Glaciology*, **13**, 3–11.
- WHILLANS, I., BENTLEY, C. and VAN DER VEEN, C., 2001, Ice streams B and C. In *The West Antarctic Ice Sheet: Behavior and Environment* (American Geophysical Union), pp. 257–281.

- WILCHINSKY, A., 2007, The effect of bottom boundary conditions in the ice-sheet to ice-shelf transition zone problem. *Journal of Glaciology*, **53**, 363–367.
- WILSON, J. and GALLANT, J., 2000, *Terrain Analysis: Principles and Applications* (New York: Wiley).
- WU, X. and JEZEK, K., 2004, Antarctic ice-sheet balance velocities from merged point and vector data. *Journal of Glaciology*, **50**, 219–230.
- ZEBKER, H. and GOLDSTEIN, R., 1986, Topographic mapping from interferometric Synthetic Aperture Radar observations. *Journal of Geophysical Research*, **91(B5)**, 4993–4999.
- ZEBKER, H., ROSEN, P., GOLDSTEIN, R., GABRIEL, A. and WERNER, C., 1994a, On the derivation of coseismic displacement fields using differential radar interferometry: The Landers earthquake. *Journal of Geophysical Research*, **99(B10)**, 19,617–19,634.
- ZEBKER, H., WERNER, C., ROSEN, P. and HENSLEY, S., 1994b, Accuracy of topographic maps derived from ERS-1 interferometric radar. *IEEE Transactions on Geoscience and Remote Sensing*, **32**, 823–836.
- ZOU, W., LI, Z. and DING, X., 2006, Effects of the intervals of tie points used in co-registration on the accuracy of digital elevation models generated by InSAR. *The Photogrammetric Record*, **21**, 232–254.
- ZOU, W., LI, Z. and DING, X., 2007, Determination of optimum window size for SAR image co-registration with decomposition of auto-correlation. *The Photogrammetric Record*, **22**, 238–256.
- ZWALLY, H., SCHUTZ, B., ABDALATI, W., ABSHIRE, J., BENTLEY, C., BRENNER, A., BUFTON, J., DEZIO, J., HANCOCK, D., HARDING, D., HERRING, T., MINSTER, B., QUINN, K., PALM, S., SPINHIRNE, J. and THOMAS, R., 2002, ICESat's laser measurements of polar ice, atmosphere, ocean and land. *Journal of Geodynamics*, **34**, 405–445.